HAL
open science

study of the multivalent carbohydrate/protein interactions on silicon biosensors

Jie Yang

To cite this version:

Jie Yang. study of the multivalent carbohydrate/protein interactions on silicon biosensors. Chemical Sciences. Ecole polytechnique X, 2014. English. NNT : . tel-01086711

HAL Id: tel-01086711

https://pastel.hal.science/tel-01086711v1

Submitted on 24 Nov 2014

HAL is a multi-disciplinary open access archive for the deposit and dissemination of scientific research documents, whether they are published or not. The documents may come from teaching and research institutions in France or abroad, or from public or private research centers.

L'archive ouverte pluridisciplinaire **HAL**, est destinée au dépôt et à la diffusion de documents scientifiques de niveau recherche, publiés ou non, émanant des établissements d'enseignement et de recherche français ou étrangers, des laboratoires publics ou privés.

Ecole Polytechnique

Laboratoire de Physique de la Matière Condensée

Thèse en vue de l'obtention du diplôme de

DOCTEUR DE l'ECOLE POLYTECHNIQUE

Spécialité: sciences des matériaux

Par

Jie YANG

Sujet

Etude des interactions multivalentes carbohydrate/protéine sur des biocapteurs de silicium

Soutenance le 23/09/2014 devant le jury composé de:

Dr. Anne IMBERTY	**Présidente du jury**
Dr. Bruno FABRE	**Rapporteur**
Dr. Yoann ROUPIOZ	**Rapporteur**
Dr. François OZANAM	**Examinateur**
Dr. Aloysius SIRIWARDENA	**Examinateur**
Dr. Anne chantal GOUGET-LAEMMEL	**Directrice de thèse**
Pr. Sabine SZUNERITS	**Co-directrice de thèse**

Acknowledgement

This work was performed in the Laboratoire de Physique de la Matière condensée of Ecole Polytechnique since October 2011. First of all, I would like to thank Ecole Polytechnique to offer me the EDX grant for the three years financial support.

I gratefully thank the members of the jury for evaluating my thesis. Firstly, I shall thank Dr. Anne Imberty from CERMAV/Grenoble, for accepting to preside over my defense. Moreover, I thank Dr. Bruno Fabre from Université de Rennes 1 and Dr. Yoann Roupioz from CEA/Grenoble to judge my thesis as reporters. It was a quite precious experience to discuss with them on my work from different disciplinary perspectives.

I am grateful for Dr. Aloysius Siriwardena, a sharp and humorous glycobiologist who acts as an examinator for my thesis. I appreciate quite for his guidance to synthesize the glycan precursors, for attending our routine discussions, for presenting me the frontier of glycomics and proteomics, and for his help in the correction of our papers. It is because of him that I fall in love with the glycobiology.

I wish to thank Dr. Francois Ozanam, the director of PMC, for paying great carefulness to correct my thesis. I was so impressed by his wisdom and profound knowledge on silicon physics and chemistry. Each time when I encountered the bottleneck in my experiment, I realized that I could solve the problems through a short talk with him because he can always provide me key answers and useful suggestions to overcome the difficulties. He is absolutely indispensable for the fruitful results of my work.

I feel highly indebted to my co-supervisor, Prof. Sabine Szunerits, who was also the director of my master thesis. I shall firstly thank her for recommending me to PMC for this PhD thesis. She is one of the most intelligent, generous and knowledgeable professors that I have ever met. It is her that opens a new insight for me to the biointerface chemistry and triggers my love with the LSPR world. Her fast-thinking personality and charming character are important to help me complete the thesis. At the meantime, I am also indebted to Dr. Rabah Boukerroub for devoting considerable time and efforts into the comments of my work and our papers.

My deepest gratitude goes here and foremost to my supervisor, Dr. Anne-Chantal Gouget, for her proposals about this interesting interdisciplinary thesis, as well as the instructive advices and helpful guidance over the three years. I shall thank her for providing me all the available resources and largest convenience to complete my work. During the practical work, I suffered often from those biochemical problems that were hard to explain because these questions seemed to be out of our expertise. Moreover, this work also made me to do a lot of tedious repeating experiments to pursue a reliable result. But she offered me complete confidence and often a warm-hearted “I trust you” to encourage me to bravely try my own ideas. We have in fact bypassed the normal relationship of supervisor-student, but we are close friends that talk and discuss almost every day. Working with her is one of the greatest pleasures in my life. I am so impressed by her humour and enthusiasm for every good result. I shall also thank her for spending a long time and great carefulness to correct my thesis and speeches, from the text structure to language expression, and even to each word, spelling, and marks. I feel deeply proud of being her first PhD student after she passed the HDR.

High tribute shall be paid to the members of my group “Electrochimie et Couches Minces”, notably Jean-Noël Chazalviel for making the miraculous numerical simulation which helped to well explain my experimental results. I shall thank Anne Moraillon for tutoring me to manipulate spotting and fluorescence imaging. I shall thank Catherine Henry de Villeneuve for the time-consuming experiment on tapping mode AFM imaging and her patient explanations to my questions. I shall thank Fouad Maroun and Philippe Allongue for occasional discussions. I shall also thank the PhD students in our group, Timothy Aschl, Nan Di, Marine Brunet. I enjoyed every moment to discuss with them about the scientific topics.

Lastly, I would express my heartful gratitude to the administrative members of the lab, especially Anne-Marie Dujardin for her help to deal with all those administrative affairs, Patrice Delaroque for daily “salutations”, Denis Coupvent-Desgraviers for the talks about Chinese culture, Elodie Quillard for the daily chatting in the last year where we found numerous common interests to get rid of our tiredness. I also want to give my best thanks to all other permanent members of the lab. It is a great pleasure to work and stay with all of them for the three years. I shall also express my last thanks for the PhD students and Post-docs, with whom I feel always happy for each entertainment moment: Lucie, Long, Daniel, Lili, Nicolas, Duc, Maxime, Maria, Manon, Fabian, Quantin, Dapajyoti, Supriyo, Alexander…

Contents

General introduction ..... - 7 -
Chapter 1: State of the art ..... - 11 -
1.1 Functionalization of hydrogenated-silicon surfaces ..... - 12 -
1.2 Antifouling surface ..... - 19 -
1.3 Binding isotherm analysis of protein assay ..... - 21 -
1.4 Metal-enhanced fluorescence ..... - 25 -
Chapter 2: Build-up of glycosylated monolayers on crystalline silicon surfaces ..... - 29 -
2.1 Introduction ..... - 30 -
2.2 Formation of azide-terminated surfaces ..... - 33 -
2.3 Formation of glycosylated surface ..... - 43 -
2.4 Conclusion ..... - 57 -
2.5 Experimental section ..... - 58 -
Chapter 3: Interaction of glycosylated surfaces with proteins ..... - 63 -
3.1 Introduction ..... - 64 -
3.2 Effects of OEG length and rinse on the (non)specific binding ..... - 67 -
3.3 Binding efficiency with the surface glycan density ..... - 76 -
3.4 Reusability of the glycosylated surfaces ..... - 88 -
3.5 Conclusion ..... - 90 -
3.6 Experimental section ..... - 91 -
Chapter 4: Quantification of proteins on crystalline silicon (111) surfaces by infrared spectroscopy ..... - 93 -
4.1 Introduction ..... - 94 -
4.2 IR calibration experiment of protein ..... - 95 -
4.3 Quantification of lectins on glycosylated surfaces ..... - 103 -
4.4 Conclusion ..... - 110 -
4.5 Experimental section ..... - 111 -
Chapter 5: Metal-enhanced fluorescence microarrays for glycan-protein detection ..... - 113 -
5.1 Introduction ..... - 114 -
5.2 Utilization of a-$Si_{1-x}C_x$:H thin films on silicon substrate: IR-ATR study ..... - 116 -
5.3 Utilization of a-$Si_{1-x}C_x$:H thin films on glass slide: MEF effect ..... - 119 -
5.4 Application of the microarrays in protein assay ..... - 133 -
5.5 Conclusion ..... - 136 -
5.6 Experimental section ..... - 137 -
General conclusion ..... - 141 -

List of abbreviations ..... - 143 -
ANNEX ..... - 145 -
I. Atomic force microscopy ..... - 145 -
II. Attenuated Total Reflection Fourier Transform Infrared spectroscopy and the quantification of surface molecules ..... - 147 -
III. X-ray photoelectron spectroscopy ..... - 152 -
IV. Spotter and fluorescence imaging ..... - 152 -
V. Plasma-enhanced chemical vapor deposition ..... - 154 -
References ..... - 155 -

General introduction

Specific protein-carbohydrate (also termed as "glycan" in biochemistry) interactions are important for numerous physiological processes, including cell growth and development, autoimmunity and fertilization, or pathological processes like bacterial and viral infection, inflammation and cancer metastasis.[1-3] These interactions occur between specific glycan epitopes such as typically found in complex glycoproteins, glycolipids or proteoglycans usually present on cell surfaces, and various proteins including antibodies, enzymes and lectins, which bind to them selectively (**Fig 1a**).[4, 5] For example, the mannose-binding lectin present on the liver cells recognizes the glycans on the surfaces of many pathogens such as *human immunodeficiency virus* (HIV) and *hepatitis C virus* (HCV) as a response to infection. The understanding of protein-glycan interactions is therefore of high importance for the development of new vaccines or therapeutic innovations.

Indeed, with more than half of the human proteins being glycan-conjugated, the use of surface bioanalytical tools that are capable of probing the protein-glycan interactions is undoubtfully one of the main driving forces to prompt the advance of glycoproteomics, as they have witnessed the flourishing development of genomics (DNA-DNA interaction) and proteomics (protein-protein interaction) over the past 20 years. However, the study of protein-glycan interactions has been lagged well behind for several difficulties. First, carbohydrates can be very difficult to obtain in large quantities and/or in homogeneous form due to the structural complexity and diversity. Second, the interaction of individual glycan epitopes with their protein receptor usually displays only low affinity (millimolar to micromolar range). So in nature, high-affinity and selective recognition between lectins and their glycan partners is achieved by multivalent interactions, which is usually observed when multiple copies of a particular glycan interact in concert with its protein counterpart itself featuring two or more glycan recognition sites.[3] Formation of these multivalent complexes, in turn, depends on appropriate spacing and orientation of glycan ligands present on the surface, imposing a stringent requirement for surface modifications (**Fig 1b**).

With the advance of new synthetic routes of carbohydrates, several surface techniques are currently employed for evaluating protein-carbohydrate interactions, including surface plasmon resonance (SPR)[6-12], microgravimetry[13-18] and other electrochemical approaches[19-23]. Compared with them, microarray technique is also one of the hotly pursued tools as it provides high-throughput screening and parallel processing while using only miniscule amounts of probe molecules.[24] The glycan microarrays, displaying numerous synthetic oligosaccharides and/or polysaccharides on a sensing surface in a spatially defined arrangement, ensure the sensitive and accurate mapping of many protein-glycan interactions at the same time *via* coupling with other approaches[25], such as SPR imaging[26, 27] and fluorescence.[28-32] Moreover, the glycan microarray reflects actually the cellular features of living organisms and promises to allow a more detailed understanding of the molecular basis of protein-glycan binding events.[33]

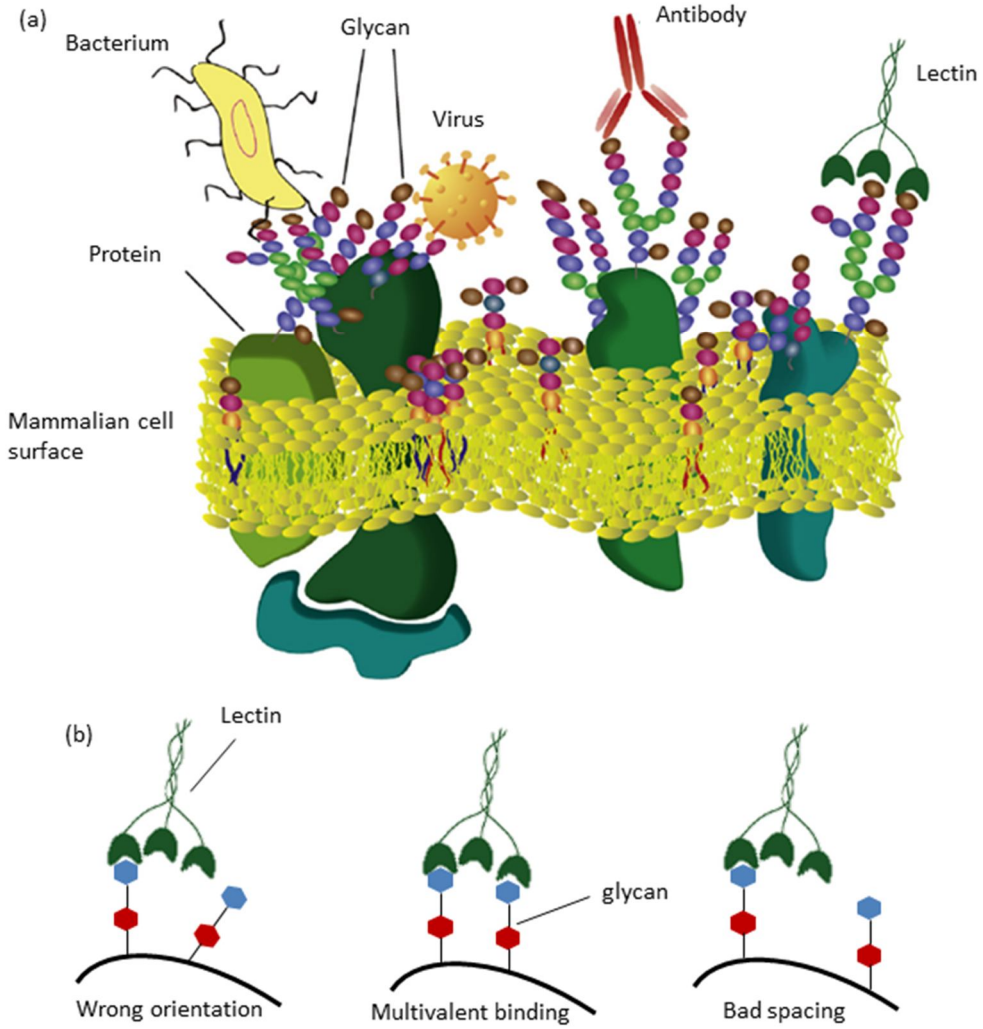

Figure 1 (a) Interaction of proteins or living organisms with glycan-terminated glycoproteins and glycolipids on cell surface; (b) dependence of high avidity multivalent binding on optimal spacing and orientation of glycan ligands.[34]

Although glycan microarray technology has become a key tool to help glycobiologists for diagnostics, many challenges remain. On the contrary to DNA sensors, the density and spacing of glycan ligands presented at the interfaces is highly crucial to favor the multivalent interactions, so it is challenging to control the immobilization of glycan probes in a controlled and quantitative way. Moreover, the protein approaching at interfaces tends to be adsorbed non-specifically, leading to the loss of its biological activity and the deteriorated selectivity of the microarray. Therefore, special attention has to be paid to limit the non-specific adsorption. Lastly, the constant demand for a higher sensitivity or lower detection limit triggers more advanced detection methods being coupled with the design of the protein chips.[35]

To circumvent these challenges, one should firstly consider the choice of chemistry for linking glycans to surfaces *reliably* and *reproducibly*. Among the surface functionalization

methods, physisorption approaches are generally convenient but, in the case of small sugars, suffer from limitations due to the weakness of the van der Waals interaction forces with the surface.[36, 37] Self-assembled monolayers (SAMs) of thiol-functionalized carbohydrates are often used since their interactions with proteins can be followed *in situ* and in real time by SPR.[28, 38-41] Alternatively, the pyrrole-derivatized oligosaccharides can be used to link glycans to SPR subtrates through electrochemical copolymerization.[6, 26] The above methods require the preparation of carbohydrate derivative precursors. Other schemes were also reported without prerequisite derivatization of carbohydrates using perfluorophenyl azide-modified surfaces which allows the non-selective photochemical attachment of carbohydrates *via* C-H bond.[27, 42-44] In addition, hydrazide or aminoxyl-terminated surfaces are also capable of linking carbohydrates at the anomeric center.[22, 45, 46]

From the viewpoint of substrate considerations, silicon-based substrates such as porous, crystalline or amorphous silicon could be a good choice since they offer excellent optical or electrical advantages that make them attractive for the bulk manufacturing of microelectronics and sensors. The dominant strategy for functionalizing silicon surfaces is based on the common siloxane chemistries on easily-prepared Si/SiO_2 surface.[22, 45, 46] However, the moisture sensitivity of silanization, instability of bound silanes and low surface coverage limit its exploitation for sensing.[47, 48] A more stable silicon functionalization strategy relies on the formation of organic monolayer through robust Si-C covalent bonds, obtained by the modification of hydrogen-terminated silicon surfaces *via* hydrosilylation chemistry using functional 1-alkenes.[49-54] Besides, the hydrogenated silicon and the subsequent functionalized monolayer is also of high interest to be followed by many well-established techniques, like infrared spectroscopy in attenuated total reflection geometry (IR-ATR), atomic force microscopy (AFM), X-ray photoelectron spectroscopy (XPS), cyclic voltammetry (CV), etc.

There are two common ways of grafting glycan molecules on hydrogen-terminated silicon surfaces. It has been reported the direct chemical attachment of glycan molecules *via* the hydrosilylation of 1-alkene functionalized glycan precursors.[55, 56] On the other hand, Cai et al. reported a step-by-step functionalization strategy on hydrogenated silicon surfaces. The main advantage of the latter method is that the density and self-assembly of the organic monolayer can be established in a well-defined manner under mild chemical conditions. Therefore, such a method is more favored for the elaboration of glycan sensors.

In the laboratory PMC, the group “Electrochimie et couches minces” has studied the organic monolayer on hydrogenated silicon surfaces for more than 15 years.[57-62] Notably, A. Faucheux et al. studied the hydrosilylation of 1-alkene type precursors on hydrogenated crystalline silicon surfaces *via* photochemical or thermal activation.[63] For instance, *via* the hydrosilylation of undecylenic acid, a fairly dense carboxylic acid-terminated monolayer can be formed, which allows the further attachment of biomolecules through simple amidation strategy.[64]

With this well-optimized functionalization method, L. Touahir completed a revolutionary work during his thesis where he took advantage of the optical property of amorphous silicon-carbon (denoted as a-$Si_{1-x}C_x$:H) thin film coated on metal surfaces, onto which a new architecture of DNA microarray was built up.[65-72] The a-$Si_{1-x}C_x$:H thin film was treated analogously to generate hydrogenated silicon bonds for the grafting of carboxylic acid-

terminated monolayer. Starting from this surface, the immobilization of oligonucleotide strand was performed *via* an easy amidation reaction by spotting approach. The most striking property of this new conception of DNA microarray is that numerous optical approaches could be coupled, such as metal-enhanced fluorescence (MEF)[68-70], localized surface plasmon resonance (LSPR)[72] and SPR[67, 71], leading to a signal readout with ultrahigh sensitivity (~a detection limit of femtomolar for LSPR-enhanced fluorescence)[68], good reproduciblity and possibly in real-time.

Motivated by these acquired resources, my thesis aimed ultimately at the development of a-$Si_{1-x}C_x$:H thin film based glycan microarray for the detection of specific lectins using MEF. Prior to this aim, effort was devoted to the following points: first, the control of the chemistry of immobilizing glycans; Second, the optimization of the surface glycans in terms of density and spacing to favor the multivalent binding; third, the minimization of non-specific adsorption; last, the improvement of the detection sensibility. To illustrate clearly this work, the thesis is deployed in five chapters.

The first chapter is dedicated to the introduction of some principles and theoretical concepts: functionalization of hydrogen-terminated silicon surfaces; surface antifouling property; binding analysis methodologies and metal-enhanced fluorescence.

The second chapter is devoted to the build-up of the glycosylated architecture on crystalline silicon (111) surface. We used a step-by-step modification process which was followed and analyzed by different techniques, including quantitative IR-ATR, AFM and XPS. These techniques offered a general view of “how many” molecules are immobilized and how the organic monolayer looks like.

The third chapter describes the interactions of these fabricated glycan-surfaces with specific and non-specific lectins. Efforts were made to limit the non-specific adsorptions whereas for specific bindings, the relationship of the glycan ligand density with the binding efficiency of lectins was studied and the binding affinity was measured.

The forth chapter takes advantage of quantitative IR-ATR to determine the density of protein bound to glycosylated surfaces. The quantitative result was correlated with AFM results, thus had allowed establishing reliable models to interpret the multivalent interaction of glycan with its specific lectin.

The last chapter is dedicated to the elaboration of the glycan microarrays on a-$Si_{1-x}C_x$:H thin film coated on metal nanostructures for the detection of specific lectins by LSPR-enhanced fluorescence. This part of work concerns notably how the new conception of glycan microarrays was engineered to obtain good selectivity and high sensitivity.

This work was completed in collaboration with Prof. Sabine Szunertis from the IRI institute of the University of Lille1 for the preparation of LSPR substrate and Dr. Aloysius Siriwardena from the University of Jules-Verne for the synthesis of glycan derivatives.

CHAPTER 1

State of the art

.

1.1 Functionalization of hydrogenated-silicon surfaces

1.1.1 Choice of substrate

Silicon is one of the most "famous" substrates used in microelectronics and (bio)sensors. There are different forms of silicon that can be chosen as material substrate, such as porous, crystalline silicon and amorphous silicon thin films, ... In this thesis, we used two types of silicon: crystalline and amorphous silicon. The functionalization of silicon for the immobilization of glycans was established on crystalline silicon because it allows perfectly controlled chemistry and is appealing to be characterized by quantitative IR-ATR, AFM and XPS techniques. While for the elaboration of glycan microarrays using fluorescence as the measurement technique, thin films of amorphous silicon-carbon alloy were employed. When deposited on a glass substrate, they offer a more favorable optical configuration than bulk silicon.

Crystalline silicon exhibits an ordered arrangement of Si atoms. The crystallographic (111) face is generally used for a well-controlled surface functionalization as it allows the formation of smooth hydrogenated surface at atomic level, making it a model system for AFM studies (**Fig 1.1**).

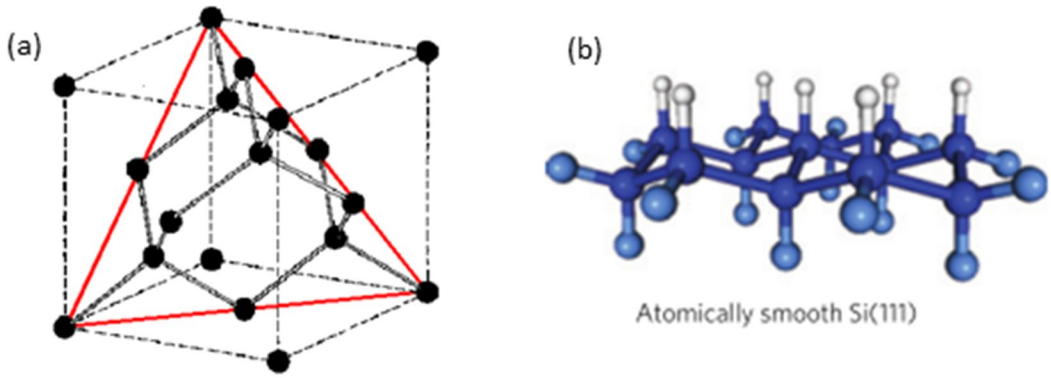

Figure 1.1 (a) Cubic lattice of crystalline silicon with the (111) face represented in red; (b) formation of atomically hydrogenated smooth (111) face upon etching in NH_4F. Si: blue; H: white.[73]

Compared with crystalline silicon, amorphous silicon (a-Si) presents a disordered structure at large scale (**Fig 1.2b**). Due to the distortion of the a-Si structure, a great number of silicon atoms are not readily bonded and unpaired electrons are present. Those non coordinated defects are called dangling bonds. Physically, these dangling bonds are highly unstable and

can be passivated by hydrogen leading to the formation of hydrogenated amorphous silicon (a-Si:H).

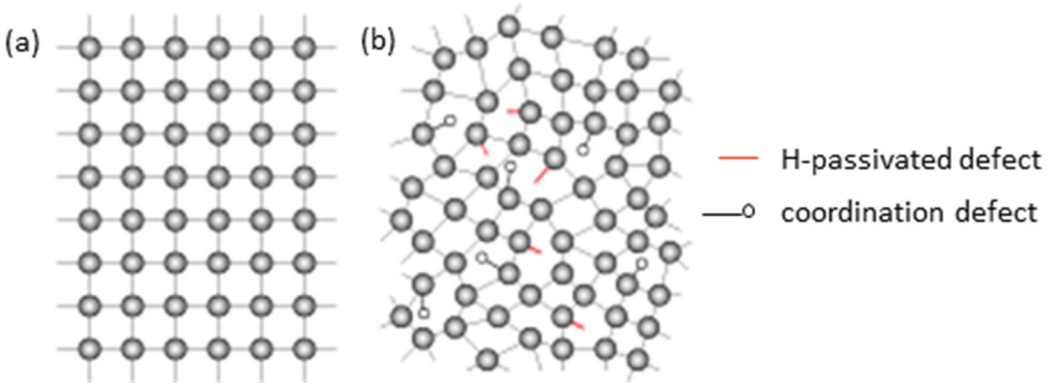

Figure 1.2 Schematic representation of the structure of crystalline silicon (a) and hydrogenated amorphous silicon (b).

The optical property of a-Si:H can be further changed by adding carbon into the random network to form amorphous silicon-carbon alloy (a-$Si_{1-x}C_x$:H). The smaller radius of carbon atom increases the band gap of a-$Si_{1-x}C_x$:H compared with a-Si:H, leading to a reduced refractive index. **Fig 1.3** shows the real and imaginary parts of the refractive index of a-$Si_{1-x}C_x$:H as a function of carbon content. As the carbon content is increased, the refractive index decreases. The a-$Si_{1-x}C_x$:H can be deposited on any type of materials as thin films in a controlled manner notably by plasma-enhanced chemical vapor deposition (PECVD) at low power.

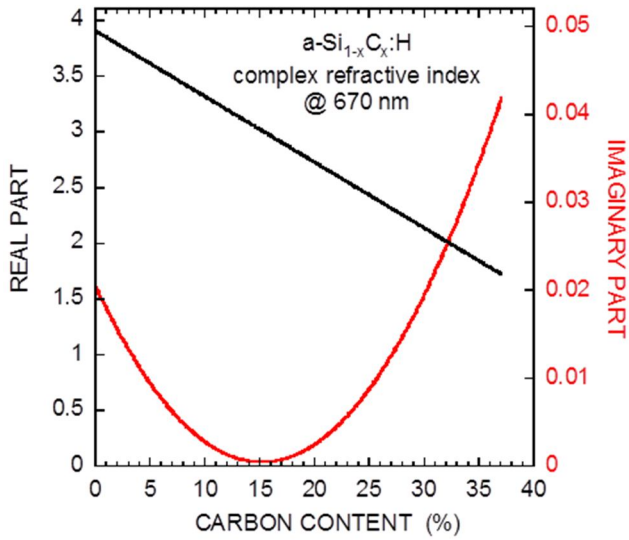

Figure 1.3 Diagram of the real (black) and imaginary (red) parts of the refractive index of a-$Si_{1-x}C_x$:H measured at 670 nm, as a function of carbon content.

In the laboratory PMC, Solomon et al. studied the relationship between the methane content in gas phase and the resulting carbon content in the deposited film.[74] By controlling the growth speed of the film and the methane/silane ratio, the a-$Si_{1-x}C_x$:H thin film with the desired carbon content and thickness can be obtained.

1.1.2 Hydrogenated silicon surface

From the end of 1960s, we have known that the silicon can be passivated by a treatment in hydrogen fluoride (HF) with the formation of Si-H bonding.[75] In the beginning of 1980s, the the formation of hydrogen-terminated silicon was studied by Ubara *et al.*,[76] Higashi and Y. Chabal *et al.*[77-83] They demonstrated that the highly polarized Si-F bond is formed after the dissolution of interfacial oxide, which then induces the polarization of $Si^{\delta-}$-$Si^{\delta+}$-F back bond. In the subsequent attack of HF, the $Si^{\delta-}$-$Si^{\delta+}$ bond is cleaved. As a consequence, the first layer of Si is fluorinated and removed, leaving the underlying Si layer being hydrogenated (**Fig 1.4**).

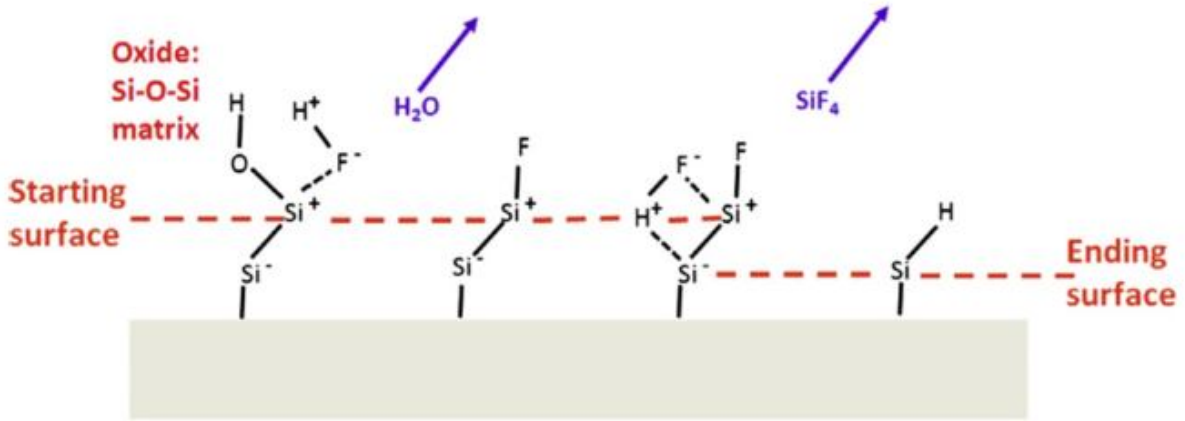

Figure 1.4 Mechanism leading to the formation of H-terminated Si surface by HF etching.[54]

The hydrogenated silicon surfaces are easily prepared and relatively stable in air, which makes them particularly interesting for the use in (bio)sensors. The homogeneity of the formed H-terminations and the surface microstructure are highly dependent on pH of the fluoride solution.[79] The etching in acidic condition (i.e., HF solution) results in the formation of a rough surface containing monohydride, dihydride and trihydride (denoted as SiH_x),[82, 84] whereas solely monohydride (SiH) is formed in basic condition (i.e., NH_4F solution).[78, 80] On Si (111) surfaces these monohydride bonds are ideally ordered and normal to the surface (**Fig 1.1b**).

In 1995, Allongue et al. demonstrated the coexistence of two dissolution pathways of silicon in NH_4F solution: a chemical way and an electrochemical way (**Fig 1.5**).[85] Both routes lead to the substitution of Si-H bond by Si-OH bond. The chemical route occurs preferentially at step atoms while the electrochemical path is much less site dependent. This model states that molecular water is the oxidizing agent and the F^- species are thought to be catalysts of the reaction, helping in solubilizing the Si atoms. He also pointed out that the solution should be basic (pH=8-9) and oxygen-free solution are important to favor the formation of flat surface without surface pitting.[86,87]

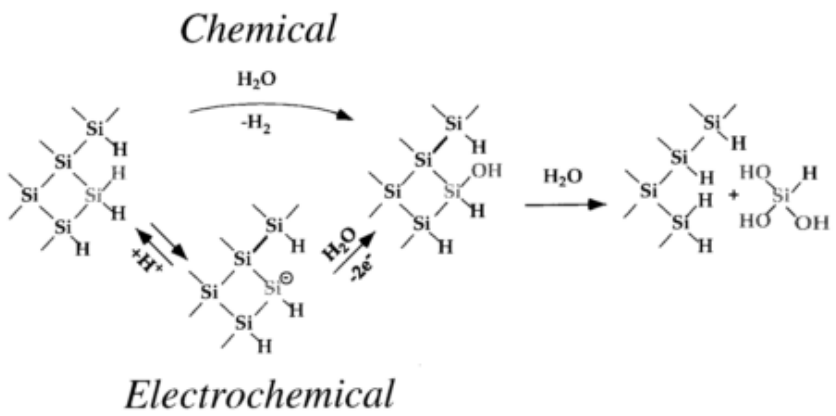

Figure 1.5 Molecular model focusing on the initial step of Si dissolution from a kink site including an electrochemical (bottom) and a chemical (top) route.[85]

For AFM studies, we chose a one-side polished silicon (111) wafer with a miscut of 0.2° toward the $(11\bar{2})$ direction. Upon a controlled etching in NH_4F, the staircase structure can be formed with each terrace exhibiting a flatness at the atomic level (**Fig 1.6**). For IR studies, we chose a double side polished silicon (111) prism to prepare SiH_x or SiH surfaces. The SiH_x surface was mainly studied because the resultant rough microstructure is similar to that on a-$Si_{1-x}C_x$:H thin films.[64] The etching of a-$Si_{1-x}C_x$:H thin films was performed in HF vapor.

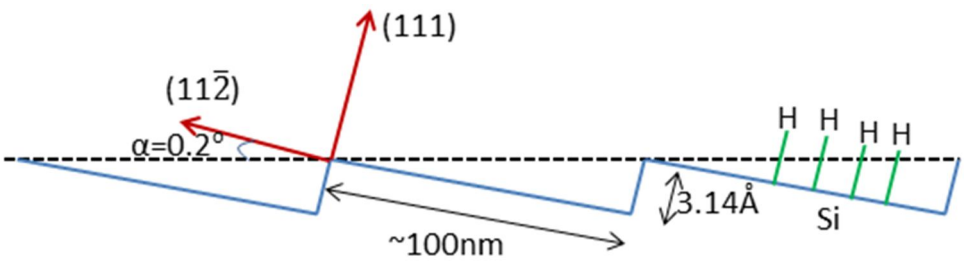

Figure 1.6 Scheme of the formation of staircase structure upon a controlled etching in NH_4F. The surface is Si(111) with a miscut of 0.2° toward the $(11\bar{2})$ direction.

1.1.3 Hydrosilylation reaction

At the beginning of 1990s, Linford et al. proposed the first grafting of organic species on a hydrogenated silicon surface using a hydrosilylation reaction to form an alkyl monolayer attached on the surface *via* Si-C bonds. The raction was initiated by the presence of diacyl peroxides.[88] Later on, other reaction routes were discovered notably for unsaturated alkyl compounds *via* thermal,[89, 90] Lewis acid-catalyzed,[50, 91-94] or photochemical activation.[95-100] The hydrosilylation consists of the insertion of the unsaturated double or triple bond into the Si-H bond. The utilization of photochemical activation, such as UV or Vis irradiation, is advantageous since it is relatively mild (at room temperature), fast (a few hours) and leads to an appreaciable yield. The UV-activated hydrosilylation is supposed to obey a radical-initiated mechanism (**Fig 1.7**), where the silicon dangling bond is generated upon UV irradiation which reacts with the C=C double bond to form the Si-C bonding.[52] The radical present on the alkyl chain is able to abstract a neighbouring H to terminate itself.[95, 101] Zuilhof *et al.* proposed successively an electron/hole pair mechanism to account for the hydrosilylation activated by visible light,[99, 100, 102] similar to the exciton-mediated mechanism occuring on porous silicon proposed by Stewart *et al.*[98] Moreover, Hamers *et al.* also proposed a photoemission pathway for UV-initiated grafting of alkenes on H-terminated silicon surfaces.[103]

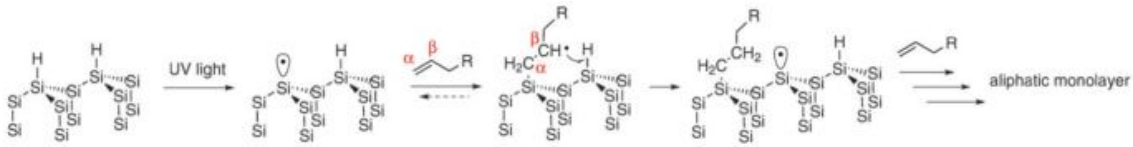

Figure 1.7 Scheme of the chain propagation mechanism for 1-alkenes reacting with Si(111) silyl radical.[52]

The hydrosilylation of ω-functionalized 1-alkene precursors on hydrogenated silicon surfaces is important and interesting for further functionalization strategies (**Fig 1.8**).[51, 53, 104] One of the most important functionalized monolayers is the carboxydecyl-terminated monolayer, which is often used as the starting surface for multi-step functionalization allowing covalent attachment of (bio)molecules.[105, 106]

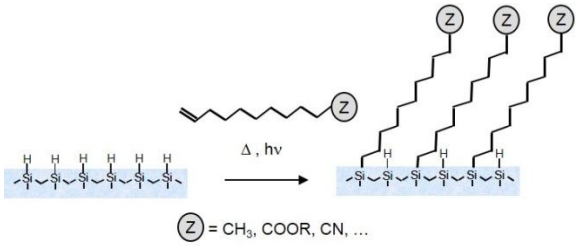

Figure 1.8 Schematic representation of the formation of organic monolayer through hydrosilylation.[63]

Such a monolayer can be easily obtained by the direct photochemical grafting of undecylenic acid on the hydrogenated Si(111) surfaces, as demonstrated by Faucheux et al. in the laboratory PMC.[63] It was proved that there was no side reaction between the carboxyl group and Si surface and the reaction process was oxide-free. Moreover, the Si/molecular layer presents excellent electronic properties (such as a low density of state). It is also important to rinse the reacted surfaces in hot acetic acid to remove the physisorbed unreacted undecylenic acid molecules. In addition, the density of the monolayer was quantifiable by IR-ATR, confirming the formation of a fairly dense monolayer was anticipated.

1.1.4 Amidation reaction

The carboxylic acid-terminated surface is interesting to be further functionalized through a variety of coupling strategies, typically, the esterification and amidation reactions by reacting with alcohols and amines. The esterification is an equilibrium reaction that suffers seriously from hydrolysis, whereas the amidation produces stable amide bonds. However, the direct amidation is usually achieved by condensation of acid-amine salt at high temperature which limits its application in biosynthesis.[107, 108] Therefore the amidation of biomolecules under mild chemical conditions was developped using peptide coupling reagents, like carbodiimide, aminium or phosphonium salts of benzotriazole derivatives, ….[109] The amidation reaction undergoes an intermediate activation step where the carboxyl moiety is transferred to a good leaving group, which is subsequently aminolyzed by the amine-derivatized (bio)molecules.

One of the mostly employed coupling strategies to obtain activated surfaces is to use ethyl(dimethylaminopropyl) carbodiimide (EDC) in the presence of *N*-hydroxysuccinimide (NHS) (**Fig 1.9**). The advantage of this strategy for linking biomolecules lies in its low cost, non-toxicity, water solubility and the self-hydrolysis in water which does not need additional purification. The use of NHS is to form a quite stable intermediate NHS-ester in order to improve the final amidation yield. In this reaction, the –OH of carboxylic acid is added on the imide bond of EDC to form the unstable O-acyl urea which is subsequently replaced by NHS to form stable “active” NHS-ester.

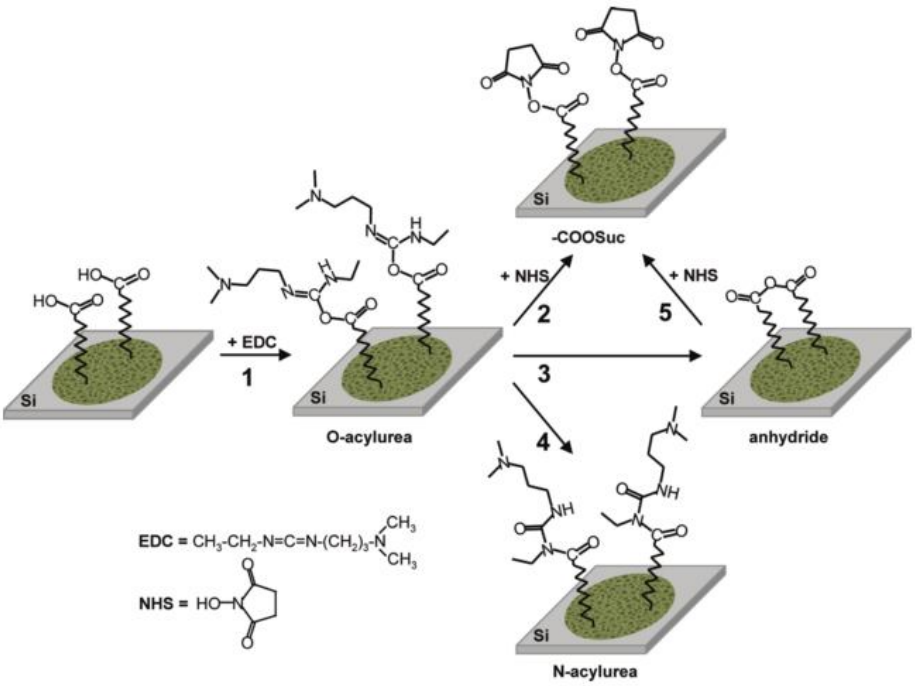

Figure 1.9 Scheme describing the activation reaction on carboxyl-terminated porous silicon surfaces. Initially, the surface acid groups react with EDC resulting in the formation of O-acyl urea (**1**). Subsequently, various paths are available with the formation of succinimidyl ester (**2**), anhydride (**3**), N-acyl urea (**4**). **4** is side reaction, yielding an unwanted byproduct.[110]

In the laboratory PMC, S. Sam and L. Touahir et al. have previously studied the activation step by working with porous or crystalline silicon surfaces. They demonstrated that the use of equivalent amount of EDC and NHS (5-10 mM) at 15°C is important to avoid uncompleted or side reactions and obtain good ester-NHS terminated monolayers.[42, 43]

The successive aminolysis takes place on the ester-NHS terminations which is substituted by the amino molecules.

1.2 Antifouling surface

The elimination of non-specific protein adsorption is a challenge for the fabrication of protein sensors. To discuss an adsorption behavior occurring at solution/interface, one should consider the property of three partners: protein, surface and solution.[111] These factors influence comprehensively the protein adsorption. The protein property includes, i.e., pI, polarity, hydrophilicity, etc, the solution property includes, i.e., temperature, pH, ionic strength, etc and the surface property includes, i.e., surface charge, polarity and morphology, etc.[112] For example, the pH of buffer affects the charge of the protein outer surface, thus alters its interaction with the charged surface.[113]

A surface able to resist non-specific protein adsorption is called “antifouling” surface. In the field of material science, antifouling property can be achieved by modifying the surface with a protein-resistant biofilm, such as hydrophilic polymers (i.e., polysaccharide) and zwitterionic polymers.[114-119] In general, a good antifouling surface structure is anticipated to be hydrophilic, containing groups of hydrogen-bond acceptors but not donors and overall electrically neutral.[120] Among a variety of artificial antifouling structures, poly(ethylene glycol) (PEG) is one of the most often used molecules for its good water solubility, nontoxicity, non-immunogenicity and biocompatibility.

The mechanism of protein resistance and the role of PEG involved in the protein repellence have not yet been fully understood. Currently, there are two theories mostly accepted. One “physical” view relies on the excluded volume theory to explain the behavior of the PEG on the surface, stating that the available volume for each polymer segment is reduced when protein get close to the PEG-coupled surfaces, consequently a repulsive force is generated due to the loss of conformational entropy of the PEG chains.[121, 122] Another “chemical” view focuses on the role of water bound around the PEG chains which readily forms a water matrix of high density to help buffering the protein attaching to the surface (**Fig 1.10**).[123-127]

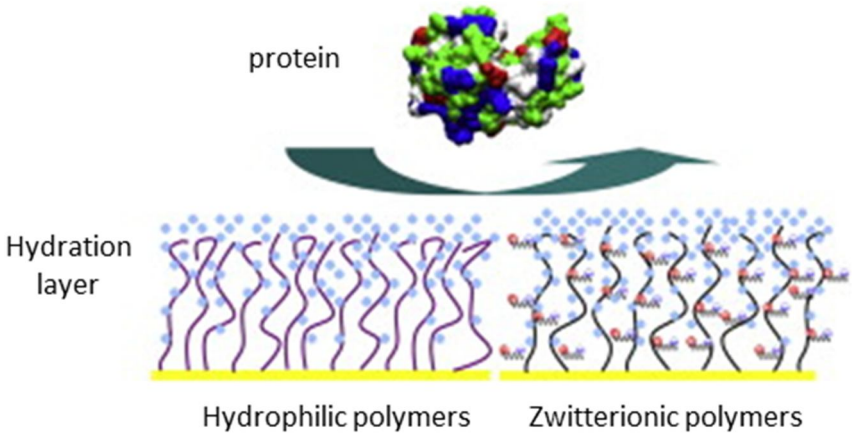

Figure 1.10 Scheme for the hydration layer formed on hydrophilic and zwitterionic polymers serving to resist the protein adsorption.[127]

The antifouling extent of the PEG monolayer is highly dependent on the length, conformation and density of the chains on the surface.[128-132] Normally, a longer and a denser PEG monolayer is deemed to have better antifouling property. In the laboratory PMC, E. Perez studied the antifouling property of oligo/poly(ethylene glycol) monomethyl ether on hydrogenated silicon surfaces during his thesis.[133] In one way, the molecule OEG carrying an hydroxyl group at one end and methoxyl group on the other end (abbreviated as $H(EG)_nOMe$, n=3-16) was grafted directly on hydrogenated silicon surface through Si-O bond. The as-formed OEG monolayers were rather dense (2×10^{14} cm^{-2}) and yielded excellent repellence towards *bovine serum albumin* (BSA), which is one of the most adhesive proteins on the surface. However, the polarized Si-O bond suffered from hydrolysis, leading to the reduced antifouling performance with time. In the other way, the OEG monolayers were built by the hydrosilylation of vinyl-terminated OEG precursors (abbreviated as $CH_2=CH-C_{p-2}(EG)_n$ with the $3 < p < 11$ and $3 < n < 16$) on hydrogenated silicon surfaces. By playing with various *p* and *n* values of the alkyl and ethylene glycol units, it was able to achieve a powerful resistance to proteins when *n* is large enough ($n > 12$) and *p* is small enough. The density of these OEG monolayers was much lower (1×10^{14} cm^{-2}) so that the good antifouling property was thought to arise *a priori* from the entanglement of OEG chains.[134]

1.3 Binding isotherm analysis of protein assay

Biointeractions can be always described as a formula like $R + L \leftrightarrow RL$, where R stands for receptor, L for ligand and RL for the formed complex. The ligand usually refers to small molecule whereas receptor refers to large molecule. In surface bioanalysis, the term "probe-target interaction" is also often used, where the "probe" refers to the molecule immobilized on the biosensor and the "target" refers to the molecule in the analyte. The binding affinity is an important parameter in biochemistry that measures the strength of the interaction. For example, the determination of the binding affinity is important in pharmacology to evaluate the efficacy of drugs to the target cells or proteins. The binding affinity can be described by the association constant (K_a) or its inverse the dissociation constant (K_d). For a particular binding issue studied by biosensors, the experimental data can be treated to obtain the isotherm curve for the calculation of the association constant. This curve plots the amount of adsorbed target molecules by the sensor as a function of their concentrations in analyte. Plenty of models were established to interpret the obtained binding curves.

1.3.1 Langmuir model

It is one of the mostly used models in biological experiments. Several assumptions are established:

- The surface is perfectly homogeneous.
- The protein is ideally immobile after being absorbed on the surface.
- All ligands are equivalent.
- Monovalent interaction between protein and surface ligand.
- No interactions between protein molecules on adjacent sites

For a surface binding event,

$R + L \leftrightarrow RL$ (R: protein receptor in solution; L: ligand site on surface)

The association constant: $K_a = \frac{[RL]}{C_R \times [L]} = \frac{[RL]}{C_R \times ([L_{total}] - [RL])} = \frac{\theta}{C_R \times (1-\theta)}$ (θ is the surface coverage; C_R is the protein concentration in the analyte).

Therefore, $\theta = \frac{K_a C_R}{1 + K_a C_R}$ or $\frac{C_R}{K_d + C_R}$

In our experiment, $\theta = \frac{A}{A_m}$ (A is the IR absorbance response for a given concentration of proteins and A_m is the saturated maximum response).

1.3.2 FFG model and Temkin model

The Langmuir model is far from the real binding conditions that limits its application in many experimental cases. For example, in the presence of cooperative interactions among the protein receptors or in case of multivalent interactions between receptors and ligands, the theoretical assumptions should be modified.

In the Langmuir equation, K_a characterizes the strength of binding which can be alternatively described by an adsorption energy E_{ads}, $K_a = \frac{1}{C^{\ominus}}\exp(-\frac{E_{ads}}{RT})$. Assuming that there are intermolecular interactions among the protein receptors, the energy term has to take these interactions into account that E_{total}=$E_{ads} + \alpha\theta$, so the apparent association constant $K_a{}' = \frac{1}{C^{\ominus}}\exp(-\frac{E_{total}}{RT}) = \frac{1}{C^{\ominus}}\exp(-\frac{E_{ads}+\alpha\theta}{RT}) = \frac{1}{C^{\ominus}}\exp(-\frac{E_{ads}}{RT} - \beta\theta)$ (making $\beta = \frac{\alpha}{RT}$).

The Langmuir equation is thus modified,

$$\theta = \frac{K_a{}'C}{1+K_a{}'C} \leftrightarrow C = \frac{\theta}{(1-\theta)K_a{}'} = \frac{\theta}{(1-\theta)\frac{1}{C^{\ominus}}\exp(-\frac{E_{ads}}{RT}-\beta\theta)} = \frac{\theta}{(1-\theta)\ \frac{1}{C^{\ominus}}\exp(\frac{-E_{ads}}{RT})}e^{\beta\theta} = \frac{\theta}{(1-\theta)K_a}e^{\beta\theta} \quad ,$$

K_a still represents the adsorption constant of the binding and β measures the intermolecular interactions.[135]

In case of $\beta < 0$, the intermolecular force is attractive, the model is called Frumkin-Fowler-Guggenheim (FFG) model.

In case of $\beta = 0$, the intermolecular force is not present, the model is Langmuir model.

In case of $\beta > 0$, the intermolecular force is repulsive, the model is called Temkin model.

1.3.3 Freundlich model

Freundlich isotherm is an empirical phenomenon observed on the heterogeneous surface with different adsorption sites. Its equation is $\theta = \alpha_F C^{1/n}$. α_F is an indicator of adsorption capacity, while 1/n is a function of the strength of adsorption in the adsorption process. If n = 1, the adsorption is linear with the concentration. If 1/n < 1, it indicates a normal adsorption. If 1/n > 1, it indicates a cooperative adsorption.[136]

The Freundlich model has been reported to describe the non-specific adsorption of proteins contacting the nanoparticles coated heterogeneous surface.[137-140]

Fig 1.11 resumes the shape of the above isotherm curves, where the Langmuir equation is united together with FFG and Temkin models.

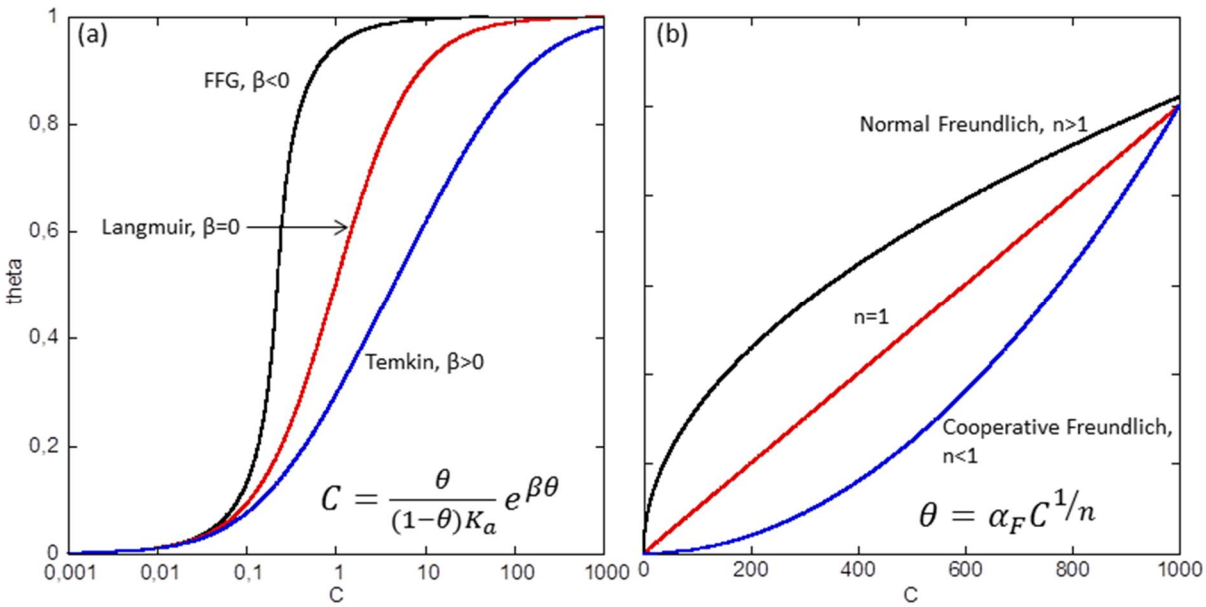

Figure 1.11 Modeled curve shape for different isotherms: (a) Langmuir, FFG and Temkin models; (b) Freundlich model.

1.3.4 Scatchard plot

The Langmuir equation, $\theta = \frac{K_a C}{1+K_a C}$ can be also expressed as $\frac{\theta}{C} = K_a - K_a\theta$. This equation can be fitted by plotting θ / C as a function of θ, the y-intercept is K_a, and the slope is $-K_a$.

When the Langmuir model is not obeyed, the Scatchard plot is not a straight line. As shown in **Fig. 1.12**, a concave-up curve may indicate the presence of non-specific binding, negative cooperativity between receptors or multiple classes of binding sites with different K_d values, whereas a concave-down curve is indicative of positive cooperativity.[141]

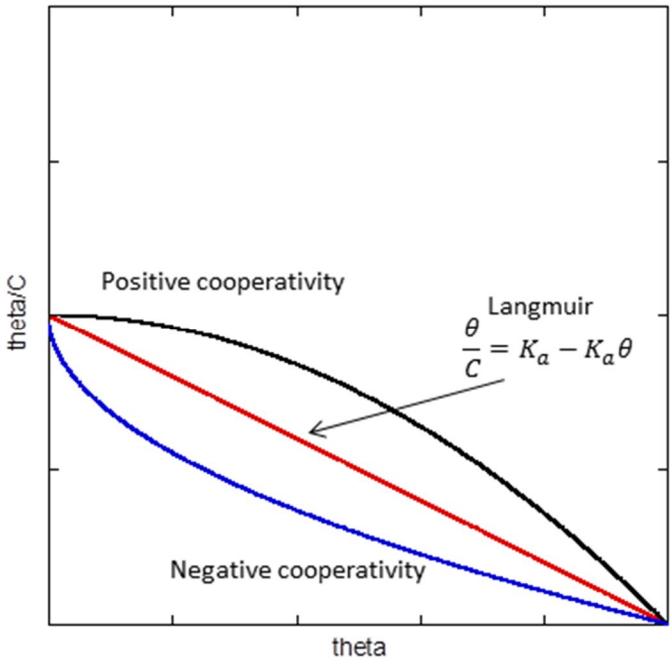

Figure 1.12 Modeled curve shape for linear and non-linear Scatchard plot.

Usually the choice of different models is difficult to predict for an unknown binding activity. One of the treatments is to look at the shape of the isotherm curve, such as the plots in **Fig 1.11**, and look for the presence of asymptote. The Langmuir, FFG and Temkin models show an y-asymptote as the concentration increases whereas the Freundlich model is not saturable. Then, in case of asymptote present binding curves, a steep "climbing rate" of concentration indicates the FFG model whereas a moderately increased curve may be indicative of Temkin model. In all cases, the application of these isothermal models relies on the experimental data. To make a correct conclusion, it is important to obtain as many data points as possible in a large concentration range and utilize as sensitive analysis methods as possible.

1.4 Metal-enhanced fluorescence

Fluorescence is one of the most common techniques used for biochips because of its versatility, ease of use and ultrahigh sensitivity. Many target biomolecules can be labeled with fluorophores like cyanine Cy3 ($\lambda_{excitation}$ = 550 nm, $\lambda_{emission}$ = 570 nm) or Cy5 ($\lambda_{excitation}$ = 650 nm, $\lambda_{emission}$ = 670 nm). One of current challenges of fluorescence technique lies in the constant demand for pursuing higher sensitivity to detect trace amount of analyte.

The fluorescence yield of a fluorophore located close to a substrate depends on the refractive index of the substrate and the distance between the fluorophore and the substrate. One method to improve the fluorescence yield is the use of metallic or multilayer dielectric mirror. The metal mirror can serve as an efficient reflector of both excitation and emission light, leading to an enhancement of fluorescence yield. Using this concept, a new architecture of DNA biochip was designed by Touahir et al. based on the a-$Si_{1-x}C_x$:H thin films which was deposited on aluminum mirror.[70] The use of a-$Si_{1-x}C_x$:H thin films guarantees the formation of stable monolayers through covalent Si-C bond and provides a dense grafting yield of probe molecules. For instance, by the use of transparent a-$Si_{0.8}C_{0.2}$:H coating, the Cy5-labeled DNA was immobilized on the surface. **Fig 1.13** represents the calculated fluorescence yield of Cy5 as a function of the thickness of the a-$Si_{0.8}C_{0.2}$:H coating on different metal mirrors. The fluorescence yield exhibits an interference pattern. By choosing a proper thickness of a-$Si_{0.8}C_{0.2}$:H (~40 nm), the fluorescence yield can be enhanced by a factor of ~15 in presence of aluminum mirror compared with the deposition of a-$Si_{0.8}C_{0.2}$:H on bare slide (film thickness of ~124 nm).

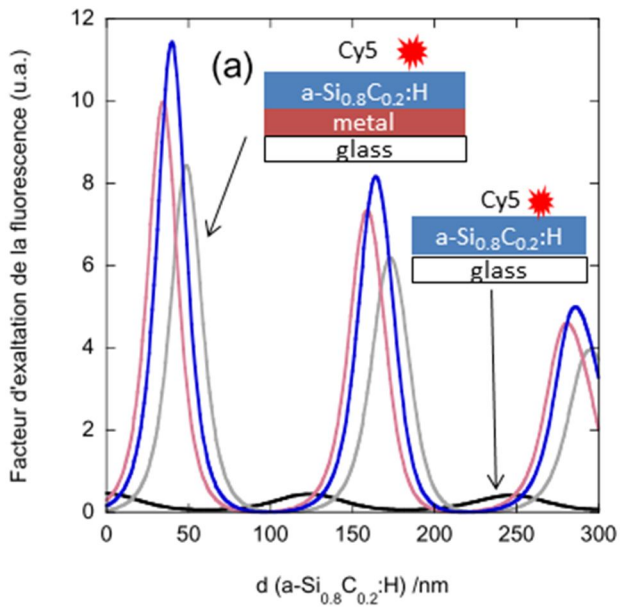

Figure 1.13 Calculation of the fluorescence enhancement factor as a function of the thickness of a-$Si_{0.8}C_{0.2}$:H coated substrates: glass (black); gold (pink); silver (blue); aluminum (gray).

A second efficient method to enhance the fluorescence sensing is the use of noble metallic thin films or nanostructures. On a flat metallic surface, the free electrons on the metal surface can be excited upon the interaction with the incident light so that the so-called propagative surface plasmon resonance (SPR) is generated along the surface (**Fig 1.14a**). The noble metals are the mostly used as the SPR source, such as gold or silver, because their SPR can be induced by visible light. The SPR is obtained by using a proper optical geometry, like the Kretschmann configuration.

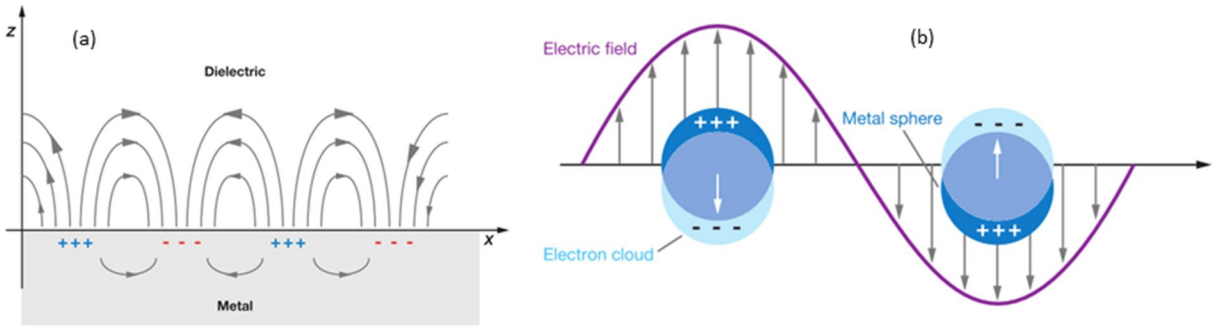

Figure 1.14 Schematic diagrams illustrating (a) a surface plasmon (or propagating plasmon) and (b) a localized surface plasmon.[142]

Whereas in the case of metallic nanostructures, upon the interaction with incident light, the free electrons exhibit collective oscillation of conducting electrons around the nanostructures and the so-called localized surface plasmon resonance (LSPR) is generated (**Fig 1.14b**). The LSPR is more easily obtained than SPR as it can be induced by simply a normal incident visible light, whereas exciting SPR requires a correct matching of the incident angle. The utilization of SPR or LSPR allows a direct detection of target molecules without labeling.[67, 71, 72, 143-153] They also produces favorable fluorescence enhancement effect,[68, 69] as a result of the enhanced electric field along the metal interface or surrounding the metallic nanoparticles.[154-157] Such an effect is called plasmon-enhanced fluorescence.

In the laboratory PMC, L. Touahir also studied the elaboration of plasmonic biosensors based on a-Si_{1-x} C_x:H coated silver or gold films/nanoparticles.[68, 69] In these designs, the choice of the carbon content and thickness of a-$Si_{1-x}C_x$:H thin films is important in order to reserve the optical property in terms of the SPR or LSPR sensitivity. In case of SPR-enhanced fluorescence, a multiple layered structure, a-$Si_{0.8}C_{0.2}$:H (3 nm)/ a-$Si_{0.63}C_{0.37}$:H (3 nm)/Ag (38 nm)/glass was established to favor the immobilization of DNA strand. It was found a limit of detection at 500 fM for the hybridization of the complementary strand.[69]

In the design of LSPR-enhanced fluorescence, the LSPR was obtained by a deposition of gold nanoparticles (AuNPs) on the glass slide, which was covered by a-$Si_{1-x}C_x$:H thin films. The LSPR property in terms of its intensity and position is affected by the refractive index of the a-$Si_{1-x}C_x$:H thin films. **Fig 1.15** represents the LSPR spectra of different a-$Si_{1-x}C_x$:H coatings on AuNPs. The AuNPs exhibits a LSPR at ~550 nm, which shifts towards higher wavelength

after the coating of a-$Si_{1-x}C_x$:H thin films. A lower doping of carbon in a-$Si_{1-x}C_x$:H leads to a higher red shift and larger width of LSPR.

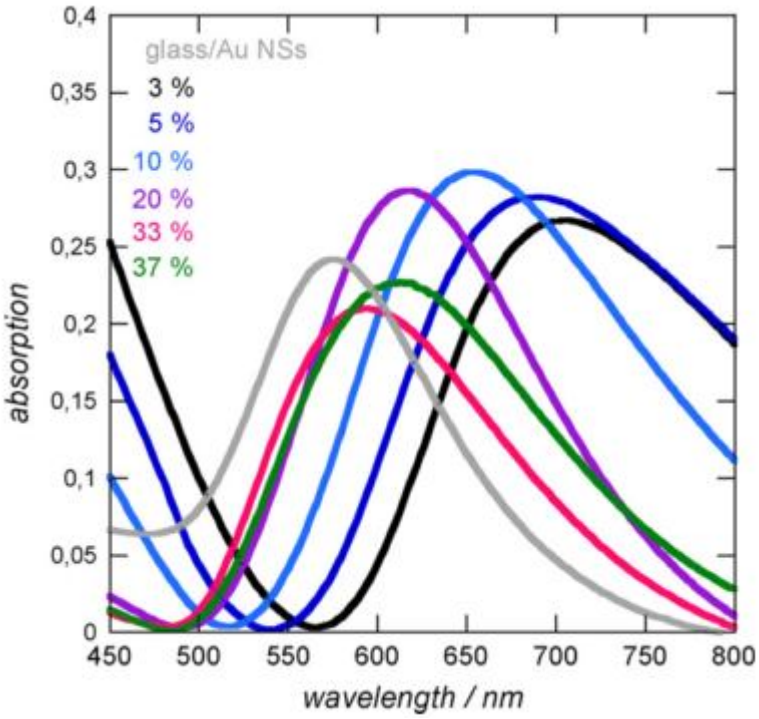

Figure 1.15 UV–Vis absorption spectra in air of an uncoated glass/Au NPs interface (—) and after coating with a 20 nm thick film of a-$Si_{0.97}C_{0.03}$:H (—); a-$Si_{0.95}C_{0.05}$:H (—); a-$Si_{0.90}C_{0.10}$:H (—); a-$Si_{0.80}C_{0.20}$:H (—); a-$Si_{0.67}C_{0.33}$:H (—); a-$Si_{0.63}C_{0.37}$:H (—).[72]

In order to favor the LSPR-fluorescence coupling, the LSPR position should be located close to the excitation/emission wavelength of fluorophore.[158-161] For Cy5, the best coupling of LSPR with fluorophore was found for a-$Si_{0.8}C_{0.2}$:H coating (λ_{LSPR}=614 nm).

More importantly, the level of LSPR-enhanced fluorescence depends on the distance between the fluorophore and the metallic nanostructures. When the fluorophore is located closer than ~ 5 nm from the nanostructured metal surface, the quenching is the dominant effect that vanishes significantly the fluorescence.[162-164] At larger distances, the enhancement starts to override the quenching and the fluorescence reaches its maximum at about 10 nm from the metallic nanoparticles, a distance above which the enhancement effect progressively decreases.[165] This AuNPs-fluorophore distance can be easily tuned by varying the thickness of amorphous coatings. **Fig 1.16** shows the measured fluorescence intensity of Cy5-labeled oligonucleotide immobilized on a-$Si_{0.8}C_{0.2}$:H coated AuNPs.[68] The optimum fluorescence appeared at a coating thickness of 5 nm. By considering the length of the oligonucleotide-terminated monolayer, the AuNPs-fluorophore distance was estimated around ~15 nm. Finally, such a LSPR-enhanced DNA sensor also displayed an ultrahigh sensitivity with a limit of detection at the femtomolar level.

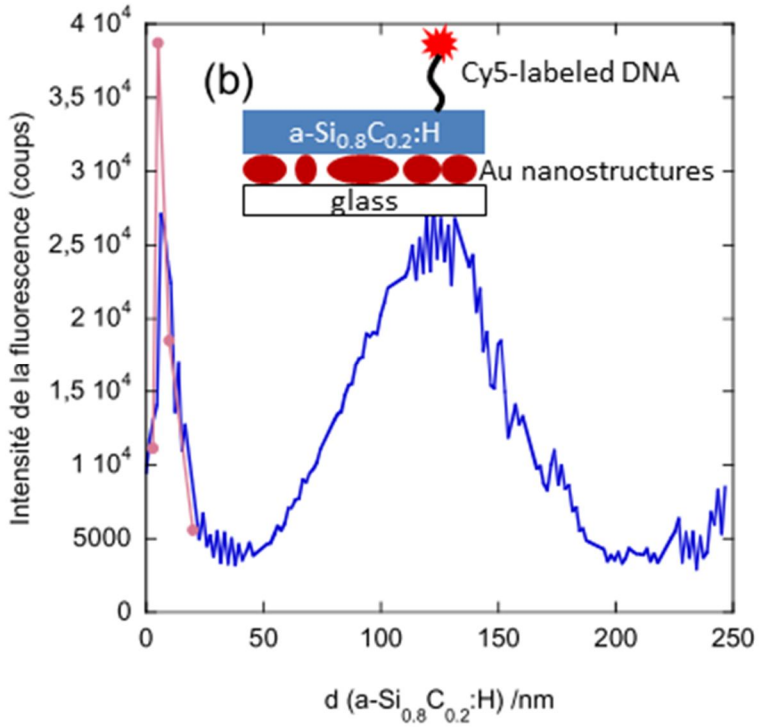

Figure 1.16 Experimental fluorescence intensity for different thickness of a-$Si_{0.8}C_{0.2}$:H coated on AuNPs-embedded slide. The data in blue was obtained on one slide with variable thicknesses and in pink on different slides.

In this thesis, we will adopt the conception of LSPR-enhanced fluorescence for the elaboration of glycan microarrays. It is important to optimize the fluorescence effect in terms of the LSPR position and AuNPs-fluorophore distance.

CHAPTER 2

Build-up of glycosylated monolayers on crystalline silicon surfaces

.

2.1 Introduction

This chapter describes the grafting of glycans starting from carboxydecyl-terminated monolayer on crystalline Si(111) surfaces. Such a build-up has to take into account the following points: for one, the incorporation of antifouling layer in order to minimize the non-specific protein adsorption; for another, the control of the immobilization of glycans with proper spacing and density on the surface in order to favor strong and selective binding with specific lectin partners.

The antifouling property can be simply realized by the amidation of an amino oligo(ethylene glycol) (OEG) linker on the carboxydecyl-terminated surface. There are many commercially available OEG molecules with different chain lengths and different terminations such as the amine, carboxy and azido functional groups, which could provide further conjugation with glycans. To anchor glycan derivatives, we decided to use the Cu(I)-catalyzed Huisgen 1,3-dipolar cycloaddition ("click" chemistry) between azide and alkyne functions leading to the formation of triazole.[166, 167] This reaction is one of the most efficient conjugate method and is largely used as a surface modification strategy for the fabrication of glycan-terminated surfaces.[17, 20, 168, 169]

Two routes may be envisaged for the attachment of glycans *via* Cu(I)-catalyzed cycloaddition reaction (CuAAC): the first is to graft the propargyl-derivatized glycan on a pre-functionalized surface with azido groups; the second is to link the azido-derivatized glycan to an alkynyl-terminated monolayer. For the preparation of azido-terminated silicon surfaces, it is impossible to use the direct hydrosilylation of azido-functionalized 1-alkene because the azido group is likely to decompose *via* the formation of a highly reactive nitrene intermediate during photochemically- or thermally- activated hydrosilylation.[168] Nevertheless, the required azide-functionalized surface can be formed in two steps where the hydrogenated silicon is initially reacted with bromo-terminated 1-alkene *via* hydrosilylation followed by a reaction with sodium azide.[170] On the other hand, the direct binding of alkynyl-functionalized molecules to silicon *via* Si−C bonds has been reported by Gooding and co-workers.[171, 172] They used commercially available 1, 8-nonadiyne to introduce alkynyl groups onto the silicon surface in a thermal hydrosilylation. Subsequent grafting of azide-terminated oligo(ethylene oxide) was achieved *via* Cu(I)-catalyzed click reaction with a modest yield of 42−51%.[171, 172] Decreasing the density of the alkynyl chains by co-deposition with alkyl chains increased the yield of the click reaction to 90% but did not provide sufficient density of oligo(ethylene oxide) (OEO) chains on the silicon substrates to limit their nonspecific adsorption of proteins. This same issue was recently revisited by Cai and coworkers who linked trimethylgermanyl protected α, ω-alkenyne groups to silicon *via* a photochemical hydrosilylation strategy.[168] Subsequent removal of the protection group and click reactions with azido-derivatized mannose proceeded in a single step in good yield (~71%). The resultant mannose-immobilized surface was well recognized by *E.Coli* carrying mannose-specific fimbriae.

Considering the advantages and disadvantages of these examples, we sketch up a multi-step functionalization protocol to build up a glycosylated silicon surface. **Fig 2.1** depicts schematically the stepwise assembly of the glycan-modified silicon (111) substrates.

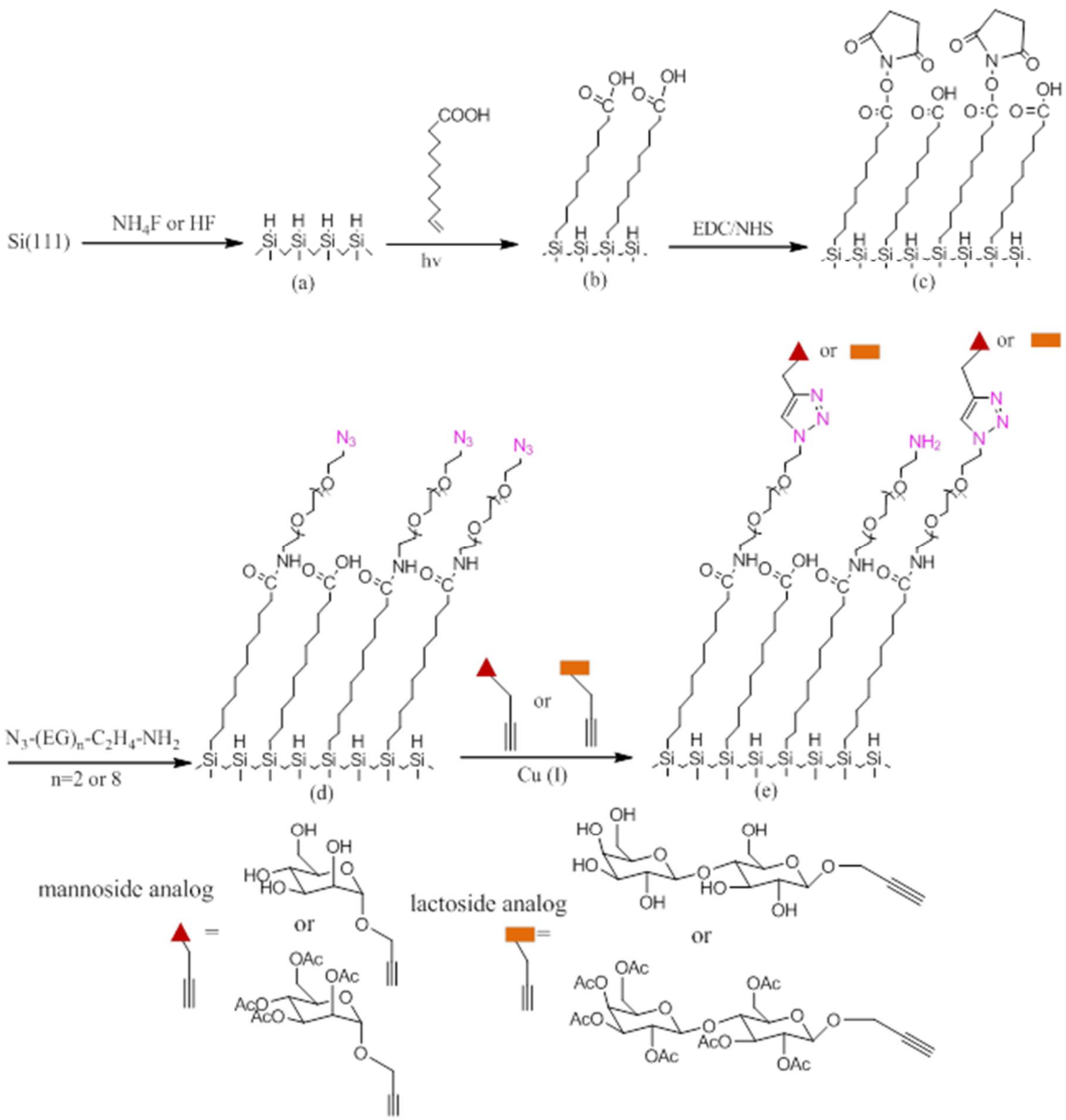

Figure 2.1 Multistep modification scheme to form the glycosylated crystalline silicon surface: (a) surface etching in HF or NH_4F; (b) photochemical hydrosilylation of undecylenic acid; (c) activation in EDC/NHS with the formation of NHS-ester terminated monolayer; (d) aminolysis by OEG spacers bearing terminal azido moieties: $H_2N{-}C_2H_4\text{-}EG_8{-}N_3$ (EG_8) or $H_2N{-}C_2H_4\text{-}EG_2{-}N_3$ (EG_2); (e) "click" reaction with a propargyl-derivatized mannoside or lactoside.

Firstly, the silicon wafer is etched in HF or NH_4F solution to generate the hydrogen-terminated surface. Secondly, the carboxydecyl-terminated monolayer is obtained by photochemical hydrosilylation of undecylenic acid. Thirdly, the carboxylic acid-terminated surface is activated by EDC/NHS to form NHS-ester terminus. Fourthly, to introduce the OEG chain, we chose the commercial OEG molecule carrying an amine ($-NH_2$) function at one terminus and an azido group ($-N_3$) at the other end. The choice of using surface-linked N_3 groups instead of the surface-linked alkynyl moieties is mainly due to the ease of characterization by IR and XPS of the azide function.[173] We have selected two OEG molecules: $NH_2-C_2H_4-EG_2-N_3$ (EG_2) and $NH_2-C_2H_4-EG_8-N_3$ (EG_8), since the chain length of OEG molecule plays an important role in tuning the antifouling property.[134] Lastly, the glycan-terminated surface is realized by the "click" reaction through the as-formed azide-terminated surface with alkynyl-derivatized glycans. Two glycans were chosen, alkynyl-mannoside and lactoside. The per-acetylated alkynyl-mannoside and lactoside were also used for quantitative IR measurements.

All the chemical modifications were carefully analyzed by quantitative IR-ATR and AFM imaging to have a perfect control of the grafting density and the cleanliness of the surfaces. In parallel, additional XPS analysis was performed, especially for the investigation of the "click" reaction.

2.2 Formation of azide-terminated surfaces

2.2.1 Hydrogenation

The first step is the etching of the oxidized Si/SiO_x surface in hydrogen fluoride (HF) or ammonium fluoride (NH_4F). **Fig 2.2** shows the IR-ATR spectra of crystalline Si(111) surface etched in NH_4F and HF solutions, the reference spectra being the oxidized surface. The negative bands at the range of 1000-1300 cm^{-1} characterize the stretching mode of Si-O-Si bond present on the Si surface prior to etching. For both polarizations, a sharp peak appearing at 1060 cm^{-1} is observed, corresponding to the transverse optical (TO) Si-O-Si vibration (**Fig. 2.2a-d**), whereas only p-polarization witnesses the corresponding longitudinal optical (LO) phonon vibration at 1240 cm^{-1} (**Fig. 2.2b, d**). The positive bands from 2000 to 2150 cm^{-1} indicate the formation of hydride Si-H bonds. The etching in HF solution (**Fig. 2.2c, d**) results in the formation of different types of silicon hydride: monohydride SiH ~2080 cm^{-1}, dihydride SiH_2~2102 cm^{-1} and trihydride SiH_3 ~2132 cm^{-1}.[75] All of these hydrides (represented as SiH_x) are visible in both polarizations, indicating that the hydrogenated surface is generally rough. However, the etching in NH_4F solution (**Fig. 2.2a, b**) results in the sole formation of a sharp monohydride peak (noted as SiH) ~2080 cm^{-1} observed in p-polarization only, indicating that the monohydride bond is perpendicular to the (111) face where an atomically flat surface is formed.[83]

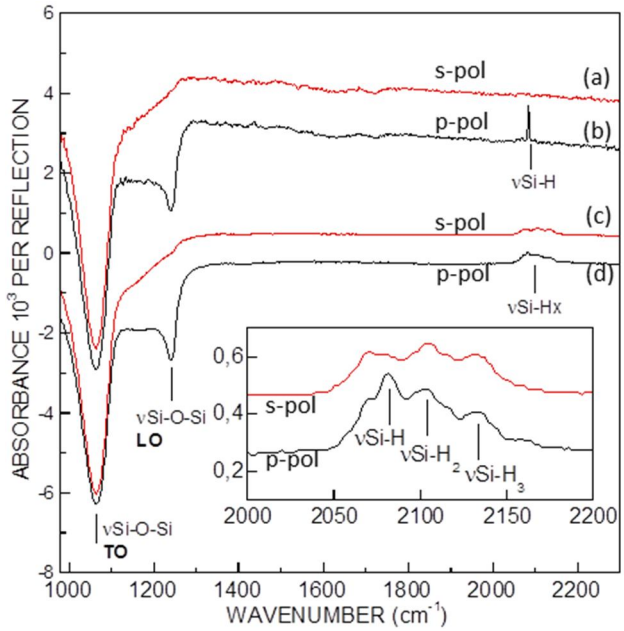

Figure 2.2 IR-ATR spectra in s- (red) and p- (black) polarization of SiH (a and b) and SiH_x surfaces (c and d). The reference spectra are the oxidized silicon surface (SiO_x). The inset is the enlarged νSiH_x region of the spectra c and d.

The AFM images shown in **Fig. 2.3** reveal the formation of the ideally flat SiH surface. The staircase structure is created with a spacing corresponding to the miscut of 0.2° toward the $(11\bar{2})$ direction, where we can distinguish the height of each step around 3.1 Å, close to the calibrated monatomic distance (3.14 Å).[174] The mean separation between two adjacent steps is ~100 nm. These images show that the preparation process allows obtaining surfaces of high quality without any apparent defect. In addition, the staircase structure is of particular interest to be used for monitoring the modifications taking place afterwards.

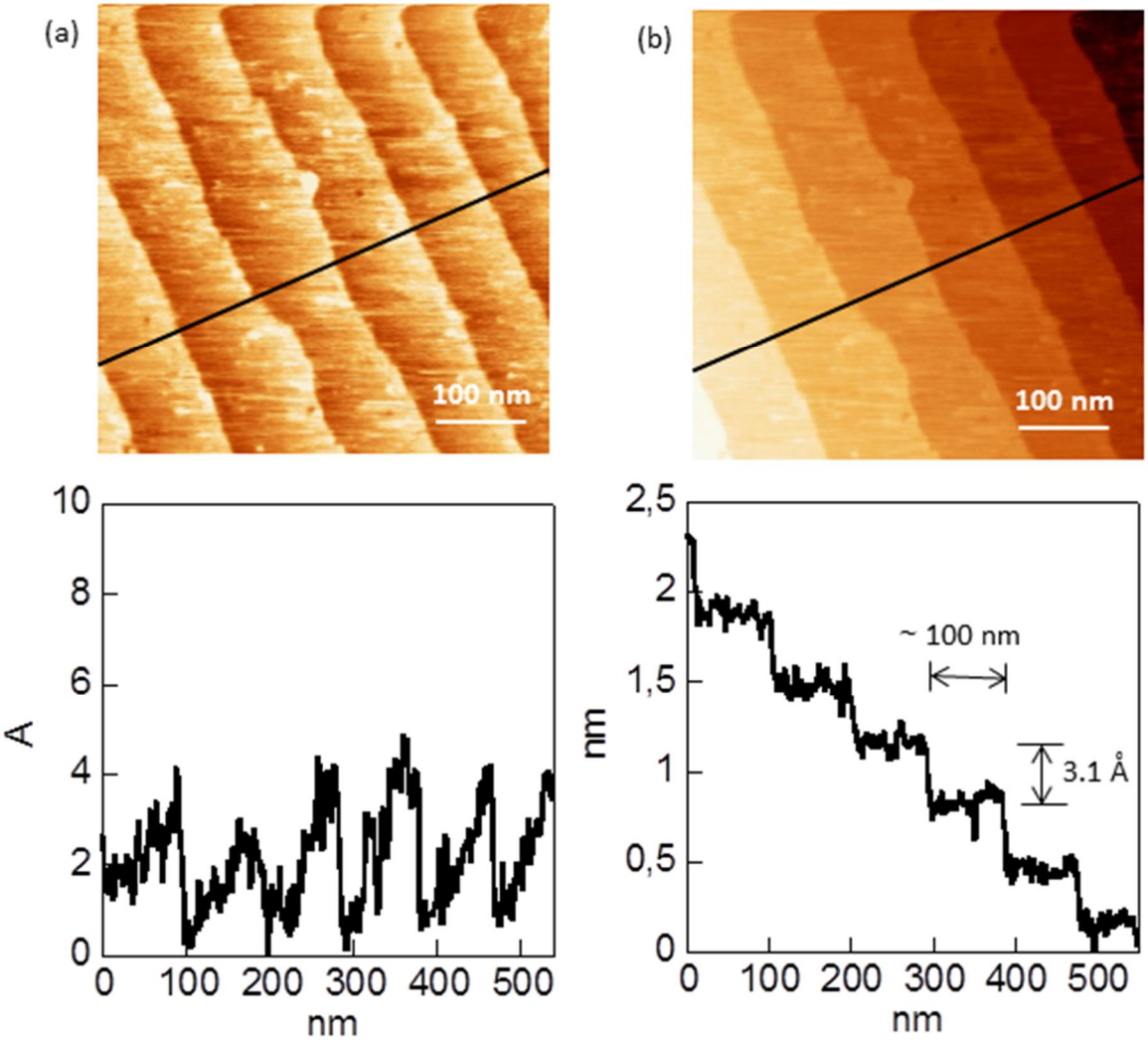

Figure 2.3 AFM images at 0.5×0.5 μm^2 of SiH surface (a); tilted SiH surface with a step height of 0.31 nm (b). The underneath profile corresponds to the mark in the image.

2.2.2 Hydrosilylation reaction

The hydrogen-terminated surfaces were reacted with undecylenic acid through photochemical hydrosilylation, leading to the formation of carboxydecyl-terminated monolayers. The final rinse in hot acetic acid is important to get rid of the physisorption of unreacted undecylenic acid to the carboxyl-terminated surface so as to guarantee the cleanliness of the surface.[63] **Figure 2.4** shows the IR-ATR spectra of the carboxydecyl monolayer. The intense peak at ~1710 cm^{-1} is characteristic of νC=O, the band at ~1410 cm^{-1} of the C−OH in plane mode, and the two bands at ~2855 and 2930 cm^{-1} of the symmetric and anti-symmetric νCH_2, respectively. In particular for the SiH surface (**Fig 2.4b**), the peaks of νCH_2 band are located at 2846 and 2918, indicating that the carboxydecyl chains on monohydride surface adopt well-defined conformation, more regular than on the SiH_x surface.[132] The narrower and sharper νCO band is also a consequence of such a regularity. We also note that no Si−O−Si band appears around 1050 cm^{-1} for both surfaces during the photochemical hydrosilylation.

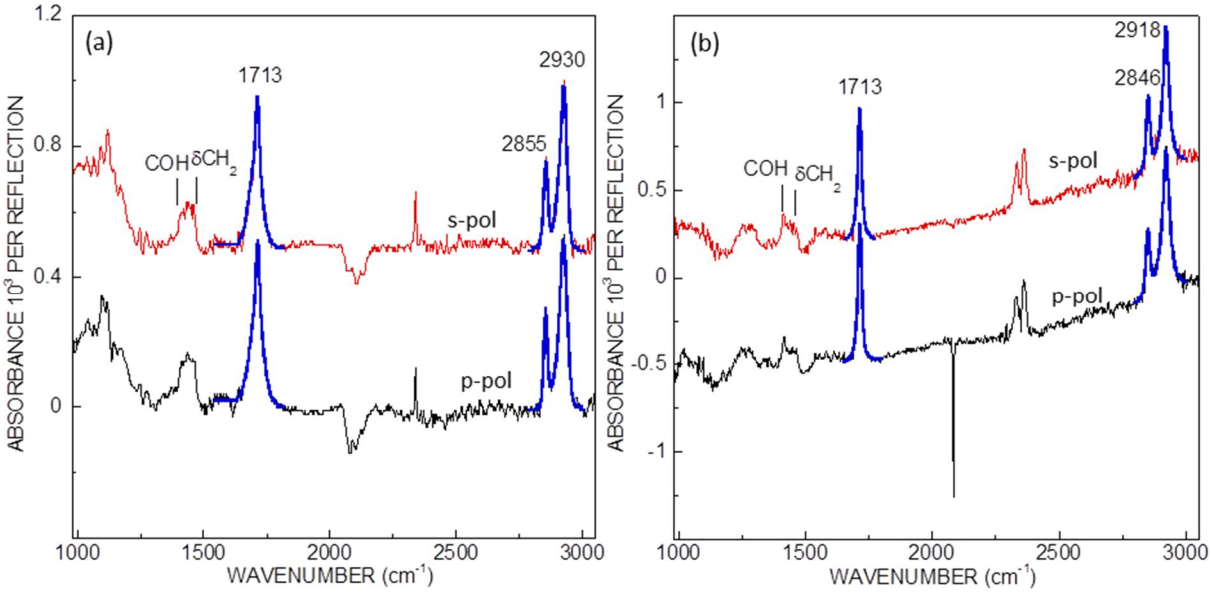

Figure 2.4 IR-ATR spectra in s- (red) and p- (black) polarization of acid-terminated surfaces. The reference spectra are the SiH_x (a) and SiH surfaces (b). The fit of νCO and νCH_2 bands is highlighted in blue.

In addition, the IR-ATR spectroscopy allows a quantification of the grafted carboxydecyl chains from the integrated area of the νCO or νCH_2 bands in s- and p-polarization, as described in detail by Faucheux *et al.* (cf Annex).[63] The surface concentration of carboxydecyl groups is found to be about $2.0 \pm 0.2\times10^{14}$ cm^{-2} for the SiH_x surface and $2.4 \pm 0.2\times10^{14}$ cm^{-2} for the SiH surface, being slightly lower than that reported on atomically flat (111) silicon surfaces ($N = 2.5\pm0.2\times10^{14}$ cm^{-2}).[64, 175] Molecular modeling performed by Sieval *et al.* on the factors of the tilt angle of the chain from the surface normal (35.5°), the diameter of the decyl chain (4.3Å) and the distance between two adjacent Si-H bonds (3.84

Å), concluded that the maximal grafting density cannot exclude ~50%, in which the chains are anchored on every two Si-H bonds.[104, 176] By knowing that the ideal SiH surface yields a density of 7.8×10^{14} cm^{-2} for surface hydrogen atoms, the coverage of carboxydecyl chains over the Si-H sites for the two surfaces is therefore 25% and 30%, respectively. The lower coverage of the SiH_x surface is plausible because of its larger roughness.

The AFM images of the carboxydecyl-terminated surface are shown in **Fig. 2.5.** The neat staircase structure is preserved after the hydrosilylation reaction, indicating the good homogeneity of the carboxydecyl chains.

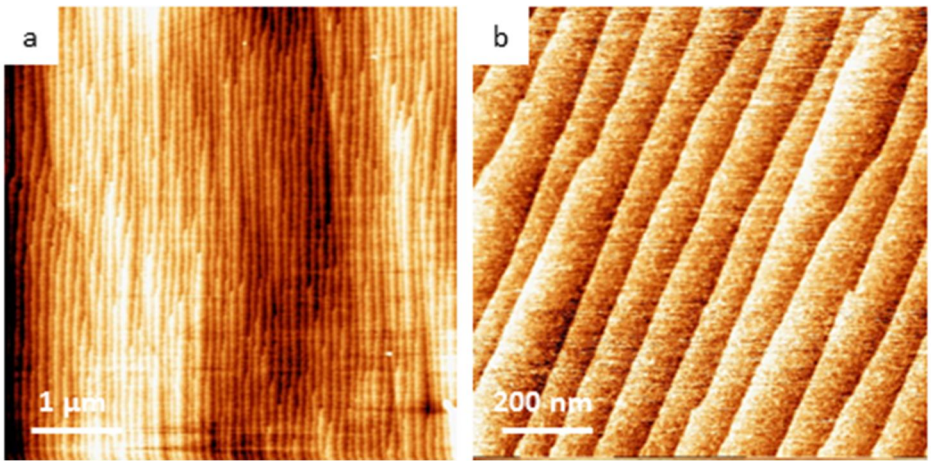

Figure 2.5 AFM images at 5×5 μm^2 (a) and 1×1 μm^2 (b) of the carboxydecyl-terminated surface.

2.2.3 Activation reaction

The acid functions are then activated in a mixture of EDC/NHS (5mM/5mM) to form the NHS-ester terminated monolayer. **Fig. 2.6** shows the IR-ATR spectra of the formation of NHS-ester functions. Several characteristic peaks of the NHS-ester confirm the success of the activation reaction: the triplet band at 1820, 1785 and 1745 cm^{-1} corresponds to the νCO of NHS ester, the symmetric and antisymmetric νCO of the succimidyl cycle, respectively; the bands at 1370 and 1205 cm^{-1} correspond to the symmetric and antisymmetric νC-N-C of succimidyl cycle, respectively; the band at 1065 cm^{-1} correspond to the succimidyl νN-C-O.[110] The density of NHS ester can be quantitatively analyzed by fitting the νCO triplet band, as developed by Moraillon et al. (cf Annex).[64] The quantity of NHS-ester terminations is found to be $N \approx 1.6\times10^{14}$ cm^{-2} for the SiH_x surface and $N \approx 2.2\times10^{14}$ cm^{-2} for the SiH surface, corresponding to an activation yield of 80% and 93%, respectively. The AFM images as shown in **Fig. 2.7** validate the formation of neat NHS ester-terminated surface, with well-preserved terraces.

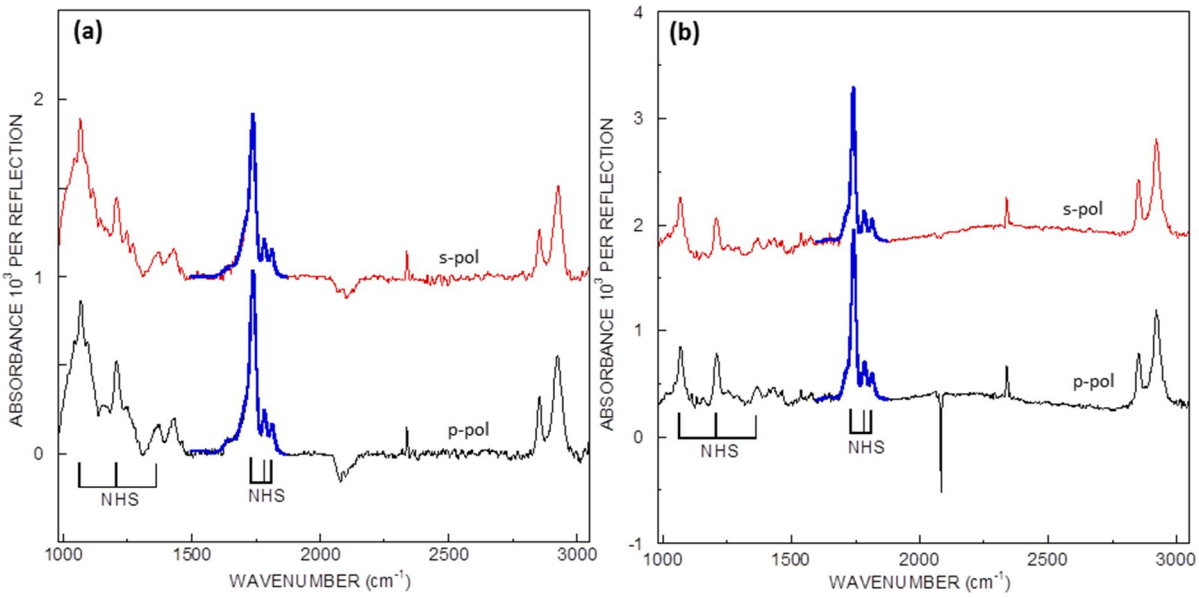

Figure 2.6 IR-ATR spectra in s- (red) and p- (black) polarization of NHS ester-terminated surfaces. The reference spectra are the SiH_x (a) and SiH surfaces (b). The fit of νCO bands of NHS ester is highlighted in blue.

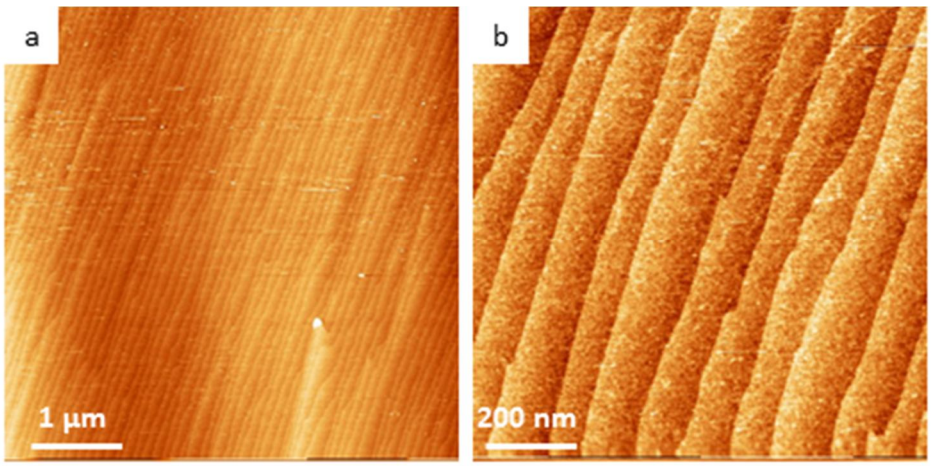

Figure 2.7 AFM images at 5×5 μm^2 (a) and 1×1 μm^2 (b) of the NHS ester-terminated surface.

2.2.4 Aminolysis reaction

a) Aminolysis by EG_8

The aminolysis with amino OEG molecules is performed at room temperature in PBS 1X buffer. **Fig. 2.8** displays the corresponding IR-ATR spectra. We clearly observe the disappearance of the NHS-ester triplet and the appearance of the amide bands. Two bands at 1642 and 1548 cm^{-1} are characteristic to the νCO and νCNH of the amide group (amide I and II, respectively). The vibrational bands at 1105 and ~2820−2960 cm^{-1} are attributed to the νC−O−C and νOCH_2 of the ethylene glycol chain, respectively. Moreover, the band characteristic of the stretching mode of the azido group is present at 2109 cm^{-1} and superimposed to the negative band of the νSiH_x (**Fig 2.8a**). This band is more apparent on the SiH surface (**Fig 2.8b**). We also notice the presence of residual carboxylic acid peak at ~1730 cm^{-1}, which can be integrated to deduce the aminolysis yield in comparison with the initial area of the carboxydecyl-terminated surface (**Fig 2.4**).[177] A common way is to fit the triple band between 1500 and 1800 cm^{-1} in which the area at ~1730 cm^{-1} is obtained. The density of OEG chain is found to be 1.6×10^{14} cm^{-2} for the SiH_x surface and 1.7×10^{14} cm^{-2} for the SiH surface, corresponding to an aminolysis yield of ~100% and ~77%, respectively.

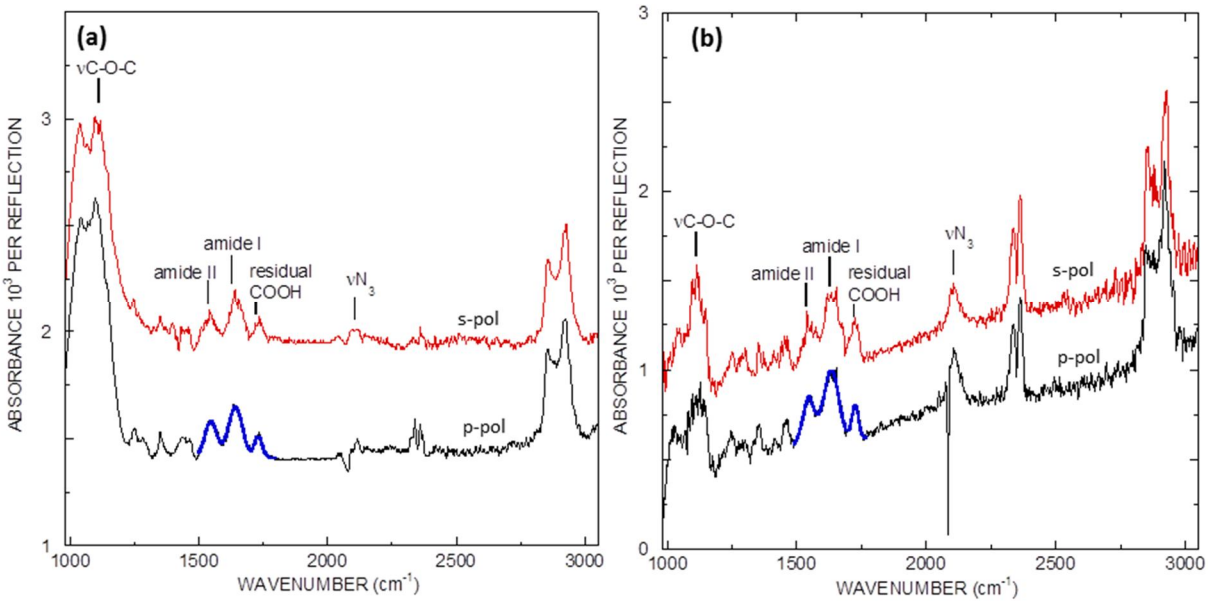

Figure 2.8 IR-ATR spectra in s- (red) and p- (black) polarization of azido-terminated surfaces. The reference spectra are the SiH_x (a) and SiH surfaces (b). The fit of the triple bands corresponding to the amide II, I and the carbonyl of the residual carboxylic acid is highlighted in blue.

Another direct quantification of the density of OEG chain can be obtained from the νCH_2 band of ethylene glycol units. Their contribution can be obtained by using the carboxyl-terminated surface as a reference instead of the SiH_x surface, so that all the positive bands in the νCH range arise from the OEG segments (**Fig. 2.9a,b**). On both surfaces, the νN_3 band is positive and almost with the equivalent areas, revealing that the amount of azide-terminated

chains is the same. The broad band from 2800-3000 cm^{-1} corresponds to the νCH_2 of OEG chains. Perez *et al.* have succeeded to quantify the grafted Si-$(EG)_n$OMe molecule by IR-ATR, where he obtained the contribution of each ethylene glycol unit.[134] In our case, n=8, the density of OEG chains is found to be 1.6×10^{14} cm^{-2} for the SiH_x surface and 1.7×10^{14} cm^{-2} for the SiH surface, very close to the result obtained by the previous method. The global amidation yield (activation and aminolysis) is therefore determined to be 80% and 72% for the two surfaces, respectively.

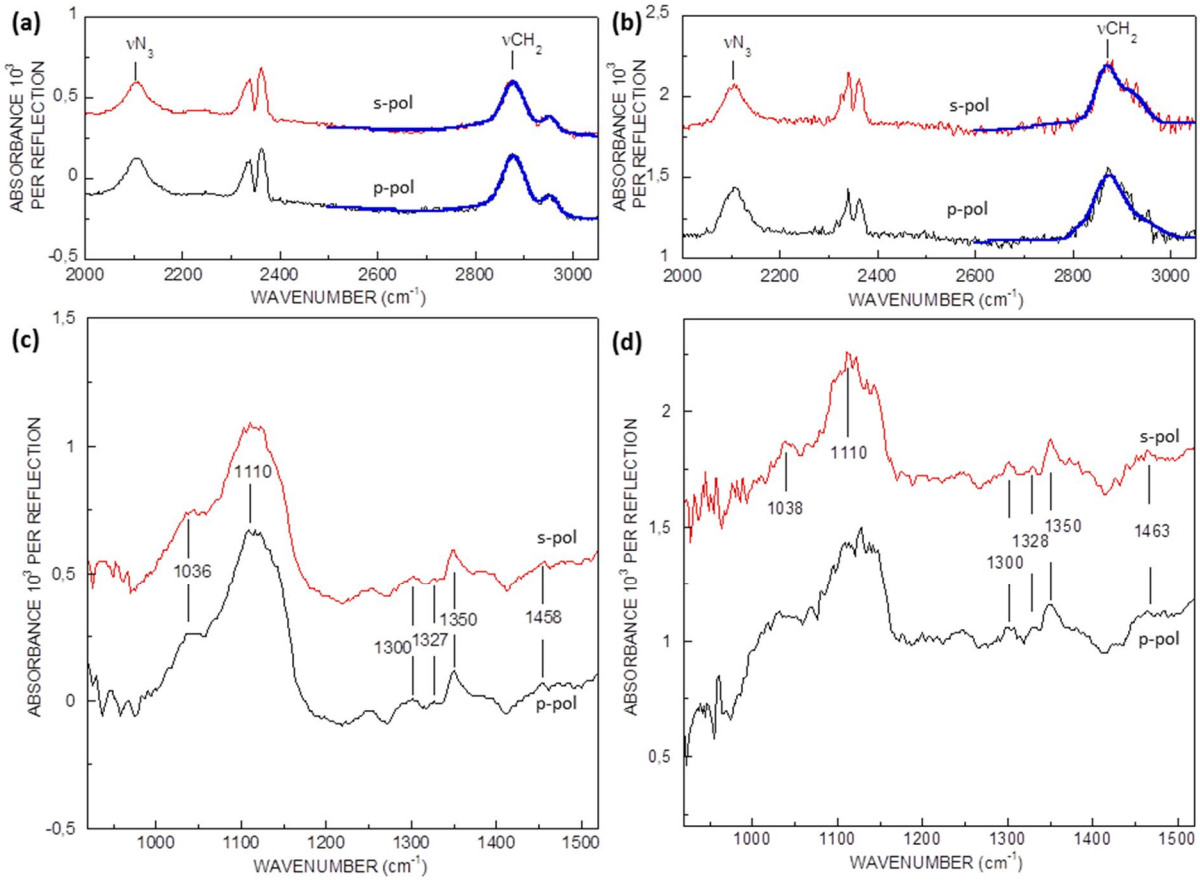

Figure 2.9 IR-ATR spectra in s- (red) and p- (black) polarization of azido-terminated surfaces in the region of 2000-3050 cm^{-1} (a,b) and 950-1520 cm^{-1} (c,d). The reference spectra are carboxydecyl-terminated surfaces grafted on SiH_x (a,c) and SiH surfaces (b,d). The fit of the νCH_2 bands in (a,b) is highlighted in blue.

It is worth noticing that the best-defined structure of the SiH surface leads to the same density of N_3-terminus as the rougher SiH_x surface. The analysis of IR fingerprint region (< 1500 cm^{-1}) of OEG chains is shown in **Fig 2.9c** and **d**, a plenty of bands relating to the conformation of O-CH_2CH_2 segments appear at ~900-1500 cm^{-1} and are listed in **Table 2.1**. Their peak positions are compared with those of PEG molecule in crystalline or amorphous states as listed in **Table 2.1**. The data shows the grafted OEG chains are more likely an amorphous state where the chains are elongated in randomly helical conformations such as trans-gauche-trans (TGT), TGG or TTG, etc, featuring a length around ~2.5 nm (a length of

2.78 Å for each ethylene glycol unit).[132] Therefore, we hypothesize that the linking of flexible OEG chains adopts a random or even more entangled conformation that makes its steric hindrance be the limit of higher amidation yield.

	PEG crystal	**PEG amorphous**	**On SiH_x surface**	**On SiH surface**
CH_2 scissor (gauche)	1470 (s)	1460 (p, s)	1458 (p, s)	1463 (p, s)
CH_2 wag (gauche)	1345 (p)	1352 (p)	1350 (p, s)	1350 (p, s)
CH_2 wag (trans)		1325	1327 (p, s)	1328 (p, s)
CH_2 twist	1283 (s)	1296 (s)	1300 (p, s)	1300 (p, s)
C-O, C-C stretching	1119 (s)	1107 (p)	1110 (s)	1107 (p)
		1038 (s)	1036 (s)	1038 (s)

Table 2.1 Peak position of OEG chains picked up from **Fig. 2.9 c, d** and the standard peak position of crystalline and amorphous PEG. (N.B, p, s = p or s-polarization).

In order to characterize the azido function, XPS is also performed. **Fig 2.10** shows the XPS narrow scan of the Si_{2p}, O_{1s}, C_{1s} and N_{1s} region of the acid- to the azide-functionalized surfaces. In the Si_{2p} spectrum, we confirm that both surfaces are not oxidized since no band is visible at ~103 eV (**Fig 2.10a**).

The O_{1s} narrow scan of the acid-terminated surface (**Fig 2.10b**) can be attributable to the contribution of O-C and O=C at equivalent ratio, whereas the two contributions were nicely fitted by imposing a ratio of 6.4:1 in case of azide-terminated surface, in considering the amidation yield of 0.8 (8 O-C in OEG chains and 1 C=O in carboxydecyl chains so that (C-O):(C=O) = 8×0.8:1 = 6.4:1).

The C_{1s} of acid-terminated surface (**Fig 2.10c**) can be fitted as 3 peaks. The peak at 290 eV corresponds to the carbonyl of the acid, the peak at 287 eV is assigned to the CH_2 in the α position of the acid function and the peak at 285 eV is for the carbon on decyl chains. We obtain a ratio of 1:1:9 for C=O (290 eV): C-COOH (287 eV): C-C (285 eV). For the azide-terminated surface, the C-N, C-O and C-N_3 are approximately at the same binding energy, so the area ratio is distributed at C(O)NH (288.8 eV) : C-O (288.2 eV) : C-C (285 eV)=1: 0.8× 18: 10 =1:14.4:10. All of the above assignments can well fit the XPS data and support the quantification result of IR.

Besides, the most interesting analysis is the high resolution XPS narrow scan of the N_{1s} region (**Fig 2.10d**). The band at 405.4 eV is attributed to the azide function and arises from the central electron-deficient nitrogen ($N=N^{+}=N^{-}$) and another at 401.8 eV corresponding to the two lateral nitrogen atoms ($N=N^{+}=N^{-}$). These two bands appear with a ratio 2:1, in accordance with the incorporation of an N_3 group. An additional band at 400.7 eV is attributed to the nitrogen atom of the amide function.

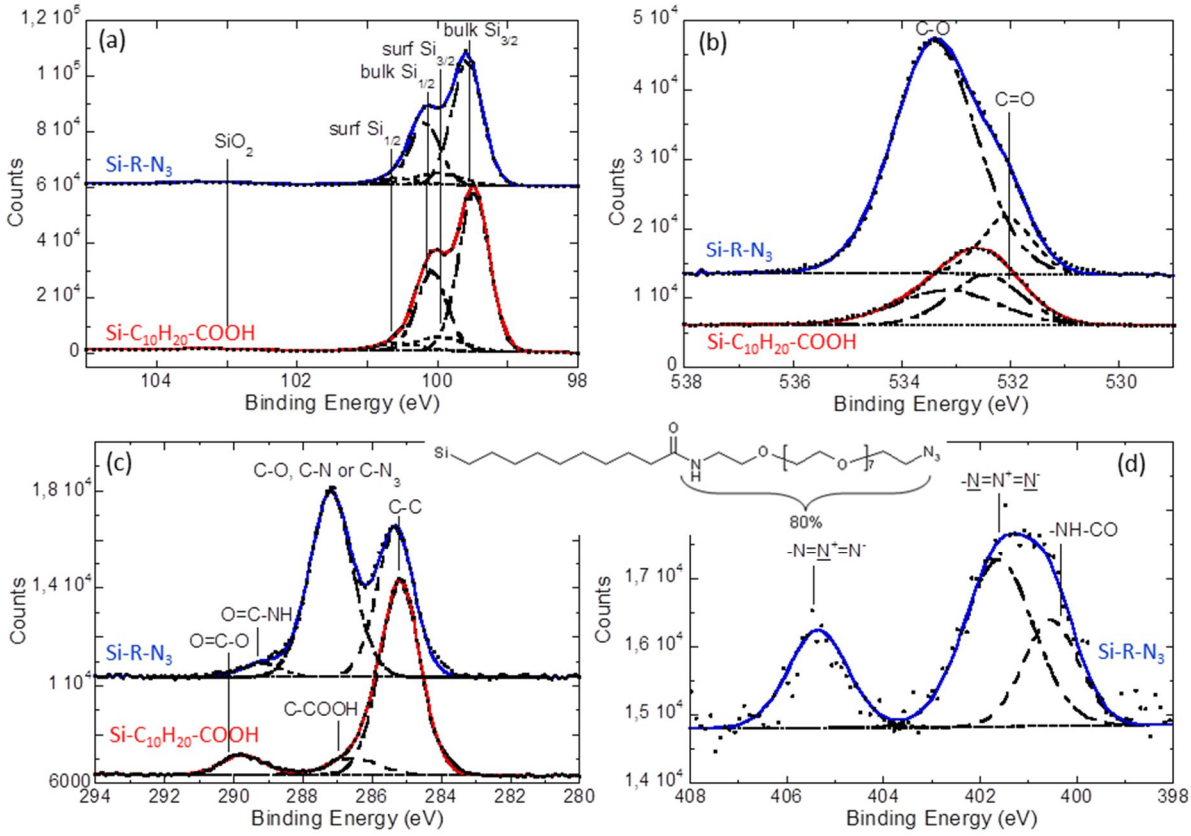

Figure 2.10 High resolution XPS spectra and composition assignment of the acid and azide-terminated surfaces in regions of Si_{2p} (a), O_{1s} (b), C_{1s} (c) and N_{1s} (d).

The AFM images of the azide-terminated surface are shown in **Fig. 2.11**. The staircase structure is again preserved after the attachment of OEG chains of 2.5 nm length.

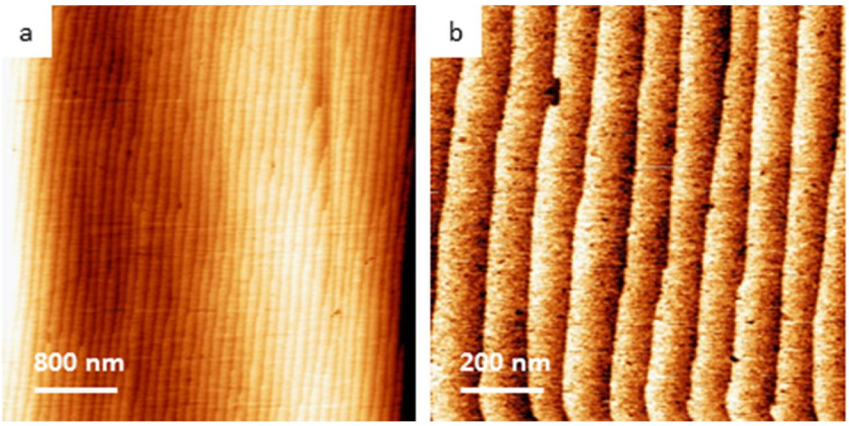

Figure 2.11 AFM images at 4×4 μm^2 (a) and 1×1 μm^2 (b) of the azide-terminated surface.

b) Aminolysis by EG_2

To evaluate the antifouling property of OEG layer, a shorter NH_2-C_2H_4-$(EG)_2$-N_3 is analogously amidated. **Fig 2.12** displays the IR-ATR spectra of the acid-, NHS ester- and azide-terminated surfaces. Using the same quantification methods as described before, we obtain a density of 2.0×10^{14} cm^{-2} for acid-moiety, 1.8×10^{14} cm^{-2} for NHS ester-moiety and 1.8×10^{14} cm^{-2} for N_3-moiety, corresponding to activation and aminolysis yield of 90% and 100% (amidation yield of 90%). The higher amidation efficiency is probably due to the smaller steric hindrance of the shorter EG_2 chains.

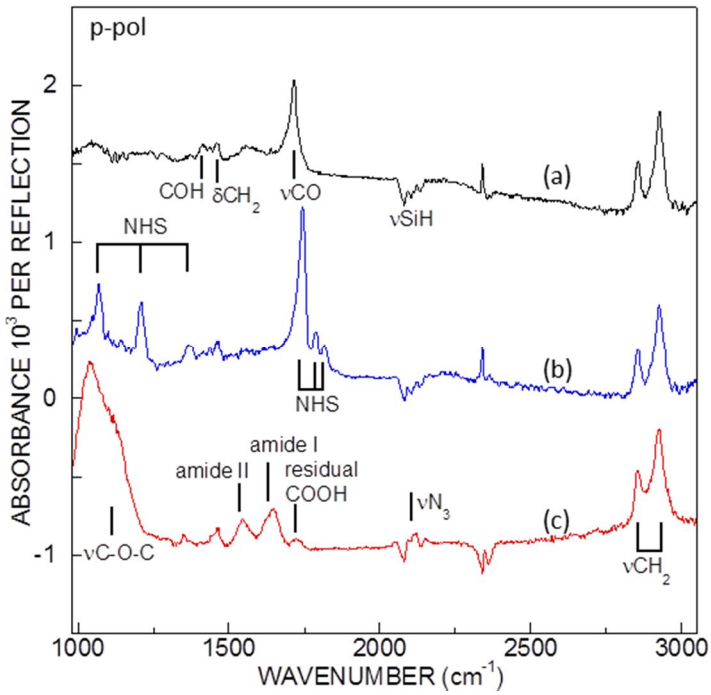

Figure 2.12 IR-ATR spectra in p-polarization of acid- (a), NHS ester- (b) N_3-EG_2-terminated surfaces (c). The reference spectra are the SiH_x surface.

2.3 Formation of glycosylated surface

2.3.1 Synthesis of alkynyl-derivatized glycan precursor

a) Introduction to the glycosylation

The structural diversity, complexity and heterogeneity of carbohydrates have limited for a long time the synthetic access. The preferential derivatization is difficult due to the presence of multiple hydroxyl groups. Moreover, the glycan could be isomerized in either straight-chain or heterocyclic ring conformation through the hemiacetal or hemiketal bonds (cyclic form is usually dominant). The conversion from the chain to the cyclic form makes the carbon atom of the carbonyl be connected by two oxygens, leading to a higher electropositivity than other carbon atoms. This carbon called anomeric carbon plays a role as stereogenic center to generate two possible configurations during the formation of hemiacetal or hemiketal bonds: the oxygen atom may take a position either above or below the plane of the ring. The resulting possible pair of stereoisomers is called anomers: α-anomer refers to that the -OH substituent on the anomeric carbon is on the opposite side (*trans*) of the CH_2OH side branch and the β-anomer refers the -OH substituent is on the same side (*cis*), as shown in **Fig 2.13** for the D-mannose. Due to the steric hindrance of the neighboring hydroxyl group, α-configuration is in fact dominant in case of D-mannose. Most of the derivatization strategies take advantage of the active anomeric carbon to substitute the 1-hydroxyl position by other functional groups. The derivatization occurring on the anomeric carbon is called glycosylation and the resulting glycan is called glycoside.

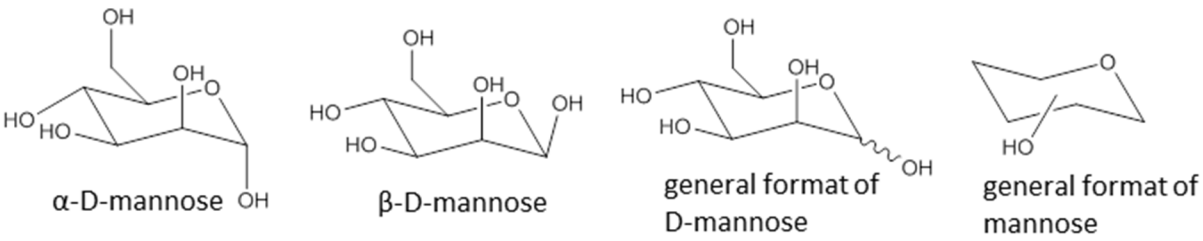

Figure 2.13 Different structure formulas to stand for mannose.

b) Derivatization of alkynyl groups

The derivatization to introduce alkynyl groups on glycans adopts the following strategy as shown in **Fig 2.14** for D-mannose. The D-mannose (**1**) is firstly acetylated with acetic anhydride by the catalysis of pyridine to form the per-O-acetyl mannose (**2**). The acetylation involves the reaction of all hydroxyl groups of **1** without the stereo selectivity of the anomeric carbon, as manifested in the mechanism in **Fig 2.15**.[178, 179] The successive nucleophilic substitution with propargyl alcohol leads to the formation of alkynyl-acetylated mannose (ManOAc. **3**). As explained in the mechanism in **Fig 2.16**, the acetyl group on anomeric carbon is activated by the Lewis acid BF_3OEt_2, resulting in the formation of oxocarbenium intermediate which is stabilized through the neighboring acetyl group. The following propargyl alcohol can only attack the opposite side, thus the stereo selective α-ManOAc.[180-182]

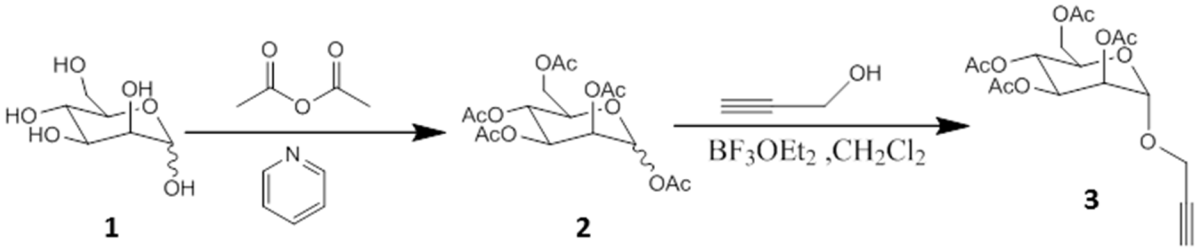

Figure 2.14 Synthesis route of peracetylated α-propargyl mannoside.

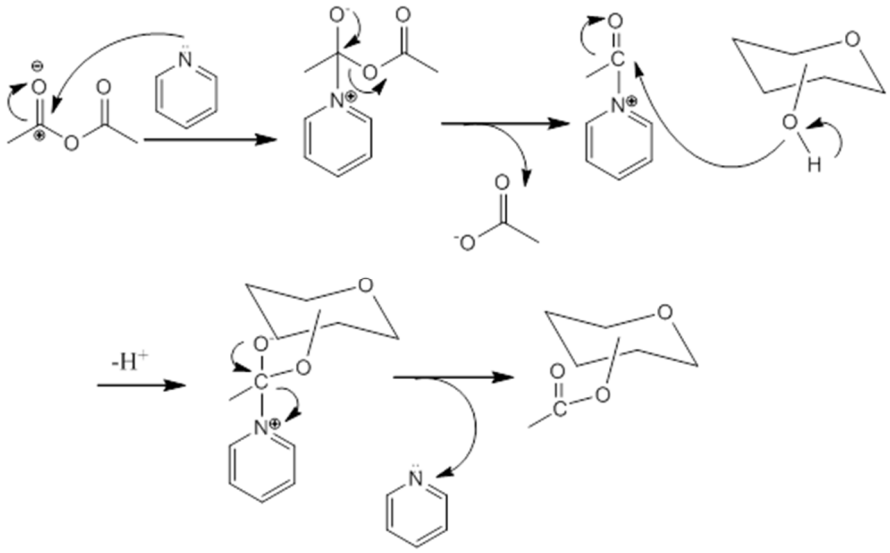

Figure 2.15 Reaction mechanism for pyridine-assisted per-acetylation of mannose (**1→2**). Note that there is no stereo isomerization preference on anomeric position.

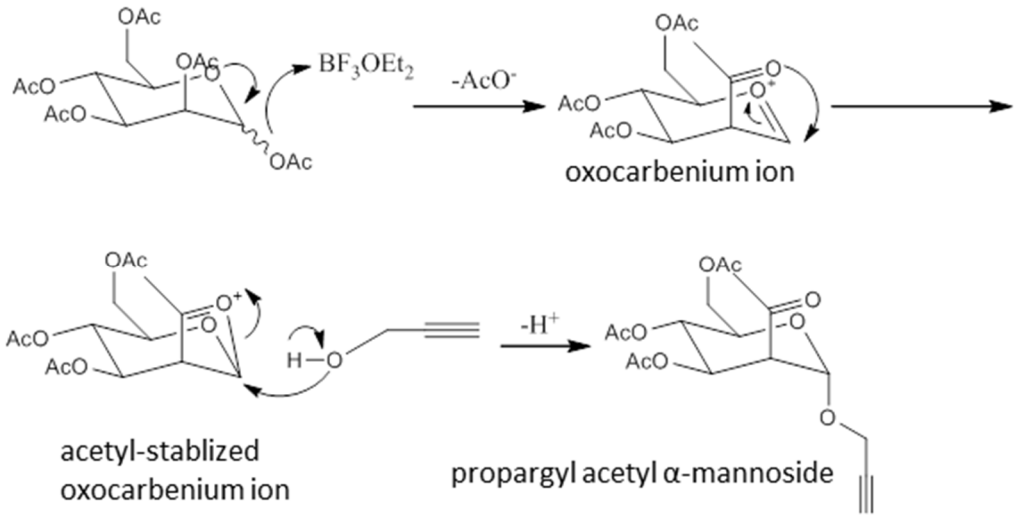

Figure 2.16 Reaction mechanism for BF_3OEt_2-assisted nucleophilic substitution with propargyl alcohol (**2→3**). Note that the formation of oxocarbenium ion intermediate is stabilized by the neighboring acetyl group leading to the formation of stereoselective α-anomer.

After deacetylation, α-propargyl mannoside (**4**) is formed (**Fig 2.17**). **Fig 2.18** shows the ^{13}C-NMR spectra of the anomeric carbon for molecules **1-4**, it is notable that two anomers exist in **1** and **2** whereas only one α-anomer is found in **3** and **4** after the substitution reaction.

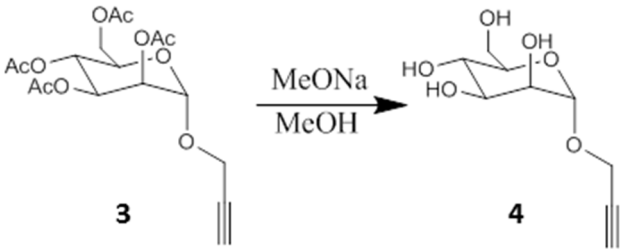

Figure 2.17 Deactylation of ManOAc leading to the propargyl mannoside.

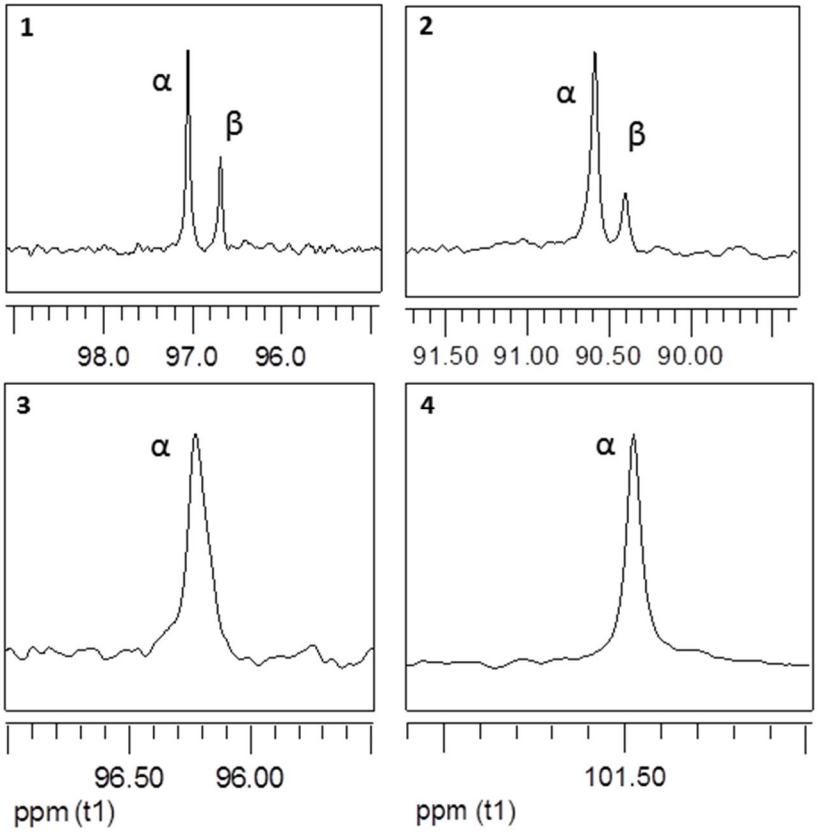

Figure 2.18 ^{13}C-NMR spectra of the anomeric carbon position for molecules **1-4**.

Analogously, the derivatization of alkynyl group on lactose results in the unique formation of β-propargyl lactoside (**Fig 2.19**).

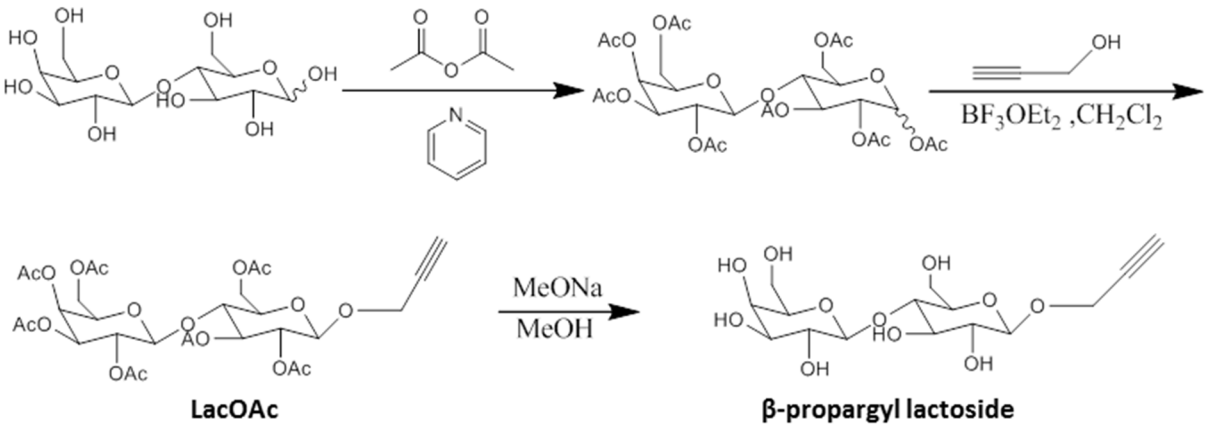

Figure 2.19 Synthesis route of β-propargyl lactoside.

2.3.2 "Clicking" of alkynyl per-acetylated glycans

a) "Clicking" of ManOAc

We performed the "clicking" of propargyl per-acetylated mannoside (ManOAc) because it contains a characteristic band of the acetyl νC=O that can be easily characterized by IR-ATR. The "clicking" of ManOAc was performed on azido-terminated surface in the presence of Cu(I) catalyst generated *in-situ* from $CuSO_4$ and sodium ascorbate. We used a polar mixture (DMSO/H_2O/EtOH mixture) to favor the dissolution of ManOAc. The sodium ascorbate reduces the Cu(II) into the catalyst Cu(I) and stabilizes it through coordination.[167, 183, 184] The AFM images of ManOAc-clicked surface in **Fig. 2.20** confirm the formation of neat surface without physisorption. The roughness of terraces is slightly increased due to the appearance of black holes of ~0.5 nm depth, which plausibly arises from the formation of glycan domains.

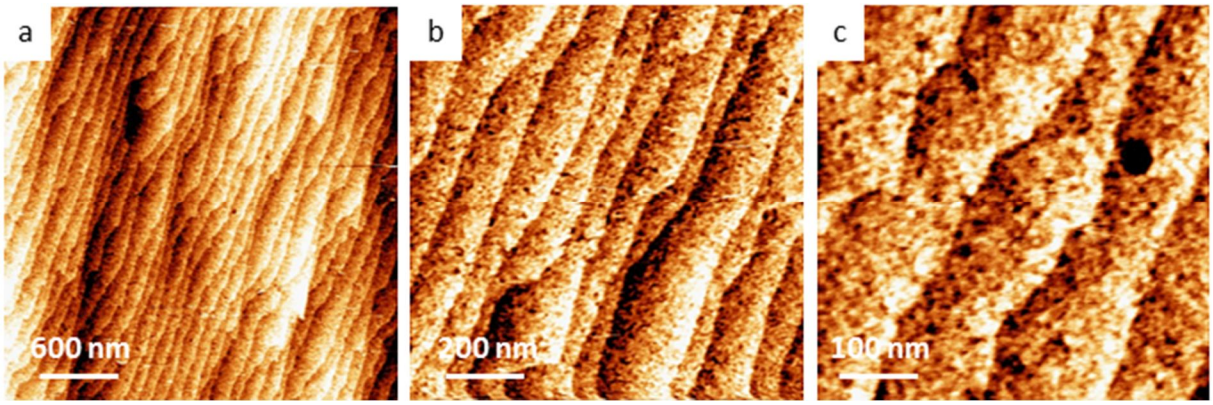

Figure 2.20 AFM images of the ManOAc-terminated surface at different scales: 3×3 μm^2 (a), 1×1 μm^2 (b) and 500×500 nm^2 (c).

Fig 2.21a represents the IR-ATR spectra of the "clicked" ManOAc surface. The success of the reaction is confirmed by the presence of the band at 1754 cm^{-1} assigned to νC=O of the acetyl groups and by the absence of the νN_3 band at 2109 cm^{-1}. The broad band centered at 1050 cm^{-1} is ascribed to the νC-O-C of the mannoside cycle and also probably to the partial oxidation of the silicon surface occurring in the presence of the Cu(I) catalyst. The amount of clicked acetylated mannose is determined through the integration of the acetyl group bands at 1754 cm^{-1}. For this, we fitted globally the triple band in the 1500-1800 cm^{-1} range. The contribution of ManOAc is obtained by a subtraction of the contribution of the residual COOH fitted in the spectrum of the azide-terminated surface (**Fig 2.8a**). Another easier fitting method is to divide the spectrum of ManOAc-terminated surface with that of the azide-terminated surface so that the acetyl group band from the ManOAc is more clearly offered (**Fig 2.21b**).

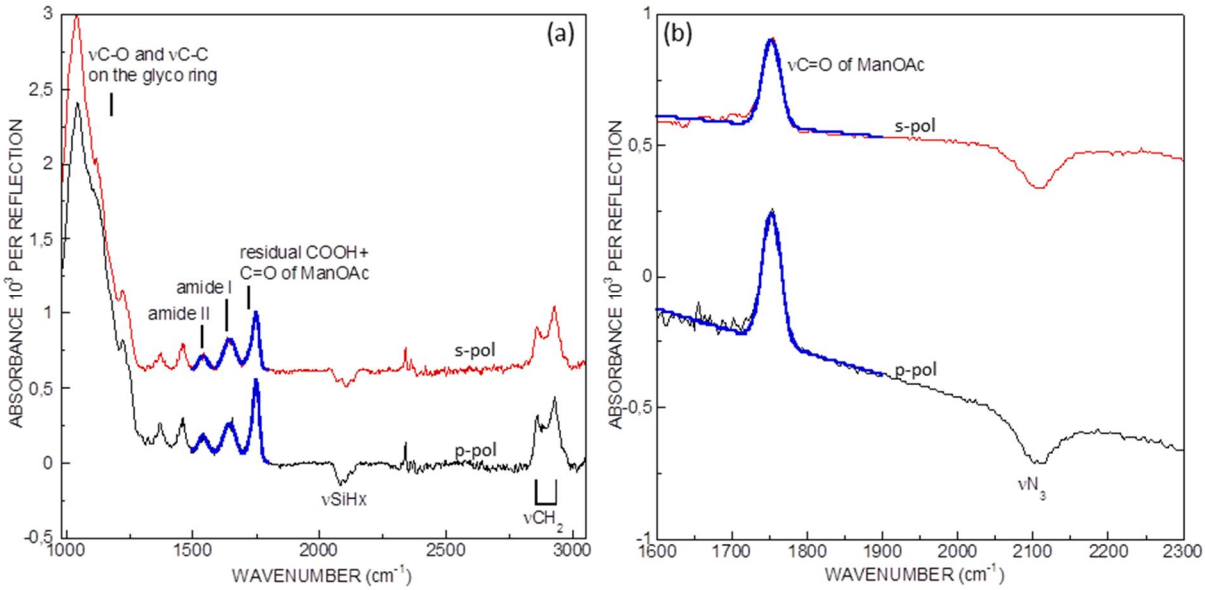

Figure 2.21 IR-ATR spectra in s- (red) and p-polarization (black) of ManOAc-terminated surfaces, the reference being the SiH_x surface (a) and azide-terminated surface in the region of 1600-2300 cm^{-1} (b). The fit of carbonyl bands is highlighted in blue.

b) Calibration of ManOAc by in-situ IR-ATR

The IR-ATR calibration of ManOAc molecule was performed for the first time. Acetonitrile was chosen as the calibration solvent for the good ManOAc solubility to and the absence of IR peak in the carbonyl region. **Fig 2.22** shows the spectra in s-polarization of ManOAc at varying concentrations in acetonitrile where the integrated absorbance Abs_s^0 of the νCO band is plotted linearly versus the concentration *C*. The calibrated Abs_s^0 / C value is thus given to be 0.00169 (cm mM)$^{-1}$. By incorporating this value into the equation (see Annex), for an incident angle of prism of ~ 48°, we obtain the quantity of ManOAc grafted on the surface as the followings:

$$N_{\parallel} = 5.7 \times 10^{15}\ A_s$$
$$N_{\perp} = 1.08 \times 10^{16}\ A_p - 9.76 \times 10^{15}\ A_s$$
$$\text{and } N_{total} = N_{\parallel} + N_{\perp} = 1.08 \times 10^{16}\ A_p - 4.06 \times 10^{15}\ A_s$$

where $A_{s,p}$ stands for the integrated absorbance of the νCO band of ManOAc-terminated surface measured in s- and p-polarization, $N_{\parallel,\perp}$ is the density of ManOAc in s- and p-polarization, and N_{total} is the total density of ManOAc. Therefore the amount of clicked ManOAc is found to be 1.2×10^{14} cm^{-2}, which corresponds to a yield of ~75% for the "click" reaction.

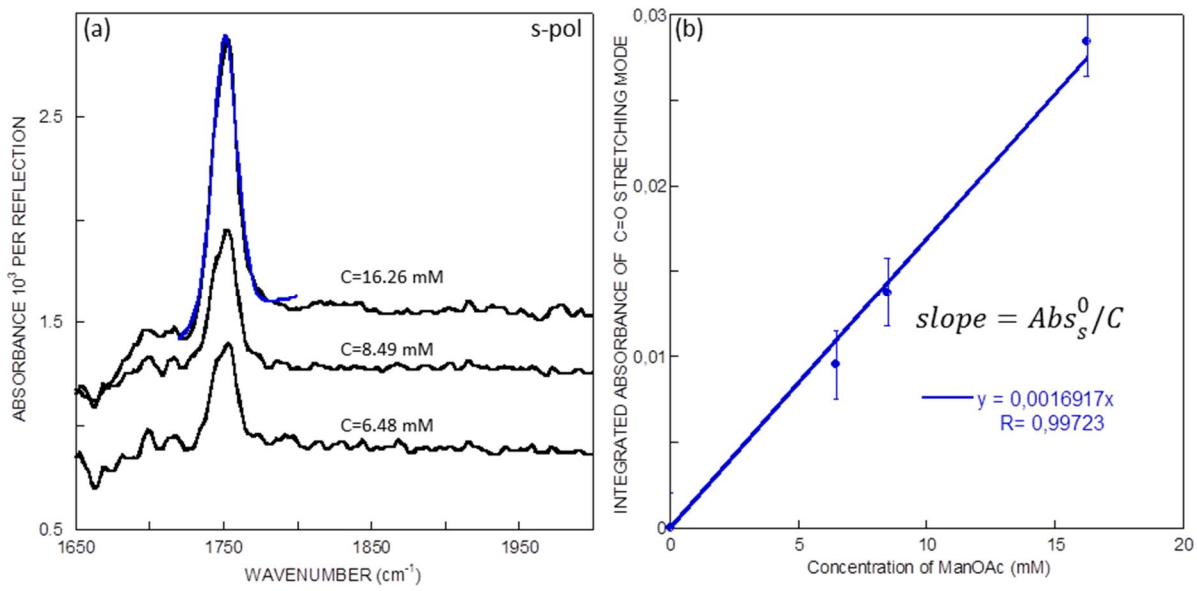

Figure 2.22 (a) IR-ATR calibration spectra in s-polarization of ManOAc in acetonitrile solution at three concentrations. The fit of the carbonyl band is highlighted in blue. (b) Integrated absorbance as a function of ManOAc concentration.

c) "Clicking" of LacOAc

Using the same quantification equations, the density of LacOAc-terminated surface can also be calculated. The LacOAc-terminated surface is clicked on azide-terminated surface by using the same chemical condition as ManOAc. **Fig 2.23** shows the IR spectra of azide and LacOAc-terminated surfaces. The carbonyl contribution from the LacOAc is obtained from the LacOAc terminated-surface with reference to the azide-terminated surface. By using the same equation as for ManOAc and considering that the number of acetyl functions on LacOAc is 7, the density of LacOAc is determined as 6.12×10^{13} cm^{-2}, corresponding to a click yield of 38%. The lower click yield than observed for of ManOAc is likely due to the more bulky size of LacOAc.

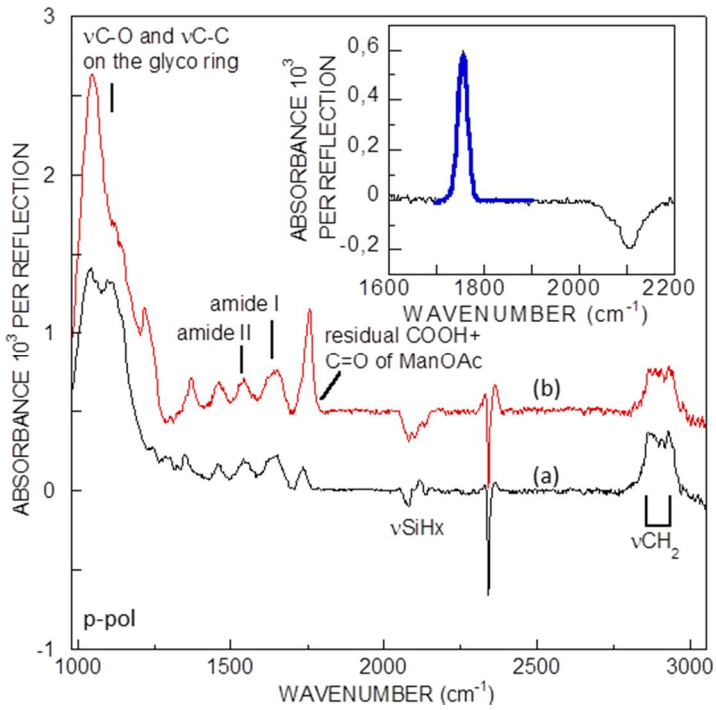

Figure 2.23 IR-ATR spectra in p-polarization of azide- (a) and LacOAc-terminated surfaces (b) with respect to the SiH_x surface. The inset is the spectrum of LacOAc-terminated surface with respect to the azide-terminated surface. The fit of carbonyl bands is highlighted in blue.

2.3.3 "Clicking" of alkynyl glycans

Contrary to the "clicking" of ManOAc, the propargyl mannoside was clicked in PBS 1X buffer in the presence of Cu(I) catalyst. As evidenced by IR-ATR (**Fig 2.24**), the total disappearance of the νN_3 band is indicative of the completion of the reaction with quantitative yield. There is also a greatly increased band at ~1070 cm^{-1}, which arises probably from the oxidation of the surface due to the use of Cu(I) ions but also more plausibly from the νC-O-C of the mannose cycle, as demonstrated by the IR signal of the D-mannose in water solution.

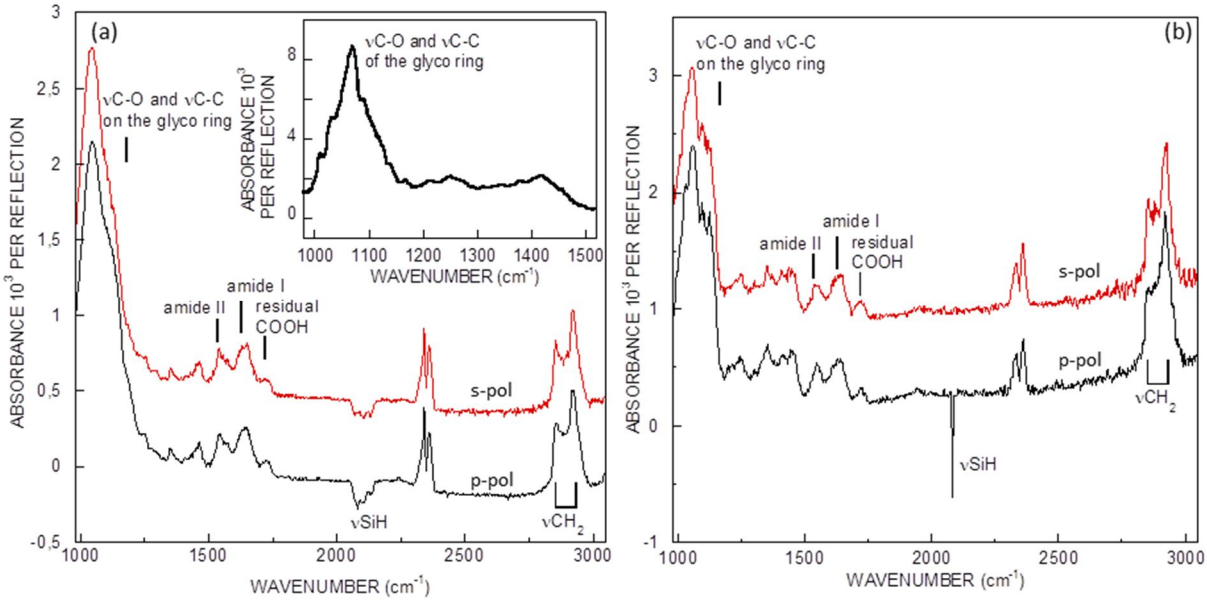

Figure 2.24 IR-ATR spectra in s- and p-polarization of mannose-terminated surfaces, the reference being the SiH_x (a) and SiH surface (b). Inset in (a) is the IR-ATR spectrum of D-mannose in water solution

The lack of "reliable" IR marker of the mannose-terminated surface makes it difficult to quantify its density. Therefore, an alternative colorimetric method based on the phenol-sulfuric acid assay (PSA) was used for calculating the mannose density (**Fig 2.25**).[185, 186] The sugar present on the surface is effectively cleaved off during treatment with concentrated sulfuric acid and transferred into the solution. The method is based on the measurement of the UV-Vis absorption spectroscopy at ~480 nm which is given by a colored aromatic conjugate product formed between phenol and a reducing carbohydrate. On the basis of a calibration curve of D-mannose reacted with phenol and sulfuric acid in solution, the amount of mannose on the surface is found to be 1.1 (± 0.2) × 10^{14} cm^{-2} and the yield of the click reaction is determined to be 70% (± 15%), with minor error in line with the quantification result of the ManOAc-terminated surface by IR-ATR. The less than 100% value suggests that part of the N_3-termini does not participate in the "click" reaction, no residual νN_3 band is observed, which suggests that azide groups might be degraded under the click conditions.

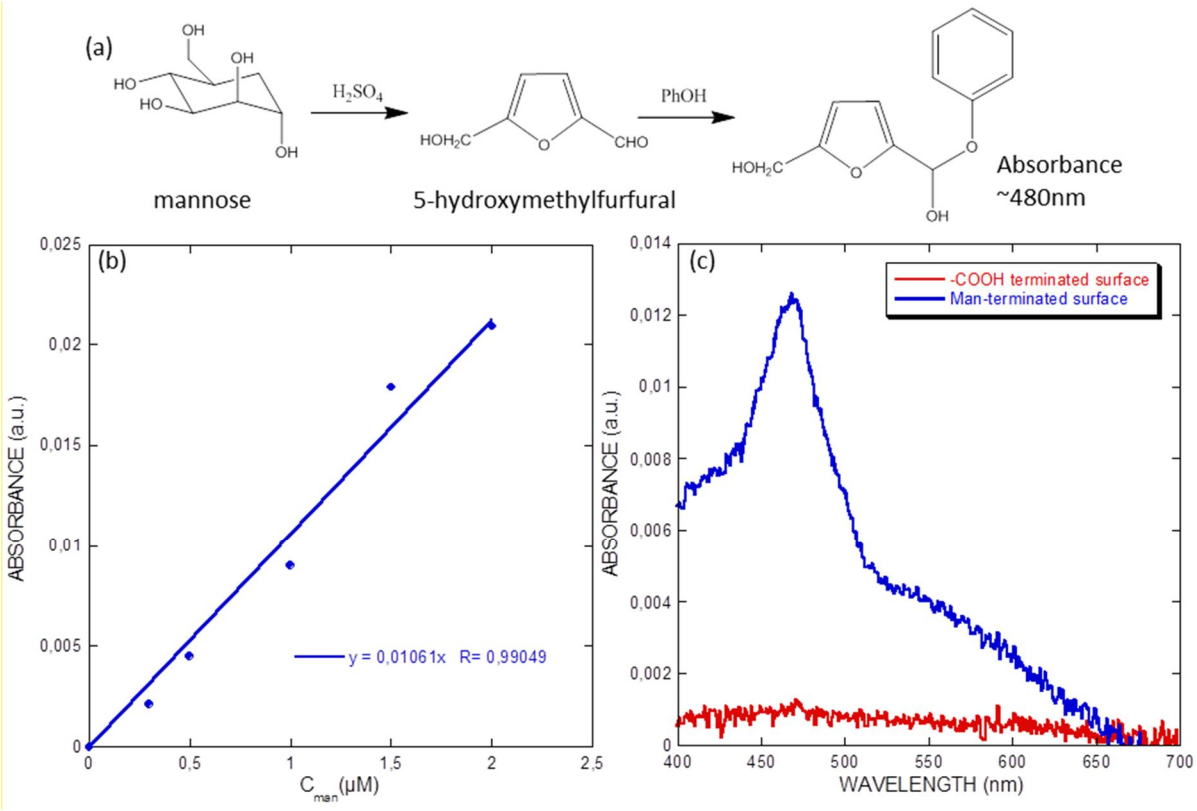

Figure 2.25 UV-Vis calibration curve generated using varying concentrations of D-mannose in water solution (b) and the UV-Vis signal of PSA treated acid- and mannose-terminated silicon surfaces (c). The chemical formula (a) describes the formation of the aromatic conjugate compound.

To check the latter point, the stability of the azide-functionalized surface was tested in contact with a click solution without the presence of alkynyl precursors. IR-ATR monitored the evolution as a function of time in the range of 1950−2250 cm^{-1} with the reference spectra being the SiO_x surface (**Fig 2.26a**). The band detected in this range is in fact the superimposition of the νN_3 and νSiH_x, where the latter νSiH_x band is isolated in the spectrum of the NHS ester-terminated surface (**Fig 2.26b**). Quantitative analysis shows that, after only 4 h of immersion in the click medium, ~65% of the azide functions have already reacted. One potential explanation for its degradation is that azide is reduced to amine function.

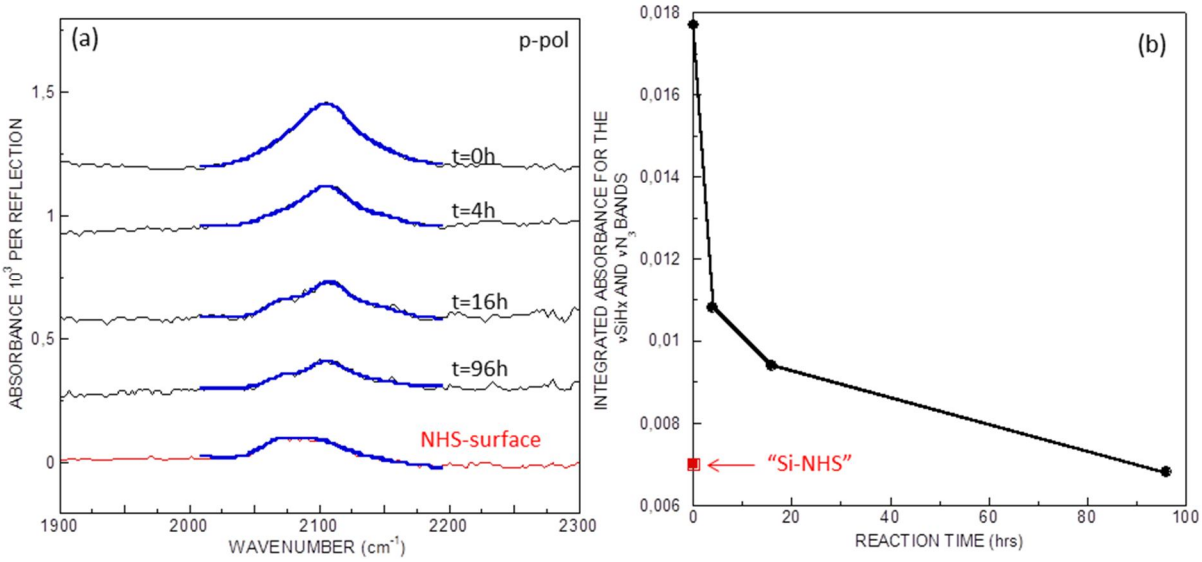

Figure 2.26 Stability of the azide-functionalized surface after immersion in a click solution (containing $CuSO_4$ and sodium ascorbate but without propargyl-mannose) as a function of time. (a) FTIR-ATR spectra in p-polarization of the azide-functionalized surface, measured after immersion at different time and the NHS ester-terminated surface. The reference spectra are the oxidized silicon surface, SiO_x. The fits of the νSiH_x and νN_3 peaks are represented in blue. (b) Integrated absorbance of the νSiH_x and νN_3 of the azide-terminated surface before and after 4 h, 16 h, and 4 days of immersion. The symbol ■ refers to the integrated absorbance of SiH_x and • to that of the sum of SiN_3 and SiH_x.

To understand the transformation from azide to the 1, 2, 3-triazole, XPS is used for a more detailed analysis of the mannose-decorated surface (**Fig 2.27**). The appearance of a SiO_2 band in the narrow scan of Si_{2p} (**Fig 2.27a**) probably arises from the Cu induced oxidation of the surface. Comparison between the high-resolution XPS spectrum of the N_{1s} band before (**Fig 2.10d**) and after clicking the mannose to the surface (**Fig 2.27b**) yields the following conclusions: the peak at high binding energies (405.4 eV) characteristic of the central nitrogen in the azido function ($N{=}N^+{=}N^-$) is absent, and two distinct peaks at 402.7 (N−C) and 401 eV (N=N) characteristic of the triazole are instead observed.[187, 188]

To interpret the XPS spectrum of the N_{1s} band quantitatively, it must be kept in mind the band at 401 eV also contains a contribution from the nitrogen of the amide bond (cf **Fig 2.10d**). A less intense peak appearing at 400 eV is attributed to an additional contribution from an $-NH_2$ moiety and might derive from the reduction of the azide function. Considering the click yield of 0.75, one might expect contributions of 0.75 for the triazole N (402.7 eV), 0.75×2 for N=N (401 eV), 1 for the amide N (401eV) and 0.25 for the reduced $-NH_2$ moiety (400 eV). Finally, the N_{1s} band is deconvolved to 402.7/401/400 eV with a ratio of 0.75/2.5/0.25 (0.75 : (0.75×2 +1) : 0.25), which seems to fit well the obtained data.

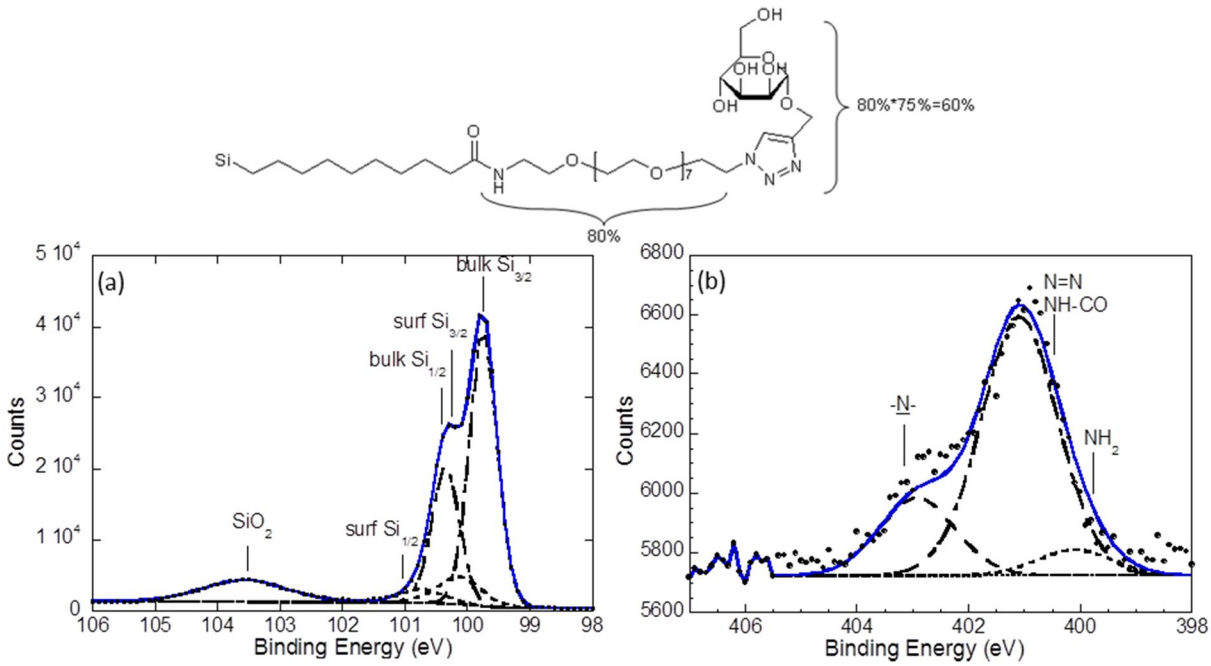

Figure 2.27 High resolution XPS spectra of Si_{2p} (a) and N_{1s} (b) bands and the composition assignment.

In parallel, the propargyl lactoside was clicked and the reaction was followed by IR-ATR (**Fig 2.28**). With the appearance of νC-O ~1050 cm^{-1} and the disappearance of νN_3 ~2010 cm^{-1} after the reaction, the immobilization of lactose is confirmed. Without performing the PSA method, the density of lactose on the surface can be postulated from the quantification result of LacOAc, which yields a value around 6.1×10^{13} cm^{-2}, with a click yield of 38%.

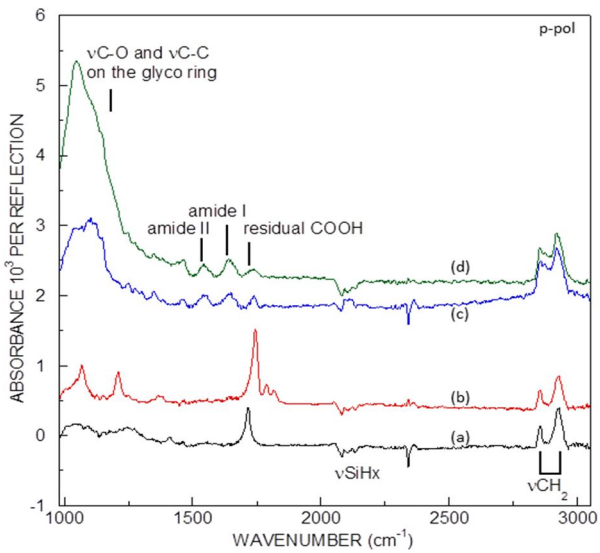

Figure 2.28 IR-ATR spectra in p-polarization of acid- (a), NHS ester- (b) N_3- (c) and lactose-terminated surfaces (d) with respect to the SiH_x surface.

The AFM images after clicking propargyl mannoside and lactoside **(Fig 2.29)** keep the staircase structure, confirming the formation of a uniform organic layer without physisorbed molecules. However, the flatness of each step is greatly altered due to the presence of 0.5 nm depth variations appearing as black holes. In a control experiment using an azido-terminated surface immersed into the "click" medium without the glycan present, no such a variation is observed, suggesting that these inhomogeneities are derived from glycan domains.

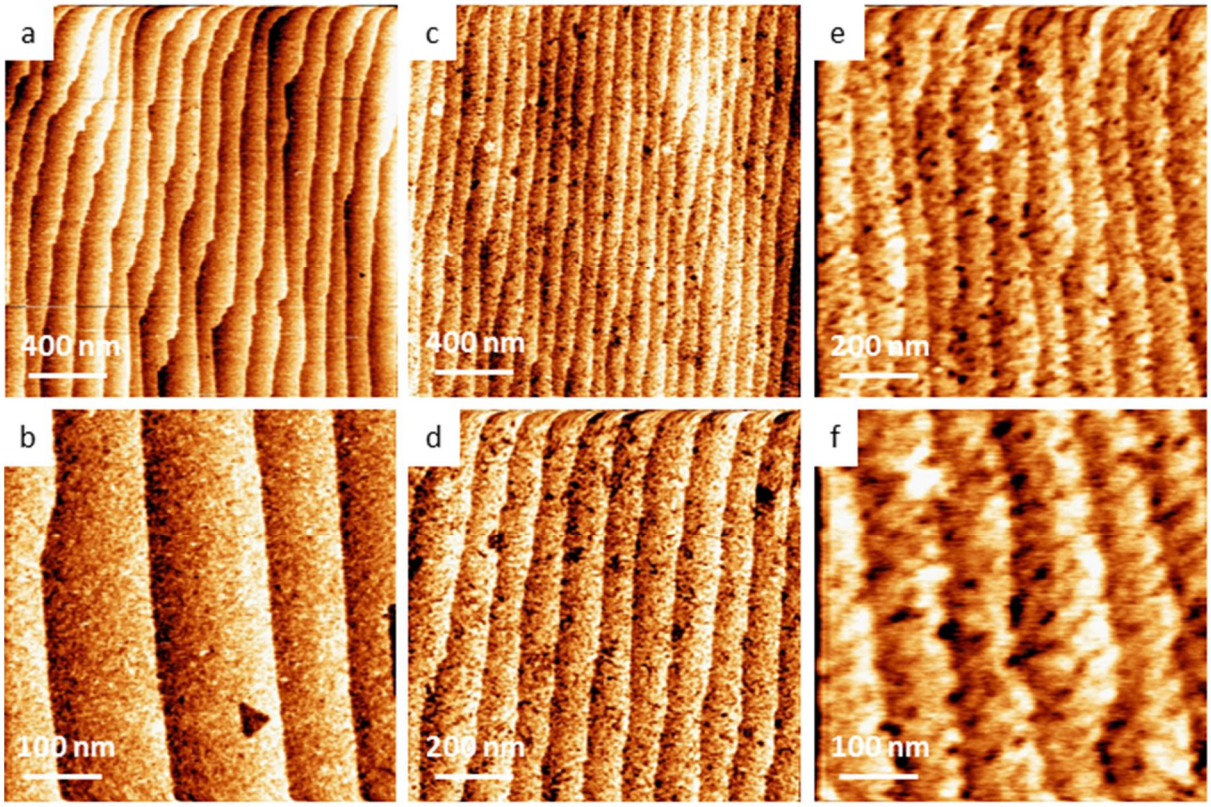

Figure 2.29 AFM images of the N_3-terminated surface immersed in click solution without alkynyl-derivatized glycans (a, b) and the mannose-(c, d) and lactose-terminated surfaces (e, f).

2.3.4 Modeling of the glycosylated surface

The ManOAc, LacOAc, propargyl mannose and lactose molecules are modeled using Chem3D software. From a rough measurement of the distance between two extreme atoms, the size of the four molecules is estimated to be 0.88, 1.26, 0.7 and 1.1 nm. Nevertheless, the

actual size of these molecules should take into account the rotation of the glycosidic bond, which is expected to be higher than the estimated values. From the quantitative analysis of these glycan-terminated monolayers, we know that the ManOAc- or mannose-terminated surfaces occupy a surface concentration of ~1.2×10^{14} cm^{-2}, corresponding to an average area of 0.83 nm^2 for each ManOAc or mannose terminus. This unit area can be described by a square of 0.91 nm×0.91 nm, close to the size of the ManOAc (0.88 nm) or mannose molecules (0.7 nm). Analogously, the LacOAc- or lactose-terminated surface occupy a surface concentration of ~6.12×10^{13} cm^{-2}, corresponding to a unit area of 1.63 nm^2 (1.27 nm×1.27 nm) for each LacOAc or lactose terminus, also very close to the size of LacOAc (1.26 nm) or lactose molecules (1.1 nm). Therefore, it is possible to conclude that the “click” reaction makes the immobilization of glycans under a closely compact form so that it appears difficult to “click” more glycans due to the limited steric hindrance.

2.4 Conclusion

We have presented in this chapter the step-by-step functionalization protocol to immobilize glycan molecules at the basis of carboxydecyl-terminated crystalline silicon surface. The hetero OEG molecules carrying amine and azide functions were amidated *via* an activation step on the carboxydecyl-terminated surfaces to give the formation of an azide-terminated surface, onto which the alkynyl-derivatized glycans were immobilized *via* Cu(I)-catalyzed Huisgen 1,3-dipolar cycloaddition reaction. Each step was carefully controlled by IR-ATR. The utilization of quantitative IR-ATR also allowed the density of the acid-, NHS ester- and N_3-terminated surfaces and of the corresponding reaction yield to be determined. The density of glycan-terminated surface was alternatively estimated by IR-ATR from the "clicking" of acetylated glycan analogues. To unambiguously support the data, the density of a mannose-terminated surface was determined by UV-Vis spectroscopy through the phenol-sulfuric acid assay. In addition, AFM was used to visualize the formation of the organic monolayer attached to the SiH surface, evidencing the formation of a clean surface without physisorption at each step. The complementary quantitative IR-ATR study revealed the generation of the same density of the glycan ligands on the SiH surface as they are on the SiH_x surface, even though the grafting of the carboxydecyl chain was more efficient in the former case. Furthermore, the "click" reaction has particularly been investigated by XPS showing the transformation of nitrogen from the azide to the triazole.

Based on the obtained molecule density at each modification step, the presence of the glycosylated monolayer can be schematically described as in **Fig 2.31**. The first layer is the carboxydecyl chain with a density of ~2×10^{14} cm^{-2}, followed by an amide bond-linked OEG chain plausibly owning an entangled conformation and a density of ~1.6×10^{14} cm^{-2}. The glycans are located atop the surface through a 1, 2, 3-triazole ring. The glycans are settled in a highly compact distribution with a density of ~1.2×10^{14} cm^{-2} for mannose and ~6.1×10^{13} cm^{-2} for lactose.

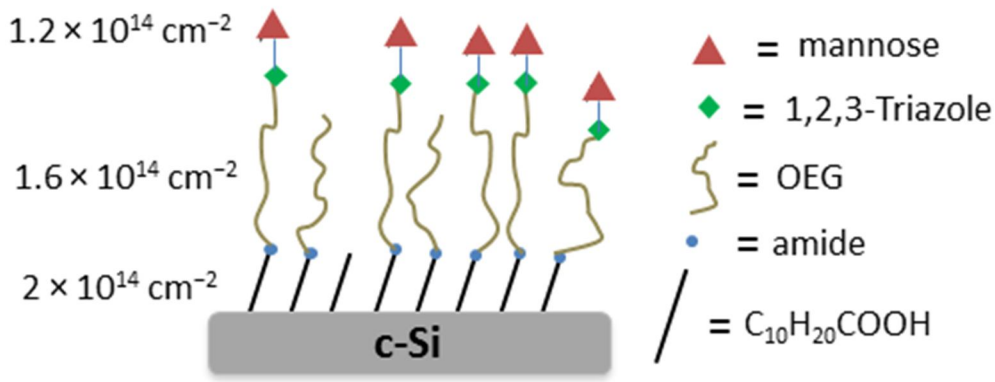

Figure 2.31 Schematic representation of the constructed mannose-terminated monolayer.

2.5 Experimental section

2.5.1 Molecules, proteins and substrates

All chemicals were of reagent grade or higher and were used as received without further purification. All cleaning reagents (H_2O_2, 30%; H_2SO_4, 96%, absolute EtOH anhydrous) and etching reagents (HF, 50%; NH_4F, 40%) were of RSE grade and supplied by Carlo Erba. The undecylenic acid (99%) was supplied by Acros organics. All other chemicals were purchased from Sigma-Aldrich. Ultrapure water (Milli-Q, 18 MΩcm) was used for the preparation of the solutions and for all rinses.

The silicon sample for AFM study was cut from one-side polished n-type (111) silicon wafers (CZ, ρ=5−10 Ω cm, 525 μm thickness, Siltronix, France) with a miscut of 0.2° toward the $(11\bar{2})$ direction. The silicon sample for IR-ATR study was homemade double-side polished n-type (111) silicon prisms (FZ, ρ=30-40 Ω cm, Siltronix, France). They were shaped as 20×14×0.5 mm^3 platelets, then two opposite sides were 48°-51° bevelled, giving ~22 reflections.

2.5.2 Synthesis of alkynyl-derivatized glycans

***Per-O-acetyl-α-propargyl Mannoside* (ManOAc).** In a two-round-bottom flask containing D-mannose (3 g, 16.65 mmol) and anhydrous pyridine (51 mL), acetic anhydride (15 mL) was added dropwise at 0 °C under argon. After 4 h, at room temperature, the mixture was quenched by adding aqueous HCl (1 M, ca. 500 mL). The mixture was extracted with dichloromethane (CH_2Cl_2), the organic phase dried over sodium sulfate (Na_2SO_4) and filtered, and the solvent evaporated under vacuum to give the crude product (5.42 g, 83.4%). The practically pure per-O-acetyl mannose (2g, 5.13 mmol) was placed in a two-necked round-bottom flask under argon and dissolved in dry CH_2Cl_2 (32 mL), and then, propargyl alcohol (1.21 mL, 20.51 mmol) was added followed by the dropwise addition of boron trifluoride etherate (BF_3OEt_2) (3.39 mL, 26.8 mmol) at 0 °C. After 22 h, the reaction mixture was quenched by slow addition of a saturated sodium bicarbonate ($NaHCO_3$) solution. The mixture was extracted carefully (generation of CO_2) with CH_2Cl_2, and the organic phase was dried over Na_2SO_4 and concentrated *in vacuo*. The title compound was obtained pure by flash chromatography using cyclohexane/ethyl acetate (7/3) (26%).

^{1}H NMR (300 MHz, $CDCl_3$) δ = 1.98 (s, 3H, CH_3); 2.03 (s, 3H, CH_3); 2.10 (s, 3H, CH_3); 2.16 (s, 3H, CH_3); 2.47 (t, 1H, CH≡); 4.06 (m, 2H, CH_2−C≡); 4.26 (d, 2H, CH_2−OAc); 4.28 (dt, H); 5.02 (d, H, anomeric C−H); 5.25−5.4 (m, 3H). ^{13}C NMR δ = 20.50−20.90 (4C, CH_3); 54.93 (1C, CH_2−C≡); 62.30 (1C, CH_2−OAc); 66.02 (1C, CH); 68.91 (1C, CH); 68.96 (1C, CH); 69.34 (1C, CH); 75.50 (1C, −C≡); 77.84 (1C, ≡CH); 96.22 (1C, anomeric C); 169.65 (1C, C=O); 169.79 (1C, C=O); 169.91 (1C, C=O); 170.59 (1C,C=O).

HR-MS: m/z=408.7 (ManOAc+Na^+).

***α-Propargyl Mannoside* (Man).** Per-O-acetyl propargyl-α-mannoside (200 mg, 0.518 mmol) was dissolved in dry methanol (MeOH) (12 mL), and sodium methoxide (MeONa) was added (18.9 mg, 0.349 mmol). The reaction mixture was stirred vigorously for 2 h, then treated with Amberlite resin (acid form) until neutral pH is obtained, filtered, and concentrated *in vacuo* to yield the title compound (110 mg, 97.4%).

^{1}H NMR (300 MHz, MeOH-d_4) δ= 2.85 (t, H, CH≡); 3.45−3.59 (m, 4H); 3.80 (m, 2H, CH_2OH); 4.27 (d, 2H, CH_2−C≡); 4.96 (d, H, anomeric C−H). ^{13}C NMR δ = 54.87 (1C, CH_2−C≡); 62.82 (1C, CH_2−OH); 68.49 (1C, CH); 72.05 (1C, CH); 72.52 (1C, CH); 75.10 (1C, CH); 76.01 (1C, −C≡); 80.69 (1C, ≡CH); 99.87 (1C, anomeric C).

HR-MS: m/z=240.8 (Man+Na^+).

***Per-O-acetyl- β -propargyl Lactoside* (LacOAc).** In a two-neck round bottomed flask containing a mixture of lactose (5 g, 13.88 mmol) and anhydrous pyridine (85.03 mL), under argon, acetic anhydride (25 mL) was added dropwise at 0°C. After 4 h, at room temperature, the mixture was quenched by dropwise addition of aqueous HCl (12 M). The mixture was extracted with CH_2Cl_2 and the organic phase was dried over Na_2SO_4 and filtered. The solvent was evaporated *in vacuo* to give the gel-like white crude product (8.7 g, 80.6%). The practically pure per-O-acetyl-lactose (6.3 g, 9.3 mM) was placed in a two-neck round-bottomed flask under argon and dissolved in dry CH_2Cl_2 (50.65 mL), and then, propargyl alcohol (1.92 mL 30.84 mM) was added followed by the dropwise addition of BF_3OEt_2 (5.12 mL, 40.5 mM) at 0°C and then allowed to come to room temperature. After 22 h, the reaction was quenched by slow addition of a saturated $NaHCO_3$ solution. The mixture was extracted carefully with CH_2Cl_2 and the organic phase was dried over Na_2SO_4 and concentrated *in vacuo*. The title compound was obtained by flash chromatography using cyclohexane/ethyl acetate (1/1) as eluent (1.01 g, 16.3%).

.

^{1}H NMR (300 MHz, $CDCl_3$) δ=1.90 (s, 3H, -CH_3); 1.978 (s, 3H, -CH_3); 1.980 (s, 3H, -CH_3); 1.987 (s, 3H, -CH_3); 1.994 (s, 3H, -CH_3); 2.06 (s, 3H, -CH_3); 2.08 (s, 3H, -CH_3); 2.39 (t, 1H, ≡CH); 3.72-3.83 (m, 2H, CH-OAc); 3.57-4.041 (m, 4H, CH_2-OAc); 4.27 (d, 2H, -CH_2-C≡); 4.42 (d, 1H, anomeric CH of Gal); 4.67 (d, 1H, anomeric CH of Glc); 4.82-5.29 (m, 6H, CH-OAc). ^{13}C NMR δ=20.50-20.84 (7C, CH_3); 55.85 (1C, -CH_2-C≡); 60.81 (1C, -CH_2-OAc); 61.81 (1C, -CH_2-OAc); 66.60 (1C, -CH-OAc); 69.09 (1C, -CH-OAc); 70.71(1C, -CH-OAc); 70.97 (1C, -CH-OAc); 71.30 (1C, -CH-OAc); 72.68 (1C, -CH-OAc); 72.75 (1C, -CH-OAc);

72.83 (1C, -CH-OAc); 75.43 (1C, ≡CH); 76.11 (1C, -C≡); 97.86 (1C, anomeric -CH of Glc); 101.02 (1C, anomeric -CH of Gal); 165.47 (1C, C=O); 166.40 (1C, C=O); 168.78 (1C, C=O); 168.98 (1C, C=O); 169.72 (1C, C=O); 170.03 (1C, C=O); 170.11 (1C, C=O); 170.31 (1C, C=O).

HR-MS: m/z=696.9 (LacOAc+Na^+).

β-Propargyl Lactoside **(Lac).** The crude per-*O*-acetyl propargyl lactoside (1.01 g, 1.5 mmol) was dissolved in dry MeOH (60 mL), and MeONa was added (54 mg, 1 mmol). The reaction mixture was stirred vigorously for 2 h, and then treated with Amberlite resin (acid form) until neutral pH is obtained, then filtered and concentrated *in vacuo*. The mixture was purified by flash chromatography using ethyl acetate/MeOH (9/1) (70 mg, 12.3%).

^{1}H NMR (300 MHz, MeOH-d_4) δ=2.87 (t, 1H, ≡CH); 3.35-3.94 (m, 12H, -CH-OH); 4.37 (d, 1H, anomeric –CH of Gal); 4.42 (d, 1H, CH_2-C≡); 4.50 (d, 1H, anomeric –CH of Glc). ^{13}C NMR δ=56.64 (1C, -CH_2-C≡); 61.89 (1C, -CH_2-OH); 62.54 (1C, -CH_2-OH); 70.35 (1C, CH-OH); 72.58 (1C, CH-OH); 74.56 (1C, CH-OH); 74.85 (1C, CH-OH); 76.34 (1C, CH-OH); 76.40 (1C, CH-OH); 76.62 (1C, CH-OH); 77.12 (1C, CH-OH); 79.99 (1C, -C≡); 80.57 (1C, ≡CH); 101.98 (1C, anomeric -CH of Glc); 105.13 (1C, anomeric -CH of Gal).
HR-MS: m/z=402.6 (Lac+Na^+)

2.5.3 Preparation of glycan-derivatized surfaces.

The mixture H_2SO_4/H_2O_2 (piranha) solution is a strong oxidant. It reacts violently with organic materials. It can cause severe skin burns. It must be handled with extreme care in a well-ventilated fume hood, while wearing appropriate chemical safety protection. HF is a hazardous acid, which can result in serious tissue damage if burns are not appropriately treated. Etching of silicon should be performed in a well-ventilated fume hood with appropriate safety considerations: face shield and double layered nitrile gloves.

Etching of surface. The silicon platelet was first cleaned in a 1/3 H_2O_2/H_2SO_4 piranha solution at 100 °C and rinsed with Milli-Q water. The silicon prism applied in the IR-ATR study was subsequently etched in a 50% HF solution for 5 s and rinsed with Milli-Q water. The silicon wafer applied in the AFM study was obtained by chemical etching for 15 min in oxygen-free 40% NH_4F (ca. 0.05 M ammonium sulfite was added to the etching solution and ultrasonicated for 15 min to be well dissolved).

Acid-Terminated Surface. The as-formed hydrogen-terminated Si surface was placed at room temperature in a Schlenk tube containing previously deoxygenated neat undecylenic acid solution and irradiated at 312 nm (6 mW cm^{-2}) for 3 h.[105] The excess of unreacted and

physisorbed reagent was removed by a final rinse in hot acetic acid (75°C) for 30 min.[175] Then, the sample was dried under nitrogen flow.

NHS ester-Functionalized Surface. The conversion of the acid to the corresponding succinimidyl ester was accomplished as follows: the acid-terminated surface was immersed in 10 mL of an aqueous solution of NHS (5 mM) and EDC (5 mM) and allowed to react for 90 min at 15 °C.[110] The resulting surface was copiously rinsed with Milli-Q water and dried under a stream of argon.

Azido-OEG Surface. The NHS-terminated surface was reacted with 20 mM of $NH_2{-}C_2H_4{-}OEG{-}N_3$ in 1X PBS at pH ~ 8 overnight at room temperature. The resulting surface was copiously rinsed with 1X PBS, followed by a surfactinated rinse (1X PBS/0.1% SDS for 15 min; 0.2X PBS for 5 min; 0.1X PBS for 5 min) and finally with Milli-Q water.[134] The azido-OEG surface was dried under a stream of argon.

Clicking of alkynyl molecules. The azido−OEG surface was immersed in degassed solutions of 3 mM ManOAc or LacOAc in DMSO/EtOH/1X PBS (1/8/5 v/v/v) containing 5 mol % $CuSO_4$ and 15 mol % sodium ascorbate. After 5 h, the sample was washed twice with CH_2Cl_2, EtOH and EDTA solution (0.1 M), 1X PBS/0.1% SDS for 10 min; 0.2X PBS for 5 min; 0.1X PBS for 2 min and finally rinsed thoroughly with deionized water. The clicked surface was then dried under a stream of argon. To click Man or Lac, the solution was simply 1X PBS by keeping the same concentration and the rinse was the same without EtOH.[177]

2.5.4 Phenol-sulfuric acid assay

To make the calibration curve, 60 µL of phenol (5%), 60 µL of mannose solution (a series of concentrations, 5.1, 8.5, 17, 25.5 and 34 µM) and 900 µL of sulphuric acid (96%) were mixed at 15 °C for 20 min before measuring the UV−vis spectra. Quantification of mannose clicked on the silicon prism was possible by dipping the prism into a stirred mixture of 60 µL of phenol (5%), 60 µL of water, and 900 µL of sulphuric acid at 15 °C for 20 min, decanting the solution into the quartz cell for UV−vis and comparing the measurement relative to the calibration curve. The reference sample is an acid-terminated silicon prism.

The UV−vis spectra were recorded in the range 400−700 nm with a Cary 300 spectrophotometer and a quartz cell Hellma 6040-UV type (10 mm light path for a maximum 1400 µL volume).

CHAPTER 3

Interaction of glycosylated surfaces with proteins

.

3.1 Introduction

This chapter concerns the investigation of the interaction of glycan-modified surfaces with their specific and non-specific lectins. Two kinds of well-known plant lectin proteins are used here: lectin *lens culinaris* (LENS) and lectin *peanut agglutinin* (PNA). As depicted in **Fig 3.1**, the LENS is specific to α-mannoside and not specific to β-galactoside (unit contained in lactose). On the contrary, the PNA is specific to β-galactoside and not specific to α-mannoside.

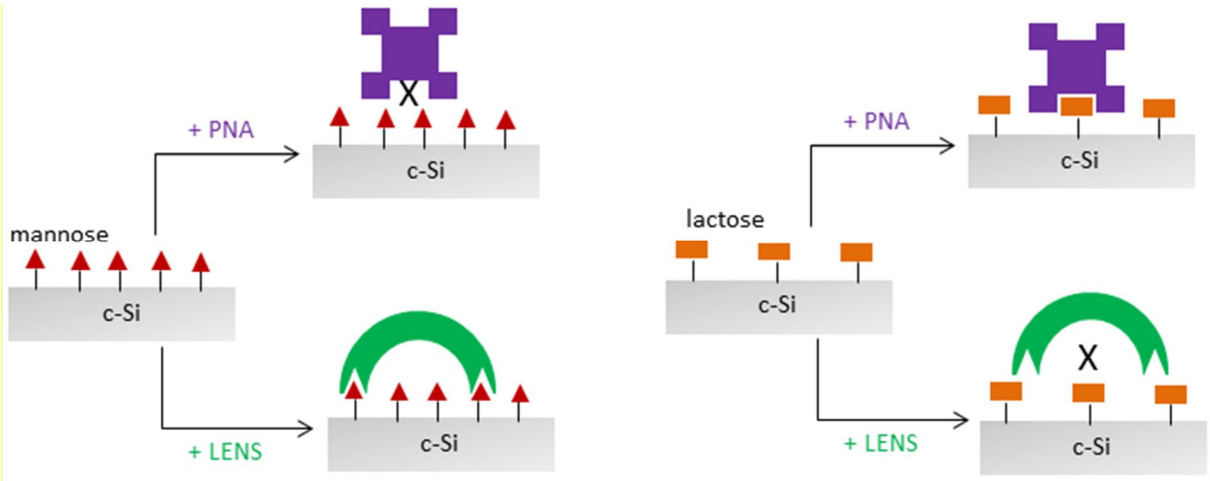

Figure 3.1 Scheme describing the specificity of LENS and PNA to mannose and lactose-terminated surfaces.

In contrast to DNA molecules, the biological activity of protein attached to its 3D structure is fragile and much influenced upon surface contact (i.e., denaturation). For conceptions of glycan microarrays or biochips, one of the main challenges is to avoid the denaturation of proteins (loss of their activity) and the non-specific adsorption on the surface of the chip. It has been reported in many examples of surface detection method that the influence of non-specific adsorption was not taken into account as long as the specific binding signal takes much over the non-specific one.[21, 22, 38, 189, 190] In these methods, the specificity was obtained by simply subtracting the overlapping of non-specific background. Nevertheless, such a treatment may cause errors in overestimating the "real" quantity of proteins that are specifically bound and underestimating their binding affinity.[191] The influence of non-specific adsorption might be more risky in the case of a binding activity such as the protein-glycan interaction (affinity is only in the micromolar range). Therefore, the elimination of non-specific adsorption is particularly important to warrant a reliable assay result.

As introduced in the section 1.2, the surface property and buffer play important roles in regulating the adsorption behavior of proteins. Therefore, in this chapter, both effects have been studied to control the specificity of the lectin-glycan interactions using IR-ATR and AFM. Firstly, the antifouling performance of the surface has been investigated by using OEG

chains of two different lengths intercalated in the glycosylated monolayer, the longer EG_8 and shorter EG_2. Secondly, the influence of the buffer rinse has been investigated after the interaction with lectins by using a simple rinse in PBS solution (PBS 1X) and a surfactinated rinse in sodium dodecyl sulfate (SDS) solution (0.1%SDS/PBS 1X). The surfactinated rinse is well-known to efficiently eliminate the physisorption due to its detergent and denaturation effect.[134, 192-195]

In a second step, the optimization of the multivalent binding has been further studied. As exhibited from the crystallographic structures in **Fig 3.2**, the two lectins own multiple "pockets"-like binding sites which are realized by various oligomerizations of subunits. LENS possesses two mannose-binding cavities owing to its dimeric structure and PNA possesses four galactose-binding cavities owing to its tetrameric structure.

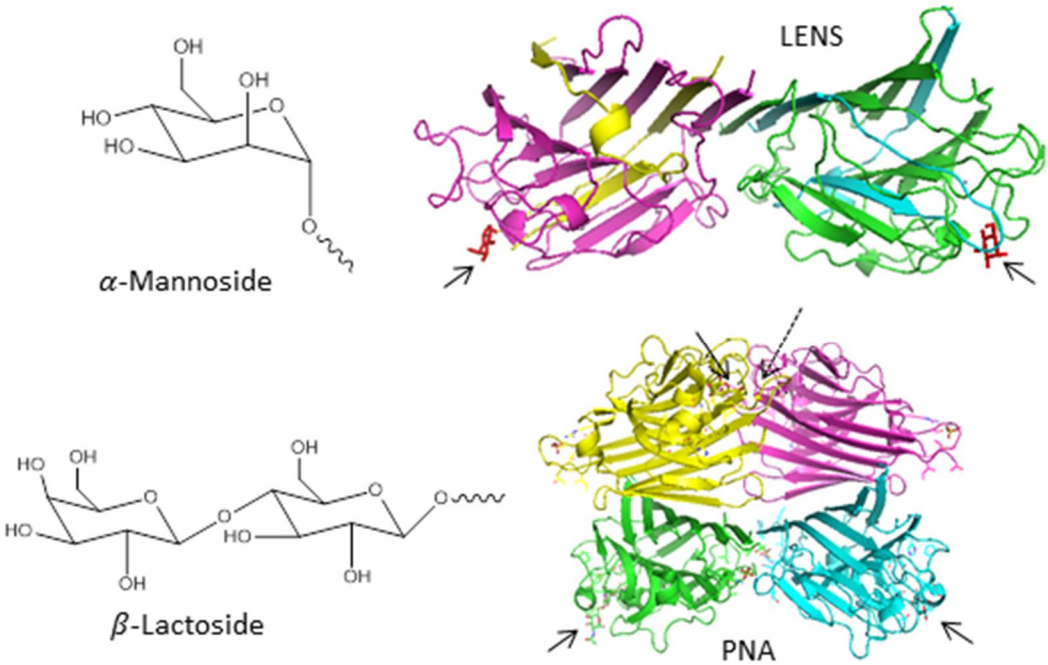

Figure 3.2 Crystallographic structures of LENS (pdb file: 1LES) and PNA (pdb file: 2DVB) and their specific glyan ligands. The glycan binding sites are indicated by arrows.

As presented in the general introduction, formation of the multivalent interactions depends on the appropriate spacing and orientation of glycans.[34] In case of the glycans immobilized on a surface, the multivalent binding of a lectin depends ultimately on the effective surface concentration of immobilized glycans. This can be in principle tuned by diluting the glycan derivative with non-sugar spacer molecules prior to linking of the sugar onto the interface. For example, Smith *et al.* immobilized a mixture of different glycans on thiolated self-assembled monolayers (SAMs) and studied the binding yield of different receptors by SPR imaging.[11] They revealed that the amount of proteins loaded onto the surface decreases non-linearly as the surface glycans are diluted, similar to what observed by Szunerits et al.[20] However, Sato *et al.* diluted the surface glycan densities on thiolated SAMs by shorter and smaller spacer

chains and they demonstrated by SPR that the amount of bound proteins appeared maximum at a proper dilution instead of complete coverage of glycan,[40] similar to what obtained by Svedhem et al.[196] Both cases came to the conclusion that the protein is bound with the cluster of surface glycans by its multivalent structure. The optimized binding condition can only be achieved when the glycan are located with as many sites as possible which properly fit to the multi-hollow structured lectin.

Therefore to understand whether similar dilution effect can be applied for our glycosylated monolayers, we have studied the influence of the glycan density on the binding efficiency of lectin by diluting the glycan probes with propargyl alcohol at different concentrations (10 mol% and 1 mol%) during the “click” chemistry on azide-terminated surface. The density of the diluted glycan chains grafted on the surface was determined using IR-ATR. Then, the binding efficiency of specific lectins with the diluted glycan-terminated surfaces was characterized by IR-ATR and AFM. Furthermore, the binding affinity was measured using IR-ATR by analyzing the binding isotherm curves. Finally, the reusability of the lectin-treated surfaces was addressed by AFM.

3.2 Effects of OEG length and rinse on the (non)specific binding

3.2.1 Study using IR-ATR

a) On mannose-terminated surface

In the previous chapter we obtained the mannose-terminated surface with two different lengths of intercalated OEG chains: EG_8 and EG_2, giving the chain density of ~ 1.6×10^{14} cm^{-2} and 1.8×10^{14} cm^{-2}, respectively. The mannose-terminated surface was firstly interacted with the non-specific PNA (at 1 mg/mL, or 9.7 µM, Mw=103 kDa) as a control experiment, under the static incubation for 1 h followed by a PBS (10 min) and then a SDS rinse (10 min). Then the surface was incubated with specific LENS (at 1 mg/mL, or 19.2 µM, Mw=52 kDa) followed again by a PBS and a SDS rinse.

Fig 3.3a displays the IR-ATR spectra of the interaction of mannose-EG_2 terminus with non-specific PNA followed by the rinse in PBS and SDS solutions. The high intensity of both amide I (~1648 cm^{-1}) and II (~1548 cm^{-1}) bands after the contact with PNA implies the presence of non-specific adsorption of PNA. After a SDS rinse, the non-specific adsorption is slightly reduced, but still superior to the initial mannose-terminated surface, indicating that the non-specific adsorption cannot be completely eliminated. **Fig 3.3b** shows the contact of the surface with specific LENS after a PBS rinse, which gives much stronger amide bands than PNA. Followed by a SDS rinse, similarly, the protein signal is reduced but cannot be completely removed. The contribution from the protein can be evaluated using the integrated absorbance of amide I band of the lectin-treated surface subtracting that of the initial mannose-terminated surface. The use of amide I band to represent the characteristic protein signal is based on two reasons. Firstly, this band arises mainly from the νC=O with minor contributions from the out-of-phase νC-N whereas the amide II band is a mixture of N-H bending, C-N stretching and C-C stretching which is significantly influenced by the side chain functional groups.[197] The amide I band is most commonly used for secondary structure analysis since its position is essentially determined by the backbone conformation. Secondly, the fits of amide I band are less influenced by the overlapping with multiple small bands, as it is the case for amide II band at lower wavenumbers. **Fig. 3.3c** summarizes the values of the integrated area of amide I band from proteins followed by different rinses. From the histogram, we can clearly see that the specificity of LENS over PNA can be distinguished under both rinses. However, this test suggests that the short EG_2 chain cannot completely limit the non-specific adsorption.

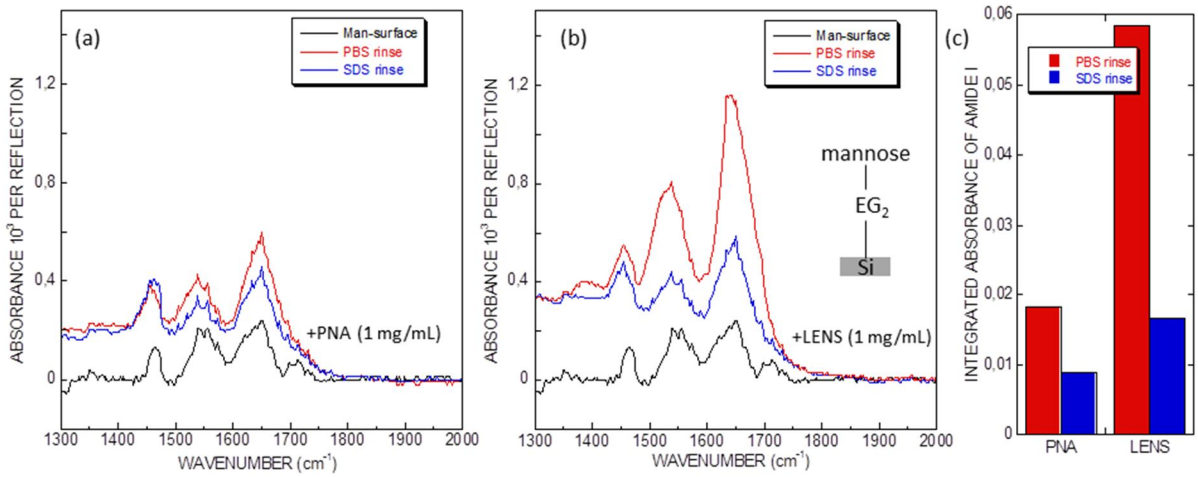

Figure 3.3 IR-ATR spectra in p-polarization of mannose-EG_2-terminated surface interacted with PNA (1 mg/mL) (a) and LENS (1 mg/mL) (b) after PBS and SDS rinse. (c) Histogram representing the integrated absorbance of amide I for the two lectins and rinses.

A longer EG_8 chain intercalated on mannose-terminated surface is thus tested as shown in **Fig 3.4**. The interaction with PNA after a PBS rinse almost reproduces the surface without any addition of protein, indicating the excellent protein repellence of the antifouling EG_8 chains (**Fig 3.4a**). Moreover, the addition of LENS under the same PBS rinse clearly gives an increase in amide bands (**Fig 3.4b**). After a more violent SDS rinse, the specific binding signal is reduced (**Fig 3.4c**).

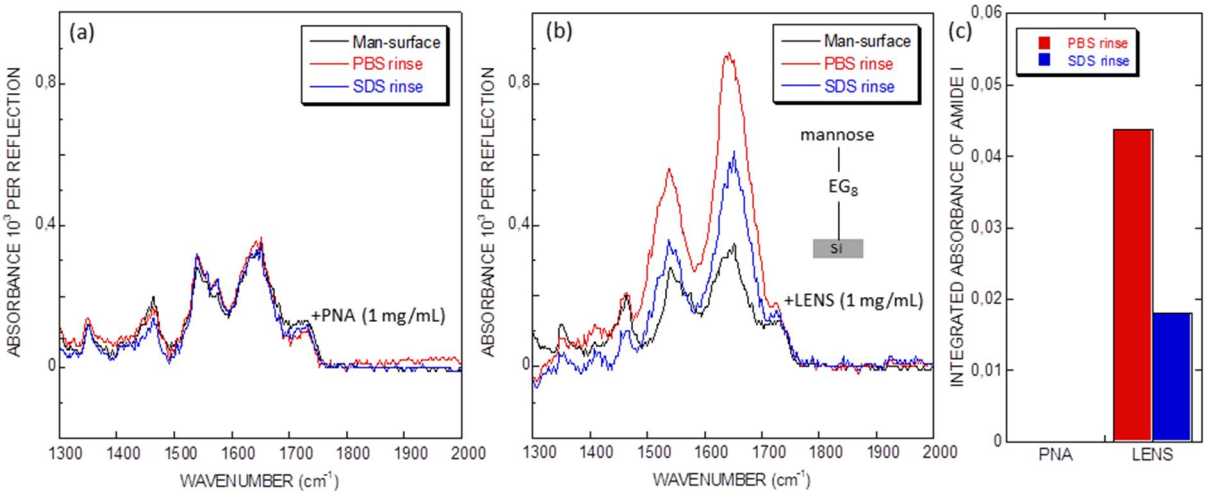

Figure 3.4 IR-ATR spectra in p-polarization of mannose-EG_8-terminated surface interacted with PNA (1 mg/mL) (a) and LENS (1 mg/mL) (b) after PBS and SDS rinse. (c) Histogram representing the integrated absorbance of amide I for the two lectins and rinses.

Similar lectin binding test was applied to a mannose-EG_8 layer grafted on the SiH surface by using the SDS rinse (**Fig 3.5**). In the previous chapter, it was demonstrated that the density of EG_8 chain and mannose is identical to that on a SiH_x surface. As expected, there is no adsorption upon the exposure to PNA. After the interaction with LENS, the amide I band also increased, close to the previous result. Therefore, for the following studies, we will only use the EG_8-incorporated glycan monolayer.

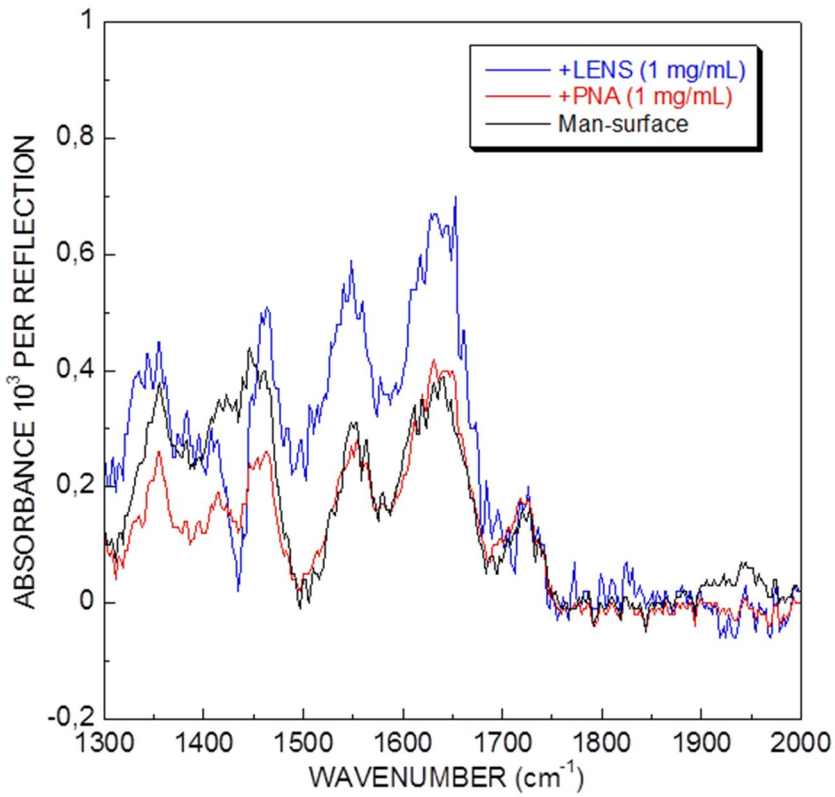

Figure 3.5 IR-ATR spectra in p-polarization of mannose-EG_8-terminated surface started from the SiH surface and its interaction with PNA (1 mg/mL) and LENS (1 mg/mL) followed by a SDS rinse.

b) On lactose-terminated surface

The specificity of PNA to lactose has conversely been verified on a lactose-terminated surface. **Fig 3.6a** shows the IR spectra of the lactose-EG_8 surface exposed first to LENS after a PBS rinse, which gives a subtle increase of amide bands. Followed by a SDS rinse, the non-specific adsorption of LENS can be totally removed. **Fig 3.6b** shows then the interaction of the surface with specific PNA. The specificity of the surface to PNA is discernible for its

much higher increase of amide band. After a SDS rinse, similar to the previous case, the binding signal of PNA is again reduced (**Fig 3.6c**).

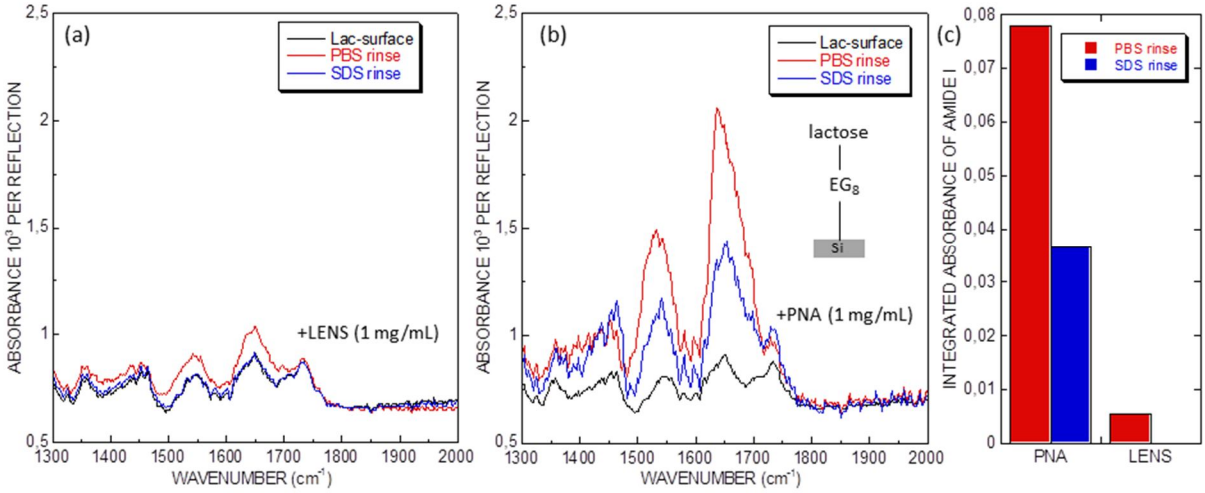

Figure 3.6 IR-ATR spectra in p-polarization of Lac-EG_8-terminated surface interacted with LENS (1 mg/mL) (a) and PNA (1 mg/mL) (b) after PBS and SDS rinse. (c) Histogram representing the integrated absorbance of amide I for the two lectins and rinses.

c) Discussion

The above experiments were repeated several times. We observed that the interaction with specific lectins after a PBS rinse did not offer a reproducible value of the increase factor of the amide I band, but showed instead a great variation of ~25%. However, the interaction after a SDS rinse is much more reproducible with a 5% variation in the increase factor of the amide I band.

With regard to the non-specific adsorption, the infrared results motivate three remarks. Firstly, the intercalation of the EG_8 chain is necessary to limit the non-specific adsorption. Secondly, the utilization of a simple PBS rinse is adequately enough to eliminate the non-specific adsorption of PNA but not sufficient to LENS. Thirdly, a supplementary SDS rinse is necessary to remove completely the non-specific adsorption.

However, the fact that a great loss is observed in the amide I band after the SDS rinse raises a specific question concerning the SDS effect. One might argue that the SDS rinse partially disrupts the specific binding. To explain the role of SDS rinse, we propose a hypothesis that the SDS rinse only removes the unwanted physisorption.

In the case of the non-specific protein, as shown in **Fig 3.7**, it only exists non-specific protein-surface interactions severely limited by the antifouling surface. During the contact of specific proteins with the glycosylated surface, the protein-glycan binding is firstly achieved leading to the formation of a packed protein monolayer. Such a "chemisorption" effectively reformulates the charge, hydrophilicity and morphology of the surface state by exposing the protein as the interface with the solution, which might provoke further interactions, with the free proteins in solution if these protein-protein interactions are cooperative.[112, 198] These "protein-protein" interactions are intrinsically formed through a series of weak hydrophilic, hydrophobic or electrostatic forces, in another words, there is "physisorption" of a multilayer of lectins.

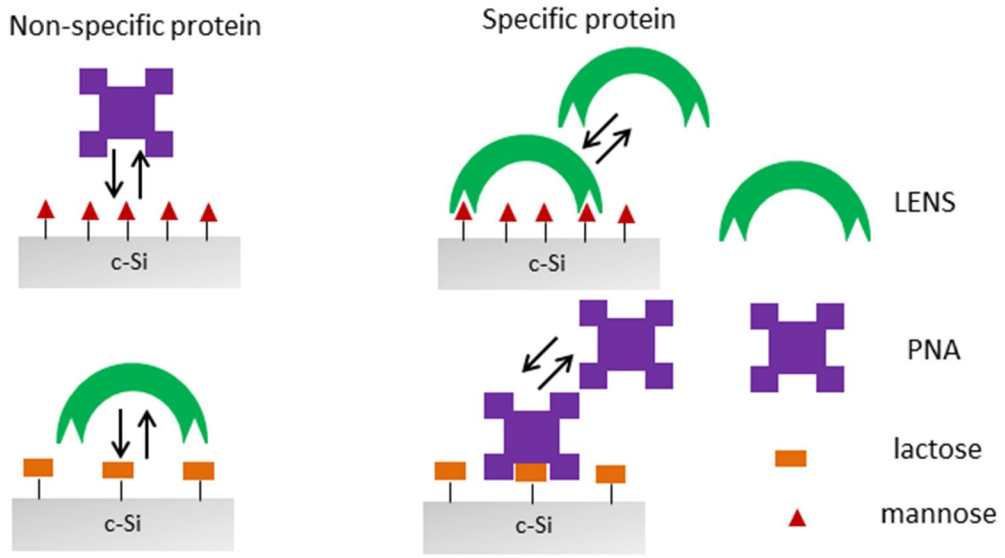

Figure 3.7 Scheme representing different behaviors of specific and non-specific proteins on glycan-terminated surfaces.

Under a mild PBS rinse (the same as the incubation buffer), both the chemisorption and physisorption are preserved. While under a more stringent SDS rinse, physisorption is disrupted and physisorbed proteins are removed from the surface so that the surface is only covered by specific proteins through "chemisorption". For instance, the exposition to LENS on lactose-terminated surface provides only subtle amount of non-specific adsorption, whereas the exposition to PNA produces not just the specific binding, but also a great "induced" protein-protein physisorption. These different interactions can be quantitatively assessed by comparing the change of amide I band from PBS to SDS rinse, as shown in the histogram of **Fig 3.8**.

- *Non-specific adsorption (physisorption):*
  the amide I band from non-specific lectin after PBS rinse
  the amide I band from specific lectin after PBS rinse subtracted that after SDS rinse

- *Specific binding:* the amide I band from specific lectin after SDS rinse

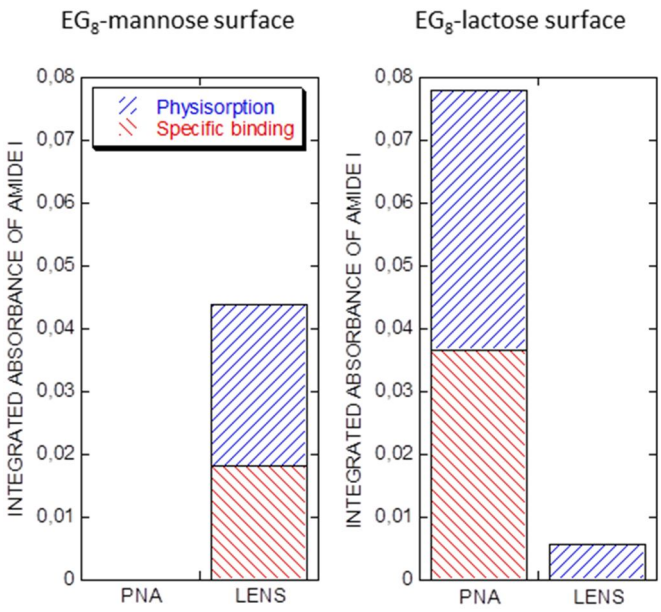

Figure 3.8 Histogram representing the integrated absorbance of the amide I band in p-polarization of proteins after interaction with glycan-terminated surfaces and its composition of different interactions. The data of mannose-terminated surface are from **Fig 3.4c** and those of lactose-terminated surface are from **Fig 3.6c**.

3.2.2 Study using AFM

To be consistent with the quantitative IR result, the specificity of glycosylated surfaces was investigated using the same protocol by AFM. CM-AFM is more sensitive than IR because it visualizes directly an individual protein molecule or clustered ones. A minimum contact force of the tip was applied during the capture of CM-AFM images to avoid damage or distortion of the soft protein molecules. In addition, the CM-AFM can apply a larger contact force of the tip to “wipe out” the “soft” molecules in a locked region so as to provide a contrast background to see the surface of substrate.

Fig 3.9 displays the CM-AFM images of mannose-terminated surface interacted with PNA and LENS after PBS and SDS rinses. The exposure to PNA after a PBS rinse does not change the staircase topography but little amount of loosely spreaded white deposits is observed (**Fig 3.9a**). The SDS rinse removes efficiently all the white spots resulting in the recovery of initial Si (111) profile (**Fig 3.9b**). On the other hand, the exposure to LENS after a PBS rinse (**Fig 3.9c, d**) results, in a complete loss of the staircase profile present prior to exposure. Even under a SDS rinse (**Fig 3.9e, f**), the surface still reveals a substantial quantity of lectin remaining linked to mannose-terminated Si (111), indicating the robustness of such a binding. The molecular height of the deposited LENS was estimated to be 1~2 nm after the PBS rinse

and ~ 1 nm after the SDS rinse. The data lead to conclude that the interaction of the mannose-terminated Si(111) with LENS contains two different events: the specifically bound lectin is robust and preserved on the surface, whereas the physisorbed lectin is easily disrupted by the SDS rinse, as it is the case for PNA-treated surface.

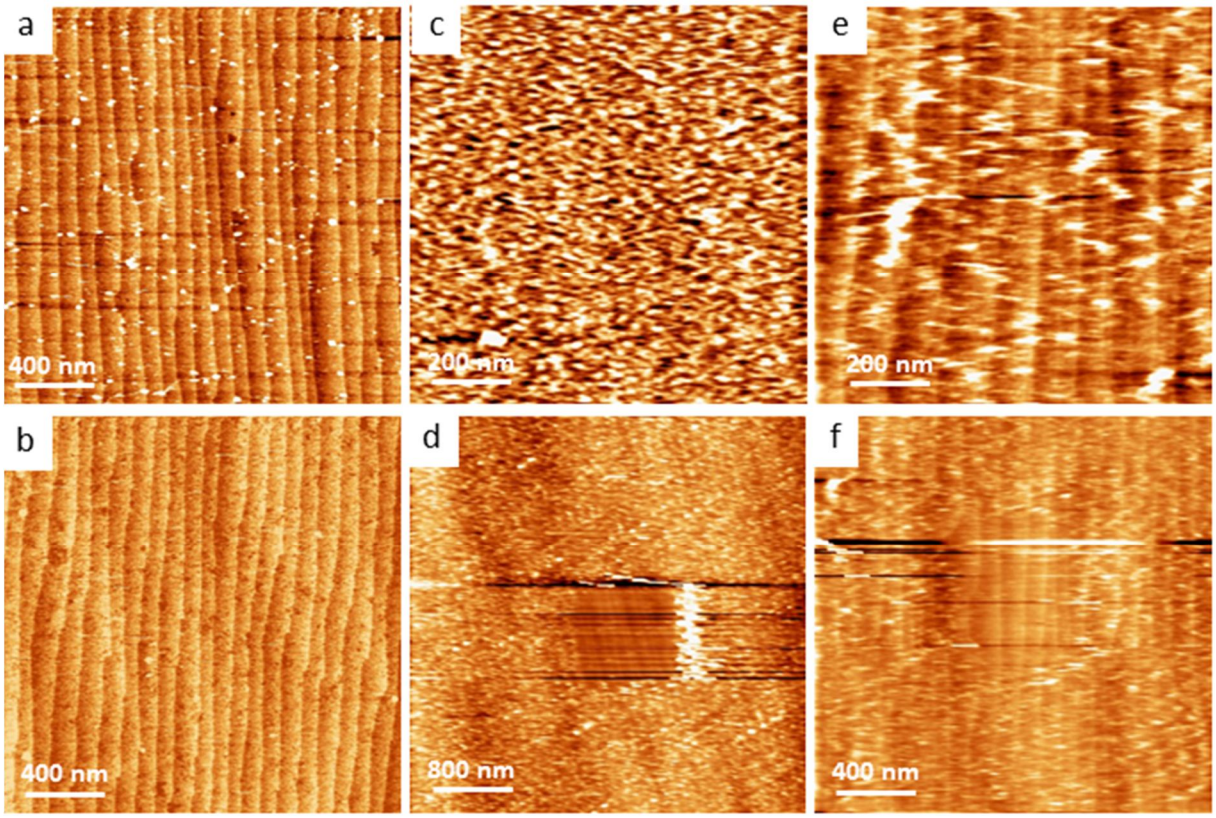

Figure 3.9 CM-AFM images of mannose-terminated surfaces exposed to PNA (1 mg/mL) followed by a PBS (a) and SDS rinse (b); exposed to LENS (1 mg/mL) followed by a PBS (c, d) and SDS (e, f) rinse. The centered square in d and f is created by several scans on smaller locked region.

When this same study was performed with lactose-modified silicon surfaces, analogous results were obtained (**Fig 3.10**). Non-specific adsorption of LENS provides some white deposits (**Fig 3.10a**) which were easily disrupted by a SDS rinse (**Fig 3.10b**). The stronger specific bindings are clearly distinguished again due to a complete coverage of the surface (**Fig 3.10c, d**). The SDS rinse removes partially the lectin layer in preserving the specific bindings (**Fig 3.10e, f**). The height of the PNA lectins was estimated to be 2-4 nm after the PBS rinse and to be ~2 nm after the SDS rinse.

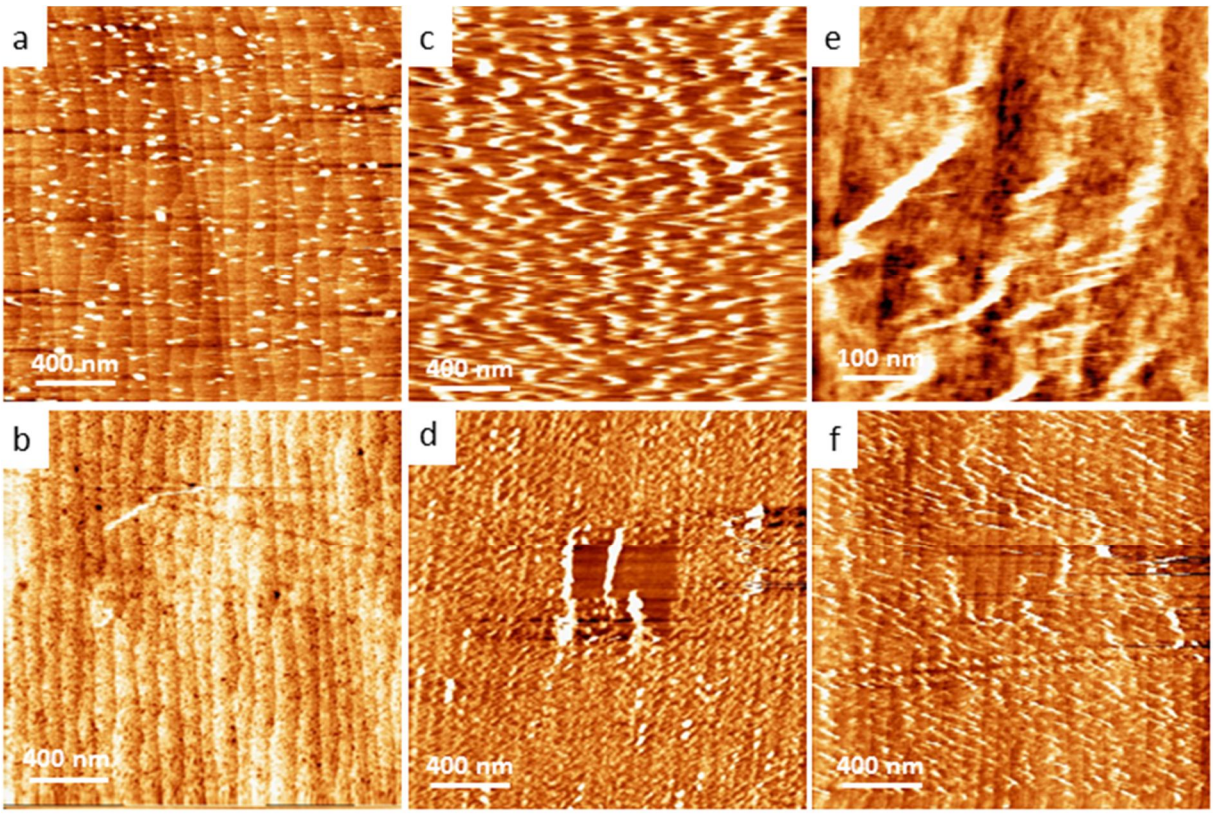

Figure 3.10 CM-AFM images of lactose-terminated surfaces exposed to LENS (1 mg/mL) followed by a PBS (a) and SDS (b) rinse; exposed to PNA (1 mg/mL) followed by a PBS (a) and SDS (b) rinse. The centered square in d and f is created by several scans on smaller locked region.

The above two controlled experiments are in good agreement with the infrared results, yielding several conclusions:

1) The non-specific adsorption results in protein molecules loosely packed on the surface. However it is impossible to distinguish if these white spots are individual or aggregate protein molecules because the lateral resolution of the CM-AFM tip is >20 nm.

2) The specific binding upon a PBS rinse completely covers the substrate profile, indicating the formation of a compact monolayer or multilayer.

3) The SDS rinse removes a lot of specific lectins but preserves some. Those remained on the surface are unambiguously specific bindings.

4) The thickness change from PBS to SDS rinse indicates the formation of multilayer in case of specific lectins, which is a consequence of “protein-protein” interactions.

From the topographic profile, the height of LENS is ~1 nm and PNA ~2 nm. However, from the X-ray crystallographic data, the dimension of LENS is 8×3.7×2.3 nm and PNA 6.5×6.5×3.7 nm (protein databank).[199, 200] This may suggest that the protein molecules adopt a "side on" instead of "end on" conformation, which fits their "multivalency" with the surface ligand. Again one question is raised about the lower height than the theoretical values. One of the explanations could be ascribed to the contact mode technique where the tip scratched the surface, resulting in the deformation and distortion of molecules. Another important consideration is that the images were captured at solid/air interface. It has been reported in some papers that at air/solid interface, AFM usually underestimates the protein molecular size, which is likely due to the desolvation induced structure change.[201-204] Conversely, the obtained protein size is closer to that offered by X-ray data when the AFM is operated at liquid/solid interface.[205-207]

3.3 Binding efficiency with the surface glycan density

The density of surface glycans was tuned by diluting the alkynyl-derivatized glycans with smaller propargyl alcohol during the "click" process, as shown in **Fig 3.11.**

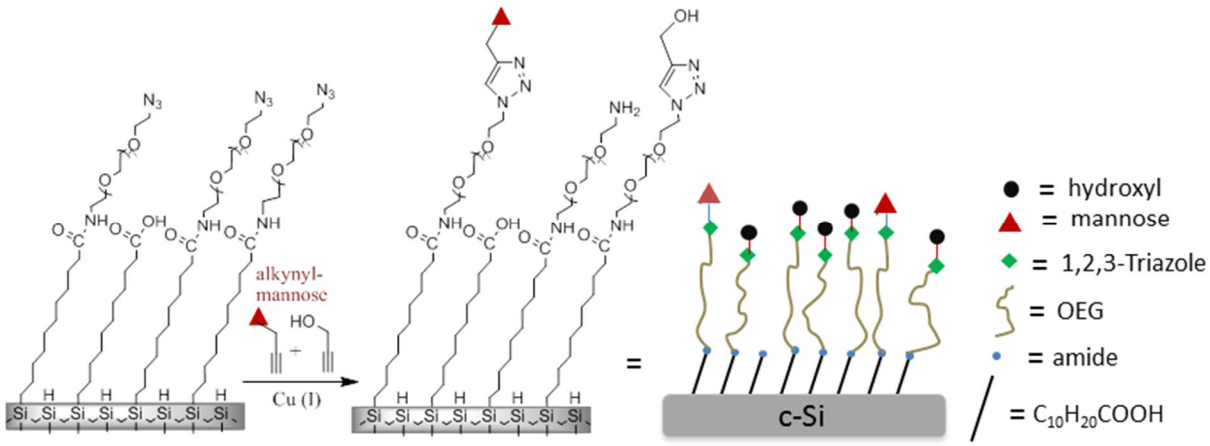

Fig 3.11 Scheme of the formation of diluted glycosylated surface.

3.3.1 Determination of diluted glycan density

In this work, the mannosyl probes were diluted with shorter propargyl alcohol molecules at different ratios (10 mol% and 1 mol%). **Fig 3.12** represents their IR spectra. Obviously, there is no difference for the diluted mannosyl characteristic bands except the slightly varying intensities at ~1050 cm^{-1} related to the νC-O-C. It is neither impossible to use the PSA method to quantify the density of surface mannose by UV-Vis spectroscopy because of the limited sensitivity of the colorimetric experiment.

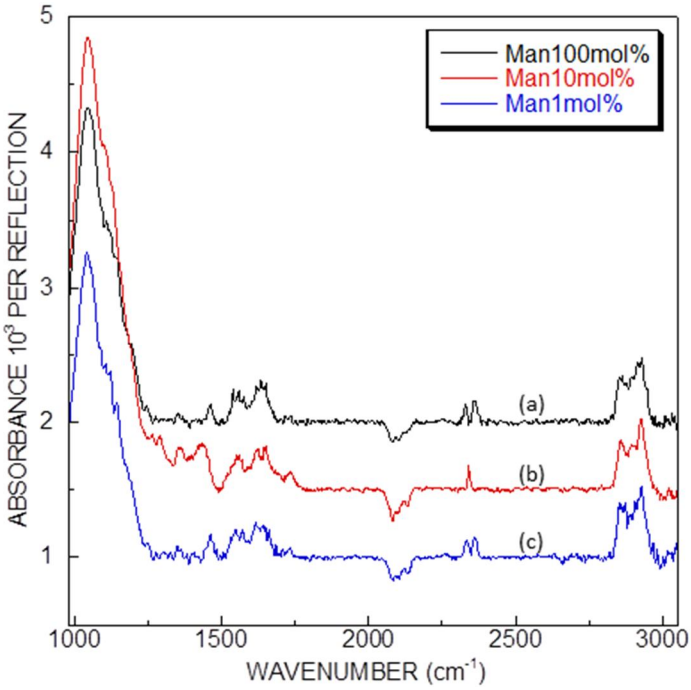

Figure 3.12 IR-ATR spectra in p-polarization of mannose-terminated surfaces at different molar fractions: 100 mol% (a), 10 mol% (b) and 1 mol% (c). The reference spectra are the SiH_x surface.

Therefore, we chose to perform again the indirect IR quantification of the ManOAc "clicked" on azide-terminated surfaces as described in the previous chapter. **Fig 3.13** shows the IR-ATR spectra of the three diluted ManOAc surfaces at the same ratios in propargyl alcohol with respect to the azide-terminated surface. The characteristic band, νC=O of ManOAc is clearly observed even for 1% diluted surface. The density of ManOAc was quantitatively determined to be 5.25×10^{13} cm^{-2} for 10 mol% and 7.2×10^{12} cm^{-2} for 1 mol% dilution. In chapter 2, we have already demonstrated that the density of 100 mol% mannose or 100 mol% ManOAc on the surface is restricted by their steric hindrance resulting in a clicking yield of maximum 75% the remaining 25% azide-functions being degraded. In the present case, with the presence of the less sterically hindered propargyl alcohol, the click yield needs to be again assessed. For this purpose, we clicked the acetylated propargyl alcohol (propargyl acetate) on azide-terminated surface as shown in **Fig 3.13d**. The obtained density of propargyl acetate is 1.5×10^{14} cm^{-2}, compared with the initial density of azide-functions of 1.6×10^{14} cm^{-2}, which gives a click yield of 96%, higher than that of mannose, suggesting an almost complete conversion.

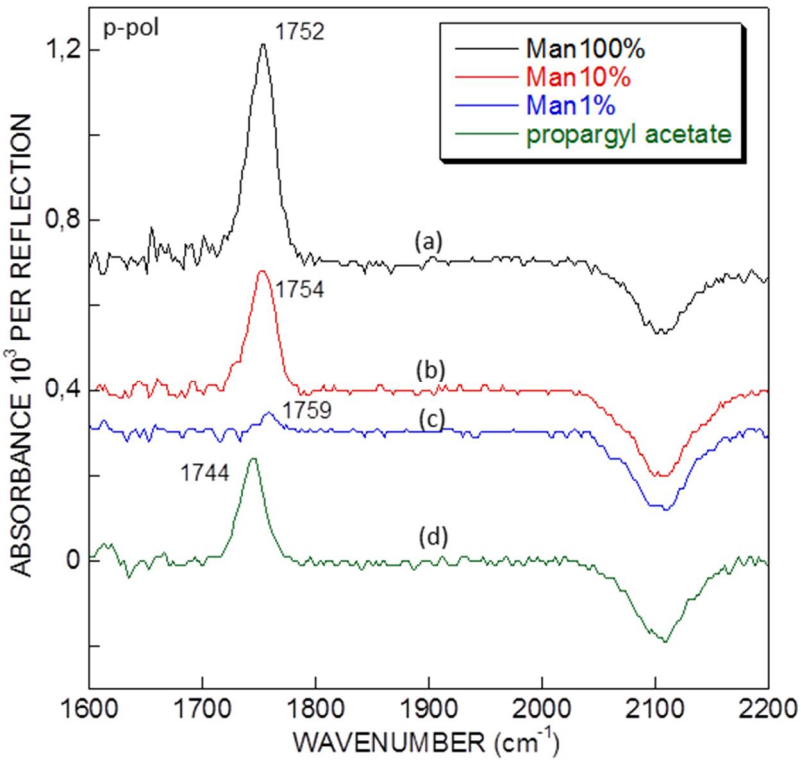

Figure 3.13 IR-ATR spectra in p-polarization of diluted ManOAc-terminated surfaces at 100 mol% (a), 10 mol% (b) and 1 mol% (c) and the clicking of propargyl acetate (d). The reference spectra are the azide-terminated surfaces.

Then, on 10 mol% ManOAc-terminated surface, the density of ManOAc is 5.25×10^{13} cm^{-2} and the remaining azide sites (1.6×10^{14} - 5.25×10^{13} $=10.75\times10^{13}$ cm^{-2}) can reasonably be assured to be fully converted by reacting with propargyl alcohol. Thus, from a 10 mol% mixture of ManOAc in the precursor solution, we obtained a molecular layer containing a 33% molar fraction in grafted ManOAc. Likewise, from a solution with a molar fraction of 1 mol%, a surface fraction of 4% is obtained. **Fig 3.14** plots the surface fraction of ManOAc versus the solution fraction. The nonlinear variation indicates that the diluted ManOAc monolayers are richer in glycan than the mixture solution, which is attributed to faster kinetics for glycan coupling than for propargyl alcohol. These enhanced kinetics could be due, e.g. to favored surface adsorption, as seen previously in other mixed monolayers on silicon.[63]

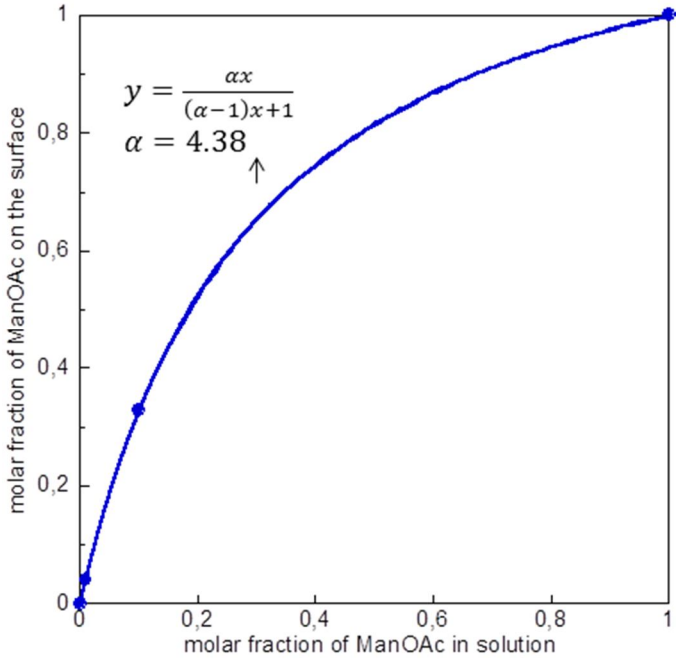

Figure 3.14. Plot of the molar fraction of clicked ManOAc on the surface as a function of that in solution**.** The data are fitted by the kinetic equation shown beside the curve, where α value characterizes the kinetic ratio of ManOAc over propargyl alcohol.[63]

3.3.2 Influence of the glycan density on the binding efficiency

a) Study using AFM

The interaction efficiency and the specificity of these "clicked" diluted mannose- or lactose-terminated surfaces with lectins were then evaluated by AFM imaging. **Fig 3.15** shows the topography of 10 mol% and 1 mol% diluted mannose and lactose-terminated surfaces. The appearance of "black holes" formed due to the glycan domains is less prominent compared with the non-diluted surfaces (**Fig 2.29**).

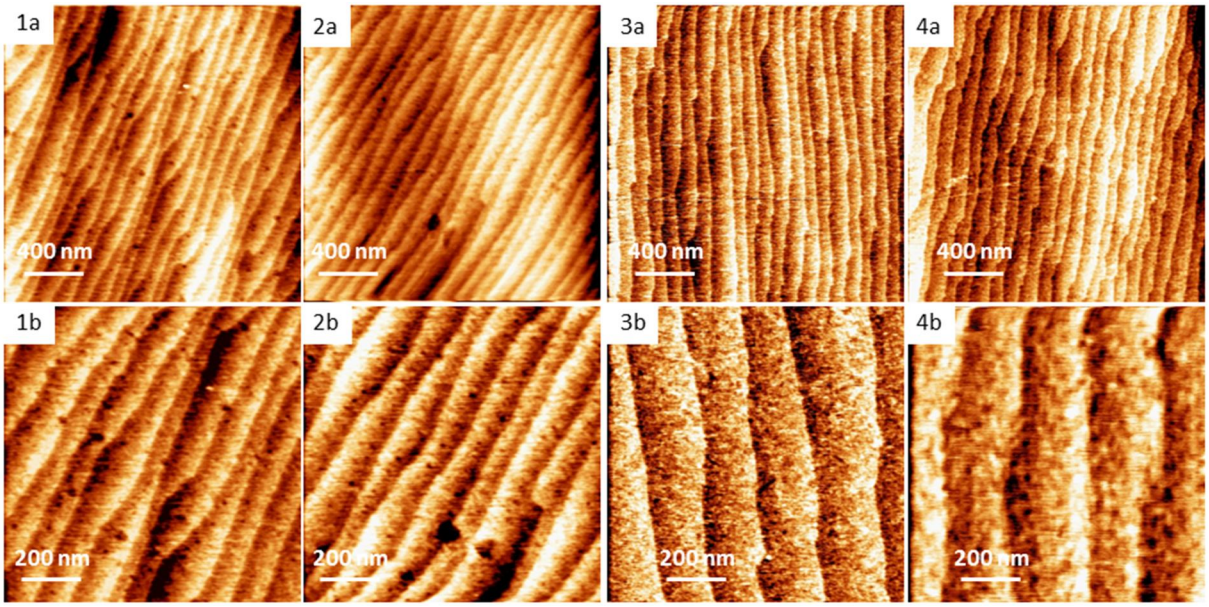

Figure 3.15. CM-AFM images at various scales of 10 mol% (1a,b) and 1 mol% diluted mannose-terminated surfaces (2a.b), 10 mol% (3a,b) and 1 mol% diluted lactose-terminated surfaces (4a,b).

When these surfaces are exposed to different lectins after a SDS rinse, the specificity of the interaction yields the behaviors summarized in **Fig 3.16**. and **Fig 3.17**. Once again, no physisorption is detectable on mannose-terminated surfaces after their interaction with nonspecific PNA lectin (**Fig. 3.16-1a, 2a**) whereas the interaction with LENS results in specific bindings (**Fig. 3.16-1b-d, 2b-d**). With regard to the binding efficiency, it is clear to observe that the 10 mol% mannose-terminated surface is much more efficient to load the lectin than the highly diluted 1 mol% and non-diluted mannose-terminated surfaces (**Fig 3.9e**). For 10 mol% mannose-terminated surface, the LENS covers completely the silicon substrate with the formation of a compact "carpet"-like layer. To measure its height, the AFM image of **Fig 3.16-1d** were captured after the tip wiping for several times at a smaller locked region, giving the thickness of 1-2 nm for the lectin layer. The diluted lactose-terminated surfaces (**Fig 3.17**) behave exactly the same as the diluted-mannose surfaces, showing excellent PNA-selectivity and the optimum binding yield is found at a 10 mol% dilution. The detected thickness of PNA layer is ~2 nm.

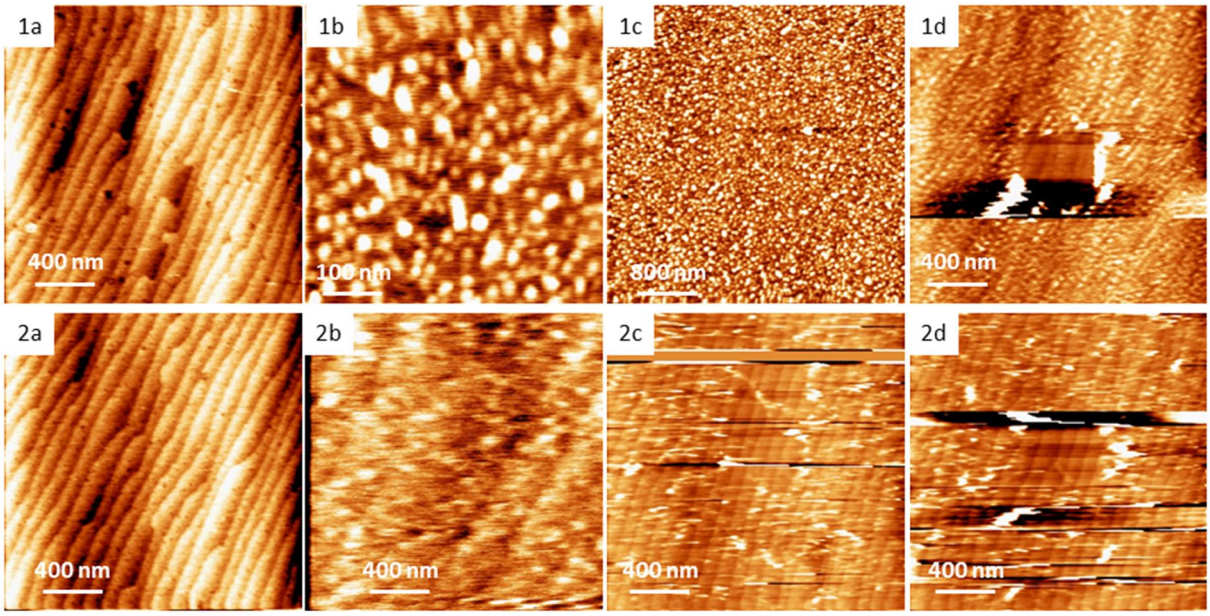

Figure 3.16. CM-AFM images at different scales of 10 mol% (1) and 1 mol% mannose-terminated surfaces (2) interacted with PNA (1 mg/mL) (1a, 2a) and LENS (1 mg/mL) (1b-d, 2b-d) followed by a SDS rinse. The centered square in 1d and 2d is created by several scans on smaller locked region.

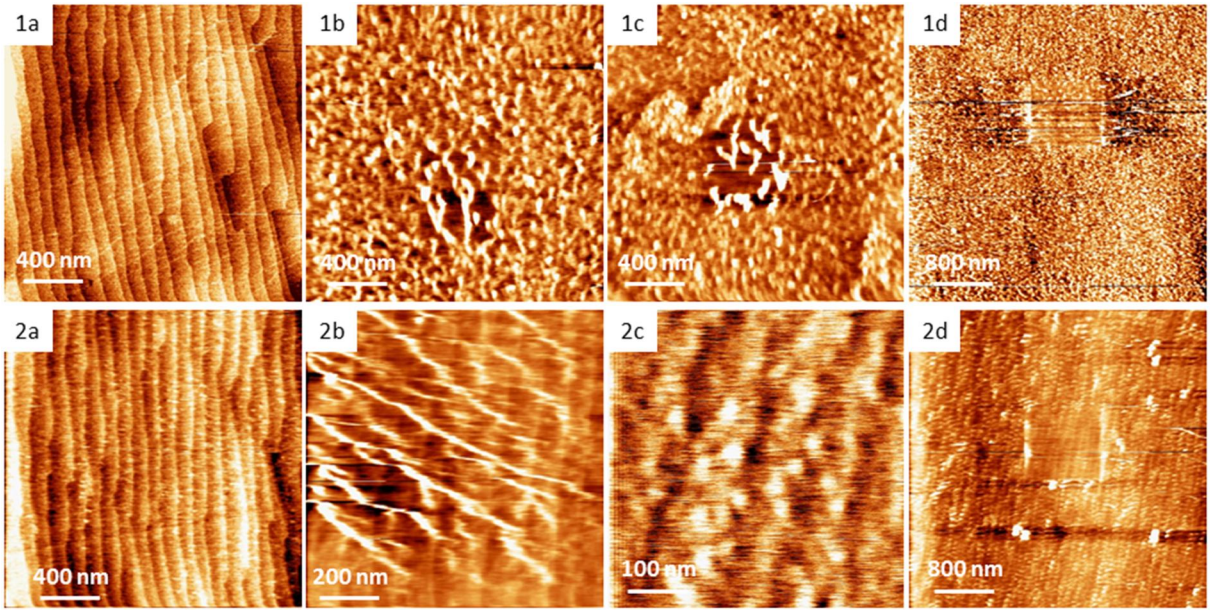

Figure 3.17. CM-AFM images at different scales of 10 mol% (1) and 1 mol% lactose-terminated surfaces (2) interacted with LENS (1 mg/mL) (1a, 2a) and PNA (1 mg/mL) (1b-d, 2b-d) followed by a SDS rinse. The centered square in 1c, 1d and 2d is created by several scans on smaller locked region.

In addition, a powerful AFM in tapping mode (TM-AFM) with higher lateral resolution (~10 nm) was employed for PNA-covered 10 mol% and 1 mol% diluted lactose surfaces (**Fig 3.18**). It is monitored that the PNA molecules are distributed like homogeneous "particles" with minor "clustered" molecules. The density of the two diluted surfaces is as well clearly discerned by looking at the "staircase profile" of substrate, which is completely shielded for 10 mol% dilution and partially hidden for 1 mol% dilution.

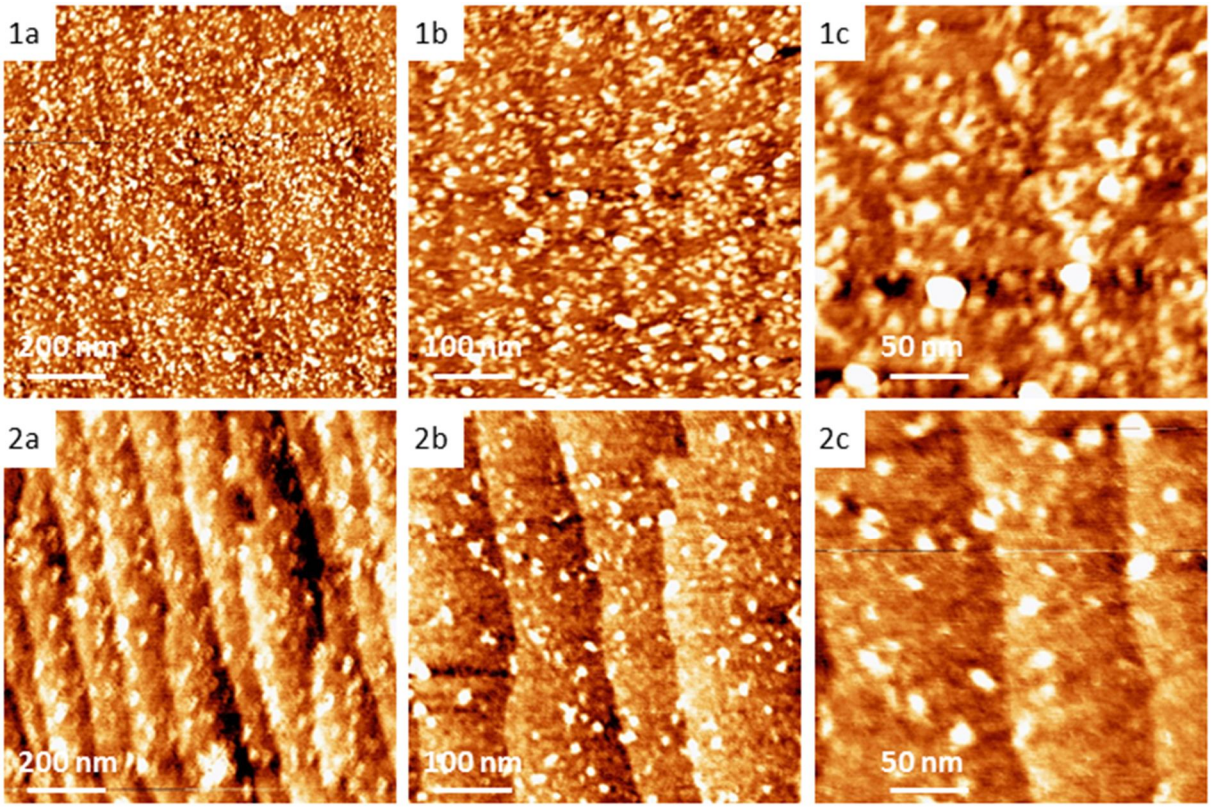

Figure 3.18. TM-AFM images at various scales for 10 mol% (**1**) and 1 mol% diluted lactose-terminated surfaces (**2**) interacted with PNA (1 mg/mL) followed by a SDS rinse.

A more "statistical" quantitative treatment can be applied to count the coverage of lectin on the two surfaces from **Fig 3.18**. By considering the background of silicon substrate ~0.7 nm and the minimum horizontal resolution (100 nm^2), the "flooding analysis" of WSxM software filters the pixels which do not meet such conditions so as to give the area occupied by those "white deposits". As a consequence, it is found that the topographic coverage of PNA is 99.02% for 10 mol% and 4.91% for 1 mol% diluted lactose-terminated surfaces (**Fig 3.19**). Of course, such an analysis is not absolutely quantitative because the computed coverage depends on the choice of the filtering parameters. Nevertheless, the above AFM results allow us to conclude that the 10 mol% dilution is the optimum surface to bind specific lectins, both for mannose and lactose-surfaces.

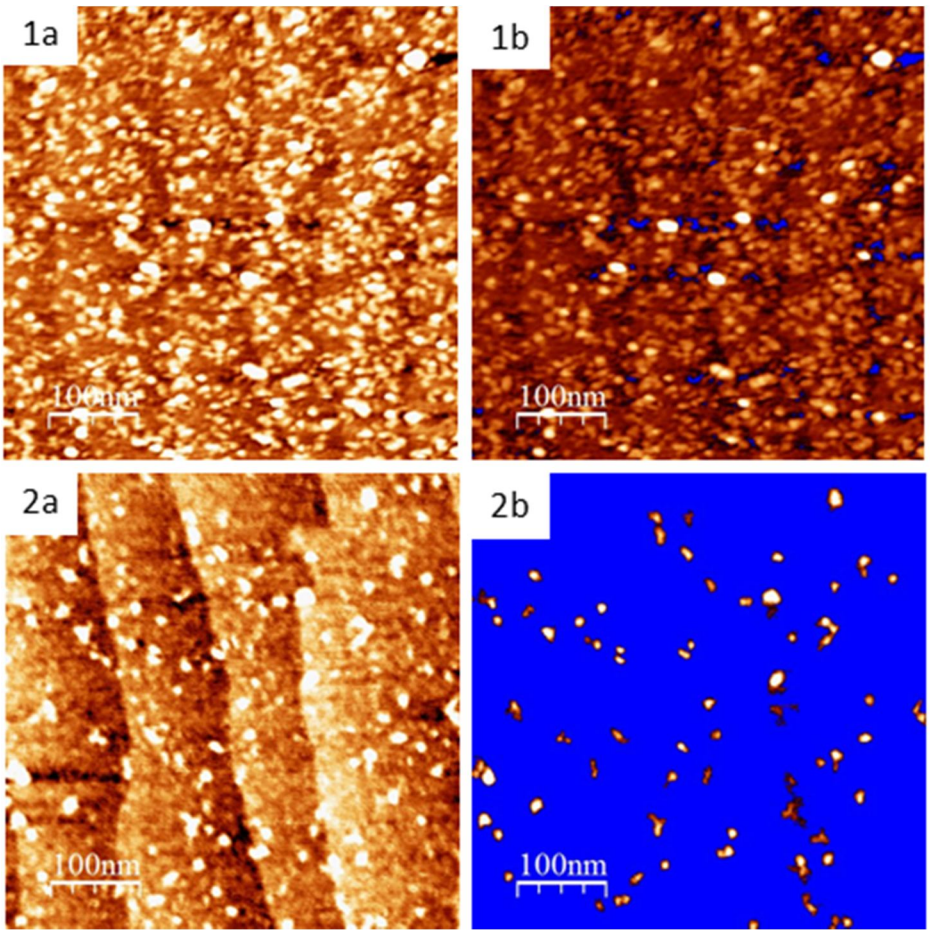

Figure 3.19. TM-AFM images of 500×500 nm for PNA-covered 10 mol% (1a) and 1 mol%-lactose-terminated surfaces (2a). The pixels in each image with height < 0.7 nm and size < 100 nm^2 are filtered as represented in blue (1b and 2b). The coverage of remaining white spots is 99.02% and 4.91% for 1b and 2b, respectively.

b) Study using IR-ATR

To rationalize the "dilution effect" observed by AFM, quantitative IR measurement was performed analogously for 100 mol%, 10 mol% and 1 mol% mannose-terminated surfaces (**Fig. 3.20**). By fitting the amide bands of the mannose-terminated surfaces and those exposed to LENS, we can obtain the mere contribution from LENS. The amount of loaded LENS is found to be 3.5 times more on 10 mol% mannose-terminated surface as compared to 100 mol% and 1 mol% mannose-terminated surfaces. Namely, the optimal binding activity appears to be obtained at a properly diluted surface, confirming the AFM results. This phenomenon is coherent with the earlier reported papers by Sato[4] and Svedhem et al.[196], and different from

the result of Smith et al.[11], who observed the maximal binding arising on 100 mol% mannose surface. To explain the "dilution effect", firstly, it should be observed that the molecular size of the protein is much larger than that of sugar (8×3.7×2.3 nm for LENS vs ~ 0.7×0.56×0.56 nm for mannose), so a moderately diluted mannose distribution on surface does not impede the binding event. Moreover, the protein LENS possesses two mannose-binding sites which are diametrically opposed. The multivalency binding may not be favored on the over-crowded settled glycan layer whereas the diluted sugar clusters could provide enough space for the multivalent chelation. The mechanism of the multivalent binding will be rediscussed in chapter 4 on the basis of an IR quantification of the surface-bound proteins.

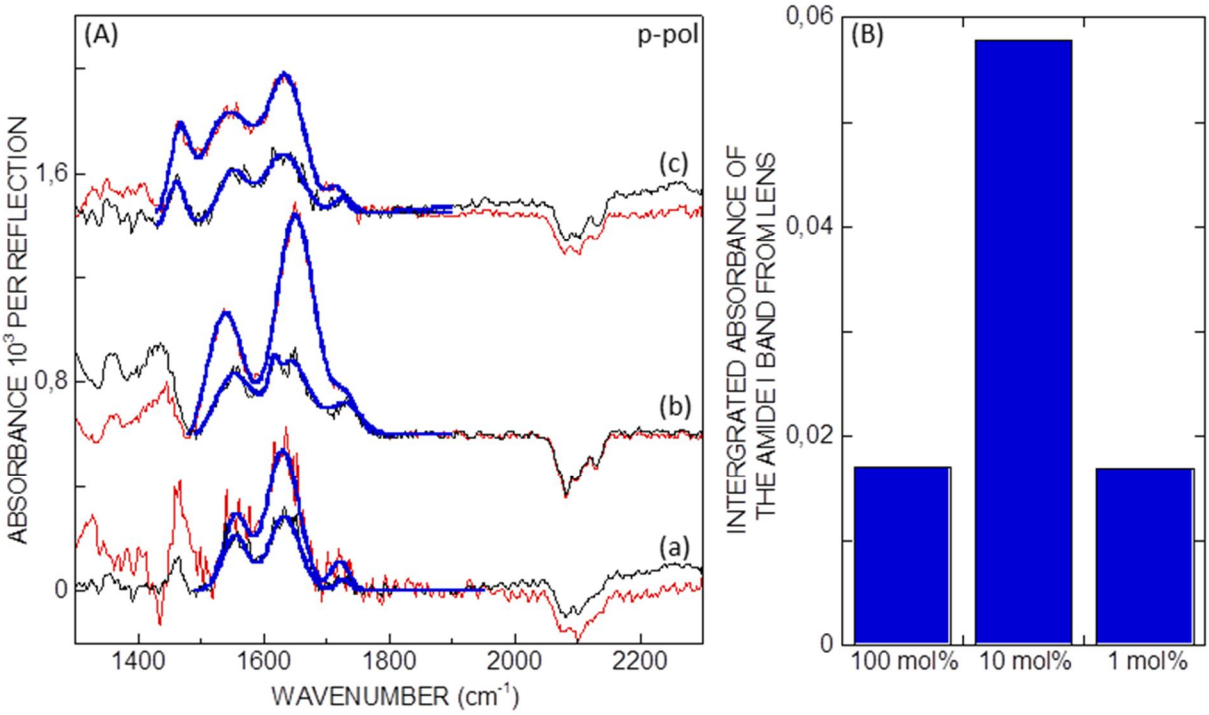

Figure 3.20 (A) IR-ATR spectra in p-polarization of 100 mol% (a), 10 mol% (b) and 1 mol% (c) mannose-terminated surfaces (in black) after interaction with LENS (1 mg/mL) followed by a SDS rinse (in red). The fitting of the amide bands is highlighted in blue. The reference spectra are the SiH_x surface. (B) Histogram of integrated absorbance of amide I band from LENS for the three surfaces.

3.3.3 Determination of glycan-protein binding affinity

The isotherm of the mannose-LENS binding was studied by FTIR-ATR for the three diluted mannose-terminated surfaces. **Figure 3.21a** represents the integrated absorbance of the amide I band as a function of LENS concentration. To interpret the binding behavior, the obtained

curves are often fitted with the classic Langmuir adsorption model (solid lines), $A = \frac{A_m K_a C}{1+K_a C}$, where A refers to the spectroscopic response, A_m the saturated response, C the protein concentration and K_a the association constant. The K_a values obtained for the three surfaces are around 10^5 M^{-1} as listed in **Table 3.1**. Alternatively, Scatchard plots were used to test the plausibility of the Langmuir isotherm, as shown in **Fig. 3.21b**. The 100 and 1 mol % SiMan surfaces lead indeed to linear plots with Ka values close to those directly obtained from the fitting in **Fig. 3.21a**, whereas the 10 mol % SiMan surface curve exhibits a nonlinear shape. This effect may be a consequence of the interaction between proteins since the 10 mol % SiMan surface is fully covered with LENS as shown in **Fig. 3.16b-d**. The fitting of the 10 mol % surface curve in **Fig 3.21a** can be largely improved by using the Frumkin-Fowler-Guggenheim (FFG) isotherm model (dashed line), $C_{LENS} = \frac{A}{(A_m - A)K_a} e^{\beta \frac{A}{Am}}$, which takes into account lateral interactions among adsorbate molecules, indicated by the β value (a negative β implies attractive forces between adsorbate molecules whereas a positive β implies repulsive forces).[135] The best results are obtained for β = −0.1 (dashed lines in **Fig. 3.21a**). From the FFG model, the K_a values of the three surfaces are still of the same order of magnitude with minor modifications (**Table 3.1**). K_a values on the order of 10^5 M^{-1} suggest that the binding is relatively strong due to multivalency for all of the surfaces instead of weak monovalency.

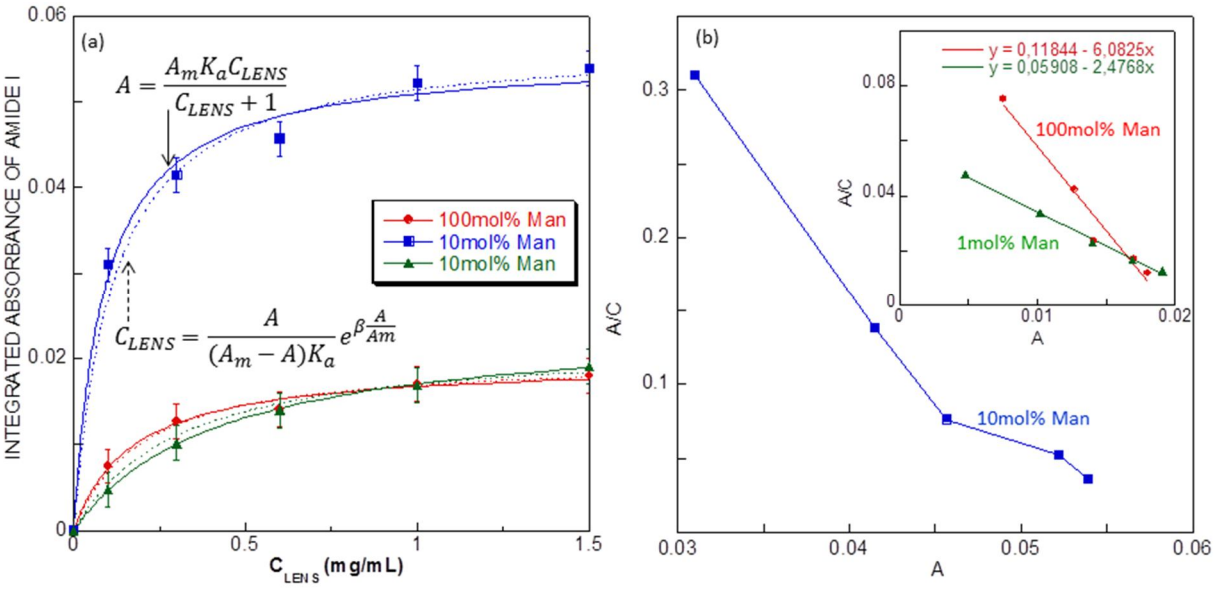

Figure 3.21. (a) Isotherm of the interaction of 100 mol%, 10 mol% and 1 mol% mannose-terminated surfaces with LENS after a SDS rinse. The data were fitted by using Langmuir model (solid lines) or FFG model (dashed lines). (b) Scatchard plots for the three surfaces where 100 mol% and 1 mol% mannose-terminated surfaces are linearly fitted (inset).

a	Langmuir ($10^5 \cdot M^{-1}$)	Scatchard plot ($10^5 \cdot M^{-1}$)	FFG ($10^5 \cdot M^{-1}$)
100 mol% Man	3.04	3.16	2.6
10 mol% Man	5.93	Non-linear	4.42
1 mol% Man	1.23	1.29	1.66

Table 3.1. The association constants of mannose-LENS binding obtained form Fig. 3.21.

In the previous section 3.2, we have proposed a hypothesis that the specific glycan-protein bindings are concomitant with the "protein-protein" interaction under the PBS rinse. To demonstrate this hypothesis, the isotherm of the interaction with LENS on three diluted surfaces after PBS and SDS rinses were monitored as shown in **Fig 3.22.** The signal of protein binding after SDS rinse shows a saturation which is fitted well by the Langmuir equation, and the one after PBS rinse is unsaturable. So we used Freundlich model to fit the isotherm after PBS rinse and a good agreement with the curve shape was observed. The Freundlich model has been used to describe the non-specific adsorption on heterogeneous surface.[137-140] This might indicate that the "protein-protein" interactions truly exist under a simple PBS rinse. These results also suggest the importance of controlling the non-specific interaction by optimizing the antifouling property of the assembly monolayer and the rinse protocol. Otherwise, the physisorption will significantly override the specific binding signals, leading to a miscalculation of binding affinity.

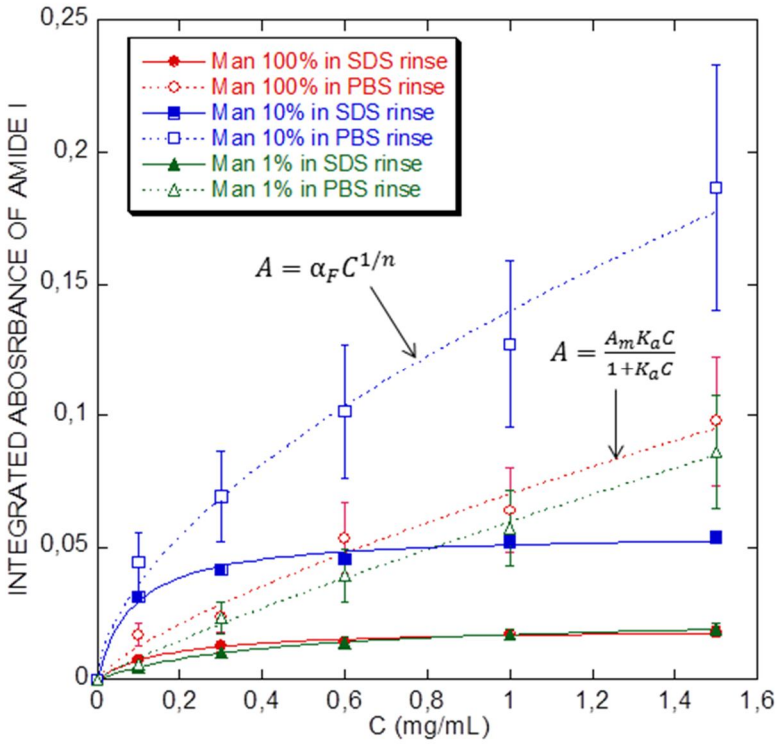

Figure 3.22. Isotherms of the interaction of 100 mol%, 10 mol% and 1 mol% mannose-terminated surfaces with LENS after a PBS rinse (empty symbol) and SDS rinse (solid symbol). The data were fitted by using Langmuir model (solid lines) or Freundlich model (dashed lines).

3.4 Reusability of the glycosylated surfaces

In order to reuse the glycan-terminated surfaces, different cleaning procedures, including immersion into H_3PO_4 or concentrated glycan solutions were tested as a means of disrupting glycan-modified surfaces with their lectin partners. While H_3PO_4 blocks the binding probably due to the denaturation of the sugar-binding site induced by protonation, the sugar wash pulls the binding equilibrium from the surface towards the liquid, leading to the release of bindings. In both mannose- and lactose-modified surfaces, acidic (**Fig. 3.23-1a, 3a**) as well as sugar washing (**Fig.3.23-1b, 3b**) disrupt weak non-specific glycan-lectin interactions. Neither of these treatments results in the disruption of the much stronger glycan-specific lectin interactions (**Figure 3.23-2, 4**), indicating their undeniable strengths. We also tried a rinse in 1% SDS (superior to the critical micelle concentration), 6 M urea, 1% helmanex, ethylene glycol and EDTA, none of the procedures investigated was however capable of fully regenerating the glycan-interface. This finding raises questions on the report of a variety of papers concerning the possibility to break glycan-lectin interactions on glycan sensors. For example, it has been declared that the glycan interfaces can be regenerated by a rinse of phosphoric acid on SPR chips.[27] However, most sensors areas are of mm^2 to cm^2 sensing area, and the observed molecular “impurities” are not probably visible. Another reason might be that the AFM is much more sensitive on the local scale than IR-ATR and other techniques like SPR.

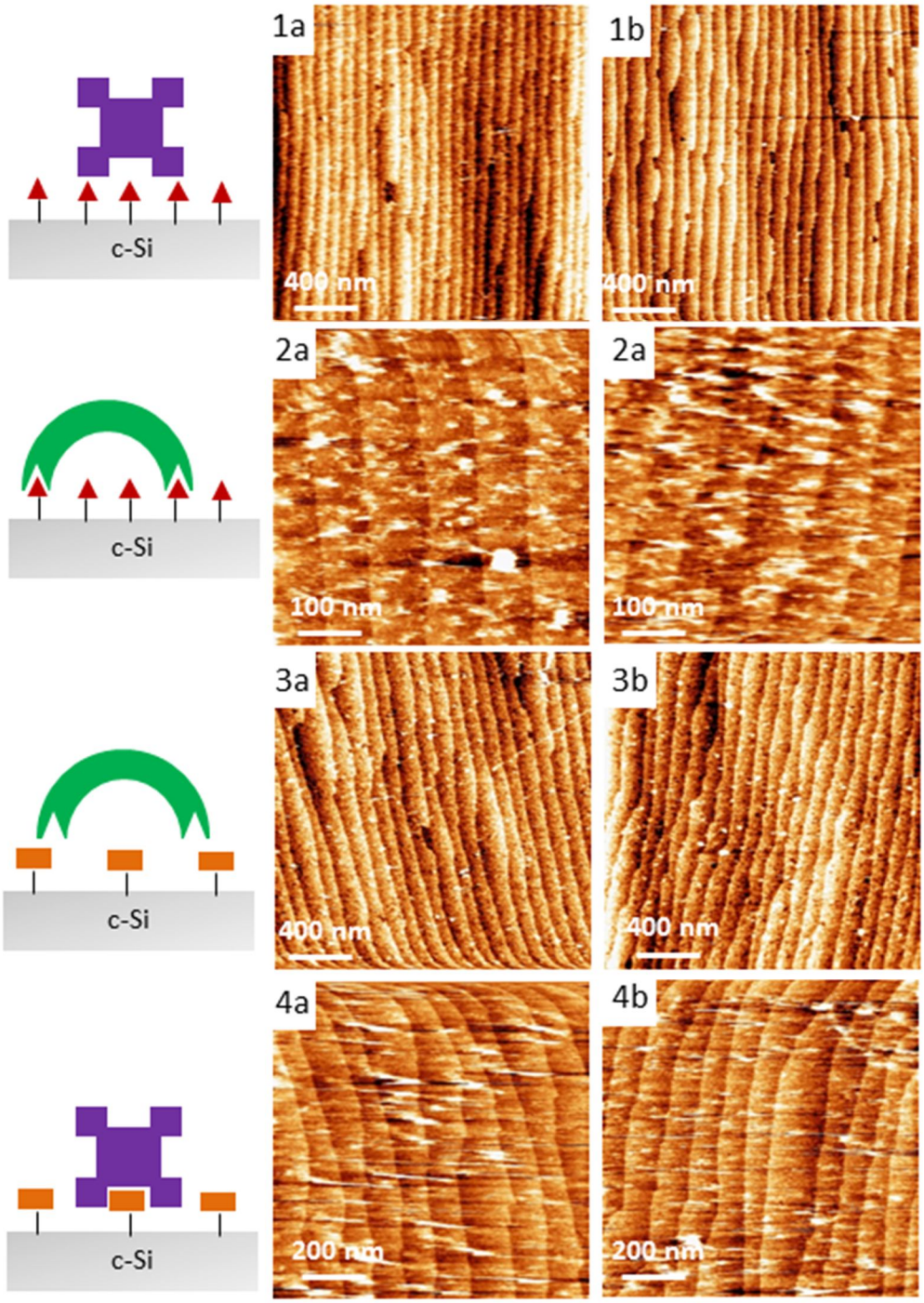

Figure 3.23. CM-AFM images of mannose-terminated surfaces (1-2) and lactose-terminated surfaces (3-4) after interaction with their non-specific lectins (1-3) followed by a rinse with 0.1 M H_3PO_4 for 1 h (1a-3a) and 0.1 M β-lactose for 1 h (1b-3b); after interaction with their specific lectins (2-4) followed by a rinse with 0.1 M H_3PO_4 for 1h (2a-4a) and 0.1 M D-mannose for 1 h (2b-4b).

3.5 Conclusion

We have shown in this chapter that the glycosylated crystalline Si(111) surfaces are well-suited for the investigation of the interactions with specific and non-specific lectins. The interaction process is followed by FTIR-ATR and AFM. Special attention should be paid to two factors in order to limit the non-specific adsorption: an enough long OEG chain to realize the antifouling property of the surface and a surfactinated rinse such as SDS rinse. After the minimization of non-specific adsorption, the interaction of the glycan-terminated surface with specific lectins results in the specific glycan-protein binding, but also ineligible protein-protein interaction. The latter can be well-eliminated by the surfactinated rinse. Through the optimization of the two factors, the specific binding is well-captured.

Moreover, the influence of the surface glycan density to the specific binding is regulated by diluting the glycan-terminated surfaces during the click reaction. The density of the diluted surface glycan is determined by quantitative IR-ATR, showing a non-linear relationship with their molar fraction in the click solution. The optimum interaction with specific lectins is found on the properly diluted glycan-terminated surfaces by both IR-ATR and AFM. This phenomenon is related to the molecular size of ligand and receptor and also the multivalency effect.

Finally, the association constant of the LENS-mannose binding is determined by isotherm curves. The value indicates that the multivalent binding is adopted between the mannose-terminated surfaces and LENS. The binding signal obtained under insufficient PBS rinse is also studied by the isotherm curve, showing the presence of non-specific adsorption, and in turn, demonstrates the importance of surfactinated rinse.

3.6 Experimental section

3.6.1 Molecules, proteins and substrates

Lectins from *Lens culinaris* (LENS) and from Arachis hypogaea (PNA) were obtained from Aldrich and were prepared in phosphate buffer saline (PBS) 1×. All other chemicals and silicon samples were as described in chapter 2.

3.6.2 Preparation of diluted glycosylated surfaces

The azide-terminated surface was immersed in degassed solution of 3 mM α-propargyl mannoside or lactoside in 1X PBS containing 5 mol% $CuSO_4 \cdot 5H_2O$ and 20 mol% sodium ascorbate. After 5 h, the sample was washed twice with EDTA solution (0.1 M), 1X PBS/0.1% SDS for 10 min, 0.2X PBS for 2 min, 0.1X PBS for 2 min and finally rinsed thoroughly with deionized water. The clicked surface was then dried under a stream of nitrogen. To click 10 mol% and 1 mol% propargyl mannoside or lactoside with propargyl alcohol, the concentration of total alkynyl functionalities was kept 3 mM in 1X PBS. To click propargyl acetate and per-O-acetyl-α-propargyl-mannoside at different ratios with propargyl alcohol, the concentration of total alkynyl functionalities was kept 3 mM in DMSO/1X PBS (v/v=1/3).

3.6.3 Interaction with lectins

20 μL of solution of either PNA or LENS (1 mg/mL) was added onto the glycan-terminated surface which was placed on a glass slide. The dropped surface is covered by a hybridization cover slide on both faces and incubated in a hybridization chamber for 1 h. After incubation, the cover slide was removed with 1X PBS, and the surface was washed with a normal 1X PBS rinse or surfactinated rinse (1X PBS/0.1% SDS for 10 min; 0.2X PBS for 2 min; 0.1X PBS for 2 min) and finally with deionized water. The lectin-treated surface was dried under a stream of argon prior to analysis.[177] To obtain the isotherm, the incubation of lectin solution started from lower to higher concentrations (0.1, 0.3, 0.6, 1 and 1.5 mg/mL) in 1X PBS.

CHAPTER 4

Quantification of proteins on crystalline silicon (111) surfaces by infrared spectroscopy

.

4.1 Introduction

This chapter focuses on the determination of the density of proteins bound to glycan-terminated surfaces. By knowing the number of glycan ligands on the surface and the number of lectin receptors bound to them, we can propose a direct addressing to the requirements needed for the optimum multivalency.

There are few techniques capable of determining quantitatively the surface concentration of adsorbed proteins. Surface plasmon resonance (SPR)[193, 208, 209] and ellipsometry[210-213] are the mostly often used methods. In these methods, the measured surface concentration is a function of the molecular refractive index and the thickness of adsorption layer. However, some strict assumptions have to be made to obtain accurate quantification, for example, a low surface roughness and a homogenous monolayer packing are required.[210] Therefore, in practice, the two techniques are often seen to couple with other methods, such as quartz crystal microbalance (QCM),[208, 211] radiolabeling,[209, 210] total internal reflection fluorescence (TIRF),[212, 213] or optical waveguide lightmode spectroscopy (OWLS),[211] in order to calibrate the detected SPR or ellipsometry signal or to provide supplementary quantification data. Circular dichroism (CD)[198] and spectra reflectance imaging (SRI)[214] were also reported for the quantification of surface protein density. In addition, microscopic imaging approaches were set up to “see” and “count” the protein molecules present on the surface, including atomic force microscope (AFM)[190] and fluorescence microimaging.[215,216] Those tools offer not precise quantification results due to the drawback of insufficient lateral resolution which might fail to discern clustered or multilayer adsorption.

In the previous chapters, we have shown the appreciable capability of IR-ATR to quantify the density of diluted surface glycans. The same method can be thus extended to protein settled on the surface for two favorable reasons. For one, the adsorbed layer of protein is thin (a few nanometers) and much lower than the extent of the evanescent wave (several hundred nanometers in IR region). For the other, protein molecules offer strong characteristic response of amide I and II bands (~1650 and 1550 cm^{-1}). IR-ATR has been reported to be used in the determination of surface protein density, however, an external calibration experiment needs to be established, like using radiography method to relate the IR signal with the surface protein quantity.[217]

In this chapter, we first describe the establishment of the *in-situ* calibration experiment to obtain the calibration value of the absorbance of protein (amide I band) in solution. Then we use this value to determine the density of specific and non-specific lectins adsorbed on the glycan-terminated surface as obtained in chapter 3. The number of proteins will be correlated with the corresponding AFM results. Moreover, the data allow for conceiving a reliable model to describe the formation of “multivalency” and the “dilution effect”, which is then supported by a simulation work. Finally, the data obtained from the calibration experiment can be treated to investigate the isotherm of non-specific protein adsorption.

4.2 IR calibration experiment of protein

4.2.1 Conventional IR calibration experiment

The principle of IR quantification is to calculate the number of molecules on the surface from the absorbance of their characteristic vibrational bands. The cross-section of these bands has to be extracted first from a calibration by measuring the same molecule in liquid phase with known concentration. A prerequisite requirement is that the molecules are homogenously dispersed in solution, which leads to a linear relationship of absorbance as a function of the solution concentration.

When the same experiment was applied for LENS in PBS solution (using an ATR prism with a standard SiO_x surface), it was found that the absorbance was continuously increasing with time due to the presence of non-specific adsorption. To avoid this adsorption, one idea is to prepare a perfect antifouling surface which completely resists the non-specific adsorption. So we prepared a silicon surface grafted with a PEG monolayer. As shown in **Fig. 4.1A**, the modification procedure started from the carboxydecyl-terminated surface, which was then activated by EDC/NHS and aminolyzed with PEG (Mw=750g/mol, containing ~ 16 ethylene glycol units) carrying an amine moiety and a methoxy termination. The IR-ATR spectra shown in **Fig. 4.1B** validate the success of PEG750-terminated surface (noted as SiPEG). Using the same quantification method as described in chapter 2, the density of carboxydecyl-, NHS ester- and PEG750-terminations were obtained to be 1.9×10^{14} cm^{-2}, 1.8×10^{14} cm^{-2} and 1.0×10^{14} cm^{-2}, respectively. The lower density of PEG as compared to the EG_8 is due to its higher steric hindrance arising from a more entangled conformation.

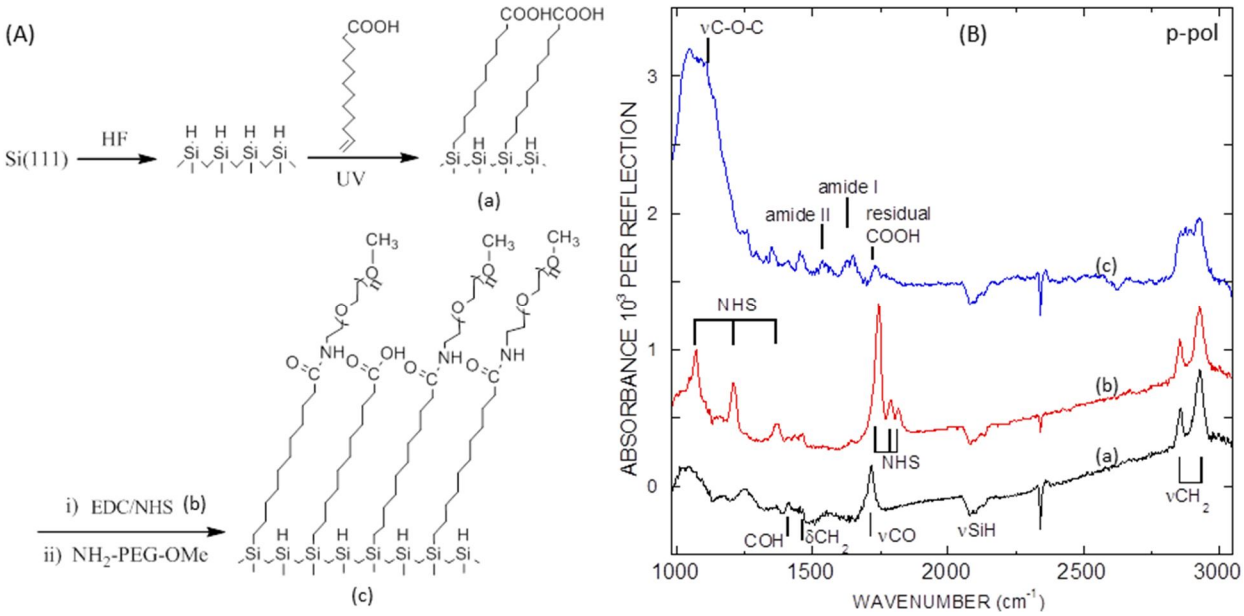

Figure 4.1 (A) Multistep modification scheme for the grafting of PEG750: (a) hydrosilylation of undecylenic acid on SiH_x surface; (b) activation by EDC/NHS and (c) aminolysis of amino PEG750; (B) IR-ATR spectra in p-polarization of different functional group-terminated surfaces, the reference being the SiH_x surface.

In an attempt to better control the IR-ATR calibration experiment, a kinetic setup was performed on both SiO_x and SiPEG surfaces at various LENS concentrations (**Fig 4.2**). On the SiO_x surface, for LENS at 1 mg/mL (**Fig 4.2a**), the amide bands increase significantly with time and does not reach an equilibrium until 2h30min. For LENS at 0.3 mg/mL (**Fig 4.2b**), similar evolution occurs and lasts until 2h. However, on the SiPEG surface, the adsorption of LENS at 1 mg/mL is still present, indicated by the increasing amide bands even though the adsorption is much significantly reduced and the equilibrium was reached in 20 min.

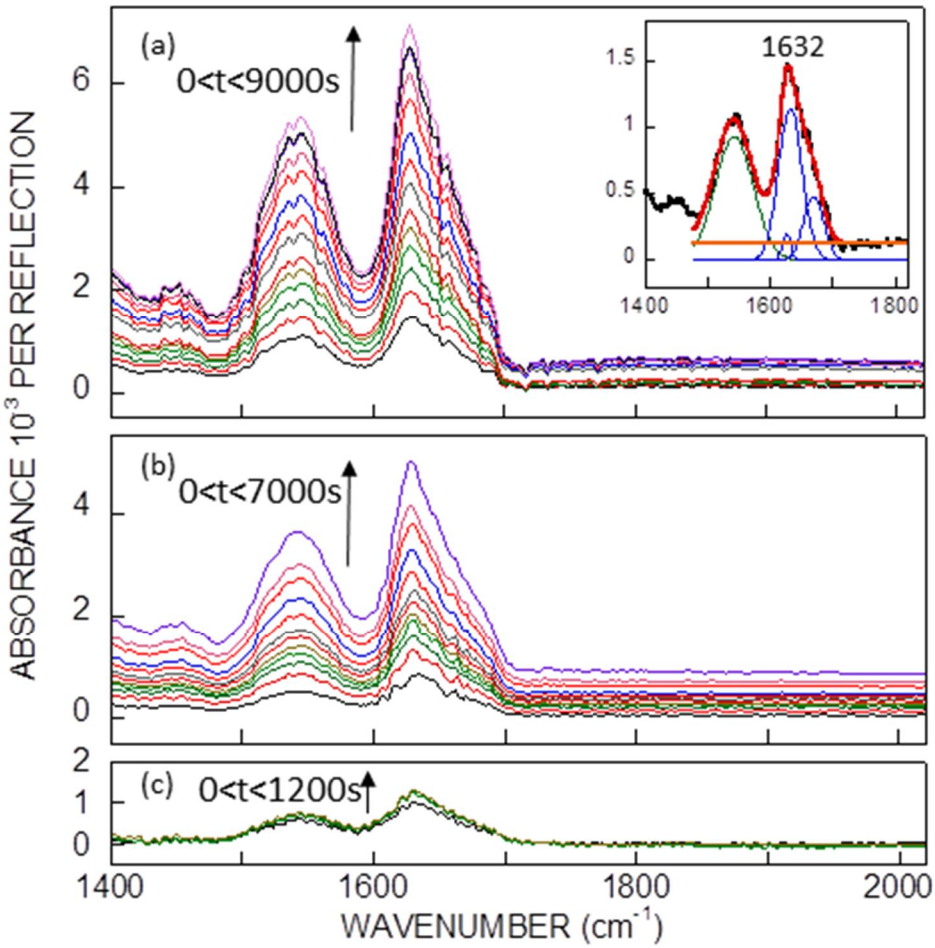

Figure 4.2. Time evolution spectra of the amide bands for LENS solution on the SiO_x surface at 1 mg/mL (a) and at 0.3 mg/mL (b) and on the SiPEG surface at 1mg/mL (c). All the above spectra were scanned in s-polarization, the reference being the PBS solution. The inset in (a) is the fit of amide band at t=802s.

The kinetic data was obtained by fitting the amide I and II bands (**Fig 4.2 inset**). The best fitting starts from 1480 to 1800 cm^{-1}, by ordering the baseline slope at 0 and three Gaussian components for the amide I band and one component for the amide II band. This fitted result generates one main contribution of amide I band at 1632 cm^{-1}, associated with the β-sheet-rich structure of the LENS molecule.[218]

The integrated absorbance of amide I band as a function of time for the three spectra is plotted in **Fig 4.3**. The data exhibit an exponential shape and can be fitted by using a first-order kinetic equation as described in the figure, indicating that the adsorption process is driven by the protein concentration in the solution. In addition, the obtained rate constants are rather similar for the two concentrations measured on the SiO_x surface ($k \sim 0.00034\ s^{-1}$), indicating a physical process independent of the concentration. However, on the SiPEG surface, the k value is 10 times higher (about 0.00338 s^{-1}) and the number of adsorbed LENS is much reduced as compared to that on the SiO_x surface.

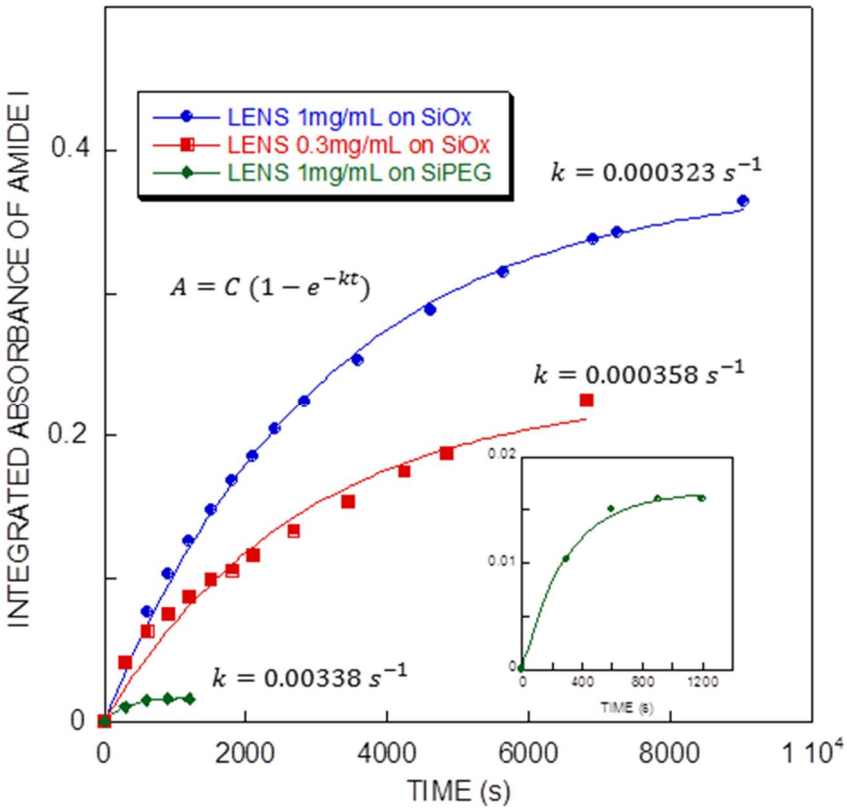

Figure 4.3. Integrated absorbance of the amide I band as a function of time for the spectra in **Fig 4.2**. The data is fitted by first-order kinetic equation shown in the plot. The inset is the enlarged plot for LENS (1mg/mL) on the SiPEG surface.

The fact that the PEG750 monolayer does not completely resist the adsorption of protein makes it difficult to obtain a calibration experiment of protein, because the obtained absorbance is in fact given by the sum of the number of protein adsorbed on the surface and dissolved in the solution. Theoretically the calibration experiment can be well-achieved on an ideal protein-resistant surface so that no adsorption is detectable. In practical, such a surface may exist by improving the antifouling property of the surface, like grafting a longer PEG or other more efficient amphiphilic polymers. However, due to the complexity of the surface preparation, we decide to give up this idea and seek for other calibration methods.

4.2.2 Indirect calibration of small amide molecules

Since any protein molecule is an assembly of several peptide chains with each amino acid (AA) unit connected through peptide bond, the amide I band can be seen as the superimposition of the νC=O of these peptide bonds. Therefore, the quantification of a protein molecule can be converted to that of a peptide bond if the number of AA for a protein is given. The quantification of peptide bond can be realized by a calibration experiment of small amide molecules, so the uncontrolled physisorption on normal SiO_x surface can be avoided.

In this sense, we calibrated the smallest amide molecule, N-methylactamide (MAA), on the SiO_x surface (**Fig 4.4**). The calibration experiment was rather straightforward, where the measured absorbance is stationary with time, indicating the absence of physisorption. The appeared amide I and II bands at 1618 cm^{-1} and 1576 cm^{-1} are not sufficiently separated, which could raise errors during the deconvolution of these bands. Nevertheless, we fitted the amide I band by one Gaussian function (**Fig 4.4a inset**). The resulting calibration curve shows good linearity (**Fig 4.4b**) and the calibrated absorbance value, A_s^0/C, is given to be 0.0005 $(cm\ mM)^{-1}$.

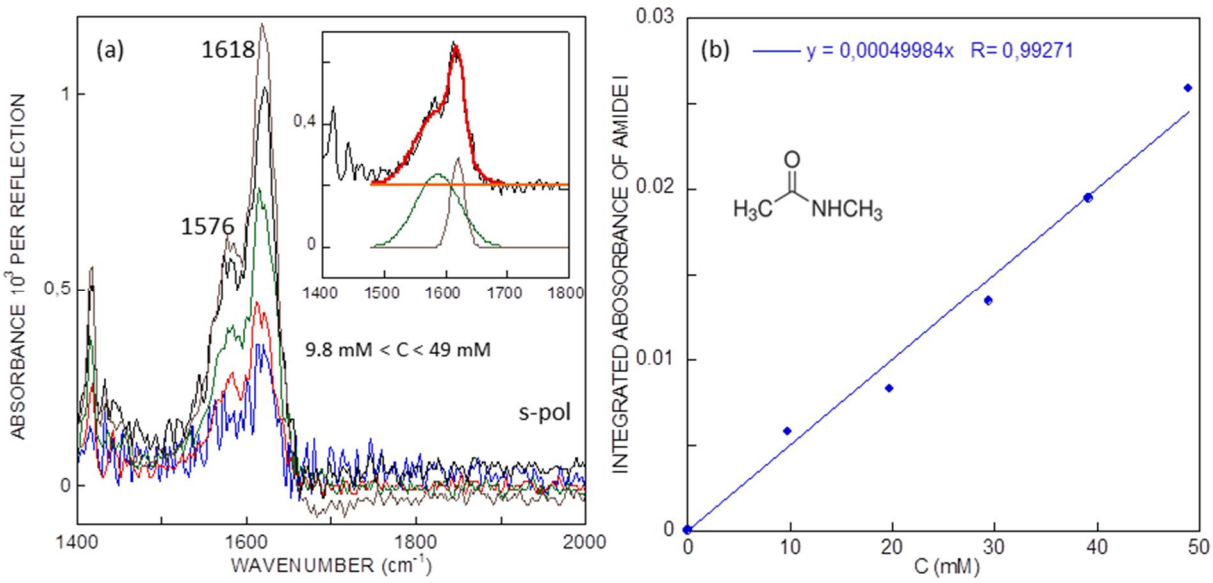

Figure 4.4. (a) IR calibration spectra (in s-polarization) of N-methylactamide in aqueous solution on the SiO_x surface, the reference being water. The inset in (a) is the fit result of amide I at C=19.7mM. (b) Integrated absorbance of the amide I band as a function of concentration fitted linearly.

4.2.3 Modified calibration of BSA

To circumvent the uncontrolled physisorption of protein, *bovine serum albumin* (BSA) was used for the calibration since it is often used as blocking agent to limit the nonspecific adsorption of proteins and turns out to readily reach a saturation concentration at the surface.

To perform the experiment, BSA solution from 0.325 mg/mL to 10.15 mg/mL were injected into the *in-situ* IR cell on either the SiO_x or SiPEG surfaces. The kinetics of each concentration was followed until the adsorption equilibrium was achieved. On the SiO_x surface, it was found that the absorbance evolution was stabilized in ~ 20 min for BSA concentrations up to 0.95 mg/mL. This stage can be defined as the presaturation. For the following BSA concentrations from 1.3 to 10.15 mg/mL, the IR signal was stabilized immediately without further evolution, indicating that the saturation of adsorption was readily achieved. On the SiPEG surface, the presaturation existed up to a concentration of 0.5 mg/mL, and no spectroscopic evolution was observed for higher concentrations. **Fig 4.5** shows the stabilized IR spectra of these concentrations on the SiO_x (**Fig 4.5a**) and SiPEG surfaces (**Fig 4.5b**). The amide I and II bands appear at 1548 and 1647 cm^{-1}, which are similar to those of LENS. The best fitting is optimized analogously between 1480 and 1800 cm^{-1} using two Gaussian functions for the amide II band and three Gaussian functions for the amide I band, containing a main component at 1647 cm^{-1} (**Fig. 4.5a inset**), due to the fact that BSA is rich in α-helix (**Fig 4.5b inset**).[218]

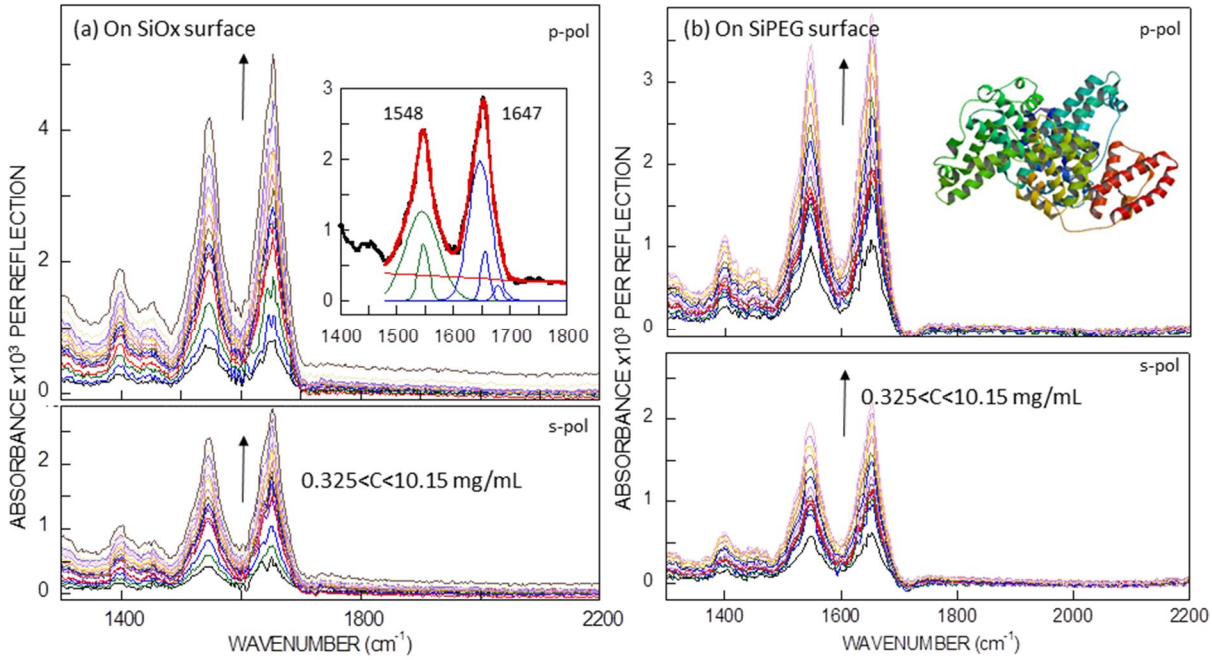

Figure 4.5. ATR-IR spectra in s- and p-polarization of BSA solutions at various concentrations on the SiO_x (a) and SiPEG (b) surfaces, the reference spectrum being water. Each spectrum was taken after the absorption stabilization was reached. The inset in (a) is the fit of the amide I and II bands for C=10.15 mM in s-pol. The inset in (b) describes the crystallographic structure of BSA.

The integrated absorbance of the amide I band versus concentration was plotted in **Fig. 4.6**. The absorbance increases much faster in the presaturation stage than that after the saturation, because of the presence of adsorption on the surface. After saturation, the measured absorbance is solely derived from the solution, therefore a linear relationship of absorbance vs. concentration is observed. We can deduce from the slope of the linear fit in s-polarization as the calibrated A_s^0/C value. The A_s^0/C value is 0.0051 (cm mg/mL)$^{-1}$ on the SiO_x surface and 0.0054 (cm mg/mL)$^{-1}$ on the SiPEG surface, indicating the reliability of the calibration experiment, since this value should be independent of the type of surface. Besides, the saturation on the SiPEG surface was achieved at a smaller BSA concentration than that on the SiO_x surface and the amount of adsorbed protein was reduced, indicating the capability of PEG monolayer in resisting the protein adsorption.

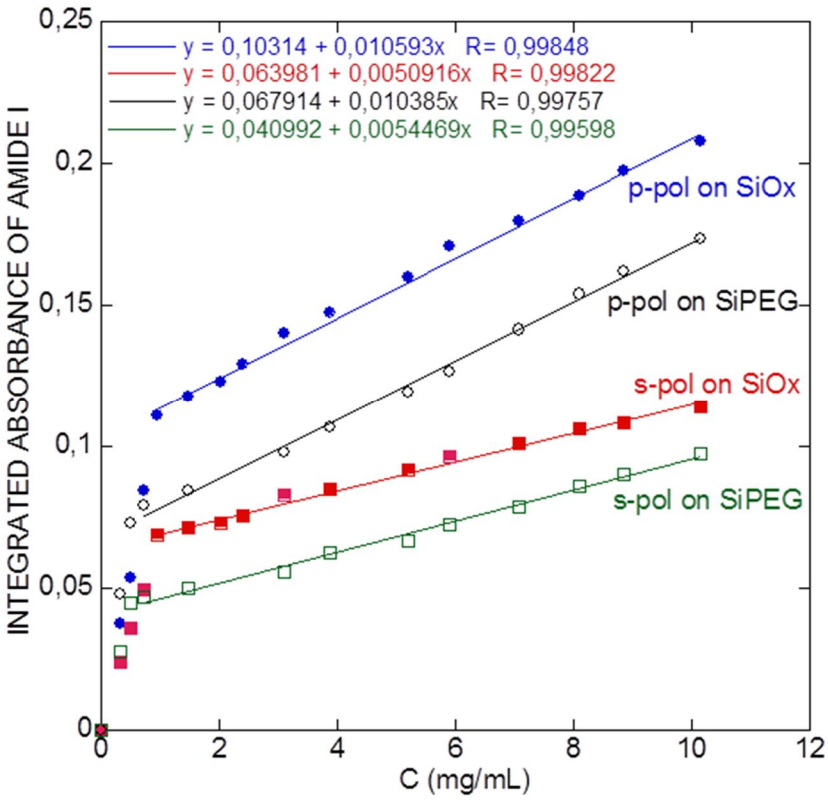

Figure 4.6. Integrated absorbance of the amide I band as a function of BSA concentration on two surfaces. The data are from the **Fig 4.5**. The data are fitted for the range after surface saturation.

In order to extend the calibration result of BSA to other proteins such as LENS, a correlation between the two molecules has to be established. Considering that the protein molecule is an assembly of a certain number of AA through peptide bond, the molecular weight (Mw) of any protein can be calculated from the average Mw of AA multiplying the number of AA, namely, $Mw\ (protein) = \overline{Mw}\ (AA) \times N\ (AA)$. For instance, one BSA molecule contains 1166 AA for a Mw of 133 kDa, with a $\overline{Mw}\ (AA)$ being 114 g/mol, whereas LENS molecule is comprised of 466 AA for a Mw of 52 kDa, with a $\overline{Mw}\ (AA)$ being 112 g/mol. So that $Mw\ (BSA) = 114 \times N$

(AA) and *Mw (LENS) = 112 × N (AA)*. The conversion from BSA to LENS is simply a factor of 114/112=1.02, a negligible influence for the quantification of LENS. Analogous in case of PNA, which consists of 944 AA for a Mw of 103 kDa, *Mw (PNA) = 109 × N (AA)*, the calibration result of BSA can be also adapted to PNA.

As a matter of fact, the $\overline{Mw}$ *(AA)* of the most of proteins has a value of ~ 110 g/mol, empirically. As far as the number of AA in protein is given, the calibration result of BSA can be extended for other proteins.

In addition, in the previous section, a calibration experiment performed on MAA molecule leaded to a value of A_s^0/C at 0.0005 (cm mM)$^{-1}$ for one amide I band (denoted as $A_s^0\ (amide\ bond)$). Nevertheless, this value can be postulated for protein molecules. For instance, by using the $A_s^0\ (amide\ bond)/C$, the $A_s^0\ (LENS)/C$ is obtained by multiplying 466, given as 0.233 (cm mM)$^{-1}$, equivalent to 0.0045 (cm mg/mL)$^{-1}$ (LENS: 1 mg/mL=0.0192 mM), in good agreement with the calibration result of BSA (0.0051 (cm mg/mL)$^{-1}$ on the SiO_x surface and 0.0055 (cm mg/mL)$^{-1}$ on the SiPEG surface).

Based on these results, we choose the $A_s^0\ (BSA)/C$ value on the SiO_x surface as the calibration value, 0.0051 (mg/mL)$^{-1}$ with an uncertainty ± 10%. Finally the formula to quantify the density of protein bound to the surface can be deduced. For a silicon prism owning an incident angle of ~51°, the density of LENS on the surface is written as:

$$N_{\parallel} = 3.53 \times 10^{13} A_s$$

$$N_{\perp} = 7.69 \times 10^{13} A_p - 6.99 \times 10^{13} A_s$$

$$\text{So, } N_{total} = 7.69 \times 10^{13} A_p - 3.46 \times 10^{13} A_s$$

For PNA, the equations are:

$$N_{\parallel} = 1.75 \times 10^{13} A_s$$

$$N_{\perp} = 3.80 \times 10^{13} A_p - 3.45 \times 10^{13} A_s$$

$$\text{So, } N_{total} = 3.80 \times 10^{13} A_p - 1.70 \times 10^{13} A_s$$

4.3 Quantification of lectins on glycosylated surfaces

4.3.1 Quantification of lectins correlated with CM-AFM

As shown in chapter 3, the LENS molecule possesses a bivalent structure which must adopt "side-on" conformation on the surface to favor the multivalent binding. Indeed, the "side-on" conformation of both lectins can be described as cuboid bricks, where the two mannose-binding sites of LENS are on the bottom diagonal and the four galactose-binding sites of PNA are located on the tetrahedron vertices (**Fig 4.7**). The obtained horizontal dimension by looking from the top view is 8×3.7 nm for LENS and 6.5×6.5 nm for PNA. Theoretically, the density of a compact monolayer of lectin should not exceed 3.38×10^{12} cm^{-2} for LENS and 2.37×10^{12} cm^{-2} for PNA.

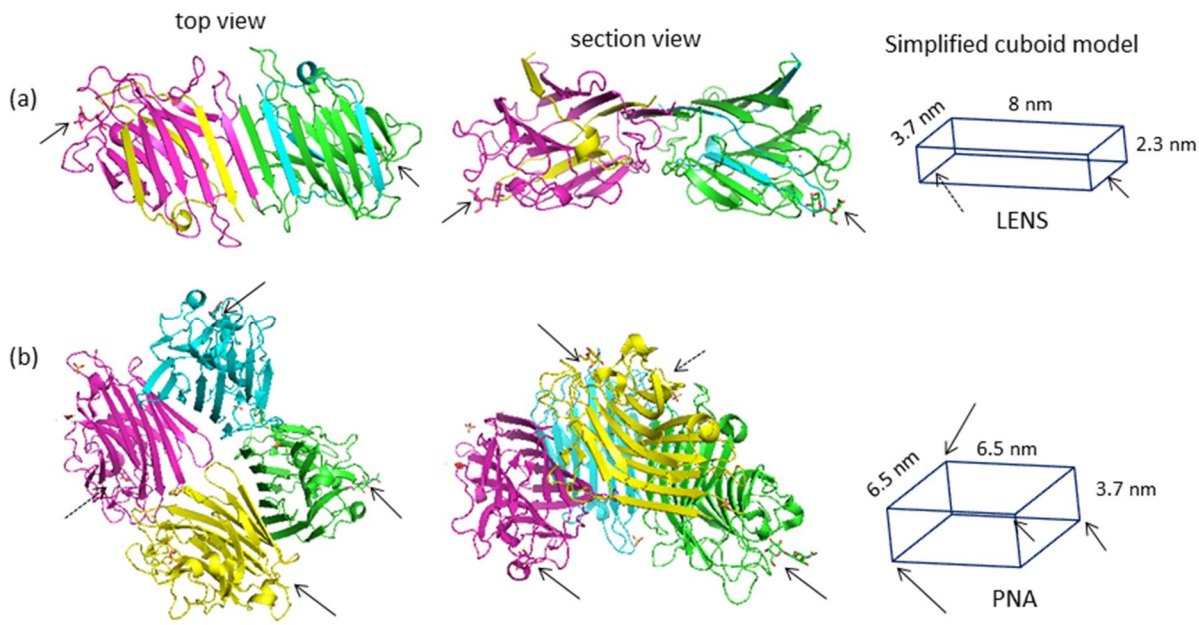

Figure 4.7 Top and section views for the crystallographic structure of LENS (pdb file: 1LES) and PNA (pdf file: 2DVB). The sugar-binding sites are indicated by arrows.

Using the deduced quantification equations, the density of lectins bound on the surface can be easily calculated for the data obtained in chapter 3. **Table 4.1** lists the calculated density of lectins and the corresponding AFM images.

Surface glycan	100 mol% mannose	100 mol% lactose
Lectin	PNA (1 mg/mL)	LENS (1 mg/mL)
Rinse method	PBS rinse	PBS rinse
Data origin	**Fig 3.4a**	**Fig 3.6a**
Glycan density	1.2×10^{14} cm^{-2}	6.12×10^{13} cm^{-2}
Lectin density	0 cm^{-2}	1.08×10^{11} cm^{-2}
Coverage	0 %	3.2%
AFM image	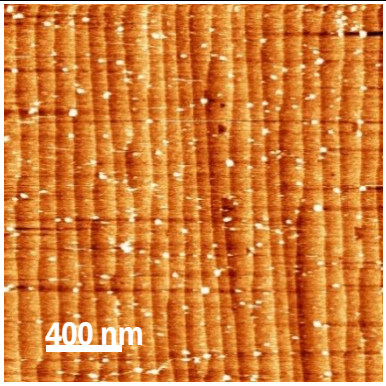	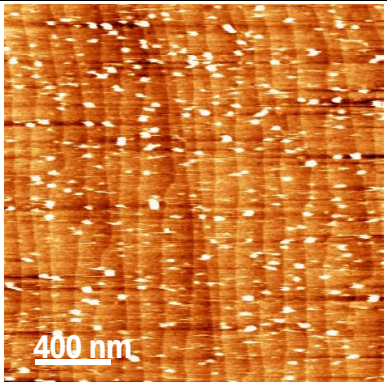
Image origin	**Fig 3.9a**	**Fig 3.10a**

Surface glycan	100 mol% mannose	
Lectin	LENS (1 mg/mL)	
Rinse method	PBS rinse	SDS rinse
Data Origin	**Fig 3.22**	**Fig 3.22**
Glycan density	1.2×10^{14} cm^{-2}	
Lectin density	3.07×10^{12} cm^{-2}	7.7×10^{11} cm^{-2}
Coverage	90.8% (~1 monolayer)	22.8%
AFM image	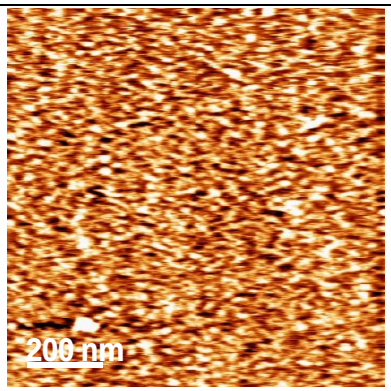	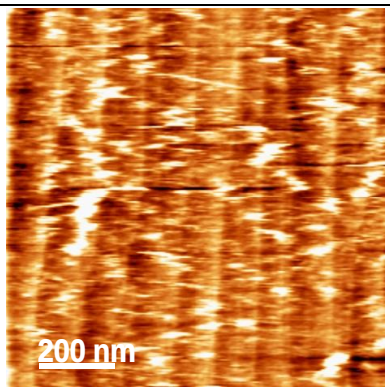
Image origin	**Fig 3.9c, d**	**Fig 3.9e, f**

Surface glycan	10 mol% mannose	
Lectin	LENS (1 mg/mL)	
Rinse method	PBS rinse	SDS rinse
Data origin	**Fig 3.22**	**Fig 3.22**
Glycan density	5.25×10^{13} cm^{-2}	
Lectin density	6.52×10^{12} cm^{-2}	2.72×10^{12} cm^{-2}
Coverage	~ 2 monolayers	80% (~ 1 monolayer)
AFM image	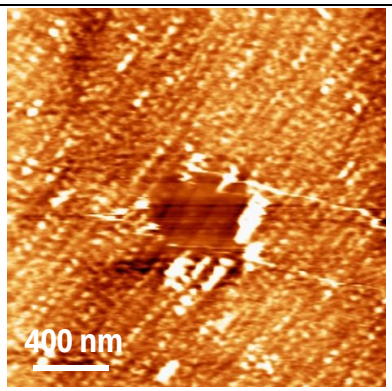	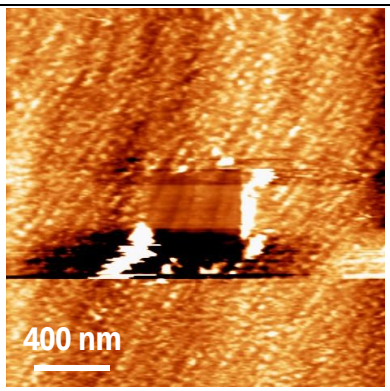
Image origin		**Fig 3.16-1b, c, d**

Surface glycan	1 mol% mannose	
Lectin	LENS (1 mg/mL)	
Rinse method	PBS rinse	SDS rinse
Data origin	**Fig 3.22**	**Fig 3.22**
Glycan density	7.2×10^{12} cm^{-2}	
Lectin density	2.77×10^{12} cm^{-2}	7.8×10^{11} cm^{-2}
Coverage	82% (~ 1 monolayer)	23.1%
AFM image	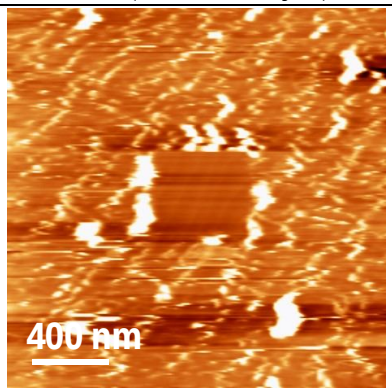	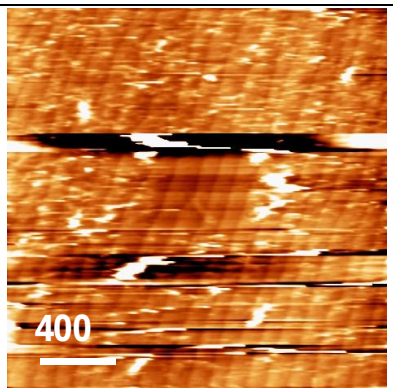
Image origin		**Fig 3.16-2b, c, d**

Surface glycan	100 mol% lactose	
Lectin	PNA (1 mg/mL)	
Rinse method	PBS rinse	SDS rinse
Data origin	**Fig 3.6a**	**Fig 3.6b**
Glycan density	6.12×10^{13} cm^{-2}	
Lectin density	1.73×10^{12} cm^{-2}	8.8×10^{11} cm^{-2}
Coverage	73%	37%
AFM image	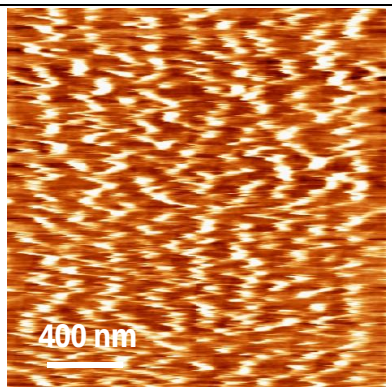	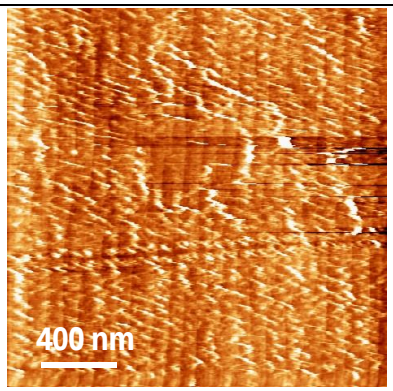
Image origin	**Fig 3.10c, d**	**Fig 3.10e, f**

Table 4.1 Quantified density of lectins bound to glycan-terminated surfaces and corresponding AFM images.

By correlating the "quantified IR data" and the AFM results, three conclusions can be drawn:

1) For non-specific lectins interacted with the glycan-terminated surface, the non-specific adsorption is present but only at a trace amount level. The calculated coverage of lectins is 0 for mannose-terminated surface and 6% for lactose-terminated surface. This small difference with respect to IR results is due to the higher sensitivity of AFM than IR.

2) The AFM images of 100 mol%, and 1 mol% diluted mannose-terminated surfaces after interaction with LENS followed by a PBS rinse show that the lectin covers completely the surfaces, in agreement with the calculated coverage of 90.8% and 80.2%, respectively. However, the 10 mol% mannose-terminated surface gives a density of ~ two lectin layers. This evidence supports that the interaction with specific lectins after inefficient PBS rinse results in not just specific binding, but also supplementary protein-protein interactions. Similar phenomenon is observed on the 100 mol% lactose-terminated surface after interaction with PNA followed by a PBS rinse.

3) For interaction with specific lectins, the SDS rinse effectively removes the physisorption, leaving only the monolayer of specifically-bound lectins. For 100 mol% and 1 mol% mannose-terminated surfaces, the AFM images reveal the formation of a loosely packed lectin layer, corresponding to a calculated coverage of ~23%. The 10

mol% mannose-terminated surface interacted with LENS after SDS rinse forms a densely packed monolayer of lectin as visualized by AFM, which is confirmed as well by the calculated coverage of ~80%.

4.3.2 The multivalency binding model for mannose-LENS

The determined densities of mannose and LENS on the surface are listed in **Table 4.2** which allows for obtaining the probe-target ratio and the distribution of mannose.

	$C_{mannose}$ [cm^{-2}]	C_{LENS} [cm^{-2}]	mannose-LENS ratio	occupied area per mannose [nm^2]
100% mannose	1.2×10^{14}	7.7×10^{11}	156:1	0.83 (0.91×0.91 nm)[a)]
10% mannose	5.2×10^{13}	2.7×10^{12}	19:1	1.96 (1.4×1.4 nm)
1% mannose	7.2×10^{12}	7.8×10^{11}	9:1	14 (3.74×3.74 nm)

Table 4.2. Summary of the measured concentrations of mannose and LENS on the surface. [a)] Each mannose site is considered as a square grid

The three surfaces exhibit a surface-concentration ratio of mannose to LENS much larger than that strictly needed for the bivalency binding (2:1), showing that many mannose ligands do not participate in the binding. These quantitative data now allow for discussing how the bivalency binding proceeds at various surfaces. Two factors are addressed: the distance between two mannose binding sites (5.9 nm) and the size of the carbohydrate recognition domain (1.4 nm) (**Fig 4.8**). Since a single mannose unit has to penetrate this domain in order to efficiently interact with LENS, a spacing of ~1.1 nm (half the domain size 0.7nm plus half the mannose size 0.35 nm) must exist between neighboring mannose units in order to allow for such an interaction. Such a spacing is available around the mannose molecules at the 10 mol% and 1 mol% mannose-terminated surfaces, but not at the non-diluted mannose-terminated surface where the mannose is distributed densely and the click yield of 75% corresponds to the limit of steric hindrance. Moreover, by considering the mannose pair distance, the largest distance between adjacent mannoses is on the 1 mol% mannose-terminated surface (3.7 nm). This means that in spite of the statistical fluctuations of positions and the flexibility of the molecular system, it is not possible to always find a couple of mannose sites away from each other by a distance around 5.9 nm. The constraints of spacing and pair distance are evidenced by the low coverage of lectin captured at the 100 mol% and 1 mol% mannose-terminated surfaces. Such constraints are certainly much less stringent on the 10 mol% mannose-terminated surface where the average distance between two adjacent mannoses (1.4 nm) seems to be optimum to fulfill the two opposite requirements: large

enough for providing sufficient binding space, and small enough for enabling bivalent adsorption.

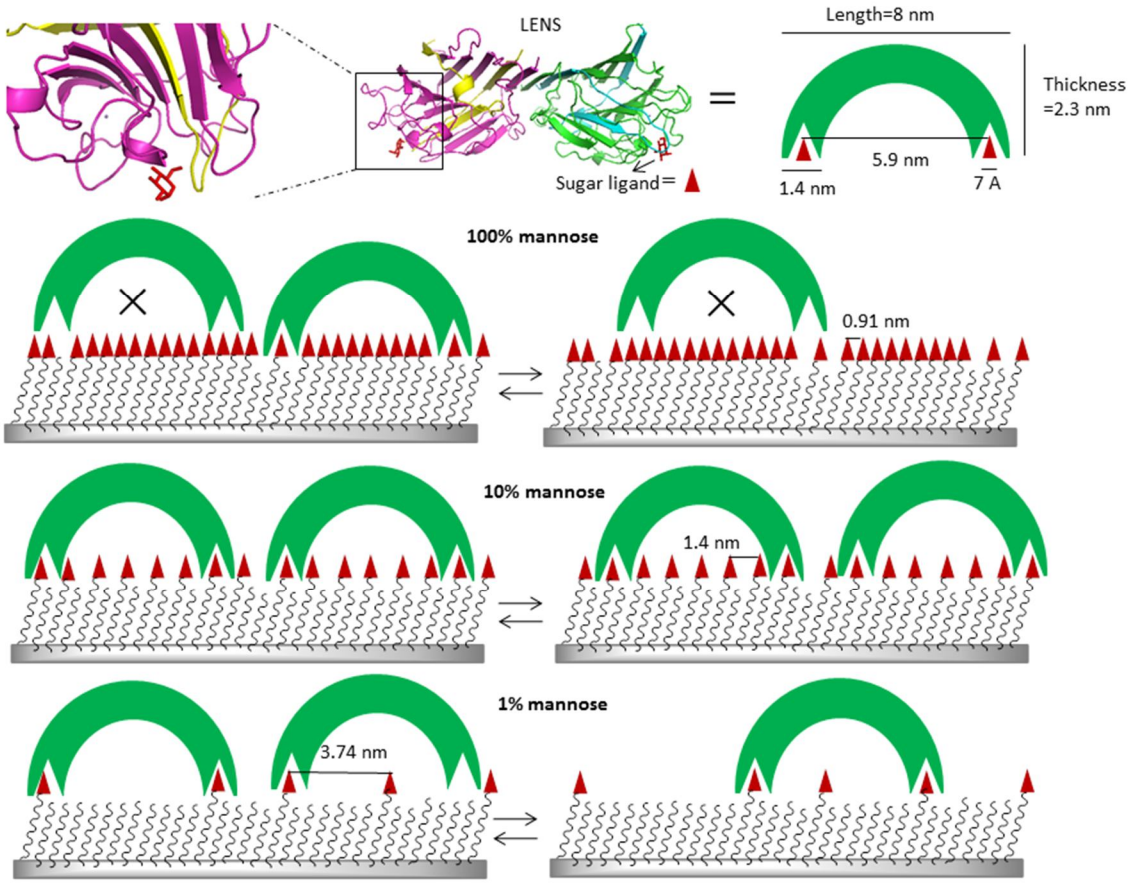

Figure 4.8. Schematic model for the binding of LENS (pdb file: 1LES) onto the surface of "clicked" mannoside diluted in "clicked" propargyl alcohol.

These assumptions have been confirmed quantitatively by numerical simulations (**Fig 4.9**). The minimum center-to-center distance between two mannose ligands 2*R* (*R* is the radius of the mannose) was determined by choosing the value that yields the maximum surface concentration found experimentally (1.2×10^{14} cm^{-2}). This value 2*R*=0.76 nm (effective diameter of the ligand group) is in typical agreement with the known size of a mannose (0.7 nm) molecule. Bivalent adsorption was allowed whenever two mannoses were spaced by a distance 5.9 nm ± x%, and the minimum distance between these two sites and all of the other mannoses was larger than 2R+δ. Various values of x% and δ were explored. The obtained concentration of adsorbed lectins C_{ads} was generally found to exhibit a flat maximum when plotted as a function of the concentration of ligand sites C_{lig} (**Fig 4.9d**). The curves actually exhibit three regions. At low C_{lig} (region I), C_{ads} is weak and increases with increasing C_{lig}. On the opposite, when C_{lig} approaches its maximum value (region III), C_{ads} decreases with increasing C_{lig}, an obvious consequence of the impossibility for a ligand site to be active when a ligand neighbor is located in its vicinity closer than 2*R*+δ. In the mid range (region II), C_{ads} is maximum and hardly sensitive to C_{lig}, an indication that there is steric hindrance between

the adsorbed lectins. As it was to be expected from these considerations, regions I and III are found to be sensitive to the choice of x% (governing the distance of a suitable mannose pair), while region III is the only part sensitive to the choice of δ (governing the available binding space). On the opposite, region II is little sensitive to x% and δ. Values x% ~ 2.5% and δ=0.14 nm are found to yield fair agreement with the experimental findings. These values sound reasonable in view of the geometry of the lectin and its adsorption sites. Note that the effective diameter of the coordination site of the lectin, 2(R+δ), appears somewhat smaller from the simulations (1.04 nm) than expected from the structure of LENS (1.4 nm). This may be due to the fact that the steric hindrance effect is less severe than the estimation from the measured diameter of the coordination shell, due to the tilting of its axis with respect to the surface normal.

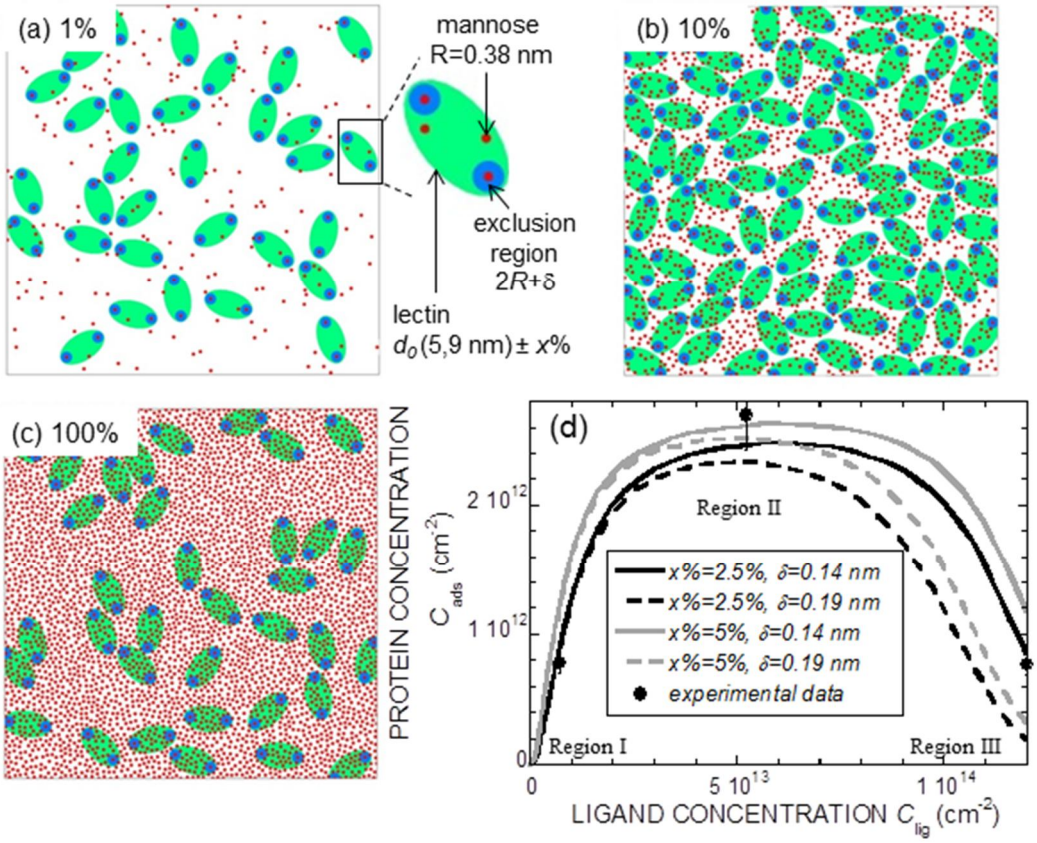

Figure 4.9. Numerical simulation results: (a-c) typical images corresponding to the three ligand concentrations used in our experiments. The ligand sites are represented by the small red dots and the adsorbed lectins by the green ellipses; distance of suitable mannose pairs d_0=5.9 nm ± x%. Spacing exclusion is defined as 2R+δ. (d) Resulting lectin concentration C_{ads} as a function of ligand concentration C_{lig}, obtained by averaging the results of 100 simulations. Two varying parameters, x% (2.5% and 5%) and δ (0.14 and 0.19 nm) are envisaged.

4.4 Conclusion

This chapter offers a study about the quantification of protein bound to the surface. In order to circumvent the uncontrolled physisorption of protein on the silicon surfaces, different calibration methods are performed. The conventional calibration experiment of protein on the SiO_x or SiPEG surface failed. One alternative calibration experiments took advantage of small amide molecule to avoid the non-specific adsorption and the calibrated absorbance value can be extended for proteins. A more precise calibration experiment aims at saturating the physisorption by BSA and the calibration curve is obtained after the saturation. The success of calibration allows us to quantify the density of lectin on the surface, showing good agreement with the corresponding AFM results. Moreover, by the aid of the calculated density of glycans or lectins on the surface, a reliable model is then established to interpret the “dilution effect”. These quantitative results suggest that optimum conditions for bivalent adsorption are a compromise on the surface concentration of glycan ligands: enough free space around each glycan together with large enough density to provide suitably spaced glycans. These ideas have been assessed by numerical simulations, which account for the experimental results quantitatively.

4.5 Experimental section

4.5.1 Preparation of PEG750-terminated silicon surfaces

The preparation of carboxydecyl-terminated and NHS-activated silicon surfaces was performed as described previously.[63,110] The freshly NHS-activated surface was immersed in a solution of 20 mM methoxypoly(ethylene glycol) amine (Mw=750) overnight. After reaction, the sample was washed in 1X PBS/0.1% SDS for 5 min, 0.2X PBS for 2 min; 0.1X PBS for 2 min and finally rinsed thoroughly with deionized water. The surface was then dried under a stream of nitrogen.

4.5.2 Kinetics of protein adsorption on oxidized silicon surface and PEG-terminated surface

The solution of LENS (0.3 and 1 mg/mL in 1X PBS) was injected into in-situ IR cell (cf Annex). The surface reference was either an oxidized silicon prism or PEG750-terminated silicon prism. The IR measurement was recorded every 5 min in the first 1 h and every 10 to 20 min afterwards.

4.5.3 ATR-FTIR calibration of methylactamide and BSA.

The solution of methylactamide (9.8, 19.7, 29.4, 39.2 and 49 mM in water) was injected into *in-situ* IR cell (cf Annex), the reference prism being the oxidized silicon surface. The IR measurement was immediately recorded. After each concentration, the cell was cleaned by injecting 3 times water.

Increased concentrations of BSA solution (0.325, 0.5, 0.725, 0.95, 1.3, 1.475, 1.775, 2.025, 2.4, 3.1, 3.6, 3.875, 4.375, 5.2, 5.52, 5.9, 7.075, 8.1, 8.85 and 10.15 mg/mL in water) were injected into *in-situ* IR cell, the reference being either the oxidized silicon prism or PEG750-terminated silicon prism. For the BSA concentrations up to 0.95 mg/mL, continuous measurements were performed for 20 min until the stabilisation of the IR signal. For the

following BSA concentrations, the IR signal was stabilized immediately after the first measurement.

4.5.4 Numerical simulation

The issue of steric hindrance among the adsorbed lectins was investigated in a numerical simulation. Ligand sites were thrown at random on a square area, of size 60×60 nm^2, with the constraint that each new site must be spaced by a minimum distance d_{cutoff} from all of the other sites. The lectins were simulated by ellipses (long axis 8.0 nm, short axis 4.3 nm). The anchoring sites were taken along the long axis, symmetric with respect to the ellipse center, and at a mutual distance d_0 =5.9 nm. For a given concentration of ligand sites on the surface, adsorption of lectins was investigated, by assuming that a lectin can be adsorbed on two ligand sites whenever three conditions are fulfilled: i) the two ligand sites are located at a distance $d_0 \pm x\%$, where x is a parameter of the simulation; ii) there is a free circular space of radius d_{imp} around the two ligands (no other ligand within a distance d_{imp}); iii) there is no overlap of the newly adsorbed lectin with previously adsorbed ones. In a first step, the pairs of ligand sites were explored at random and a lectin was adsorbed irreversibly as soon as a pair was found for which these three conditions are fulfilled. The process stopped when no suitable pair of ligand sites was left free. In a second step, an “anneal” was carried out by allowing a randomly selected lectin to desorb, and exploring the various manners of readsorbing one or two lectins instead. When readsorption of two lectins was possible, this new set was chosen, and the process was repeated many times till no further increase in the number of adsorbed lectins was obtained. This process is thought to be realistic, because the lectins are adsorbed weakly enough and desorption followed by rearrangement, leading to an optimization of the surface coverage, is possible. The number of adsorbed lectins, divided by the surface area of the square, readily gave the surface concentration.

CHAPTER 5

Metal-enhanced fluorescence microarrays for glycan-protein detection

5.1 Introduction

This chapter describes the elaboration of glycan microarrays for the detection of lectin-glycan interactions using metal-enhanced fluorescence (MEF). Here the gold nanoparticles (AuNPs) were embedded at the surface of a glass slide coated by a dielectric a-$Si_{1-x}C_x$:H thin film. The thin film was functionalized to link the glycan derivatives. The MEF effect arises from the coupling of the LSPR of AuNPs with a fluorophore attached to the target proteins. To obtain the optimum MEF, several factors should be considered. Firstly, the optical property of metal nanostructures in terms of LSPR sensibility and absorption should be favored upon the coating and functionalization. Secondly, the LSPR position should be close enough to the excitation/emission wavelength. Thirdly and the most importantly, the distance between the AuNPs and the fluorophore should be located properly to have the best field overlapping. This distance can be precisely tuned by coating different thicknesses of a-$Si_{1-x}C_x$:H thin films. The use of a-$Si_{1-x}C_x$:H thin films also helps in stabilizing the morphology of AuNPs on the slide. In addition, the functionalization established on a-$Si_{1-x}C_x$:H thin films guarantees the formation of stable monolayers through covalent Si-C bond and provides a dense layer of probe molecules.

In the laboratory PMC, L. Touahir developed an ultrasensitive DNA sensor using a 5 nm thick coating of a-$Si_{0.8}C_{0.2}$:H on gold nanoparticles (AuNPs). The DNA strand was covalently immobilized on the substrate, which allowed the detection of the complementary hybridization strand labeled by Cy5 at femtomolar level. The choice of a-$Si_{0.8}C_{0.2}$:H leads to a LSPR (614 nm) close to the excitation (650 nm) and emission (670 nm) wavelength of Cy5. Moreover, the 5 nm coating of a-$Si_{0.8}C_{0.2}$:H resulted in a Cy5-AuNPs distance of ~15 nm which allowed the optimum LSPR-fluorescence coupling.

Following the same conception of sensor architecture, we shift the multistep modification protocol of the glycan-terminated monolayer onto amorphous silicon-carbon alloy surfaces. In our approach, the gold nanoparticles are capped by a-$Si_{0.8}C_{0.2}$:H as the LSPR-active structure. The preparation of the azide-terminated monolayer is the same as for crystalline silicon surfaces. After surface etching, hydrosilylation of undecylenic acid and amidation of the amino OEG, the azide-terminated surfaces are formed. The alkynyl-derivatized glycans (mannoside and lactoside) are then linked by a spotting approach *via* copper (I) catalyzed “click” reaction (**Fig 5.1**). This as-prepared glycan microarray will be investigated by two fluorescence-labeled lectins *concanavalin A* (ConA, specific to mannose) and *peanut agglutinin* (PNA, specific to lactose).

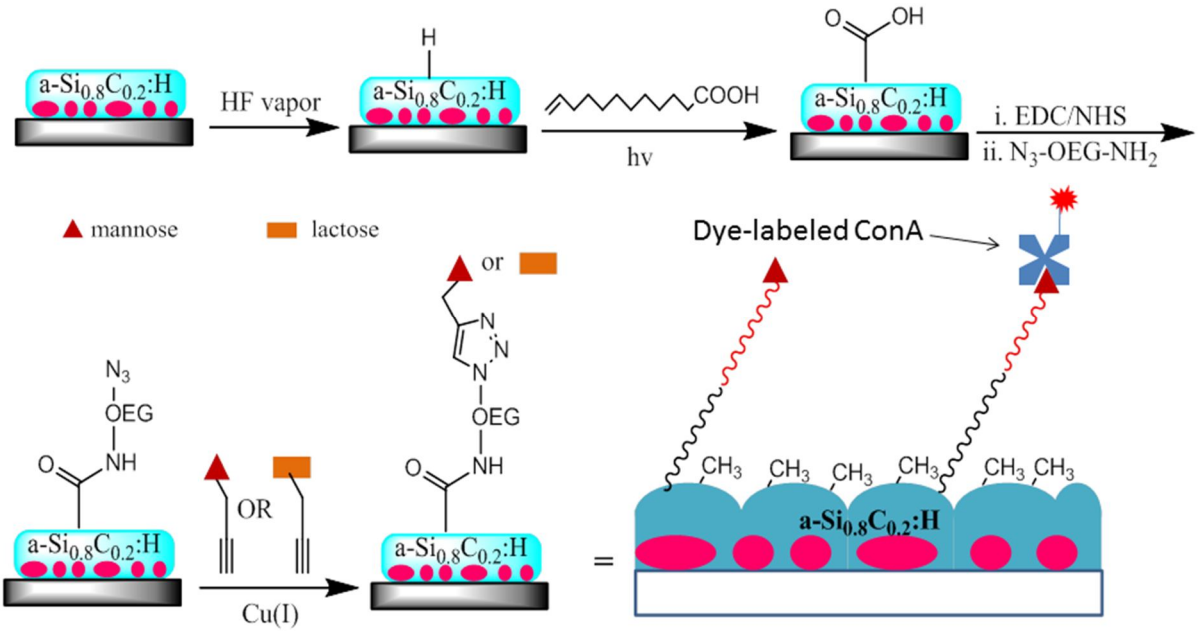

Figure 5.1 Scheme of MEF structure for the linking of glycans.

Good specificity, elimination of non-specific adsorption and high sensitivity are the key criteria for the success of glycan microarrays. Therefore, some optimizations of the array structure should be performed. To guarantee the reproducibility of the functionalization, IR-ATR will be used to follow the modification on a-$Si_{1-x}C_x$:H, which was coated on crystalline silicon surfaces. The amorphous coatings on AuNPs will be characterized by scanning electronic spectroscopy (SEM), AFM and LSPR absorption. After the functionalization of the LSPR structure to generate the azide-terminations, special attention will be paid to optimize the spotting process for the "click" reaction. Thereafter, the glycan-functionalized microarray will be tested by the two lectins to envisage the screening selectivity of lectins as well as the control of non-specific adsorption. To pursue a high sensitivity, the thickness of the a-$Si_{0.8}C_{0.2}$:H will be varied in order to find the optimum distance between the fluorophore and AuNPs.

The the glycan microarray will be later used for some conventional binding assays to show its potential power, including isothermal study and kinetic measurement.

5.2 Utilization of a-$Si_{1-x}C_x$:H thin films on silicon substrate: IR-ATR study

The surface functionalization on a-$Si_{1-x}C_x$:H thin layer for the formation of glycan-terminated monolayer was verified by IR-ATR using the crystalline silicon prism as the substrate, onto which a ~40nm of a-$Si_{1-x}C_x$:H thin layer was deposited. Three Si/C ratios were studied: a-Si:H, a-$Si_{0.9}C_{0.1}$:H and a-$Si_{0.8}C_{0.2}$:H. Firstly, the success of the deposition was confirmed for the a-$Si_{1-x}C_x$:H coated silicon in reference of the SiH*x* surface as displayed in **Fig. 5.2**. The intense band from 1860 to 2300 cm^{-1} arises from the νSi-H bonding and the broad band at 2750–3000 cm^{-1} is ascribed for the νC-H bonding. The multiple smaller peaks at 1398, 1341 and 1234 cm^{-1} are assigned to δC-H and the intense band at 1018 cm^{-1} to the Si-$(CH)_n$ wagging or rocking modes.[219] The ratio of the absorbance of νSi-H/νC-H decreases from a-Si:H to a-$Si_{0.8}C_{0.2}$:H proving the success of carbon incorporation. Moreover, the position of the νSi-H band shifts towards a higher wavenumber from a-Si:H to a- $Si_{0.8}C_{0.2}$:H: 2000 cm^{-1} for a-Si:H, 2080 cm^{-1} for a-$Si_{0.9}C_{0.1}$:H and 2098 cm^{-1} for a-$Si_{0.8}C_{0.2}$:H. Such a shift is contributed by multiple presences of CH_3-Si-H, Si-H_2 and clustered Si-H.[220, 221]

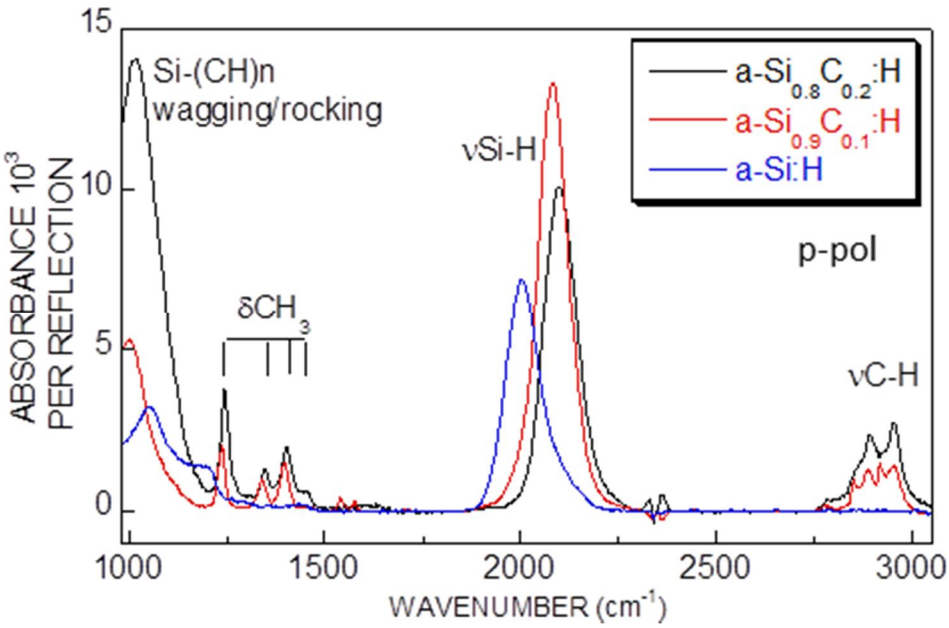

Figure 5.2 IR-ATR spectra in p-polarization of a-Si:H, a-$Si_{0.9}C_{0.1}$:H and a-$Si_{0.8}C_{0.2}$:H deposited on the crystalline silicon surfaces, with the reference being the SiH_x surfaces.

The IR-ATR spectra of the multi-step functionalization leading to the mannose-terminated surface on the a-$Si_{0.9}C_{0.1}$:H and a-$Si_{0.8}C_{0.2}$:H coatings are shown in **Fig 5.3** and **Fig 5.4**, respectively. The formation of acid-, NHS ester- and azide-terminated surfaces was confirmed by observing the appearance of characteristic bands corresponding to these termini like on crystalline surface. The quantified density of acid- and azido-terminated surfaces is listed in **Table 5.1**. It is clear that the density of the functionalized monolayer on a-$Si_{1-x}C_x$:H is lower

than that on crystalline silicon, especially the density of the acid- and azide-termini on a-$Si_{0.8}C_{0.2}$:H is only ~1/3 of that on crystalline silicon surface. We notice also that the amide I and II bands on a-$Si_{0.8}C_{0.2}$:H are too weak to be clearly distinguished but the increased intensity of νC-O-C demonstrated the success of amidation and "click" (**Fig 5.4**). The lower functionalization yield of the carbon-doped silicon is likely due to the methyl groups exposed on the surface.[69-72]

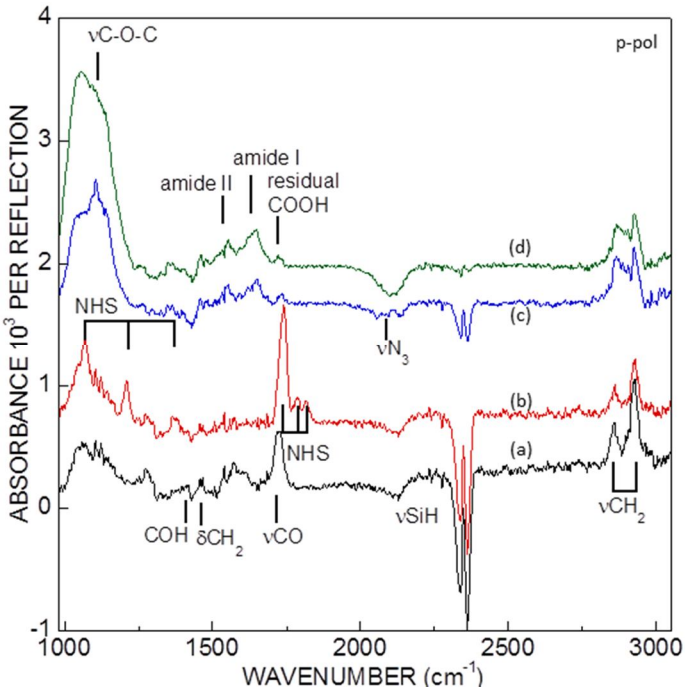

Figure 5.3 IR-ATR spectra in p-polarization of acid- (a), NHS ester- (b) N_3- (c) and mannose-terminated surfaces (d) on a-$Si_{0.9}C_{0.1}$:H layer, the reference being the a-SiH_x surface.

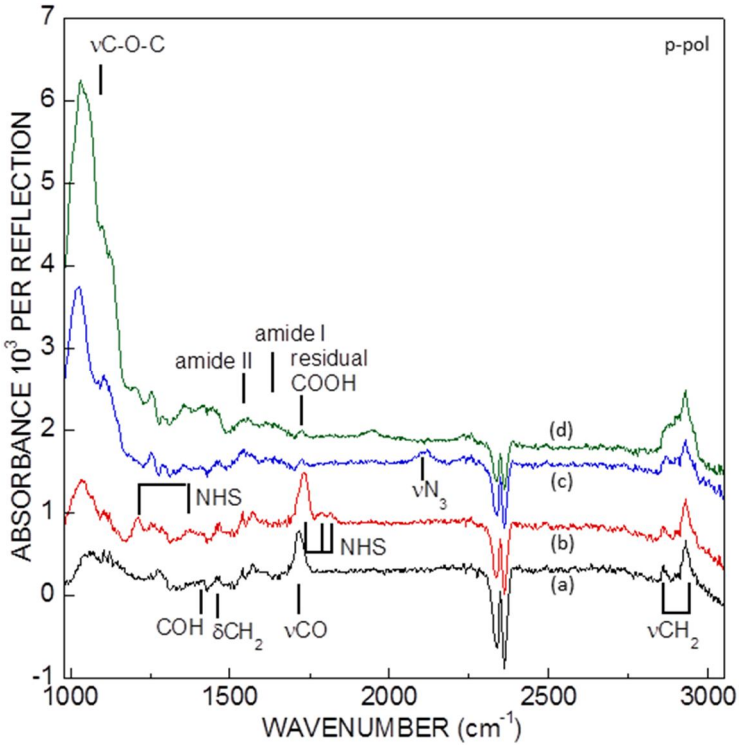

Figure 5.4 IR-ATR spectra in p-polarization of acid- (a), NHS ester- (b) N_3- (c) and mannose-terminated surfaces (d) on a-$Si_{0.8}C_{0.2}$:H layer, the reference being the a-SiH_x surface.

a-$Si_{1-x}C_x$:H layers	Figure	-COOH density	-N_3 density
a-$Si_{0.9}C_{0.1}$:H	**Fig. 5.3**	1.36×10^{14} cm^{-2}	9.5×10^{13} cm^{-2}
a-$Si_{0.8}C_{0.2}$:H	**Fig. 5.4**	7.2×10^{13} cm^{-2}	3.7×10^{13} cm^{-2}

Table 5.1 Quantified density of the functionalization on different a-$Si_{1-x}C_x$:H layers. N.B. The refractive indices of a-$Si_{0.9}C_{0.1}$:H and a-$Si_{0.8}C_{0.2}$:H are 2.65 and 2.25, respectively.

5.3 Utilization of a-$Si_{1-x}C_x$:H thin films on glass slide: MEF effect

5.3.1 Characterization of the LSPR interface

The AuNPs are obtained by thermal evaporation of a thin gold film (4 nm in thickness), followed by thermal annealing at 500°C for 1 min. As can be seen from the SEM image in **Fig 5.5**, annealing of the gold thin film leads to the formation of AuNPs with a lateral size of ~33 nm.

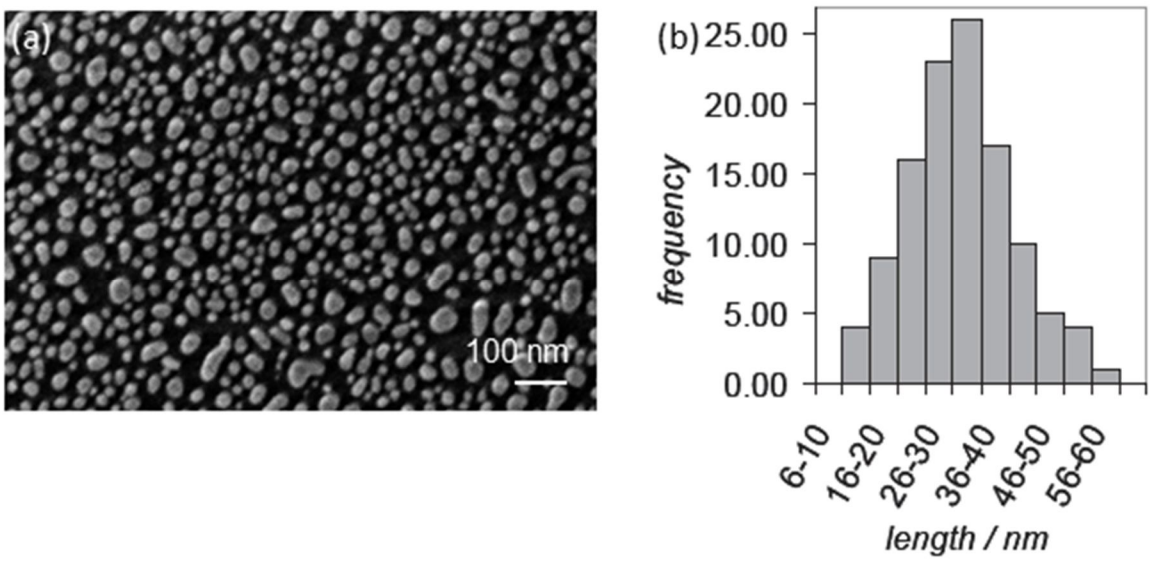

Figure 5.5 (a) SEM image of a glass/AuNPs (4 nm) formed through thermal deposition of a thin metal film on a glass slide after short high temperature annealing (500°C, 1 min) under nitrogen. (b) Histogram of the size distribution of AuNPs.[65]

The AFM images in **Fig 5.6a** reveal the height of these AuNPs to be ~13 nm. After deposition of a-$Si_{0.8}C_{0.2}$:H of various thicknesses, the roughness of the surface is reduced to be ~7 nm, but the topography of the AuNPs is generally preserved (**Fig 5.6b-d**).

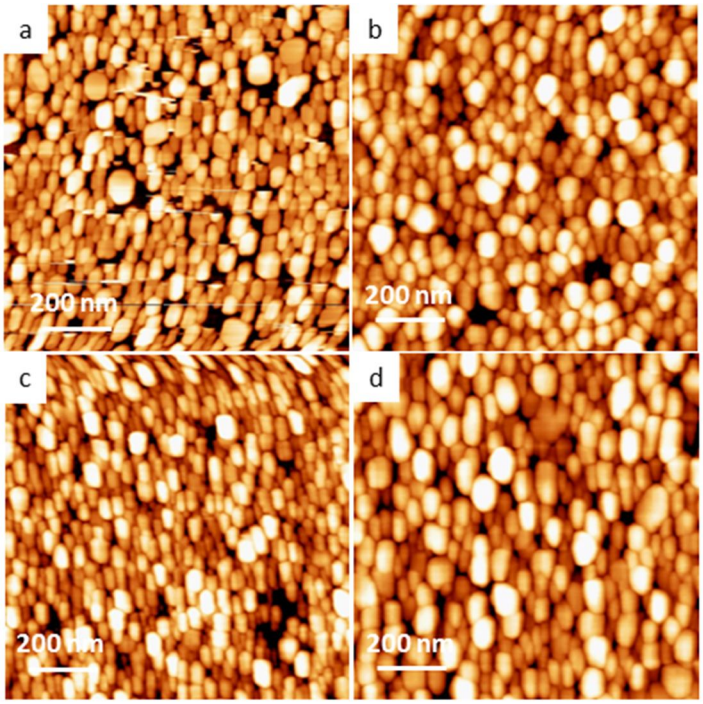

Figure 5.6 AFM images of AuNPs/glass slides before (a) and after deposition of a-$Si_{0.8}C_{0.2}$:H layer of 3 nm (b), 5 nm (c) and 8 nm (d).

The absorbance spectra of the glass/AuNPs before and after coating with *a*-$Si_{0.8}C_{0.2}$:H thin films measured in air are displayed in **Fig 5.7**. Coating the AuNPs with *a*-$Si_{0.8}C_{0.2}$:H results in a significant red shift of the plasmon band from 538 nm (AuNPs only) to 598 nm with an increase in the peak full width at half maximum (FWHM) from 70 nm (AuNPs only) to 124 nm due to the change of the refractive index surrounding the nanoparticles, which becomes more significant as the thickness increases (see **Table 5.2**).

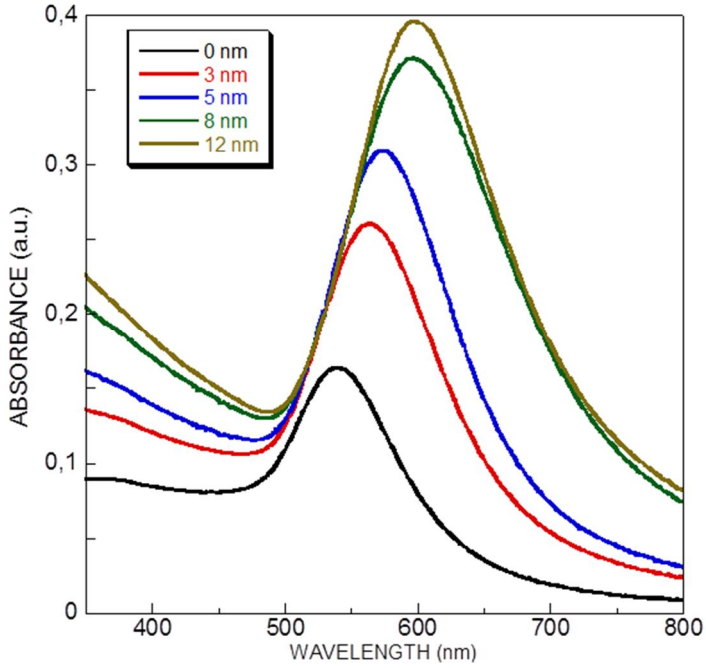

Figure 5.7 UV-Vis absorption spectra of glass/AuNPs coated with a-$Si_{0.8}C_{0.2}$:H of various thicknesses.

thickness of a-$Si_{0.8}C_{0.2}$:H	λ_{max} (nm)	FWHM (nm)
0	538	70
3	561	89
5	572	99
8	595	120
12	598	124

Table 5.2 λ_{max} and FWHM of the absorbance spectra of AuNPs/glass deposited with various thicknesses of a-$Si_{0.8}C_{0.2}$:H.

5.3.2 Optimization of spotting and association

a) Normal microarray architecture on a-$Si_{0.8}C_{0.2}$:H

In a first approach, we chose the same substrate as the one developed by L. Touahir, the 5 nm of *a*-$Si_{0.8}C_{0.2}$:H coated AuNPs glass slides, for the fabrication of glycan microarrays. The functionalization of this LSPR transducer was the same as that of the crystalline silicon, after

hydrogenation in HF vapor, hydrosilylation of undecylenic acid, activation in EDC/NHS and aminolysis of EG_8, the azide termini were formed on the surface. The "click" immobilization of propargyl glycans (mannose and lactose) was performed locally by a pin spotter which allows the deposit of a few nano liter of propargyl glycan solution containing the catalyst ($CuSO_4$ and sodium ascorbate) in buffers on the azide-terminated surfaces. The spotting allowed the formation of an array of round patterns on the surface with a pitch distance of ~0.7 mm. The spotting process was under humidity (~ 50%) and temperature (~20°C) control. After spotting, the slides were kept in a humidity of 75%. The patterns of the microarrays were visualized by a commercial scanner Diagarray.

Since the spotted propargyl glycans were not fluorescently labeled, the success of the "click" reaction was controlled by spotting together a propargyl-derivatized Alexa 647 fluorescent dye (Alexa647, $\lambda_{excitation}$=650 nm and $\lambda_{emission}$=665 nm). **Fig 5.8** shows the pattern of control spots in different buffers and at different concentrations. The best shape or homogeneity of spots appears for 200 µM (the maximum concentration for control molecule) in Phos/T.S (phosphate/tween, sarkosyl) buffer. Therefore, the Phos/T.S buffer was selected as the optimized buffer.

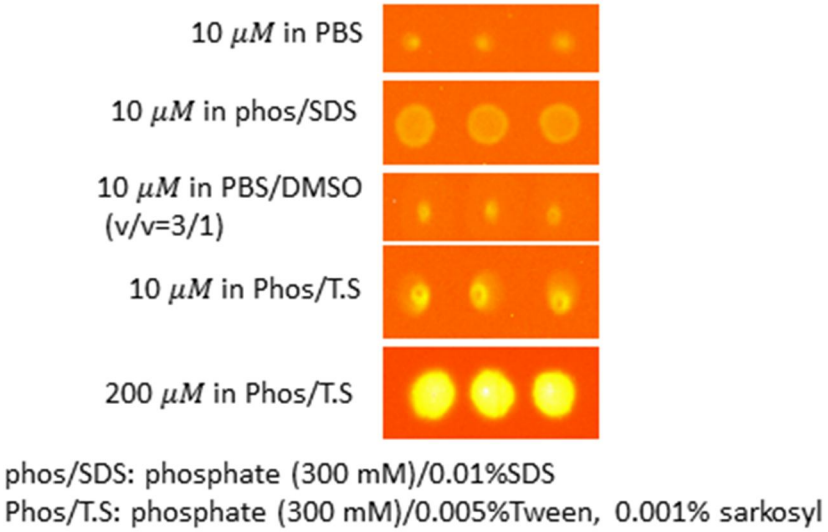

Figure 5.8 Images of control spots from the spotting of a propargyl-derivatized Alexa647 fluorescent dye in different buffers and at different concentrations. The substrate is a N_3-terminatd AuNPs slide with 5 nm of a-$Si_{0.8}C_{0.2}$:H coating.

The spotting of propargyl glycans was performed at a concentration of 3 mM. The propargyl alcohol was also spotted since it has no affinity with any lectins which can be used as the background. The following association of the glycan microarray with Alexa647-linked ConA and PNA was tested to check the specificity. Like for the incubation method in the previous chapters, the surface (containing several spotting zones on one slide) was put in contact with two lectin solutions containing 0.005% Tween20 for the sake of homogenizing the droplet. After 1h, the slide was rinsed by PBS and PBS/0.1% SDS to remove the physisorbed molecules. The images of the resulting spots are displayed in **Fig 5.9**. As expected, the

interaction of bound mannose with ConA results in a clear fluorescence signal, whereas no fluorescent signal is observed from the immobilized lactose spots. However, the incubation with lactose-specific PNA resulted in a significant smudge of the fluorescence background due to uncontrolled non-specific adsorption. In contrast with our previous work where glycan-terminated crystalline silicon surfaces were completely resistant to protein physisorption[177], *a*-$Si_{0.8}C_{0.2}$:H coated interfaces suffer from non-specific adsorption, most likely due to the lower surface density of OEG segments (3.7×10^{13} cm^{-2}, 1/4 of the OEG density on crystalline silicon surfaces). Moreover, a natural defect of *a*-$Si_{0.8}C_{0.2}$:H is the hydrophobic $-CH_3$ exposed on the surface that favors in addition non-specific adsorption of proteins as encountered here.

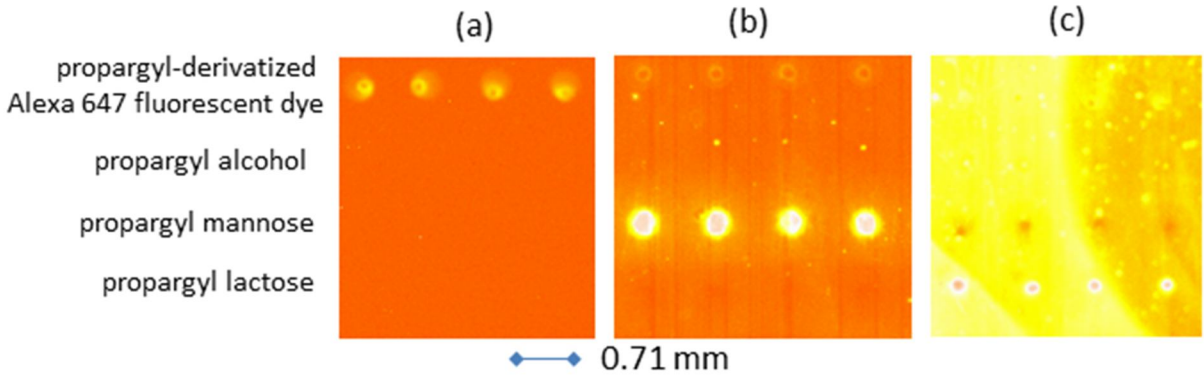

Figure 5.9 Fluorescence images of the spotted array before (a) and after interaction with ConA (0.9 mg/mL) (b) and PNA (0.9 mg/mL) (c) followed by a rinse with 1X PBS/0.1% SDS. The substrate is N_3-terminated AuNPs glass slide coated with 5 nm *a*-$Si_{0.8}C_{0.2}$:H coating.

b) Standard microarray architecture on a-$Si_{0.9}C_{0.1}$:H

In order to decrease the non-specific adsorption, efforts were made to improve the density of OEG chains. In one method, we used the 5 nm of *a*-$Si_{0.9}C_{0.1}$:H as the coating on AuNPs/slide. The OEG density on *a*-$Si_{0.9}C_{0.1}$:H 9.5×10^{13} cm^{-2} is higher than that on *a*-$Si_{0.8}C_{0.2}$:H (see **Table 5.1**). **Fig 5.10** shows the fluorescence images of the microarrays after association. To simultaneously study the "dilution effect" of glycan ligands on such a substrate, the propargyl glycans were diluted in propargyl alcohol at 100 mol%, 30 mol%, 10 mol% and 3 mol% and "spotted" in the same batch. In this experiment, excellent recognition specificity was observed for both ConA and PNA, as well as a clean antifouling background, indicating the importance of immobilizing a minimum number of OEG layers to avoid non-specific adsorption.

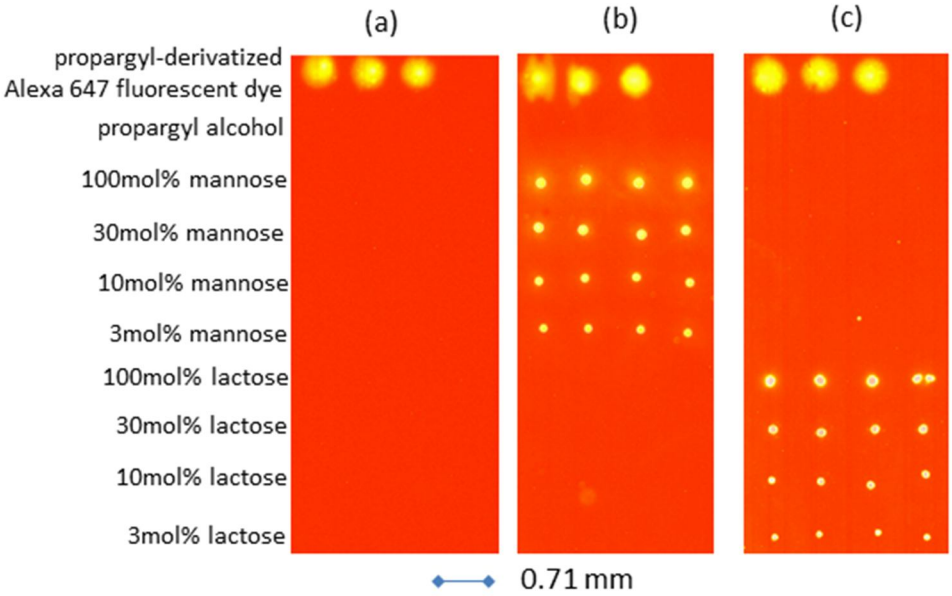

Figure 5.10 Images of the spotting of different molecules before (a) and after the interaction with ConA (0.9 mg/mL, b) and PNA (0.9 mg/mL, c) followed by a rinse of 1X PBS/0.1% SDS. The mannose and lactose are diluted in propargyl alcohol with different molar ratios. The substrate is N_3-terminatd AuNPs/slide with 5 nm of a-$Si_{0.9}C_{0.1}$:H coating.

This slide seems to be a good candidate for a MEF substrate. As can be seen from the LSPR of this substrate in **Fig 5.11**, λ_{max} = 584 nm and FWHM = 110 nm for *a*-$Si_{0.9}C_{0.1}$:H, the layer displayed good optical properties comparable with those of *a*-$Si_{0.8}C_{0.2}$:H (λ_{max} = 572 nm and FWHM = 99 nm), even if the LSPR is more red-shifted and the width is slightly larger. This slide is worth to being further studied to optimize its thickness for the best LSPR-fluorescence coupling. In this thesis, however, we intend to still use the *a*-$Si_{0.8}C_{0.2}$:H thin film to realize the same LSPR-enhanced fluorescence as to be in coherent with the result of L.Touahir.[68]

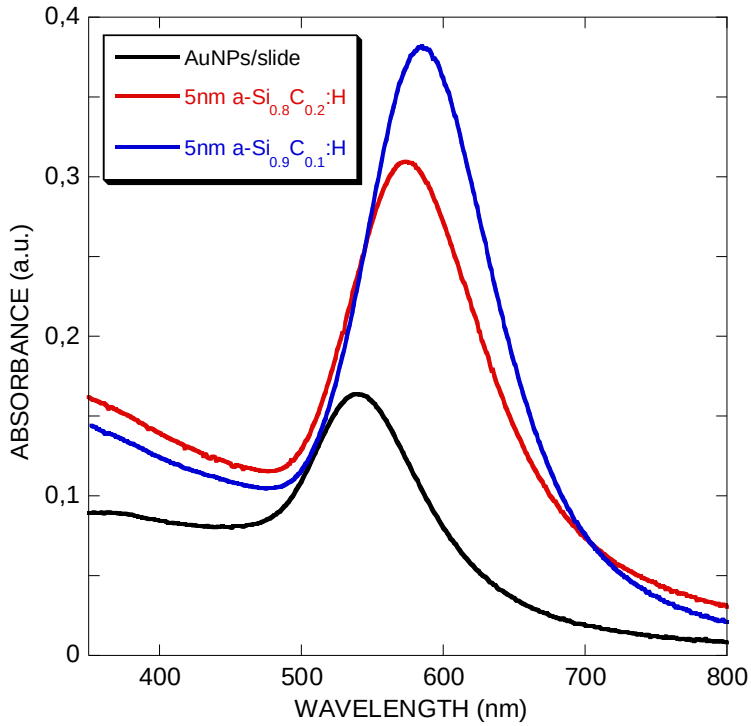

Figure 5.11 UV-Vis absorption spectra of glass/AuNPs coated with 5 nm of a-$Si_{0.8}C_{0.2}$:H and a-$Si_{0.9}C_{0.1}$:H.

c) Modified microarray architecture on a-$Si_{0.8}C_{0.2}$:H

To overcome the low grafting density on *a*-$Si_{0.8}C_{0.2}$:H surfaces, we tried to modify the architecture from the viewpoint of increasing the density of OEG chain. The increasing density of the OEG chain indeed relies on the number of carboxylic acid. Hence, we developed an easy modification scheme for increasing the surface density of acid functions (**Fig 5.12**). After the hydrosilylation of undecylenic acid, the carboxylic acid terminated *a*-$Si_{0.8}C_{0.2}$:H overcoating was first reacted with glutamic acid (Glu) before further reaction with OEG. Firstly, the readily "diluted" density of carboxydecyl chain would not impede the attachment of Glu owing to steric hindrance. As the two acid branches on glutamic acid are sufficiently distant from each other, it is hoped that the successive attachment of OEG is not impeded.

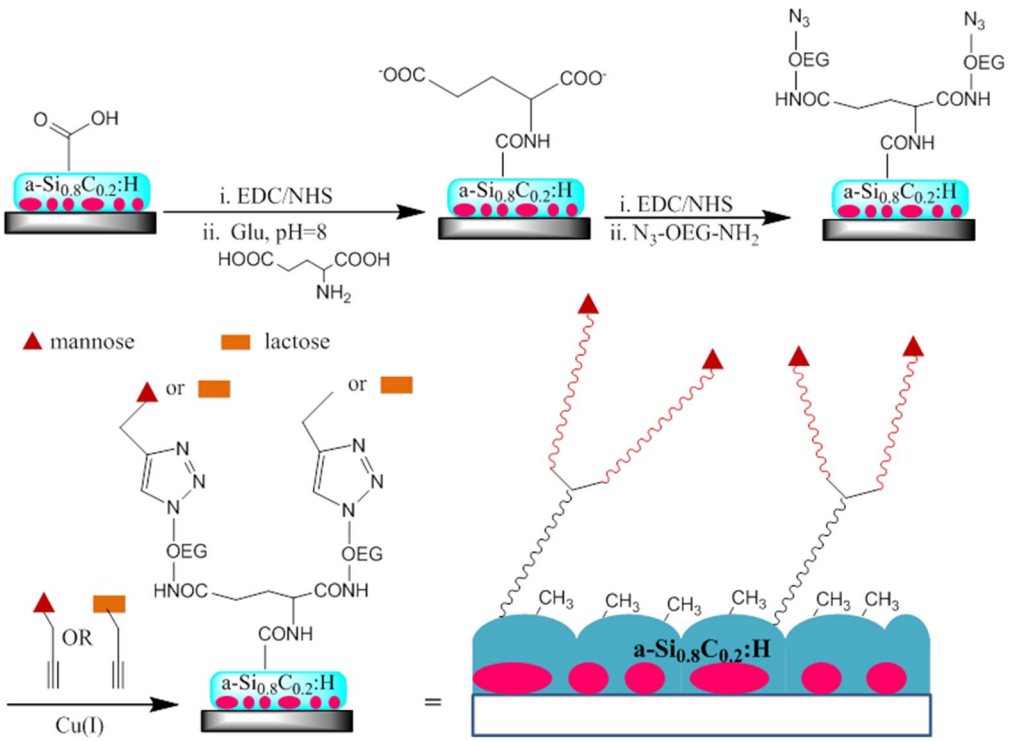

Figure 5.12 Scheme of the formation of dendrimer-like glycosylated monolayer on a-$Si_{0.8}C_{0.2}$:H.

To verify the reliability of this functionalization strategy, the a-$Si_{0.8}C_{0.2}$:H coated crystalline silicon prism was again employed to monitor the modifications by IR-ATR. The resultant IR spectra are shown in **Fig 5.13**. The first step of the modification is the hydrosilylation reaction of hydrogenated *a*-$Si_{0.8}C_{0.2}$:H with undecylenic acid. The IR-ATR spectrum (**Fig. 5.13a**) confirms the success of the grafting of carboxydecyl chains *via* Si-C covalent bonds by the presence of the $\nu_{C=O}$ of the acid function at 1716 cm^{-1} and the two ν_{CH2} of the alkyl chains at 2857 and 2930 cm^{-1}. From a quantitative analysis of the carbonyl band, we obtain a density of acid chains of 7.2×10^{13} cm^{-2} corresponding to about ~1/3 of that grafted on a crystalline silicon surface.[64] In order to increase the surface density of OEG segments and improve the resistance again nonspecific adsorption, we increased the surface density of the acid chains by a two-step amidation process using glutamic acid (Glu). The carboxylic acid terminated *a*-$Si_{0.8}C_{0.2}$:H overcoating was activated with carbodiimide (EDC) in the presence of N-hydroxysuccinimide (NHS) to form NHS-ester function. The IR spectrum clearly shows the three peaks at 1734, 1784 and 1811 cm^{-1} related to the stretching modes of the NHS-ester (**Fig. 5.13b**). The aminolysis reaction with Glu results in the disappearance of the triplet band and the appearance of the amide I vibration band at 1650 cm^{-1} together with a broad carbonyl band related to the acid function of Glu (**Fig. 5.13c**). The quantitative analysis of the activated and amidated surfaces leads to a surface concentration of 5×10^{13} and of 1×10^{14} cm^{-2}, respectively, indicating that the density of acid functional groups further increased by ~ 50% over the initial grafting step. The Glu-terminated monolayer was then modified with the amino-OEG precursor, NH_2-C_2H_4-EG_8-N_3 *via* EDC/NHS coupling to form azide-terminated monolayer. From the IR-ATR spectrum shown in **Fig. 5.13e**, the amidation was evidenced by

the increase of the amide I and II vibration bands. By comparing the peak of initial Glu moiety with that of unreacted acid function, the amidation yield can be assessed, with a value of 60% corresponding to a density of OEG chains of 6×10^{13} cm^{-2}. The final step was clicking propargyl-glycan. The presence of mannosyl units is revealed in **Fig. 5.13f** by the increase in the absorption bands related to the ν_{C-O} and ν_{C-C} at 1030-1130 cm^{-1}. Since the azide density on *a*-$Si_{0.8}C_{0.2}$:H is much lower than that on crystalline silicon surface,[177] there is less steric hindrance among mannoside molecules favoring a "click" yield approaching unity. Therefore, we estimate the density of "clicked" mannoside on *a*-$Si_{0.8}C_{0.2}$:H to be higher than 5×10^{13} cm^{-2}.

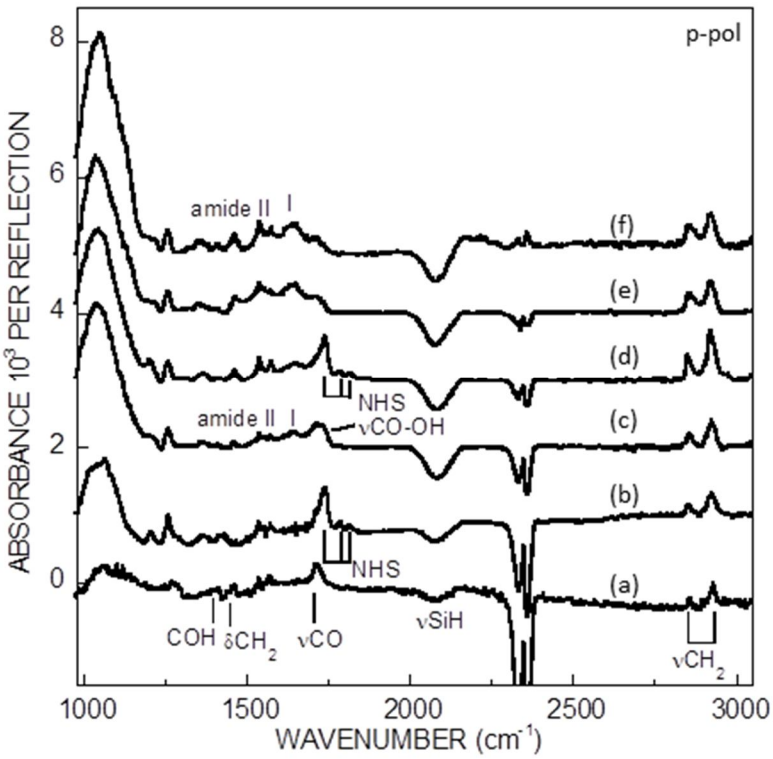

Figure 5.13 IR-ATR spectra in p-polarization of acid- (a), NHS ester- (b), Glu- (c), second NHS-ester- (d), N_3- (e) and mannose-terminated surfaces on a-$Si_{0.8}C_{0.2}$:H layer, the reference being the a-SiH_x surface.

The effect of the modified functionalization on a-$Si_{0.8}C_{0.2}$:H is manifested in **Fig. 5.14**. As can be seen, the fluorescence background is significantly improved for both ConA and PNA. In addition, the spotting scheme here also shows that the glycan density can be controlled at will by mixing propargyl alcohol in different amounts with glycans. **Fig. 5.14d** depicts the obtained fluorescence intensity using different glycan densities. For both lectins, the binding intensity of lectins is optimum for the 100 mol% glycan surfaces. However, the binding efficiency is affected by the surface glycan concentrations. The binding response of PNA is less sensitive from 30 to 3 mol% lactose concentration with an equivalent efficiency level whereas the binding response of ConA decreases with the mannose density. This phenomenon can be related to the efficiency of the multivalent binding.[11, 40, 222] On crystalline silicon, we demonstrated that the optimum conditions for multivalent interactions is a compromise on the

surface concentration of glycan ligands in terms of density and spacing.[223] This effect gives rise to a maximum efficiency in the concentration range 3-9×10^{13} cm^{-2} for bivalent interaction of mannose with *Lens culinaris* lectin (LENS). Such an order of magnitude is consistent with the behavior recorded here for ConA which exhibits a similar dimeric structure to that of LENS.

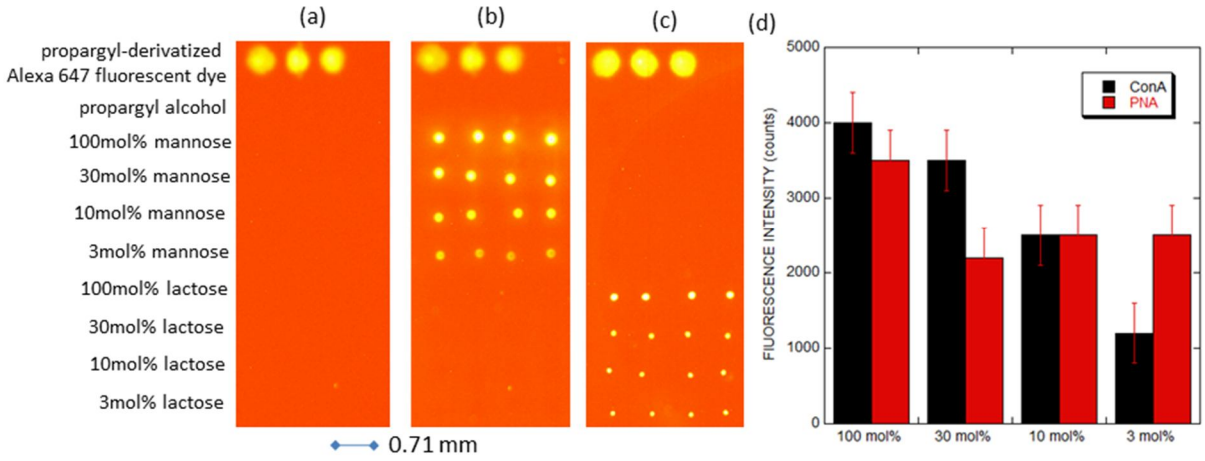

Figure 5.14 Images of the spotting of different molecules before (a) and after the interaction with *ConA* (0.9 mg/mL, b) and *PNA* (0.9 mg/mL, c) followed by a rinse of 1X PBS/0.1% SDS. The mannose and lactose are diluted in propargyl alcohol with various molar ratios. The substrate is N_3-terminatd AuNPs/slide with 5 nm of a-$Si_{0.8}C_{0.2}$:H coating obtained from the **scheme 5.12**. The fluorescent exposure time was 2 s. Measured fluorescence intensity of *ConA* and *PNA* for different diluted glycan spots (d).

5.3.3 Optimization of sensitivity

The enhancement of the fluorescence signal of a given fluorophore (in our case Alexa 647 with $\lambda_{excitation}$= 650 nm and $\lambda_{emission}$ = 665 nm) by the LSPR transducer strongly depends on the distance of metal-fluorophore as well as on the position of the plasmonic band which has to match the $\lambda_{excitation/emission}$ of fluorophore. To optimize this response, *a*-$Si_{0.8}C_{0.2}$:H coatings of varying thicknesses were deposited on AuNPs/glass substrates and the enhancement factor was evaluated by comparing with *a*-$Si_{0.8}C_{0.2}$:H interfaces deposited directly on bare glass slide (without AuNPs).

The fluorescence intensity on *a*-$Si_{0.8}C_{0.2}$:H coated bare slide is an oscillatory function of the *a*-$Si_{0.8}C_{0.2}$:H thickness (**Fig 5.15**).[68, 70] The maximum fluorescence from the constructive wave appears at a thickness of the integral multiple of $\lambda/2n$, where λ is the absorption/emission wavelength of the fluorophore and n is the refractive index of the *a*-$Si_{0.8}C_{0.2}$:H (n=2.63). For

example, the first maximum occurs at a coating of 124 nm, optically equivalent to the bare slide without any coating.

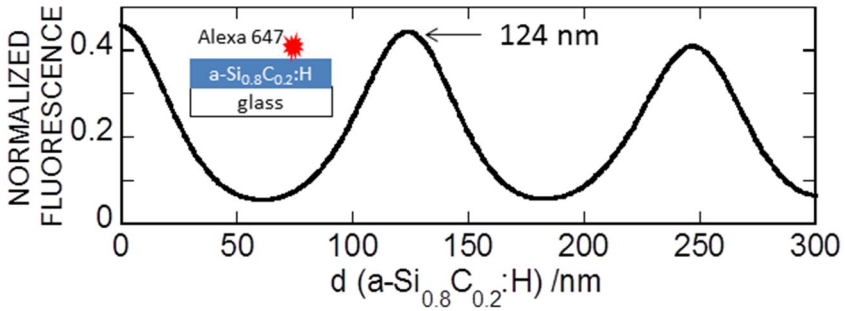

Figure 5.15 Calculated fluorescence intensity of Alexa 647 as function of the thickness of a-$Si_{0.8}C_{0.2}$:H on bare slide.

Fig 5.16 shows the signals of "control" molecules on different slides. On the AuNPs/slide, the optimum signal is achieved at 3 nm of a-$Si_{0.8}C_{0.2}$:H and the fluorescence intensity decreases progressively with the increasing thickness. Compared to the bare slide, the fluorescence intensity was observed to be enhanced by a factor of 7.

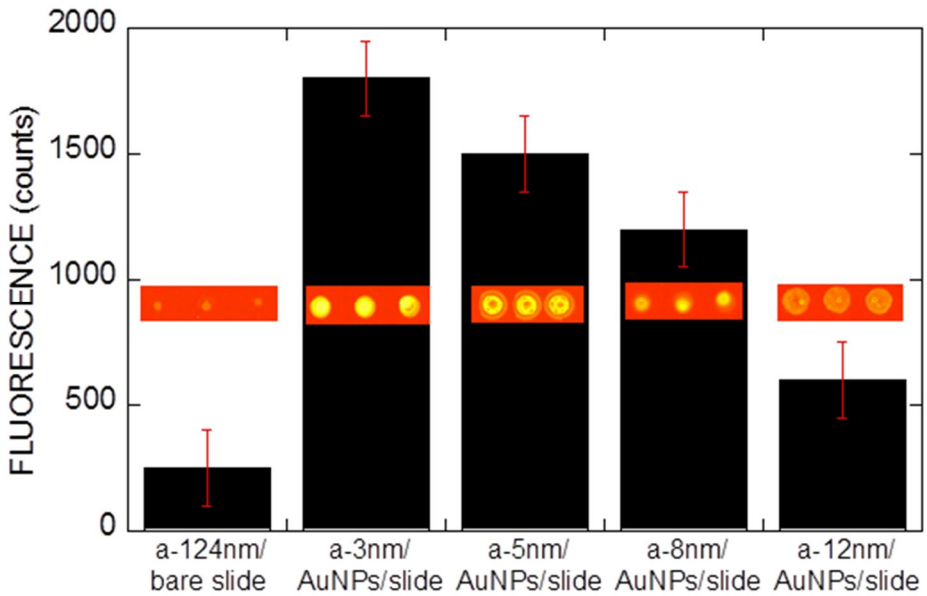

Figure 5.16 Histogram of comparison of fluorescence intensities of the "control" spot on different substrates and corresponding images. The fluorescence exposure time was 2 s.

Furthermore, **Fig 5.17** shows the signal of lectin-treated slides. The specific lectin bound spots on different structures exhibit the highest fluorescence signal with a 3 nm-thick *a*-$Si_{0.8}C_{0.2}$:H layer. This intensity is 10 times larger than that recorded on *a*-$Si_{0.8}C_{0.2}$:H structures (124 nm) for ConA on mannose spots and PNA on lactose spots.

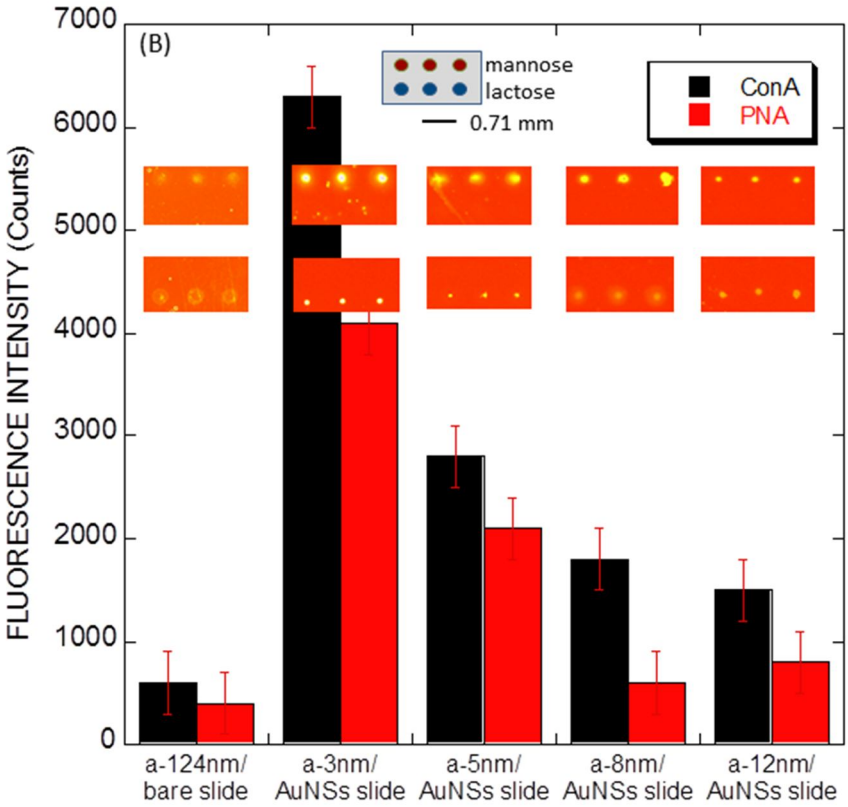

Figure 5.17 Histogram of fluorescence intensity of spotted mannose and lactose arrays after interaction with ConA and PNA (90 µg/mL) followed by a rinse of PBS/0.1% SDS on different substrates. The fluorescence exposure time was 2 s.

Based on the experimental results, the distance of metal-fluorophore can be estimated with following considerations. The thickness of carboxydecyl chain was reported to be ~1.2 nm[224], the length of OEG chain is 2.5 nm (2.74 Å for each ethylene glycol unit in case of a helical conformation)[132] and the distance from the triazole to the terminal hydroxyl group of mannose is ~0.8 nm, the total thickness of the functionalized monolayer is estimated roughly to be 4.5 nm. Accounting for the 3 nm of amorphous layer, the actual distance from the fluorophore to the AuNPs is ~7.5 nm, depending on the position of the dye molecule labeling the protein. From the dimension of ConA (7×7×5 nm) and PNA (6.5×6.5×3.7 nm), we are able to estimate that this distance is around 10 nm, which is in coherence with the theoretical optimal coupling distance,[165] even though the LSPR position of the 3 nm coating (561 nm) is somehow far from the excitation wavelength of the fluorophore (650 nm). The best overlap between the excitation wavelength of the dye and the LSPR interface is that at 12 nm, however, the overlarge FWHM and the large distance of fluorophore-AuNPs which seems to be out of the MEF enhancement window could explain its less efficient LSPR coupling effect.

The sensitivity of this protein biosensor can be alternatively expressed by the limit of detection (LOD). **Fig 5.18** shows the diagram of fluorescence intensity of the microarray interacted with various concentrations of ConA and PNA. The lowest distinguished level is

4.5 ng/mL for ConA and 90 ng/mL for PNA. By converting to the molar concentration, the detectable limit is 37.5 pM for ConA (Mw=120 kDa) and 870 pM for PNA (Mw=103 kDa), indicating that the LOD is in the medium or upper part of the picomolar range. The lower sensitivity of PNA might be derived from that the employed PNA carries only 2 dyes per molecule, while ConA has 3 dyes per molecule. The picomolar LOD of ConA-mannose binding is currently one of the lowest reported, comparable with the picomolar level for fluorescence microarrays,[46] as seen from the summary of some recently reported protein sensors (**Table 5.3**). Detection limits of ConA-mannose binding followed by quartz crystal microbalance was reported to be ~1.3 nM,[13, 17, 18] SPR (~1.5 nM)[6, 11, 26] and cantilever deflection (~9.6 nM),[225] or electrochemical ways such as voltammetry (7 nM)[19] and impedance spectroscopy (5 nM).[20] The appreciable sensitivity of the MEF-based carbohydrate arrays suggests a the promising applicability in protein assays.

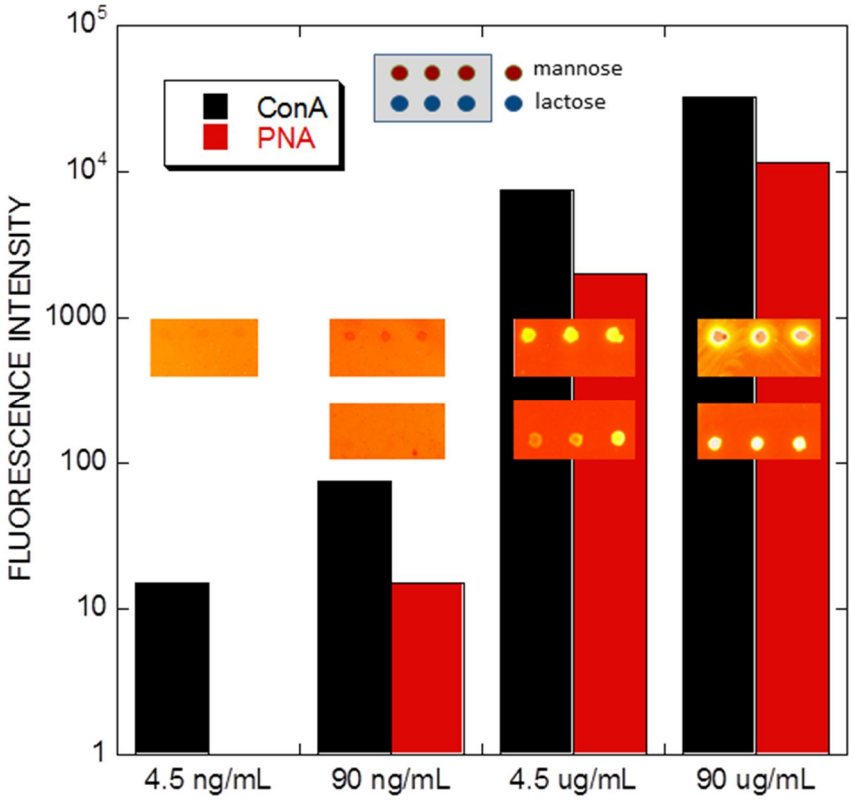

Figure 5.18 Histogram of fluorescence intensity of spotted mannose and lactose on a 3 nm thick *a*-$Si_{0.8}C_{0.2}$:H/ Au NSs arrays after interaction with ConA and PNA at various concentrations followed by a rinse of PBS. The fluorescence exposure time was 5 s. The background signal level is ~100.

Techniques	Binding types	K_d (μM)	LOD	Authors
E-SPR	PNA-lactosyl	0.45	41nM	Gondran[6]
	maackia amurensis Lectin-sialyllactosyl	0.47	83nM	
SPR	*Stromal cell-derived factor* 1α-oligosachoride		20nM	Mercey[26]
SPR imaging	ConA-mannose	0.18	3.5nM	Smith[11]
	Jacqulin-galactose	0.045	1.5nM	
SPR imaging	*ConA*-maltoheptaose		83nM	Wang[27]
QCM	ConA-mannose	0.224	130pM	Lyu[13]
QCM	ConA-mannose	1.15	90nM	Zhang[17]
QCM	Anti-Gal-galactose	0.0036	1.3nM	Zhang[18]
Colorimetry	ConA-mannose		190nM	Hone[226]
Voltametry	ConA-mannose		7nM	Sugawara[19]
Impedence spectroscopy	LENS-mannose	0.38	5nM	Szunerits[20]
Cantilever array sensor	ConA-mannose	15.3	9.6nM	Gruber[225]
	cyanovirin-N-trimannose	1.06	91pM	
Fluorescence mircroarray	ConA-mannose		9.6nM	Park[30]
Fluorescence mircroarray	ConA-mannose	0.08	25nM	Liang[29]
Fluorescence mircroarray	ConA-mannose		67pM	Zhou[46]
	E. Crystagalli -galactose		2.8nM	
Field-effect transistor	*PA-IL* Lectin-galactose	6.8	2nM	Vedala[21]
Field-effect transistor	*E. Crystagalli* -galactose		1.75fM	Zhang[22]

Table 5.3 Summary of LOD of some recently reported sensors for the detection of glycan-protein binding.

5.4 Application of the microarrays in protein assay

5.4.1 Thermodynamic binding assay

The binding assay was performed on one slide consisting of ten replicate zones, which allows incubating ten different concentrations of lectin solution at the same time. The resultant binding curve as shown in **Fig 5.19** can be fitted by the Langmuir model, giving the K_d value of 0.23 µM for mannose-ConA binding and 0.89 µM for lactose-PNA binding. In order to understand the multivalency of the bindings, we also studied the binding assay of the diluted surface glycan concentrations as we performed in **Fig 5.14**. **Table 5.4** lists the obtained K_d values. The order of K_d at the level of µM indicates that these bindings are plausibly multivalent, even when the surface glycan concentration is diluted. As we know that both ConA and PNA are tetrameric proteins, so the bindings on the surface could be at least a bivalent interaction.

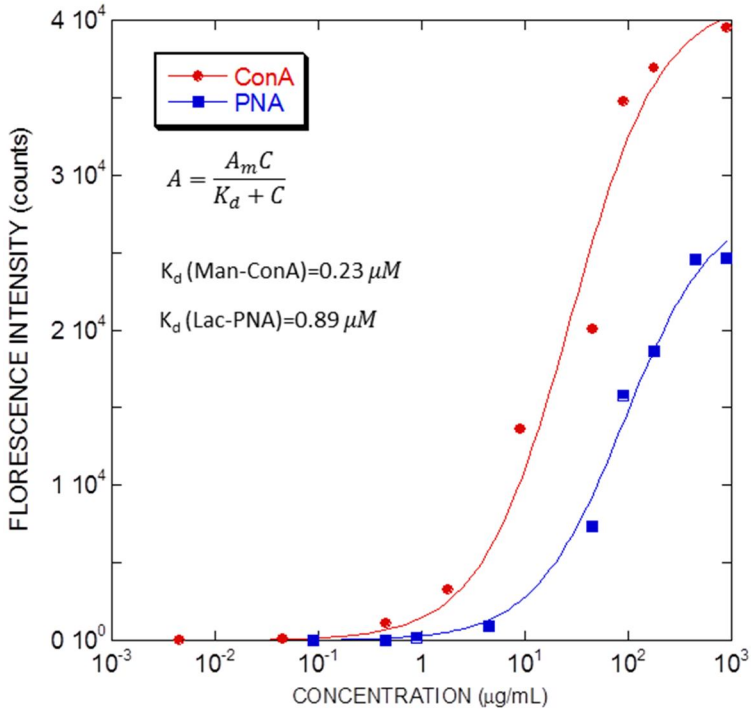

Figure 5.19 Binding isotherm of mannose-ConA and lactose-PNA measured by the 3 nm thick *a*-$Si_{0.8}C_{0.2}$:H/ Au NSs microarray. The fluorescence exposure time was 5 s. The data are fitted to the Langmuir model.

Spot types	K_d of mannose-ConA (μM)	Spot types	K_d of lactose-PNA (μM)
100% mannose	0.23	100% lactose	0.89
50% mannose	0.45	25% lactose	1.11
10% mannose	0.81	5% lactose	1.63
2% mannose	0.61	1% lactose	2.33

Table 5.4 Summary of the binding K_d values for diluted surface glycan concentrations.

5.4.2 Kinetic binding assay

The kinetic binding assay is similar to SPR assay that allows the *in-situ* readout of the binding events and their dissociation. The glycan-immobilized slide was fixed in an *in-situ* catridge where the solution of lectin is injected to be in contact with the slide in a static fluid configuration. The fluorescence microscopy records the image of spots at set time interval. **Fig 5.20** shows the images of the microarray before and after the interaction with lectin solution. The data was treated by a microarray software and a kinetic binding curve was obtained. The injection of lectin results in an exponential increase of binding and the successive rinse aims to remove those unbound lectins by 0.1% SDS, finally the specific binding is observed. This binding curve has a similar shape as the SPR sensorgram, therefore it is interesting to use the analogous treatment to obtain k_{on} and k_{off} using Langmuir equations. However, for the moment we did not achieve reasonable fittings to those data, probably because the multivalent interactions of protein with the surface are more complicated than Langmuir model. Moreover, the *in-situ* readout is in static condition instead of the fluidic condition as in case of SPR, it is likely that a mass transition process is accompanied with the binding. If the data processing problem can be overcome, the real-time measurement will make the MEF-sensor be a powerful tool for further analysis.

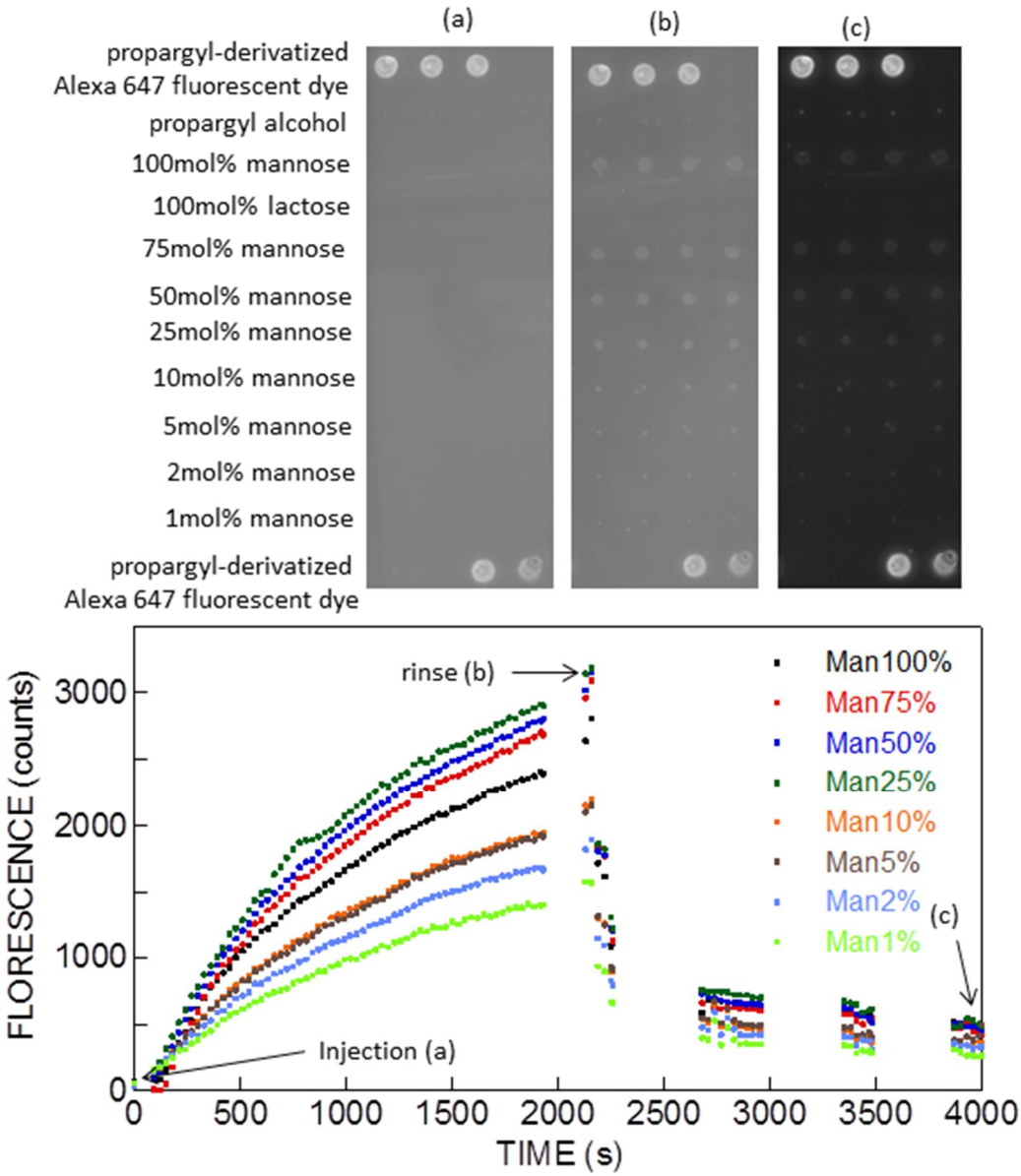

Figure 5.20 Real-time fluorescence imaging of the binding assays performed in an *in-situ* catridge: images of the spotted array before the injection of ConA (450 ng/mL) (a), at the beginning of the rinse in 1X PBS/0.1% SDS (b) and at the end of rinse (c). The kinetic diagram of the florescence intensity is plotted in the bottom frame as a function of time.

5.5 Conclusion

In this chapter we take advantage of AuNPs on a glass slide as the substrate to develop a glycan microarrays using metal-enhanced fluorescence. The AuNPs/glass substrate is coated with an a-$Si_{0.8}C_{0.2}$:H thin layer, which undergoes the multi-step modification processes to immobilize glycan molecules *via* a spotting approach. The success of the functionalization is confirmed on a-$Si_{0.8}C_{0.2}$:H coated crystalline silicon by IR-ATR. The prepared glycan microarrays allow for probing many glycan-protein interactions in a high throughput manner. To avoid the unwanted physisorption during the association of glycan-protein interaction, two ways were envisaged: in one, the functionalization on a-$Si_{0.9}C_{0.1}$:H coating is more efficient in terms of antifouling property; in another, on a-$Si_{0.8}C_{0.2}$:H coating, a two-step amidation protocol leads to the improvement of the density of OEG chains. Moreover, the enhancement effect of the LSPR-fluorescence coupling in terms of coating thickness was optimized. It was found that coating a 3 nm thick a-$Si_{0.8}C_{0.2}$:H thin film onto the AuNPs lead to an enhancement of ~13 times for the binding to specific lectins compared with non-AuNPs embedded bare slides. The detection limit was found to be in picomolar range. This sensitive glycan microarray can be used as an efficient tool to study thermodynamic and kinetic protein binding assays.

5.6 Experimental section

5.6.1 Molecules, proteins and substrates

Alexa Fluor 647 (quantum yield=0.33) labeled *concanavalin A* (ConA), *peanut agglutinin* (PNA), and NHS-conjugated Alexa Fluor 647 dye were purchased from Lifetechnologies. The glass slides (75×25 mm) were from Genewave.

Propargyl-conjugated fluorescent witness labels were prepared by adding 1 μL of propargyl amine (77 mM in DMF) solution into 10 μL of NHS-conjugated Alexa 647 molecule (10 mg/mL in DMF). The as-synthesized dye was stored in a freezer and was directly used without further purification.

5.6.2 Preparation of glass substrates

Preparation of glass substrates covered with gold nanostructures (glass/Au NSs) Glass slides (75×25×1 mm^3) were first cleaned in ethanol and piranha solution at room temperature, rinsed copiously with Milli-Q water and dried under a stream of nitrogen. The clean substrates were then transferred into an evaporation chamber. Metal nanostructures deposition was carried out by thermal evaporation of a few nm thick metal films (e. g., 4 nm thick for gold) using a MEB 550 S evaporation machine (Plassys, France). Post-deposition annealing of the metal-covered slides was carried out at 500°C for 1 min under nitrogen atmosphere using a rapid thermal annealer (Jipelec Jet First 100) leading to circular shaped dense nanostructures on glass. The reproducibility of the metal evaporation was evaluated by measuring the LSPR signals of a batch of 8 samples. The standard deviation in the wavelength (λ_{max}) and maximum absorption (I_{max}) is typically 2 nm and 0.02 abs units, respectively.

Deposition of amorphous silicon-carbon alloy. Amorphous silicon–carbon alloy layers were deposited onto glass using plasma-enhanced chemical vapor deposition (PECVD) in a “low-power” regime. Pressure = 35 mTorr, temperature = 250°C, power density = 0.06 W cm^{-2}, gas flow rate = 20 sccm (standard cubic centimeter per minute). By varying the methane ratio in the gas mixture $[CH_4]/([SiH_4]+[CH_4])$, the final carbon content in the material and thus the optical properties can be adjusted. For the deposition of a thin film of *a*-$Si_{0.8}C_{0.2}$:H, a methane/silane ratio of 6.2/69.7 was used; for *a*-$Si_{0.9}C_{0.1}$:H, methane/silane ratio is 13.3/51.1 and for *a*-Si:H, no methane is added. The layer thickness was adjusted by controlling the deposition time (typically 15 s for a 5 nm thick film).

5.6.3 Functionalization of substrates

Formation of carboxydecyl-terminated surfaces The *a*-$Si_{0.8}C_{0.2}$:H coated AuNPs/glass slide was exposed in HF vapour for 15s[70] before placing in a degassed Schlenk tube containing neat undecylenic acid solution and irradiated at 312 nm (6 mW cm^{-2}) for 3 h. The excess of unreacted and physisorbed reagent was removed by a final rinse in hot acetic acid (75°C) for 40 min.[63] Then, the sample was dried under nitrogen flow.

Formation of NHS ester-terminated surfaces The acid-terminated surface was immersed in 60 mL of an aqueous solution of NHS (5 mM) and EDC (5 mM) and allowed to react for 90 min at 15 °C.[110] The resulting surface was copiously rinsed with Milli-Q water and dried under a stream of argon.

Formation of glutamic acid-terminated surfaces The NHS ester-activated surface was reacted with 20 mM of glutamic acid (Glu) in 1X PBS at pH ~ 8 for 3h at room temperature. The resulting surface was rinsed with 1X PBS/0.1% SDS for 10 min and copiously with Milli-Q water. The Glu-terminated surface was dried under a stream of argon. For further amidation with $NH_2{-}C_2H_4{-}OEG{-}N_3$, the interface was undergoing a second activation step to generate the NHS ester-terminated surfaces.

Formation of azido-terminated surfaces The NHS-activated surface was reacted with 20 mM of $NH_2{-}C_2H_4{-}OEG{-}N_3$ in 1X PBS at pH ~ 8 for 4h at room temperature. The resulting surface was copiously rinsed with 1X PBS, followed by a surfactinated rinse (1X PBS/0.1% SDS for 15 min; 0.2X PBS for 5 min; 0.1X PBS for 5 min) and finally with Milli-Q water.[134, 177] The azido-OEG surface was dried under a stream of argon.

Spotting of glycans on glass substrates. A mixture of the respective alkynyl-glycan (16 μL, 3 mM in water), sodium ascorbate (1.43 μL, 15 mol%) and $CuSO_4$ (1.2 μL 5mol%) in buffer (13.37 μ L) was spotted onto the LSPR interface. A spotting robot from Biorobotics MicroGrid II was used and the process was performed under controlled humidity (~50%) and temperature (~20°C).

The spotting buffers are either phosphate (0.3mM)/0.01% Tween20, 0.002% sarkosyl (Phos/T.S) or phosphate (0.3mM)/0.02% SDS (Phos/SDS). The interfaces were stored in a dessicator overnight at controlled humidity (~50%), then rinsed in 1X PBS/0.1%SDS for 10 min and then Milli-Q water to remove physisorption and dried in a stream of N_2.

The spotting of the propargyl-conjugated dye molecules was achieved using propargyl-conjugated Alexa 647 (0.5 µL, 7.7mM), sodium ascorbate (5.7 μL, 101μM), $CuSO_4$ (4.8 μL, 40μM) and 8.3 μL of buffer. Different mixtures of propargyl glycans diluted in propargyl

alcohol at 30, 10 and 3 mol% were spotted in the same conditions, the total concentration of propargyl functions being kept at 3 mM.

5.6.4 Interaction with lectins

The glycan array is incubated in Alexa 647-labeled PNA or ConA solutions in 1X PBS at various concentrations containing 0.005% Tween20 for 1 h in a locked hybridization chamber. The cover slide was removed with 1X PBS and the array was thereafter washed with 1X PBS/0.1% SDS (10 min), 0.2X PBS (2 min) and 0.1X PBS (2 min) and finally with deionized water before dried under a stream of argon prior to analysis.

For the isotherm construction, the spotting of ten replicate zones was performed on the same slide. Each replicate zone contains labeled control spots as an internal reference to eliminate local inhomogeneities on the slide. A first incubation of ConA was performed simultaneously at 10 concentrations, followed by a second incubation of PNA at the same concentrations.

General conclusion

In this thesis, we developed a step-by-step functionalization protocol on hydrogenated silicon surfaces to immobilize glycan molecules for the study of the multivalent protein-glycan interactions.

In a first approach, the crystalline silicon was used as the substrate to optimize the functionalization process. We designed a multistep modification strategy starting from the well-defined carboxydecyl-terminated monolayer. After amidation of an azido-functionalized oligo(ethylene glycol) linker, followed by a “click” conjugation with alkynyl-derivatized glycans, the glycan-terminated monolayer was built up. We used the quantitative IR-ATR to carefully characterize each modification step, demonstrating that the employed functionalization protocol was highly efficient to provide a dense glycan-terminated monolayer. Moreover, the surface morphology of the glycan-terminated monolayer was perfectly controlled by AFM, confirming that the grafted chains maintained a homogenous form at atomic level.

Then, the as-fabricated glycan-terminated monolayers were used for the study of their interactions with non-specific and specific lectins by IR-ATR and AFM. The non-specific protein adsorption can be completely avoided by tuning the length of the intercalated OEG chains. A long enough OEG chain (at least 8 ethylene glycol units) was proven to be mandatory for a good antifouling property. Moreover, the combination of a surfactinated rinse helped to get rid of the protein-protein interaction. In case of the specific bindings, the compact glycan-terminated monolayer showed good selectivity with their corresponding lectins.

Further, we investigated the binding efficiency with the surface glycan concentration. By diluting the surface glycans with smaller spacer molecules during the “click” process, the density of the diluted glycan surface, determined by IR-ATR, showed that the diluted glycan monolayers are richer in glycan than the mixture solution. The binding efficiency was observed by IR-ATR and AFM and was found to be enhanced in a properly diluted glycan-terminated surface (10 mol%). The association constant of the surface mannose with specific lectins were measured at a value around 10^5 M^{-1}, indicating the presence of multivalent binding.

In order to understand the multivalent bindings from a quantitative assessment, we developed a quantification method using IR-ATR for the first time to determine the number of proteins bound to the surface. The calculated protein density was correlated with corresponding AFM images and showed a good agreement. The obtained quantity of the proteins on the surface explained well the existence of protein-protein interaction. In addition, for specific interactions, these data lead us to obtain the ratio of probe-target which provided a direct addressing about how the multivalent proceeds on the surface and demonstrated that the density of surface glycans is crucial for multivalent binding: large enough for providing

sufficient binding space, and small enough for enabling multivalent adsorption. The experimental findings were later supported by numerical simulations.

In a second approach, we developed a glycan microarray using metal-enhanced fluorescence based on thin film of amorphous silicon-carbon alloy coated on gold nanoparticles. The alkynyl glycans were directly “clicked” on the azide-functionalized substrate using a pin spotter. The as-prepared glycan microarray showed good protein selectivity with the minimization of non-specific adsorption. The use of gold nanoparticles gave access to the LSPR coupled fluorescence. The sensitivity of the fluorescence measurement was found to be enhanced ~ 13 times as compared with non-gold embedded slides. The limit of detection read in the picomolar range which was currently one of the most sensitive glycan chips. The high sensitivity of this glycan microarray made it a promising tool for reading out isothermal and real-time binding data.

The observation of multivalent protein-glycan interactions established on perfect crystalline silicon offers quantitative and visualized insights into how the multivalent binding proceeds on atomically arrayed glycan epitopes. Besides, the success of the fabrication of ultrasensitive glycan microarrays is also of high practical interest to realize fast and real-time detection of protein-glycan interactions.

For the future studies, improvements can be sought for on two aspects. Firstly, the crystalline silicon is useful to study more complicated multivalent binding behaviors related with the lectin structures, such as the monovalent FimH, pyramide-like tetrameric ConA and square-like tetrameric PA-IL,… Secondly, it would be interesting to extend the MEF glycan microarray technique to studies closer to biological needs. One of the ideas is to click the mannosylated HCV virus envelope on the microarray and study the binding capacity with different lectins, including ConA, Cyanovirin-N. By taking advantage of the high sensitivity and high throughput of the MEF microarray, it is hoped to realize a fast screening of suitable lectins against HCV virus, which would help future exploration of vaccines to cure infection diseases.

List of abbreviations

AFM ····· atomic force microscopy

BSA ····· *bovine serum albumin*

ConA ····· *concanavalin A*

CuAAC ····· copper(I)-catalyzed azide-alkyne cycloaddition

EDC ····· ethyl(dimethylaminopropyl) carbodiimide

FFG ····· Frumkin-Fowler-Geggenheim

IR-ATR ····· infrared spectroscopy in attenuated total reflection geometry

Lac ····· β-propargyl lactoside

LacOAc ····· Per-O- acetyl β-propargyl lactoside

LENS ····· *lens culinaris* Lectin

LSPR ····· localized surface plasmon resonance

Man ····· α-propargyl mannoside

ManOAc ····· Per-O-acetyl α-propargyl mannoside

MEF ····· metal-enhanced fluorescence

NHS ····· *N*-hydroxysuccinimide

OEO ····· oligo(ethylene oxide)

OEG ····· oligo(ethylene glycol)

PECVD ····· plasma-enhanced chemical vaper deposition

PEG ····· poly(ethylene glycol)

PNA ····· *peanut agglutinin* Lectin

PSA ····· phenol-sulfuric acid assay

SAM ····· self-assembled monolayers

SPR ····· surface plasmon resonance

XPS ····· X-ray photoelectron spectroscopy

ANNEX

I. Atomic force microscopy

The atomic force microscopy (AFM) is a technique to image surface morphology and structures of a wide variety of samples at the nanometre resolution. The principle of AFM is to measure the different interaction forces between a tip fixed at the end of a cantilever and the material surface, including mechanical contact force, Van der Waals forces, capillary forces, chemical bonding, electrostatic forces and magnetic forces. The curvature of the cantilever is followed by positioning a laser beam on the superior face of the cantilever which is deflected and captured by a photodetector. To avoid the surface damage caused by the tip colliding with the surface if the tip is scanned at a constant height, a feedback mechanism is employed to adjust the tip-to-sample distance to maintain a constant force between the tip and the sample. The tip or sample is mounted on a 'tripod' of three piezo crystals, with each responsible for scanning in the x,y and z directions. The scanning on x and y directions moves from nanometer to some micrometer ranges but the minimum lateral resolution is restricted by the size of tips. The sensibility in z direction can reach angstrom level.

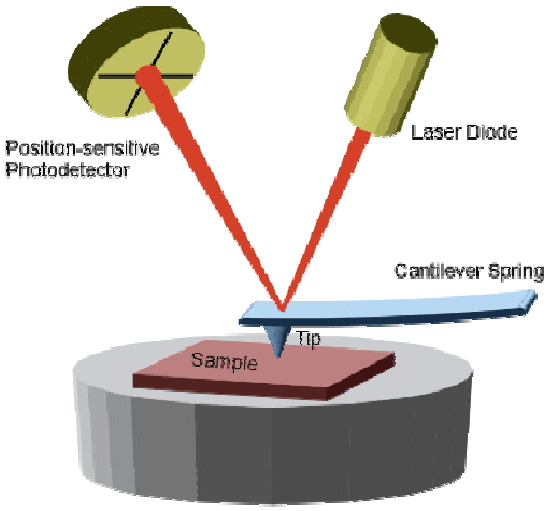

Figure I.1 Scheme for the operation mechanism of AFM.

The AFM can be operated in three main modes: contact mode, non-contact and tapping modes.

In contact mode, the tip is "dragged" across the surface of the sample and the contours of the surface are measured using the feedback signal required to keep the cantilever at a constant force. Because the measurement of a static signal is prone to noise and drift, low stiffness

cantilevers are used to boost the deflection signal. A large contact force is risky to damage the probed objects. In our work, the visualization of protein covered surface used a relatively large force to wipe out these soft biomolecules so as to provide a contrast with the material surface.

In tapping mode, the cantilever is driven to oscillate up and down near its resonance frequency by a small piezoelectric element mounted in the AFM tip holder. When the tip comes close to the surface, the amplitude of the oscillation of cantilevers is around several nanometers and driven by the interaction of surface with the tip, such as Van der Waals forces, dipole-dipole interactions, electrostatic forces, etc. An “electronic servo” using the piezoelectric actuator adjusts the height of the cantilever to maintain the oscillation amplitude at set values. A tapping AFM image is therefore produced by imaging the force of the intermittent contacts of the tip with the sample surface. This tapping mode lessens the damage done to the surface compared to that in contact mode and the employed tip can be stiffer and sharper so a higher resolution than contact mode can be achieved.

In this thesis, CM-AFM images were obtained using a Pico SPM microscope (Molecular Imaging, Phoenix, AZ) in contact mode, with silicon nitride cantilevers (Nanoprobe, spring constant = 0.12 Nm^{-1}) under a N_2 atmosphere. A force of 0.38 nN was applied for imaging the glycan-modified surfaces whereas a smaller one (0.15 nN) was applied for imaging the lectin-glycan interactions.

The TM-AFM images are obtained with the Multimode 5100 AFM/SPM microscopy (Agilent Technologies, Santa Clara, CA). The instrument was operated in AC mode with silicon nitrite probes (PPP-NCL, 21-98 Nm^{-1}) purchased from Nanosensors. Images were taken at the fundamental resonant frequency of the silicon cantilever of 146-180 kHz. Samples were scanned in a chamber purged with dry nitrogen gas. The imaging set point was kept around 100mV for all the experiments to make surface scope traces tracked and obtain the clearest images.

II. Attenuated Total Reflection Fourier Transform Infrared spectroscopy and the quantification of surface molecules

1. Operation method

The Fourier transform infrared spectroscopy in ATR geometry (IR-ATR) used in crystalline silicon substrate allows the identifications of the functional groups present on the silicon surfaces *via* the detection of characteristic vibration of chemical bonds. The silicon wafer is polished at two sides to generate bevels of typically 45°. The ATR geometry allows the infrared beam pass through the substrate with a number of reflections (~20 for a width of 1.4 cm) so that the scanned signal is amplified. The IR-ATR measurement performed in s- and p-polarizations decomposes the vibrational mode of a bond into the perpendicular (s-) and parallel (p-) directions along the surface so that the conformation of the chemical bonds on the surface can be justified.

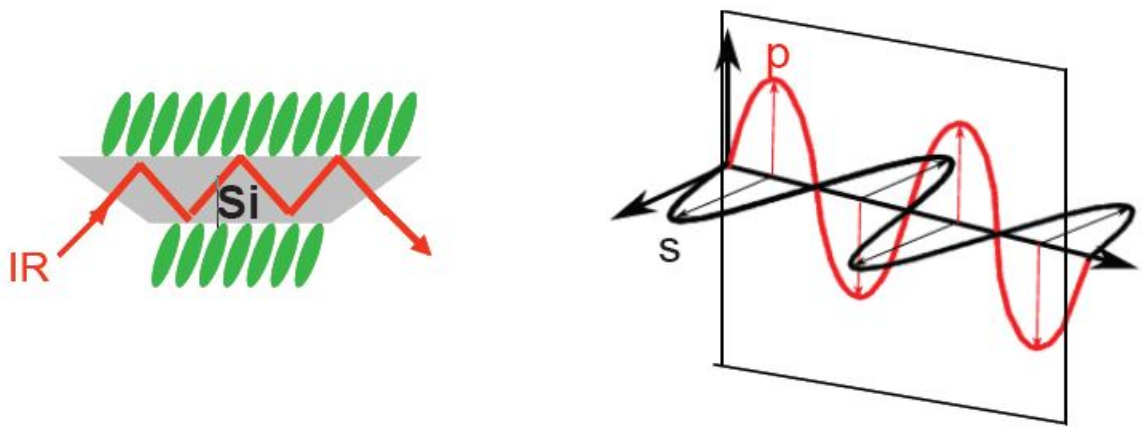

Figure II.1 Scheme representing the IR in ATR geometry operated for a silicon substrate.[65]

In this work, the spectra were recorded on a Bruker Equinox FTIR spectrometer coupled to a homemade, nitrogen-gas purged external ATR compartment. The spectra were collected with 100 scans in s- and p-polarizations over the 900−4000 cm^{-1} spectral range with a 4 cm^{-1} resolution. The calibration and the in-situ measurements were performed in a home-made PTFCE IR cell of ~ 1.5 mL volume. On the top and the bottom of the cell a PTFE tube (0.8 mm diameter) is connected allowing for the addition of different solutions without breaking the spectrometer purge. On the side there is an opening of 9 mm diameter against which the prism is pressed via a nitrile O-ring seal.

2. Quantification of surface molecule by IR-ATR

In ATR geometry, the density of molecules grafted onto a surface can be calculated from the integrated absorbance of the signal associated with a vibrational mode of the molecules. The infrared cross section of this mode has to be known first. As shown hereafter, this cross section can be simply determined if the absorption of the considered mode can be measured in a liquid-phase experiment in the same geometry.

In an assembly of molecules, a convenient way is to adopt a macroscopic description and consider the dielectric response of this assembly. In this approach, all of the relevant microscopic details (such as the dynamic dipole of the considered vibrational mode) are included in an effective dielectric function, which, in the wavenumber range of interest, will be assumed to be simply related to the dielectric function of the liquid used for the calibration. An adsorbate layer may then be regarded as a slice of thickness d and an effective dielectric function $\epsilon = \epsilon' + i\epsilon''$ at the interface between the silicon of refractive index n_s (3.42) and a non absorbing medium (air) of refractive index n_2 (1). Following Chabal[227], one may write its absorbance (i.e., the relative loss $\Delta I/I$ per reflection at wavelength λ in the infrared s- and p-polarized signals due to the presence of the layer):

$$A_s = \frac{2\pi}{\lambda}\frac{1}{n_s cos\varphi} I_y(\epsilon_y'' d) \qquad (1)$$

$$A_p = \frac{2\pi}{\lambda}\frac{1}{n_s cos\varphi}[I_x(\epsilon_x'' d) + I_z \frac{n_2^4}{\epsilon_z'^2 + \epsilon_z''^2}(\epsilon_z'' d)] \qquad (2)$$

where φ is the angle of incidence and I_x, I_y, and I_z numerical coefficients which characterizes the intensity of electric field on the surface. They are given by:

$$I_x = \frac{4n_s^2\cos^2\varphi(n_s^2\sin^2\varphi - n_2^2)}{n_2^4\cos^2\varphi + n_s^4\sin^2\varphi - n_s^2 n_2^2} \qquad (3)$$

$$I_y = \frac{4n_s^2\cos^2\varphi}{n_s^2 - n_2^2} \qquad (4)$$

$$I_z = \frac{4n_s^4\cos^2\varphi\sin^2\varphi}{n_2^4\cos^2\varphi + n_s^4\sin^2\varphi - n_s^2 n_2^2} \qquad (5)$$

For example, for an incident angle of $\varphi = 48°$, $I_x = 1.78$, $I_y = 1.96$ and $I_z = 2.10$.

Note that ϵ has been considered to be a tensor (with the z direction perpendicular to the interface plane) to possibly account for anisotropic effects due to the adsorbate configuration. With respect to this possibility, it is useful to consider the surface concentration of vibrators corresponding to the projection of the dynamic dipole of the vibrational mode in the interface plane, $N_\parallel$, and that corresponding to the projection of the dynamic dipole along the z direction, $N_\perp$, the actual surface concentration of vibrators is simply given by $N = N_\parallel + N_\perp$.

In the calibration experiments, the infrared absorption of the liquid is measured in an attenuated total reflection configuration at the interface between the same silicon surface and the liquid of complex refractive index $\widehat{n_l} = n_l + ik$.We suppose that k is small enough to

neglect the change in the penetration depth δ of the evanescent wave due to absorption. In this case, the liquid absorbance (per reflection) is written as (in s and p polarization, respectively)

$$A_s^0 = \frac{2\pi}{\lambda}\frac{1}{n_s cos\varphi} I_y^0 2n_l k \frac{\delta}{2} \quad (6)$$

$$A_p^0 = \frac{2\pi}{\lambda}\frac{1}{n_s cos\varphi} (I_x^0 + I_z^0) 2n_l k \frac{\delta}{2} \quad (7)$$

$$\delta = \frac{\lambda}{2\pi\sqrt{n_s^2 sin^2\varphi - n_l^2}} \quad (8)$$

here I_x^0, I_y^0, and I_z^0 have the same definition as I_x, I_y, and I_z. Note that the n_2=1 for samples measured at silicon/air interface whereas n_l is the refractive index of the solvent used in the calibration experiment. For example, in the calibration of ManOAc, the solvent is acetonitrile, n_l = 1.34 and the absorption wavenumber λ = 1750 cm^{-1}, for an incident angle φ = 46.75°, I_y^0 = 2.22 and δ = 433 nm.

To obtain the sought calibration, assumptions have to be made. We will therefore assume that (i) in the adsorbate to relate ϵ to $\widehat{n_l}$ layer, the absorption coefficient of the considered mode is proportional to the vibrator concentration in the layer with the same proportionality coefficient as that between the absorption coefficient and the vibrator concentration in the liquid and (ii) the real dielectric response of the adsorbate layer is isotropic and identical to that of the liquid (i.e., $n_l \approx \sqrt{\epsilon_x'} \approx \sqrt{\epsilon_y'} \approx \sqrt{\epsilon_z'}$). Physically, these assumptions mean only that the liquid mimics the same environment for the vibrators as that provided by the adsorbate layer. Denoting the concentration of vibrators in the liquid by *C*, the above assumptions yield:

$$\frac{N_\perp/d}{C/3} = \frac{\epsilon_z''}{2n_l k} \quad (9)$$

with the factor of 1/3 accounting for the random orientation of the vibrators in the liquid. For simplicity, we will also consider that there is no anisotropy in the vibrational absorption of the layer in the interfacial plane (i.e., $\epsilon_x'' = \epsilon_y''$, an assumption that could be avoided by considering two quantities N_x and N_y instead of $N_\parallel$ defined above, but in this case, the determination of these two quantities would require an extra measurement.) We obtain similarly

$$\frac{N_\parallel/2d}{C/3} = \frac{\epsilon_x''}{2n_l k} = \frac{\epsilon_y''}{2n_l k} \quad (10)$$

It is then straightforward to derive $N_\parallel$ from the ratio between the absorbance of the adsorbate layer and that measured for the liquid in s polarization:

$$N_\parallel = \frac{A_s}{A_s^0} \times \frac{Iy^0}{I_y} \times \frac{C}{3} \times \delta \quad (11)$$

Similarly, after simple algebra and considering that $\epsilon_z'^2 + \epsilon_z''^2 = \epsilon_z'^2$, one obtains $N_\perp$:

$$N_{\perp} = \frac{C}{3} \times \frac{\delta}{2} \times \frac{Iy^{0}}{I_y} \times \frac{I_y \times A_p - I_x \times A_s}{A_s^{0} \times (I_z \times \frac{1}{\varepsilon_z'^2})} \qquad (12)$$

Equation (11) and (12) are used in practice for integrated absorbances because for a given mode the integrated absorbance is more reliably extracted from experimental data than the intrinsic spectral shape. From them, we can see that to calculate the density of a certain vibrators on the surface, the IR measurement provides A_s and A_p, the only unknown is the value of $\frac{A_s^0}{C}$. So to obtain this value, the calibration experiment is needed.

The calibration experiment is operated by an in-situ IR cell where the solution of analyte is injected. To guarantee the accuracy of the calibrated value, several concentrations are measured and the values of A_s^0 is ploted versus corresponding C. A linear regression should be observed where the slope is the calibrated $\frac{A_s^0}{C}$ value.

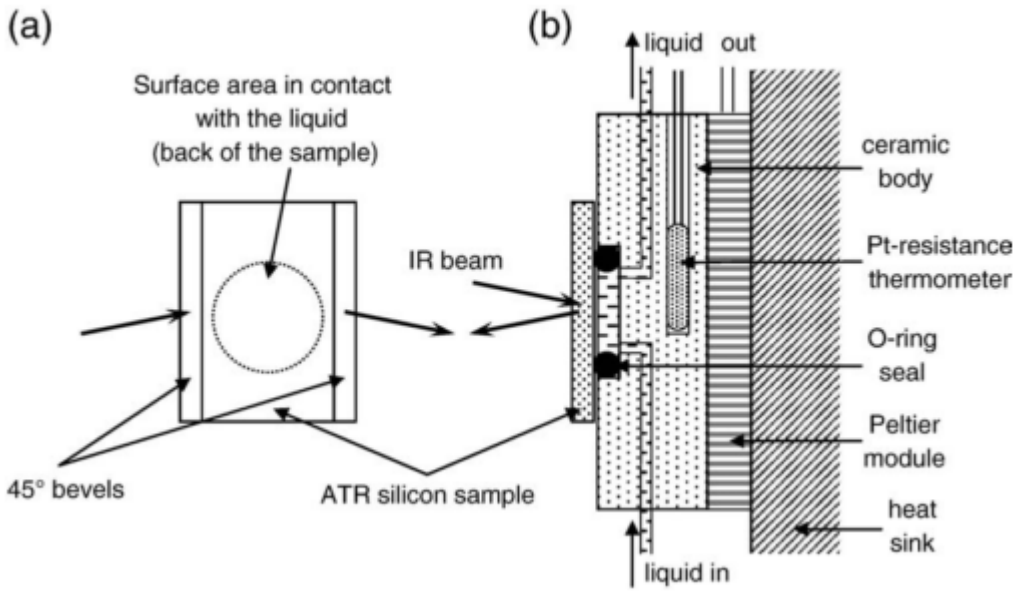

Figure II.2 Scheme of the in-situ IR arrangement. (a) Front view of the ATR silicon sample and (b) side view of the sample mounted on the circulation cell.[66]

In the laboratory PMC, Faucheux et al. made the calibration of decanoic acid in order to quantify the density of grafted carboxydecyl chain.[63] The obtained quantification equations are as the following for a calibration prism containing a bevel of 48°:

For νCH_2, δ = 265 nm at λ = 2853 cm^{-1},

$$N_{\parallel} = 1.84 \times 10^{17} A_s$$
$$N_{\perp} = 3.51 \times 10^{17} A_p - 3.19 \times 10^{17} A_s$$
$$\text{So, } N_{total} = 3.51 \times 10^{17} A_p - 1.35 \times 10^{13} A_s$$

For νCO, δ = 441 nm at λ = 1712 cm^{-1},

$$N_{\parallel} = 6.77 \times 10^{15} A_s$$
$$N_{\perp} = 1.29 \times 10^{16} A_p - 1.17 \times 10^{16} A_s$$
$$\text{So, } N_{total} = 1.29 \times 10^{16} A_p - 4.93 \times 10^{15} A_s$$

Moraillon et al. calibrated the NHS-ester by regarding the sum of the integrated absorbances of the two NHS-ester modes at 1787 and 1815 cm^{-1} as the most reliable experimental quantity for measuring the surface concentration of NHS-ester chains in the grafted layers.[64] The obtained quantification equation is as the following for a calibration prism containing a bevel of 46°, δ = 432 nm at λ = 1815 cm^{-1}, δ = 439 nm at λ = 1787 cm^{-1},

$$N_{\parallel} = 1.16 \times 10^{16} (A_{s(1787)} + A_{s(1815)})$$
$$N_{\perp} = 2.09 \times 10^{16} (A_{p(1787)} + A_{p(1815)}) - 1.90 \times 10^{16} (A_{s(1787)} + A_{s(1815)})$$
$$\text{So, } N_{total} = 2.09 \times 10^{16} (A_{p(1787)} + A_{p(1815)}) - 7.4 \times 10^{15} (A_{s(1787)} + A_{s(1815)})$$

III. X-ray photoelectron spectroscopy

XPS experiments were performed on Thermo-VG Escalab 220iXL or Thermo K-Alpha spectrometers at the “ILV_CEFS2” center in University of Versailles. A monochromatic Al Kα X-ray line was used for the excitation. The samples are kept under nitrogen before the introduction inside the preparation chamber of the XPS analyzer. The detection was performed perpendicularly to the sample surface, using a constant energy analyzer mode (pass energy 20 eV).

IV. Spotter and fluorescence imaging

The spotting process is accomplished by a spotter robot Biorobotics MicroGrid II (**Fig IV.1**). The glass slide is fixed at the programmed position. The spotting solutions (~20 µL) are placed in a microplate containing 384 wells according to the programmed spotting sequence. The spotting needle takes solution from the microplate and deposited at the programmed position on the slide. The spotting process is under controlled humidity (~50%) and temperature (~20°C). The spotted interfaces are stored in a dessicator overnight at controlled humidity (~75%).

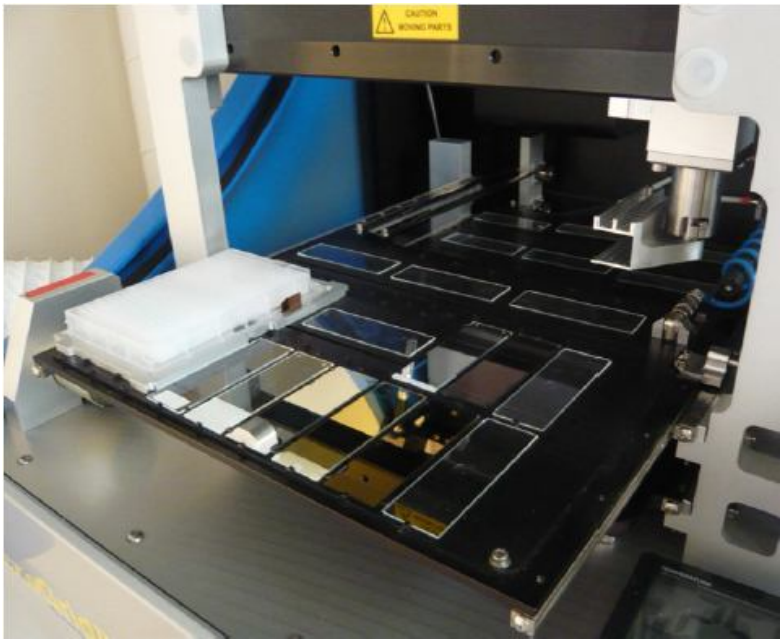

Figure IV.1 spotting robot Biorobotics MicroGrid II.

For end-point measurements, the fluorescence was measured with a commercialized fluorescence imaging instrument Diagarray scanner (Genewave, France). The slide is fixed in the sample holder and the fluorescence data is directly read out by the software Diagarray. For real-time, *in-situ* association monitoring, fluorescence was measured using a Hyblive machine (Genewave, France) (**Fig IV.2**). In this case, the photoluminescence is continuously monitored during association (the cell is filled with target solutions for recording kinetic curves). During measurements, the liquid is not circulated but stirred using surface acoustic wave devices. After association, the liquid is washed by 1X PBS/0.1% SDS for 10 min, 0.2X PBS for 2 min, 0.1X PBS for 2 min and Milli-Q water. The microarray data was treated by the Hyblizer software (Genewave, France). The microarray data was treated by the Hyblizer software (Genewave, France).

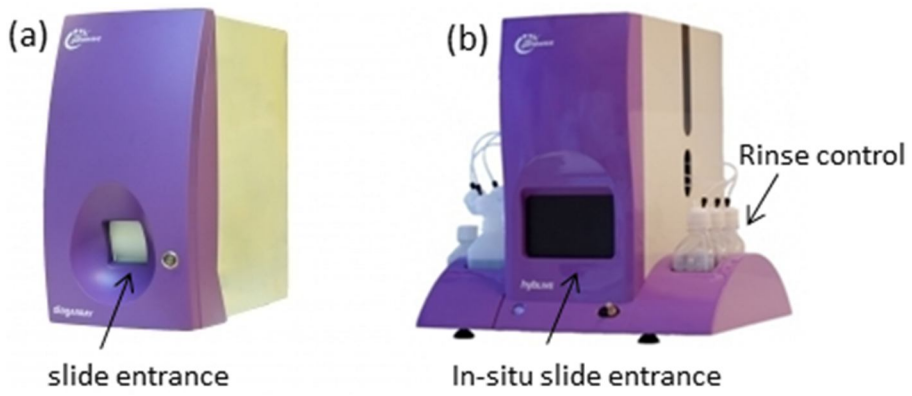

Figure IV.2 Fluorescence imaging instrument: Diagarray (a) and Hyblive (b).

V. Plasma-enhanced chemical vapor deposition

In the laboratory PMC, the deposition of a-$Si_{1-x}C_x$:H is realized by plasma-enhanced chemical vapor deposition (PECVD) at the low power regime (0.1 W/cm^2) and at low temperature (250°C). As can be seen from **Fig V.1**, gas molecules are filled into a capacitively-coupled reactor where the chemical reaction of these gases is initiated from the radiofrequency-created plasma (13.56 MHz), leading to the deposition of thin films onto the substrate. For the deposition of a-$Si_{1-x}C_x$:H, (two gases, silane (SiH_4) and methane (CH_4), are mixed at a certain ratio for desired *x* value. The pressure of gases is kept at ~40 mT and the flow rate of gases at 2 L/h. Solomon et al. studied the relationship between the CH_4 content in gas phase and the resulted carbon content in the deposited film.[74] For example, the coating of a-$Si_{0.8}C_{0.2}$:H is resulted from a SiH_4/CH_4 ratio of 6.2/69.7 and a-$Si_{0.9}C_{0.1}$:H is from that of 13.3/51.1. Moreover, the thickness of coating layer is controlled at a constant speed (1 nm/3s) when it is less than 200 nm. In this regard, the deposition of a-$Si_{1-x}C_x$:H at desired *x* value and with desired thickness can be realized.

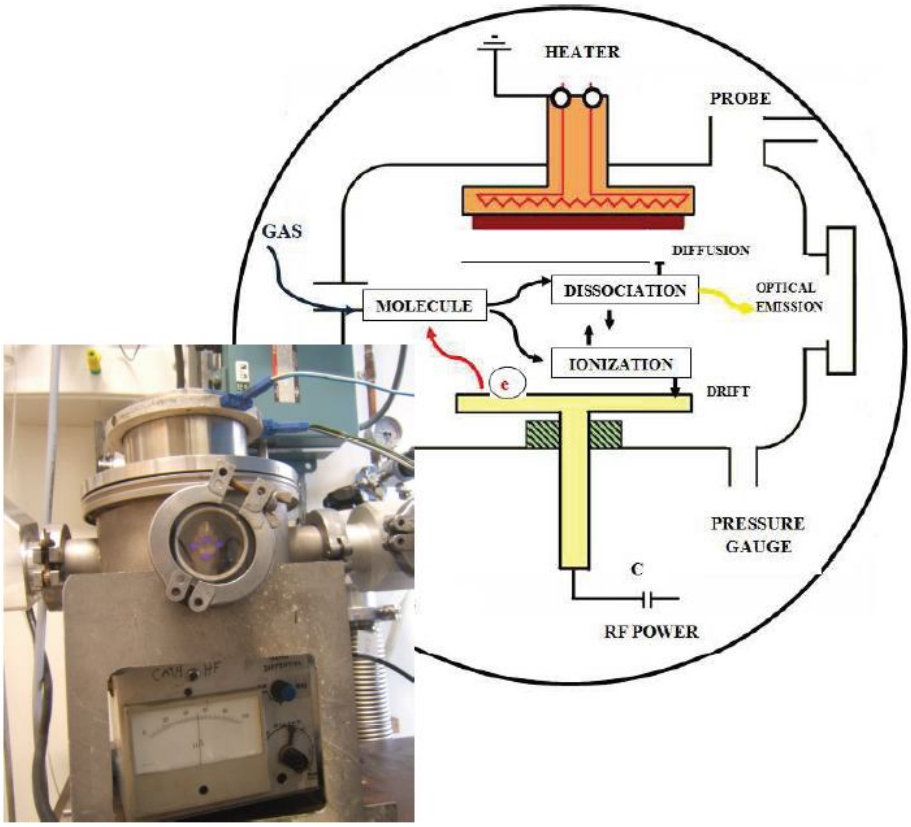

Figure V.1 Schematic representation of the PECVD process and the reactor.

References

1. Arranz-Plaza, E.; Tracy, A. S.; Siriwardena, A.; Pierce, J. M.; Boons, G.-J. *J. Am. Chem. Soc.* **2002,** 124, (44), 13035-13046.
2. Bertozzi, C. R.; Kiessling; L., L. *Science* **2001,** 291, (5512), 2357-2364.
3. Lis, H.; Sharon, N. *Chem. Rev.* **1998,** 98, (2), 637-674.
4. Ambrosi, M.; Cameron, N. R.; Davis, B. G. *Org. Biomol. Chem.* **2005,** 3, (9), 1593-1608.
5. Rudd, P. M.; Wormald, M. R.; Dwek, R. A. *Trends. Biotechnol.* **2004,** 22, (10), 524-530.
6. Gondran, C.; Dubois, M.-P.; Fort, S.; Cosnier, S.; Szunerits, S. *Analyst* **2008,** 133, (2), 206-212.
7. Maalouli, N.; Barras, A.; Siriwardena, A.; Bouazaoui, M.; Boukherroub, R.; Szunerits, S. *Analyst* **2013,** 138, (3), 805-812.
8. Muñoz, F. J.; Rumbero, Á.; Sinisterra, J.; Santos, J. I.; André, S.; Gabius, H.-J.; Jiménez-Barbero, J.; Hernáiz, M. *Glycoconj. J.* **2008,** 25, (7), 633-646.
9. Penezic, A.; Deokar, G.; Vignaud, D.; Pichonat, E.; Happy, H.; Subramanian, P.; Gasparović, B.; Boukherroub, R.; Szunerits, S. *Plasmonics* **2014,** 9, (3), 677-683.
10. Revell, D. J.; Knight, J. R.; Blyth, D. J.; Haines, A. H.; Russell, D. A. *Langmuir* **1998,** 14, (16), 4517-4524.
11. Smith, E. A.; Thomas, W. D.; Kiessling, L. L.; Corn, R. M. *J. Am. Chem. Soc.* **2003,** 125, (20), 6140-6148.
12. Subramanian, P.; Barka-Bouaifel, F.; Bouckaert, J.; Yamakawa, N.; Boukherroub, R.; Szunerits, S. *ACS Appl. Mater. Inter.* **2014,** 6, (8), 5422-5431.
13. Lyu, Y.-K.; Lim, K.-R.; Lee, B. Y.; Kim, K. S.; Lee, W.-Y. *Chem. Commun.* **2008**, (39), 4771-4773.
14. Norberg, O.; Deng, L.; Aastrup, T.; Yan, M.; Ramström, O. *Anal. Chem.* **2010,** 83, (3), 1000-1007.
15. Norberg, O.; Deng, L.; Yan, M.; Ramström, O. *Bioconj. Chem.* **2009,** 20, (12), 2364-2370.
16. Norberg, O.; Lee, I. H.; Aastrup, T.; Yan, M.; Ramström, O. *Biosens. Bioelectron.* **2012,** 34, (1), 51-56.
17. Zhang, Y.; Luo, S.; Tang, Y.; Yu, L.; Hou, K.-Y.; Cheng, J.-P.; Zeng, X.; Wang, P. G. *Anal. Chem.* **2006,** 78, (6), 2001-2008.
18. Zhang, Y.; Telyatnikov, V.; Sathe, M.; Zeng, X.; Wang, P. G. *J. Am. Chem. Soc.* **2003,** 125, (31), 9292-9293.
19. Sugawara, K.; Shirotori, T.; Hirabayashi, G.; Kuramitz, H.; Tanaka, S. *J. Electroanal. Chem.* **2004,** 568, 7-12.
20. Szunerits, S.; Niedziŏłka-Jönsson, J.; Boukherroub, R.; Woisel, P.; Baumann, J.-S.; Siriwardena, A. *Anal. Chem.* **2010,** 82, (19), 8203-8210.
21. Vedala, H.; Chen, Y.; Cecioni, S.; Imberty, A.; Vidal, S. b.; Star, A. *Nano Lett.* **2011,** 11, (1), 170-175.
22. Zhang, G.-J.; Huang, M. J.; Ang, J. A. J.; Yao, Q.; Ning, Y. *Anal. Chem.* **2013,** 85, (9), 4392-4397.
23. Shirahata, N.; Hozumi, A.; Miura, Y.; Kobayashi, K.; Sakka, Y.; Yonezawa, T. *Thin Solid Films* **2006,** 499, (1–2), 213-218.
24. Schena, M.; Shalon, D.; Davis, R. W.; Brown, P. O. *Science* **1995,** 270, (5235), 467-470.

25. Song, E.-H.; Pohl, N. L. B. *Curr. Opin. Chem. Biol.* **2009,** 13, (5–6), 626-632.
26. Mercey, E.; Sadir, R.; Maillart, E.; Roget, A.; Baleux, F.; Lortat-Jacob, H.; Livache, T. *Anal. Chem.* **2008,** 80, (9), 3476-3482.
27. Wang, H.; Zhang, Y.; Yuan, X.; Chen, Y.; Yan, M. *Bioconjugate Chem.* **2011,** 22, (1), 26-32.
28. Houseman, B. T.; Mrksich, M. *Chem. Biol.* **2002,** 9, (4), 443-454.
29. Liang, P.-H.; Wang, S.-K.; Wong, C.-H. *J. Am. Chem. Soc.* **2007,** 129, (36), 11177-11184.
30. Park, S.; Lee, M.-R.; Pyo, S.-J.; Shin, I. *J. Am. Chem. Soc.* **2004,** 126, (15), 4812-4819.
31. Tong, Q.; Wang, X.; Wang, H.; Kubo, T.; Yan, M. *Anal. Chem.* **2012,** 84, (7), 3049-3052.
32. Zhi, Z.-l.; Powell, A. K.; Turnbull, J. E. *Anal. Chem.* **2006,** 78, (14), 4786-4793.
33. Reynolds, M.; Pérez, S. *C. R. Chim.* **2011,** 14, (1), 74-95.
34. Oyelaran, O.; Gildersleeve, J. C. *Curr. Opin. Chem. Bio.* **2009,** 13, (4), 406-413.
35. Gooding, J. J. *Anal. Chim. Acta* **2006,** 559, (2), 137-151.
36. Wang, D.; Liu, S.; Trummer, B. J.; Deng, C.; Wang, A. *Nat Biotech* **2002,** 20, (3), 275-281.
37. Willats, W. G. T.; Rasmussen, S. E.; Kristensen, T.; Mikkelsen, J. D.; Knox, J. P. *Proteomics* **2002,** 2, (12), 1666-1671.
38. Grant, C. F.; Kanda, V.; Yu, H.; Bundle, D. R.; McDermott, M. T. *Langmuir* **2008,** 24, (24), 14125-14132.
39. Mann, D. A.; Kanai, M.; Maly, D. J.; Kiessling, L. L. *J. Am. Chem. Soc.* **1998,** 120, (41), 10575-10582.
40. Sato, Y.; Yoshioka, K.; Murakami, T.; Yoshimoto, S.; Niwa, O. *Langmuir* **2011,** 28, (3), 1846-1851.
41. Houseman, B. T.; Mrksich, M. *Angew. Chem. Int. Edi.* **1999,** 38, (6), 782-785.
42. Tyagi, A.; Wang, X.; Deng, L.; Ramström, O.; Yan, M. *Biosens. Bioelectron.* **2010,** 26, (2), 344-350.
43. Wang, X.; Matei, E.; Deng, L.; Koharudin, L.; Gronenborn, A. M.; Ramström, O.; Yan, M. *Biosens. Bioelectron.* **2013,** 47, (0), 258-264.
44. Liu, L.-H.; Yan, M. *Acc. Chem. Res.* **2010,** 43, (11), 1434-1443.
45. Zhou, X.; Turchi, C.; Wang, D. *J. Proteome Res.* **2009,** 8, (11), 5031-5040.
46. Zhou, X.; Zhou, J. *Biosens. Bioelectron.* **2006,** 21, (8), 1451-1458.
47. Cattani-Scholz, A.; Pedone, D.; Dubey, M.; Neppl, S.; Nickel, B.; Feulner, P.; Schwartz, J.; Abstreiter, G.; Tornow, M. *ACS Nano* **2008,** 2, (8), 1653-1660.
48. Lapin, N. A.; Chabal, Y. J. *J. Phys. Chem. B* **2009,** 113, (25), 8776-8783.
49. Aureau, D.; Varin, Y.; Roodenko, K.; Seitz, O.; Pluchery, O.; Chabal, Y. J. *J. Phys. Chem. C* **2010,** 114, (33), 14180-14186.
50. Boukherroub, R.; Morin, S.; Bensebaa, F.; Wayner, D. D. M. *Langmuir* **1999,** 15, (11), 3831-3835.
51. Boukherroub, R.; Wayner, D. D. M. *J. Am. Chem. Soc.* **1999,** 121, (49), 11513-11515.
52. Ciampi, S.; Harper, J. B.; Gooding, J. J. *Chem. Soc. Rev.* **2010,** 39, (6), 2158-2183.
53. Boukherroub, R. *Curr. Opin. Solid State Mater. Sci.* **2005,** 9, (1–2), 66-72.
54. Thissen, P.; Seitz, O.; Chabal, Y. J. *Prog. Surf. Sci.* **2012,** 87, (9–12), 272-290.
55. de Smet, L. C. P. M.; Stork, G. A.; Hurenkamp, G. H. F.; Sun, Q.-Y.; Topal, H.; Vronen, P. J. E.; Sieval, A. B.; Wright, A.; Visser, G. M.; Zuilhof, H.; Sudhölter, E. J. R. *J. Am. Chem. Soc.* **2003,** 125, (46), 13916-13917.
56. Funato, K.; Shirahata, N.; Miura, Y. *Thin Solid Films* **2009,** 518, (2), 699-702.
57. Warntjes, M.; Vieillard, C.; Ozanam, F.; Chazalviel, J. N. *J. Electrochem. Soc.* **1995,** 142, (12), 4138-4142.

58. Chazalviel, J. N.; Fellah, S.; Ozanam, F. *J. Electroanal. Chem.* **2002,** 524–525, (0), 137-143.
59. Dubois, T.; Ozanam, F.; Chazalviel, J. N., 3rd European Workshop on Electrochemical Processing of Semiconductors (EWEPS '96), Meudon, Nov. 1996.
60. Fellah, S.; Teyssot, A.; Ozanam, F.; Chazalviel, J.-N.; Vigneron, J.; Etcheberry, A. *Langmuir* **2002,** 18, (15), 5851-5860.
61. Fidélis, A.; Ozanam, F.; Chazalviel, J. N. *Surf. Sci.* **2000,** 444, (1–3), L7-L10.
62. de Villeneuve, C. H.; Pinson, J.; Bernard, M. C.; Allongue, P. *J. Phys. Chem. B* **1997,** 101, (14), 2415-2420.
63. Faucheux, A.; Gouget-Laemmel, A. C.; Henry de Villeneuve, C.; Boukherroub, R.; Ozanam, F.; Allongue, P.; Chazalviel, J.-N. *Langmuir* **2006,** 22, (1), 153-162.
64. Moraillon, A.; Gouget-Laemmel, A. C.; Ozanam, F.; Chazalviel, J. N. *J. Phys. Chem. C* **2008,** 112, (18), 7158-7167.
65. Touahir, L. *PhD thesis (PMC, Ecole Polytechnique)* **2010**.
66. Touahir, L.; Allongue, P.; Aureau, D.; Boukherroub, R.; Chazalviel, J. N.; Galopin, E.; Gouget-Laemmel, A. C.; de Villeneuve, C. H.; Moraillon, A.; Niedziółka-Jönsson, J.; Ozanam, F.; Andresa, J. S.; Sam, S.; Solomon, I.; Szunerits, S. *Bioelectrochem.* **2010,** 80, (1), 17-25.
67. Touahir, L.; Galopin, E.; Boukherroub, R.; Chantal Gouget-Laemmel, A.; Chazalviel, J.-N.; Ozanam, F.; Saison, O.; Akjouj, A.; Pennec, Y.; Djafari-Rouhani, B.; Szunerits, S. *Analyst* **2011,** 136, (9), 1859-1866.
68. Touahir, L.; Galopin, E.; Boukherroub, R.; Gouget-Laemmel, A. C.; Chazalviel, J.-N.; Ozanam, F.; Szunerits, S. *Biosens. Bioelectron.* **2010,** 25, (12), 2579-2585.
69. Touahir, L.; Jenkins, A. T. A.; Boukherroub, R.; Gouget-Laemmel, A. C.; Chazalviel, J.-N.; Peretti, J.; Ozanam, F.; Szunerits, S. *J. Phys. Chem. C* **2010,** 114, (51), 22582-22589.
70. Touahir, L.; Moraillon, A.; Allongue, P.; Chazalviel, J. N.; Henry de Villeneuve, C.; Ozanam, F.; Solomon, I.; Gouget-Laemmel, A. C. *Biosens. Bioelectron.* **2009,** 25, (4), 952-955.
71. Touahir, L.; Niedziółka-Jönsson, J.; Galopin, E.; Boukherroub, R.; Gouget-Laemmel, A. C.; Solomon, I.; Petukhov, M.; Chazalviel, J.-N.; Ozanam, F.; Szunerits, S. *Langmuir* **2010,** 26, (8), 6058-6065.
72. Galopin, E.; Touahir, L.; Niedziółka-Jönsson, J.; Boukherroub, R.; Gouget-Laemmel, A. C.; Chazalviel, J.-N.; Ozanam, F.; Szunerits, S. *Biosens. Bioelectron.* **2010,** 25, (5), 1199-1203.
73. Michalak, D. J.; Amy, S. R.; Aureau, D.; Dai, M.; Esteve, A.; Chabal, Y. J. *Nat. Mater.* **2010,** 9, (3), 266-271.
74. Solomon, I.; Schmidt, M. P.; Tran-Quoc, H. *Phys. Rev. B* **1988,** 38, (14), 9895-9901.
75. Beckmann, K. H. *Surf. Sci.* **1965,** 3, (4), 314-332.
76. Ubara, H.; Imura, T.; Hiraki, A. *Solid State Commun.* **1984,** 50, (7), 673-675.
77. Chabal, Y. J. *Surf. Sci.* **1986,** 168, (1–3), 594-608.
78. Higashi, G. S.; Becker, R. S.; Chabal, Y. J.; Becker, A. J. *Appl. Phys. Lett.* **1991,** 58, (15), 1656-1658.
79. Jakob, P.; Chabal, Y. J. *J. Chem. Phys.* **1991,** 95, (4), 2897-2909.
80. Jakob, P.; Chabal, Y. J.; Raghavachari, K.; Becker, R. S.; Becker, A. J. *Surf. Sci.* **1992,** 275, (3), 407-413.
81. Trucks, G. W.; Raghavachari, K.; Higashi, G. S.; Chabal, Y. J. *Phys. Rev. Lett.* **1990,** 65, (4), 504-507.
82. Burrows, V. A.; Chabal, Y. J.; Higashi, G. S.; Raghavachari, K.; Christman, S. B. *Appl. Phys. Lett.* **1988,** 53, (11), 998-1000.

83. Higashi, G. S.; Chabal, Y. J.; Trucks, G. W.; Raghavachari, K. *Appl. Phys. Lett.* **1990,** 56, (7), 656-658.
84. Yablonovitch, E.; Allara, D. L.; Chang, C. C.; Gmitter, T.; Bright, T. B. *Phys. Rev. Lett.* **1986,** 57, (2), 249-252.
85. Allongue, P.; Kieling, V.; Gerischer, H. *Electrochimica Acta* **1995,** 40, (10), 1353-1360.
86. Hirokazu, F.; Michio, M. *Jpn. J. Appl. Phys.* **1999,** 38, (10A), L1085.
87. Allongue, P.; Henry de Villeneuve, C.; Morin, S.; Boukherroub, R.; Wayner, D. D. M. *Electrochimica Acta* **2000,** 45, (28), 4591-4598.
88. Linford, M. R.; Fenter, P.; Eisenberger, P. M.; Chidsey, C. E. D. *J. Am. Chem. Soc.* **1995,** 117, (11), 3145-3155.
89. Bateman, J. E.; Eagling, R. D.; Worrall, D. R.; Horrocks, B. R.; Houlton, A. *Angew. Chem. Int. Edi.* **1998,** 37, (19), 2683-2685.
90. Sieval, A. B.; Demirel, A. L.; Nissink, J. W. M.; Linford, M. R.; van der Maas, J. H.; de Jeu, W. H.; Zuilhof, H.; Sudhölter, E. J. R. *Langmuir* **1998,** 14, (7), 1759-1768.
91. Buriak, J. M. *Chem. Rev.* **2002,** 102, (5), 1271-1308.
92. Buriak, J. M.; Allen, M. J. *J. Am. Chem. Soc.* **1998,** 120, (6), 1339-1340.
93. Buriak, J. M.; Stewart, M. P.; Geders, T. W.; Allen, M. J.; Choi, H. C.; Smith, J.; Raftery, D.; Canham, L. T. *J. Am. Chem. Soc.* **1999,** 121, (49), 11491-11502.
94. Schmeltzer, J. M.; Porter, L. A.; Stewart, M. P.; Buriak, J. M. *Langmuir* **2002,** 18, (8), 2971-2974.
95. Cicero, R. L.; Linford, M. R.; Chidsey, C. E. D. *Langmuir* **2000,** 16, (13), 5688-5695.
96. Effenberger, F.; Götz, G.; Bidlingmaier, B.; Wezstein, M. *Angew. Chem. Int. Edi.* **1998,** 37, (18), 2462-2464.
97. Stewart, M. P.; Buriak, J. M. *Angew. Chem. Int. Edi.* **1998,** 37, (23), 3257-3260.
98. Stewart, M. P.; Buriak, J. M. *J. Am. Chem. Soc.* **2001,** 123, (32), 7821-7830.
99. Sun, Q.-Y.; de Smet, L. C. P. M.; van Lagen, B.; Giesbers, M.; Thüne, P. C.; van Engelenburg, J.; de Wolf, F. A.; Zuilhof, H.; Sudhölter, E. J. R. *J. Am. Chem. Soc.* **2005,** 127, (8), 2514-2523.
100. Sun, Q.-Y.; de Smet, L. C. P. M.; van Lagen, B.; Wright, A.; Zuilhof, H.; Sudhölter, E. J. R. *Angew. Chem. Int. Edi.* **2004,** 43, (11), 1352-1355.
101. Cicero, R. L.; Chidsey, C. E. D.; Lopinski, G. P.; Wayner, D. D. M.; Wolkow, R. A. *Langmuir* **2001,** 18, (2), 305-307.
102. Eves, B. J.; Sun, Q.-Y.; Lopinski, G. P.; Zuilhof, H. *J. Am. Chem. Soc.* **2004,** 126, (44), 14318-14319.
103. Wang, X.; Ruther, R. E.; Streifer, J. A.; Hamers, R. J. *J. Am. Chem. Soc.* **2010,** 132, (12), 4048-4049.
104. Sieval, A. B.; Linke, R.; Zuilhof, H.; Sudhölter, E. J. R. *Adv. Mater.* **2000,** 12, (19), 1457-1460.
105. Voicu, R.; Boukherroub, R.; Bartzoka, V.; Ward, T.; Wojtyk, J. T. C.; Wayner, D. D. M. *Langmuir* **2004,** 20, (26), 11713-11720.
106. Strother, T.; Cai, W.; Zhao, X.; Hamers, R. J.; Smith, L. M. *J. Am. Chem. Soc.* **2000,** 122, (6), 1205-1209.
107. Lanigan, R. M.; Sheppard, T. D. *Eur. J. Org. Chem.* **2013,** 2013, (33), 7453-7465.
108. Montalbetti, C. A. G. N.; Falque, V. *Tetrahedron* **2005,** 61, (46), 10827-10852.
109. Valeur, E.; Bradley, M. *Chem. Soc. Rev.* **2009,** 38, (2), 606-631.
110. Sam, S.; Touahir, L.; Salvador Andresa, J.; Allongue, P.; Chazalviel, J. N.; Gouget-Laemmel, A. C.; Henry de Villeneuve, C.; Moraillon, A.; Ozanam, F.; Gabouze, N.; Djebbar, S. *Langmuir* **2009,** 26, (2), 809-814.

111. Ballet, T.; Boulange, L.; Brechet, Y.; Bruckert, F.; Weidenhaupt, M. *Bull. Polish Aca. Sci* **2010,** 58, (2), 303-315.
112. Rabe, M.; Verdes, D.; Seeger, S. *Adv. Coll. Int. Sci.* **2011,** 162, (1–2), 87-106.
113. Norde, W.; Tan, W.; Koopal, L., In *5th International Symposium ISMOM 2008*, Pucón, Chile
114. Cha, T.; Guo, A.; Jun, Y.; Pei, D.; Zhu, X.-Y. *Proeomics* **2004,** 4, (7), 1965-1976.
115. Davila, J.; Toulemon, D.; Garnier, T.; Garnier, A.; Senger, B.; Voegel, J.-C.; Mésini, P. J.; Schaaf, P.; Boulmedais, F.; Jierry, L. *Langmuir* **2013**.
116. Harbers, G. M.; Emoto, K.; Greef, C.; Metzger, S. W.; Woodward, H. N.; Mascali, J. J.; Grainger, D. W.; Lochhead, M. J. *Chem. Mater.* **2007,** 19, (18), 4405-4414.
117. Lee, B. S.; Lee, J. K.; Kim, W.-J.; Jung, Y. H.; Sim, S. J.; Lee, J.; Choi, I. S. *Biomacromolecules* **2007,** 8, (2), 744-749.
118. Holmlin, R. E.; Chen, X.; Chapman, R. G.; Takayama, S.; Whitesides, G. M. *Langmuir* **2001,** 17, (9), 2841-2850.
119. Chen, S.; Yu, F.; Yu, Q.; He, Y.; Jiang, S. *Langmuir* **2006,** 22, (19), 8186-8191.
120. Ostuni, E.; Chapman, R. G.; Holmlin, R. E.; Takayama, S.; Whitesides, G. M. *Langmuir* **2001,** 17, (18), 5605-5620.
121. Sharma, S.; Popat, K. C.; Desai, T. A. *Langmuir* **2002,** 18, (23), 8728-8731.
122. Allen, C.; Dos Santos, N.; Gallagher, R.; Chiu, G. N. C.; Shu, Y.; Li, W. M.; Johnstone, S. A.; Janoff, A. S.; Mayer, L. D.; Webb, M. S.; Bally, M. B. *Biosci. Rep.* **2002,** 22, (2), 225-250.
123. Heuberger, M.; Drobek, T.; Vörös, J. *Langmuir* **2004,** 20, (22), 9445-9448.
124. Wang, R. L. C.; Kreuzer, H. J.; Grunze, M. *J. Phys. Chem. B* **1997,** 101, (47), 9767-9773.
125. Zheng, J.; Li, L.; Chen, S.; Jiang, S. *Langmuir* **2004,** 20, (20), 8931-8938.
126. Wang, R. Y.; Himmelhaus, M.; Fick, J.; Herrwerth, S.; Eck, W.; Grunze, M. *J. Chem. Phys.* **2005,** 122, (16), -.
127. Chen, S.; Li, L.; Zhao, C.; Zheng, J. *Polymer* **2010,** 51, (23), 5283-5293.
128. Herrwerth, S.; Eck, W.; Reinhardt, S.; Grunze, M. *J. Am. Chem. Soc.* **2003,** 125, (31), 9359-9366.
129. Li, L.; Chen, S.; Zheng, J.; Ratner, B. D.; Jiang, S. *J. Phys. Chem. B* **2005,** 109, (7), 2934-2941.
130. Mao, S.; Neu, M.; Germershaus, O.; Merkel, O.; Sitterberg, J.; Bakowsky, U.; Kissel, T. *Bioconjugate Chem.* **2006,** 17, (5), 1209-1218.
131. Wyszogrodzka, M.; Haag, R. *Langmuir* **2009,** 25, (10), 5703-5712.
132. Harder, P.; Grunze, M.; Dahint, R.; Whitesides, G. M.; Laibinis, P. E. *J. Phys. Chem. B* **1998,** 102, (2), 426-436.
133. Perez, E. *PhD thesis (PMC, Ecole Polytechnique)* **2011**.
134. Perez, E.; Lahlil, K.; Rougeau, C.; Moraillon, A.; Chazalviel, J.-N.; Ozanam, F.; Gouget-Laemmel, A. C. *Langmuir* **2012,** 28, (41), 14654-14664.
135. Kurth, T.; Biresaw, G.; Adhvaryu, A. *J. Am. Oil Chem. Soc.* **2005,** 82, (4), 293-299.
136. Dada, A. O.; Olalekan, A. P.; Olatunya, A. M.; Dada, O. *IOSR J. App. Chem.* **2012,** 3, (1), 38-45.
137. Jin, B.; Bao, W.-J.; Wu, Z.-Q.; Xia, X.-H. *Langmuir* **2012,** 28, (25), 9460-9465.
138. Kim, J.-H.; Yoon, J.-Y., *Encyclopedia of Surface and Colloid Science*. Marcel Dekker, Inc.: 2002.
139. Lee, W.-H.; Loo, C.-Y.; Van, K. L.; Zavgorodniy, A. V.; Rohanizadeh, R. *J. R. Soc. Interface* **2012,** 9, (70), 918-927.
140. Yoon, J.-Y.; Park, H.-Y.; Kim, J.-H.; Kim, W.-S. *J. Coll. Interface Sci.* **1996,** 177, (2), 613-620.

141. Rajmohan, J., *Biosensor*. India, 2006.
142. Willets, K. A.; Van Duyne, R. P. *Annu. Rev. Phys. Chem.* **2007,** 58, (1), 267-297.
143. Saison-Francioso, O.; Lévêque, G.; Akjouj, A.; Pennec, Y.; Djafari-Rouhani, B.; Boukherroub, R.; Szunerits, S. *Plasmonics* **2013,** 8, (4), 1691-1698.
144. Akjouj, A.; Lévêque, G. t.; Szunerits, S.; Pennec, Y.; Djafari-Rouhani, B.; Boukherroub, R.; Dobrzyński, L. *Surf. Sci. Rep.* **2013,** 68, (1), 1-67.
145. Barka-Bouaifel, F.; Niedziolka-Jonsson, J.; Castel, X.; Saison, O.; Akjouj, A.; Pennec, Y.; Djafari-Rouhani, B.; Woisel, P.; Lyskawa, J.; Sambe, L.; Cooke, G.; Bezzi, N.; Boukherroub, R.; Szunerits, S. *J. Mater. Chem.* **2011,** 21, (9), 3006-3013.
146. Galopin, E.; Niedziółka-Jönsson, J.; Akjouj, A.; Pennec, Y.; Djafari-Rouhani, B.; Noual, A.; Boukherroub, R.; Szunerits, S. *J. Phys. Chem. C* **2010,** 114, (27), 11769-11775.
147. Galopin, E.; Noual, A.; Niedziółka-Jönsson, J.; Jönsson-Niedziółka, M.; Akjouj, A.; Pennec, Y.; Djafari-Rouhani, B.; Boukherroub, R.; Szunerits, S. *J. Phys. Chem. C* **2010,** 113, (36), 15921-15927.
148. Saison-Francioso, O.; Lévêque, G.; Akjouj, A.; Pennec, Y.; Djafari-Rouhani, B.; Szunerits, S.; Boukherroub, R. *J. Phys. Chem. C* **2012,** 116, (33), 17819-17827.
149. Niedziółka-Jönsson, J.; Barka, F.; Castel, X.; Pisarek, M.; Bezzi, N.; Boukherroub, R.; Szunerits, S. *Langmuir* **2010,** 26, (6), 4266-4273.
150. Szunerits, S.; Boukherroub, R. *Global J. Phys. Chem.* **2010,** 1, 20.
151. Szunerits, S.; Das, M. R.; Boukherroub, R. *J. Phys. Chem. C* **2008,** 112, (22), 8239-8243.
152. Szunerits, S.; Ghodbane, S.; Niedziółka-Jönsson, J.; Galopin, E.; Klauser, F.; Akjouj, A.; Pennec, Y.; Djafari-Rouhani, B.; Boukherroub, R.; Steinmüller-Nethl, D. *J. Phys. Chem. C* **2010,** 114, (8), 3346-3353.
153. Szunerits, S.; Shalabney, A.; Boukherroub, R.; Abdulhalim, I. *Rev. Anal. Chem.* **2012,** 31, (1), 15.
154. Kelly, K. L.; Coronado, E.; Zhao, L. L.; Schatz, G. C. *J. Phys. Chem. B* **2002,** 107, (3), 668-677.
155. Pack, A.; Grill, W.; Wannemacher, R. *Ultramicroscopy* **2003,** 94, (2), 109-123.
156. Emmanuel, F.; Samuel, G. *J. Phys. D-Appl. Phys.* **2008,** 41, (1), 013001.
157. Lakowicz, J. *Plasmonics* **2006,** 1, (1), 5-33.
158. Chen, Y.; Munechika, K.; Ginger, D. S. *Nano Lett.* **2007,** 7, (3), 690-696.
159. Lakowicz, J. R.; Shen, Y.; D'Auria, S.; Malicka, J.; Fang, J.; Gryczynski, Z.; Gryczynski, I. *Anal. Biochem.* **2002,** 301, (2), 261-277.
160. Pompa, P. P.; Martiradonna, L.; Torre, A. D.; Sala, F. D.; Manna, L.; De Vittorio, M.; Calabi, F.; Cingolani, R.; Rinaldi, R. *Nature Nanotechnol.* **2006,** 1, (2), 126-130.
161. Ray, K.; Badugu, R.; Lakowicz, J. R. *Langmuir* **2006,** 22, (20), 8374-8378.
162. Anger, P.; Bharadwaj, P.; Novotny, L. *Phys. Rev. Lett.* **2006,** 96, (11), 113002.
163. Aslan, K.; Gryczynski, I.; Malicka, J.; Matveeva, E.; Lakowicz, J. R.; Geddes, C. D. *Curr. Opin. Biotechno.* **2005,** 16, (1), 55-62.
164. Thomas, M.; Greffet, J.-J.; Carminati, R.; Arias-Gonzalez, J. R. *Appl. Phys. Lett.* **2004,** 85, (17), 3863-3865.
165. Malicka, J.; Gryczynski, I.; Gryczynski, Z.; Lakowicz, J. R. *Anal. Biochem.* **2003,** 315, (1), 57-66.
166. Moses, J. E.; Moorhouse, A. D. *Chem. Soci. Rev.* **2007,** 36, (8), 1249-1262.
167. Rostovtsev, V. V.; Green, L. G.; Fokin, V. V.; Sharpless, K. B. *Angew. Chem. Int. Edi.* **2002,** 41, (14), 2596-2599.
168. Qin, G.; Santos, C.; Zhang, W.; Li, Y.; Kumar, A.; Erasquin, U. J.; Liu, K.; Muradov, P.; Trautner, B. W.; Cai, C. *J. Am. Chem. Soc.* **2010,** 132, (46), 16432-16441.
169. Santoyo-Gonzalez, F.; Hernandez-Mateo, F. *Chem.Soc.Rev.* **2009,** 38, (12), 3449-3462.

170. Marrani, A. G.; Dalchiele, E. A.; Zanoni, R.; Decker, F.; Cattaruzza, F.; Bonifazi, D.; Prato, M. *Electrochimica Acta* **2008,** 53, (11), 3903-3909.
171. Ciampi, S.; Böcking, T.; Kilian, K. A.; James, M.; Harper, J. B.; Gooding, J. J. *Langmuir* **2007,** 23, (18), 9320-9329.
172. Ciampi, S.; Eggers, P. K.; Le Saux, G.; James, M.; Harper, J. B.; Gooding, J. J. *Langmuir* **2009,** 25, (4), 2530-2539.
173. Devaraj, N. K.; Collman, J. P. *QSAR & Comb. Sci.* **2007,** 26, (11-12), 1253-1260.
174. Munford, M. L.; Cortès, R.; Allongue, P. *Sens. Mater.* **2001,** 13, 259.
175. Faucheux, A.; Gouget-Laemmel, A. C.; Allongue, P.; Henry de Villeneuve, C.; Ozanam, F.; Chazalviel, J. N. *Langmuir* **2007,** 23, (3), 1326-1332.
176. Sieval, A. B.; van den Hout, B.; Zuilhof, H.; Sudhölter, E. J. R. *Langmuir* **2000,** 16, (7), 2987-2990.
177. Gouget-Laemmel, A. C.; Yang, J.; Lodhi, M. A.; Siriwardena, A.; Aureau, D.; Boukherroub, R.; Chazalviel, J.-N.; Ozanam, F.; Szunerits, S. *J. Phys. Chem. C* **2013,** 117, (1), 368-375.
178. SECEN, H.; KALPAR, A. H. *Turk. J. Chem.* **1999,** 23, 27-30.
179. Yu, B.; Xie, J.; Deng, S.; Hui, Y. *J. Am. Chem. Soc.* **1999,** 121, (51), 12196-12197.
180. Negishi, K.; Mashiko, Y.; Yamashita, E.; Otsuka, A.; Hasegawa, T. *Polymers* **2011,** 3, (1), 489-508.
181. Otsuka, A.; Sakurai, K.; Hasegawa, T. *Chem. Commun.* **2009**, (36), 5442-5444.
182. Somsák, L. *Chem. Rev.* **2001,** 101, (1), 81-136.
183. Bock, V. D.; Hiemstra, H.; van Maarseveen, J. H. *Eur. J. Org. Chem.* **2006,** 2006, (1), 51-68.
184. Rodionov, V. O.; Presolski, S. I.; Díaz Díaz, D.; Fokin, V. V.; Finn, M. G. *J. Am. Chem. Soc.* **2007,** 129, (42), 12705-12712.
185. DuBois, M.; Gilles, K. A.; Hamilton, J. K.; Rebers, P. A.; Smith, F. *Anal. Chem.* **1956,** 28, (3), 350-356.
186. Panagiotopoulos, C.; Sempere, R. *Limnol. Oceanogr.* **2005,** 3, 419–454.
187. Collman, J. P.; Devaraj, N. K.; Eberspacher, T. P. A.; Chidsey, C. E. D. *Langmuir* **2006,** 22, (6), 2457-2464.
188. Li, Y.; Wang, J.; Cai, C. *Langmuir* **2011,** 27, (6), 2437-2445.
189. Liao, W.; Wei, F.; Liu, D.; Qian, M. X.; Yuan, G.; Zhao, X. S. *Sensor Actuat. B-Chem.* **2006,** 114, (1), 445-450.
190. Liao, W.; Wei, F.; Qian, M. X.; Zhao, X. S. *Sensor Actuat. B-Chem.* **2004,** 101, (3), 361-367.
191. *Fluorescence Polarization Technical Resource Guide FOURTH EDITION.* Invitrogen Corporation.: 2006.
192. Sigal, G. B.; Mrksich, M.; Whitesides, G. M. *Langmuir* **1997,** 13, (10), 2749-2755.
193. Sigal, G. B.; Mrksich, M.; Whitesides, G. M. *J. Am. Chem. Soc.* **1998,** 120, (14), 3464-3473.
194. Bhuyan, A. K. *Biopolymers* **2010,** 93, (2), 186-199.
195. Lee, A.; Tang, S. K. Y.; Mace, C. R.; Whitesides, G. M. *Langmuir* **2011,** 27, (18), 11560-11574.
196. Svedhem, S.; Öhberg, L.; Borrelli, S.; Valiokas, R.; Andersson, M.; Oscarson, S.; Svensson, S. C. T.; Liedberg, B.; Konradsson, P. *Langmuir* **2002,** 18, (7), 2848-2858.
197. Barth, A.; Zscherp, C. *Quarterly Rev. Biophys.* **2002,** 35, (04), 369-430.
198. Wei, Y.; Thyparambil, A. A.; Latour, R. A. *Colloids Surf. B.* **2013,** 110, (0), 363-371.
199. Banerjee, R.; Das, K.; Ravishankar, R.; Suguna, K.; Surolia, A.; Vijayan, M. *J. Mol. Bio.* **1996,** 259, (2), 281-296.

200. Casset, F.; Hamelryck, T.; Loris, R.; Brisson, J.-R.; Tellier, C.; Dao-Thi, M.-H.; Wyns, L.; Poortmans, F.; Pérez, S.; Imberty, A. *J. Bio. Chem.* **1995,** 270, (43), 25619-25628.
201. Ivanov, Y.; Frantsuzov, P.; Zollner, A.; Medvedeva, N.; Archakov, A.; Reinle, W.; Bernhardt, R. *Nanoscale Res. Lett.* **2011,** 6, (1), 54.
202. Ortega-Vinuesa, J. L.; Tengvall, P.; Lundström, I. *Thin Solid Films* **1998,** 324, (1–2), 257-273.
203. Ratcliff, G. C.; Erie, D. A. *J. Am. Chem. Soc.* **2001,** 123, (24), 5632-5635.
204. Sicard, D.; Cecioni, S.; Iazykov, M.; Chevolot, Y.; Matthews, S. E.; Praly, J.-P.; Souteyrand, E.; Imberty, A.; Vidal, S.; Phaner-Goutorbe, M. *Chem. Commun.* **2011,** 47, (33), 9483-9485.
205. Gour, N.; Verma, S. *Tetrahedron* **2008,** 64, (30–31), 7331-7337.
206. Ngunjiri, J.; Stark, D.; Tian, T.; Briggman, K.; Garno, J. *Anal. Bioanal. Chem.* **2013,** 405, (6), 1985-1993.
207. Waner, M. J.; Gilchrist, M.; Schindler, M.; Dantus, M. *J. Phys. Chem. B* **1998,** 102, (9), 1649-1657.
208. Malmström, J.; Agheli, H.; Kingshott, P.; Sutherland, D. S. *Langmuir* **2007,** 23, (19), 9760-9768.
209. Stenberg, E.; Persson, B.; Roos, H.; Urbaniczky, C. *J. Coll. Inter. Sci.* **1991,** 143, (2), 513-526.
210. Benesch, J.; Askendal, A.; Tengvall, P. *Colloids Surf., B* **2000,** 18, (2), 71-81.
211. Höök, F.; Vörös, J.; Rodahl, M.; Kurrat, R.; Böni, P.; Ramsden, J. J.; Textor, M.; Spencer, N. D.; Tengvall, P.; Gold, J.; Kasemo, B. *Colloids Surf. B* **2002,** 24, (2), 155-170.
212. Lassen, B.; Malmsten, M. *J. Coll. Inter. Sci.* **1996,** 179, (2), 470-477.
213. Lassen, B.; Malmsten, M. *J. Coll. Inter. Sci.* **1997,** 186, (1), 9-16.
214. Özkumur, E.; Yalçın, A.; Cretich, M.; Lopez, C. A.; Bergstein, D. A.; Goldberg, B. B.; Chiari, M.; Ünlü, M. S. *Biosens. Bioelectron.* **2009,** 25, (1), 167-172.
215. Tessler, L. A.; Reifenberger, J. G.; Mitra, R. D. *Anal. Chem.* **2009,** 81, (17), 7141-7148.
216. Roach, P.; Shirtcliffe, N. J.; Farrar, D.; Perry, C. C. *J. Phys. Chem. B* **2006,** 110, (41), 20572-20579.
217. Fink, D. J.; Hutson, T. B.; Chittur, K. K.; Gendreau, R. M. *Anal. Biochem.* **1987,** 165, (1), 147-154.
218. Ye, M.; Zhang, Q.-L.; Li, H.; Weng, Y.-X.; Wang, W.-C.; Qiu, X.-G. *Biophys. J.* **2007,** 93, (8), 2756-2766.
219. Kroll, U.; Meier, J.; Shah, A.; Mikhailov, S.; Weber, J. *J. Appl. Phys.* **1996,** 80, (9), 4971-4975.
220. Ray, S.; Das, D.; Barua, A. K. *Sol. Energ. Mater.* **1987,** 15, (1), 45-57.
221. Shanks, H., R.; Jeffrey, F., R.; Lowry, M., E. *J. Phys. Colloques* **1981,** 42, (C4), C4-773-C4-777.
222. Dhayal, M.; Ratner, D. M. *Langmuir* **2009,** 25, (4), 2181-2187.
223. Yang, J.; Chazalviel, J.-N.; Siriwardena, A.; Boukherroub, R.; Ozanam, F.; Szunerits, S.; Gouget-Laemmel, A. C. *Anal. Chem.* **2014,** 86, 10340-10349.
224. Gorostiza, P.; Henry de Villeneuve, C.; Sun, Q. Y.; Sanz, F.; Wallart, X.; Boukherroub, R.; Allongue, P. *J. Phys. Chem. B* **2006,** 110, (11), 5576-5585.
225. Gruber, K.; Horlacher, T.; Castelli, R.; Mader, A.; Seeberger, P. H.; Hermann, B. A. *ACS Nano* **2011,** 5, (5), 3670-3678.
226. Hone, D. C.; Haines, A. H.; Russell, D. A. *Langmuir* **2003,** 19, (17), 7141-7144.
227. Chabal, Y. J. *Surf. Sci. Rep.* **1988,** 8, (5–7), 211-357.

Résumé: Les interactions spécifiques carbohydrate/protéine joue un rôle important dans de nombreux processus physiologiques et pathologiques. Cette thèse a mis au point des biocapteurs sur silicium pour l'étude de telles interactions. Dans une première approche, on a établi une stratégie de fonctionnalisation multi-étapes du silicium cristallin *via* des liaisons covalentes Si-C robustes pour accrocher des précurseurs propargyl-glycanes par chimie click. Chaque étape a été soigneusement caractérisée par IR-ATR, AFM et XPS, conduisant à la formation de monocouches denses composées d'entités oligo(éthylène glycol) et terminées par une fonction glycane (mannose ou lactose). Ces nouvelles surfaces de glycane ont montré une très bonne biorésistance aux lectines non spécifiques et une excellente sélectivité vis-à-vis de lectines spécifiques. En utilisant la spectroscopie IR quantitative et la simulation numérique, on a démontré l'importance de la concentration surfacique en glycane pour favoriser des interactions multivalentes entre les glycanes et la lectine spécifique (constantes d'affinité proche du micromolaire). Dans une seconde approche, on a mis au point une puce à glycanes constituée d'une couche mince de silicium amorphe carboné déposée sur des nanoparticules d'or sur verre. L'imagerie par fluorescence a validée la spécificité des interactions entre les glycanes clickées à la surface de la biopuce et des lectines fluorescentes. En optimisant la distance entre les lectines et les nanoparticules, l'exaltation de la fluorescence par les plasmons de surface localisées a permis d'augmenter la sensibilité de la biopuce au niveau du picomolaire.

Mots-clés: interactions glycane-protéine; biopuce à glycanes; silicium cristallin; silicium amorphe carboné; exaltation plasmonique de la fluorescence; spectroscopie infrarouge quantitative; chimie click.

Abstract: Specific carbohydrate/protein interactions play an important role in numerous physiological and pathological processes. Silicon-based biosensors have been envisaged for studying such interactions here. In a first approach, a multistep functionalization strategy was established on crystalline silicon *via* robust covalent Si-C bonds to incorporate oligo(ethylene glycol) units and generate a glycan-terminated monolayer by "click" chemistry. The functionalization process was carefully characterized by IR-ATR, AFM and XPS, leading to the formation of highly compact organic monolayers. The as-fabricated glycan-terminated surface showed good antifouling property towards non-specific lectins and excellent selectivity towards specific lectins. By using quantitative IR-ATR analysis and numerical simulation, we demonstrated the importance of the surface concentration of glycans to favor the multivalent binding of the glycan ligands on the surface with the specific lectins. In a second approach, the amorphous silicon-carbon alloy thin films coated on gold nanoparticles were used as the substrate for the elaboration of glycan microarray. Fluorescence imaging was used for the recognition specificity of the glycans clicked on the surface with the dye-labeled lectins. By optimizing the distance between the fluorophore and the nanoparticles, best localized surface plasmon resonance (LSPR)-enhanced fluorescence was achieved to improve the microarray sensitivity with a limit of detection at the picomolar level.

Keywords: glycan-protein interactions; glycan microarrays; crystalline silicon; amorphous silicon-carbon alloy; LSPR-enhanced fluorescence; quantitative IR spectroscopy; click chemistry.